

**SYNTHESIS AND CHARACTERIZATION OF COATED  
AGGLOMERATE PELLETISATION (CAP) PELLETS OF  
THORIA BASED MATERIALS FOR NUCLEAR FUELS**

**By  
P.S.SOMAYAJULU  
ENGG 01200904023**

**Bhabha Atomic Research Centre, Trombay**

*A thesis submitted to the  
Board of Studies in Engineering Sciences  
In partial fulfillment of requirements  
for the Degree of  
DOCTOR OF PHILOSOPHY  
of  
HOMI BHABHA NATIONAL INSTITUTE*



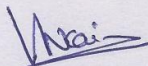
**June, 2017**



# Homi Bhabha National Institute

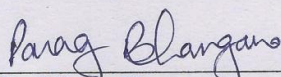
## Recommendations of the Viva Voce Committee

As members of the Viva Voce Committee, we certify that we have read the dissertation prepared by P.S.Somayajulu entitled "*Synthesis and Characterization of Coated Agglomerate Pelletisation (CAP) Pellets of Thoria Based Materials for Nuclear Fuels*" and recommend that it may be accepted as fulfilling the thesis requirement for the award of Degree of Doctor of Philosophy.



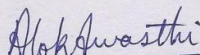
Chairman - **Prof. Vivekanand Kain**

Date: 22/06/2017



Examiner - **Prof. Parag Bhargava**

Date: 22/06/2017



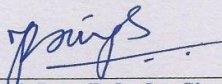
Guide / Convener/ Member 1 - **Prof. Alok Awasthi**

Date: 22/06/2017



Member 2- **Prof. Raghendra Tewari**

Date: 22/06/2017



Member 3- **Prof. Jung Bahadur Singh**

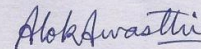
Date: 22/06/2017

Final approval and acceptance of this thesis is contingent upon the candidate's submission of the final copies of the thesis to HBNI.

I/We hereby certify that I/we have read this thesis prepared under my/our direction and recommend that it may be accepted as fulfilling the thesis requirement.

Date: 22/06/2017

Place: **Mumbai**



(ALOK AWASTHI)

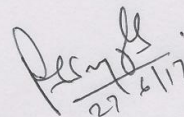
Guide



## STATEMENT BY AUTHOR

This dissertation has been submitted in partial fulfillment of requirements for an advanced degree at Homi Bhabha National Institute (HBNI) and is deposited in the Library to be made available to borrowers under rules of the HBNI.

Brief quotations from this dissertation are allowable without special permission, provided that accurate acknowledgement of source is made. Requests for permission for extended quotation from or reproduction of this manuscript in whole or in part may be granted by the Competent Authority of HBNI when in his or her judgment the proposed use of the material is in the interests of scholarship. In all other instances, however, permission must be obtained from the author.

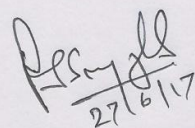


P. S. Somayajulu



## DECLARATION

I, hereby declare that the investigation presented in the thesis has been carried out by me. The work is original and has not been submitted earlier as a whole or in part for a degree / diploma at this or any other Institution / University.

  
27/6/17

P. S. Somayajulu



## List of Publications arising from the thesis

### Publications in Refereed Journal:

#### a. Published:

- 1) “Characterization of ThO<sub>2</sub>–UO<sub>2</sub> pellets made by Advanced CAP process”, T.R.G. Kutty, P.S. Somayajulu, K.B. Khan, J.P. Panakkal, Arun Kumar and H.S. Kamath, , Journal of Nucl. Mat., 2009, 384, 303–310.
- 2) “ThO<sub>2</sub>–UO<sub>2</sub> pellets made by Co–precipitation process”, T.R.G. Kutty, K.B. Khan, P.V. Achutan, P.S. Dharmi, A. Dakshinamurthy, P.S. Somayajulu, J.P. Panakkal, Arun Kumar and H.S. Kamath, Characterization of, Journal of Nucl. Mat., 2009, 389, 351–358.
- 3) “Thermal expansion and thermal conductivity of (Th,Ce)O<sub>2</sub> mixed oxides: A molecular dynamics and experimental Study”, P.S. Ghosh, P.S. Somayajulu, A. Arya, G.K. Dey, B.K. Dutta, Journal of Alloys and Compounds, 2015, 638, 172–181.
- 4) “Thermal Expansion and Thermal Conductivities of (Th,U)O<sub>2</sub> Mixed Oxides: A Molecular Dynamics and Experimental study”, P. S. Ghosh, P.S. Somayajulu, K. Krishnan, N. Pathak, A. Arya, G.K. Dey, , Journal of Alloys and Compounds, 2015, 650, 165–177.
- 5) “Experimental and Molecular Dynamics Study of Thermo–physical and Transport Properties of ThO<sub>2</sub>–5wt.%CeO<sub>2</sub> mixed oxides”, P.S. Somayajulu, P.S. Ghosh, J. Banerjee, K.L.N.C. Babu, K.M. Danny, B.P. Mandal, T. Mahata, P. Sengupta, S.K. Sali, A. Arya, , Journal of Nucl. Mat., 2015, 467, 644–659.
- 6) “Quality control of (Th,Pu)O<sub>2</sub> fuel pellet obtained by coated agglomerate pelletization”, P.S. Somayajulu, A. Sengupta, A.K. Karande, R. Malav, D.K. Das, Mohd. Afzal, Journal of Radioanalytical and Nuclear Chemistry, 2016, 308, 495–503.

- 7) “Thermal Expansion and Thermal Conductivity of (Th,Pu)O<sub>2</sub> Mixed Oxides: a Molecular Dynamics and Experimental Study”, P.S. Somayajulu, P.S. Ghosh, A. Arya, G.K. Dey, , Journal of Alloys and Compounds, 2016, 664, 291–303.

b. Accepted: —

c. Communicated:

1. “Characterisation of plutonium rich agglomerates in MOX Fuel by New Methods of Analysis of Alpha Autoradiographs”, K.V. Vrinda Devi, R. Jayshree, P.S. Somayajulu, J.N. Dubey, I.H. Shaikh, S. Chandramouleeswaran, K.B. Khan, Nuclear Instruments and methods in physics research section B.

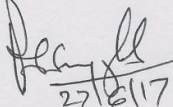
d. Other Publications:

**International/ National Conferences:**

- 1) “Characterization of ThO<sub>2</sub>–UO<sub>2</sub> fuels made by CAP process”, T.R.G. Kutty, P.S. Somayajulu, J.P. Panakkal, Arun Kumar and H.S. Kamath, International Conference on the peaceful uses of atomic energy (ICPUAE), N.Delhi, 2009.
- 2) “Characterization of co–precipitated (Th,U)O<sub>2</sub> powders by thermogravimetry”, T.R.G. Kutty, K.B. Khan, P.V. Achutan, P.S. Somayajulu, Arun Kumar and H.S. Kamath, International Conference on Characterization and Quality control of Nuclear Fuels (CQCNF), Hyderabad, 2009.
- 3) “Studies on agglomerates during Coated Agglomerate Pelletisation Process”, P.S. Somayajulu, K.M. Danny, P.S. Kutty, J. Banerjee, K.B. Khan and Arun Kumar, National Conference on Power from Thorium: Present Status and Future Directions (NCPTh), Mumbai, 2014.

- 4) “Fabrication and Characterization studies on ThO<sub>2</sub>–6%UO<sub>2</sub> fabricated by Coated Agglomerate Pelletisation Process”, P.S. Somayajulu, K.M. Danny, P.S. Kutty, J. Banerjee, B.P. Mandal, Jayshree Ramkumar, K.B. Khan and Arun Kumar, National Conference on Power from Thorium: Present Status and Future Directions (NCPTh), Mumbai, 2014.
- 5) “Gamma Scanning studies of (Th,Pu)O<sub>2</sub> MOX fuel for AHWR–CF”, K.V. Vrinda Devi, D.B. Sathe, P.S. Somayajulu and Arun Kumar, National Conference on Power from Thorium: Present Status and Future Directions (NCPTh), Mumbai, 2014.
- 6) “Determination of thermo–physical properties of ThO<sub>2</sub>–CeO<sub>2</sub> MOX using classical molecular dynamics simulations”, P.S. Ghosh, A. Arya, P.S. Somayajulu, B.K. Dutta and G.K. Dey, National Conference on Power from Thorium: Present Status and Future Directions (NCPTh), Mumbai, 2014.
- 7) “Compositional Analysis Of (Th–U)O<sub>2</sub> MOX Using Alpha Autoradiography”, I.H. Shaikh, J.N. Dubey, Jyoti Gupta, B.B. Shriwastwa, K.V. Vrinda Devi, P.S. Somayajulu, K.B. Khan and Arun Kumar, National Conference on Power from Thorium: Present Status and Future Directions (NCPTh), Mumbai, 2014.
- 8) “UV–Visible Spectroscopic analysis for optimizing etching conditions of CR39 based alpha autoradiography of (Th,Pu)O<sub>2</sub> MOX fuels”, Jayshree Ramkumar, K.V. Vrinda Devi, P.S. Somayajulu, S. Chandramouleeswaran, K.B. Khan, Arun Kumar, 19th National Conference on Solid State Nuclear Track Detectors and their Applications (SSNTDs–19), 2015
- 9) “UV–Visible Spectroscopic studies on MOX fuel irradiated CR39 film”, Jayshree Ramkumar, K.V. Vrinda Devi, P.S. Somayajulu, S. Chandramouleeswaran, K.B. Khan, ICM, 2015.

- 10) "Characterisation of ThO<sub>2</sub>-CeO<sub>2</sub> sintered pellets fabricated by POP and CAP processes using impedance spectroscopy technique", P.S. Somayajulu, K.M. Danny, D. Rajashree, T. Mahata, R.K. Lenka, P.K. Patro, K.B. Khan, ThEC15,2015.
- 11) "Alpha Autoradiography Studies of Thoria- Plutonia Experimental Fuel for Pu Homogeneity", K.V. Vrinda Devi, P.S. Somayajulu, J.N. Dubey, I.H. Shaikh, S.D. Raut, Jyoti Gupta, K.B. Khan, Arun Kumar, ThEC15,2015.
- 12) "Characterisation of (Th,Pu)O<sub>2</sub> MOX fuel by analysis of Alpha images", K.V. Vrinda Devi, J.N. Dubey, I.H. Shaikh, Jyoti Gupta, P.S. Somayajulu, K.B. Khan, 19th National Conference on Solid State Nuclear Track Detectors and their Applications (SSNTDs-19), 2015.

  
27/8/17  
**P. S. Somayajulu**

*Dedicated to*

*My parents*

*(Smt. P.Kameswari & Dr. P. Suryanarayana)*

*My Idols*

*(Dr.H.J.Bhabha and Sir J.R.D.Tata)*

**&**

***My dearest loving brother***

***Late. P.S.Murthy***

## **Acknowledgment**

*I express my sincere gratitude to my guide, Dr Alok Awasthi for not only giving me an opportunity to work under his guidance for this PhD. work but also providing me with a wonderful experience of learning under his close supervision. I am indebted to him for all the support, encouraging and comforting words which he had for me to put to rest my doubts and made me believe in me. I sincerely thank him for his invaluable suggestions and technical comments during our interactions which were very helpful in enhancing the quality of the work. I am also extremely indebted and would like to express my deepest gratitude to my former guide Dr. T.R.G. Kutty, without whom this thesis work would not have been possible. His constant encouragement during the entire course of this work, support and guidance throughout, is gratefully acknowledged.*

*I would also like to express my deepest and sincere thanks to Shri H.S. Kamath, Former Director, Nuclear Fuels Group, for sowing the creative and innovative idea and assigning me with a huge responsibility which gradually culminated into this work. I would like to thank my former senior colleagues Shri Arun Kumar, Shri Mohd. Afzal and Shri J.P. Panakkal for their keen interest in the work and much needed timely support extended. I express my sincere thanks and gratitude to Dr. K.B. Khan, Head, RadioMetallurgy Division and Shri V. Bhasin, Director, Nuclear Fuels Group, for their encouragement and help.*

*I am highly indebted to Dr. Ashok Arya, Dr. Abhijit Ghosh, Dr. R. Tewari and Dr. Deep Prakash for their invaluable help, useful suggestions, technical discussions and support they have extended. I thank them from the bottom of my heart for devoting their precious time and efforts they have put to help me in realizing this work. I would like to thank all of you individually for sacrificing your valuable time to go through the thesis, offering your valuable comments and suggestions and most of all, for being very supportive, encouraging and feeding me with very comforting words to boost my confidence.*

*I take this opportunity to express my humble thanks to Dr. Vivekanand Kain and Dr. J.B. Singh for their valuable comments and feedback which provided much deserved value addition to the work.*

*I would like to thank with profound gratitude to Shri P.S. Kutty, Dr. R.K. Bhagat, Dr. T. Mahata, Dr. J. Banerjee, Shri I.H. Shaikh, Shri K. Ravi, Shri C. Nandi, Shri P.F. Pereira, Dr.B.P. Mandal, Shri Deepak Kamble, Shri B.N. Rath and Dr. Pranesh Sengupta who went beyond the limits to extend their help to conduct valuable experiments. I wish to thank Dr.(Smt.) Smruti Dash, Shri Sumanata Mukherjee and Dr.S.K. Sali for carrying out valuable*

*experiments and extending their help. I wish to acknowledge immense contributions and assistance provided by my colleagues, Shri K.M. Danny, Shri P. Pareek, Shri F. Ali, Shri M.S. Sharma and especially Smt. Rajashree Dixit during various stages of this work and thesis preparation. I would like to express my thanks to co-authors of my papers for their valuable contributions and help especially Dr. Arijit Sengupta and Shri Parthasarathi Ghosh for building a beautiful relation of friendship. I also wish to thank all my friends for their wishes and constant pushing because of which I could successfully complete the work.*

*Lastly, I am highly indebted to my wife, Vrinda Devi for her continuous support and help on both professional and personal front, to my sons, Karthik Krishna and Suryaganesh, for sacrificing many of their plans to give me company and my sister in law for taking care of my parents and helping me to concentrate on my work. I acknowledge that without their understanding, support and cooperation, it would have been impossible to complete this work.*

## Abstract

---

A new process, coated agglomerate pelletization (CAP) process, was developed by us as an alternative to present conventional process of powder processing and pelletization (POP) to address issues related to fabrication of thorium based fuels having high specific radioactivity. This research study presents detailed investigations on the characteristics and thermal properties of the CAP pellets in comparison with the POP pellets with the aim of assessing the feasibility of CAP process for (Th,Pu)O<sub>2</sub> fuel fabrication. In POP process, ThO<sub>2</sub> and UO<sub>2</sub> powders are mixed together and compacted prior to sintering. However, in CAP process, ThO<sub>2</sub> powder is first extruded, spheroidized and then coated with UO<sub>2</sub> powder, which allows a substantial part of powder processing to be carried out in unshielded facility.

The fissile material distribution (homogeneity) in the green CAP pellets is different than that in the green POP pellets. This results in sintered pellets with different characteristics including thermal properties. The CAP and POP pellets are therefore thoroughly investigated in this work to assess the differences in their in-reactor performance. Theoretical understanding of thermal behavior of Th-based MOX fuels of relevant compositions using Molecular Dynamics (MD) simulations for pellets with actual imperfections has been developed and performed and subsequently verified with experimental results. Thermal properties are extrapolated to higher temperatures for different compositions through molecular dynamic simulation by developed methodology.

As the fuel behavior is governed by cumulative effect of various properties such as density, microstructure, chemical purity, homogeneity and thermal properties, which are investigated. Due to high radioactive nature of the samples, the availability of characterization techniques is being rather limited. Some important studies are conducted using surrogate systems of (Th,Ce)O<sub>2</sub> and (Th,U)O<sub>2</sub>. Simulation studies conducted using

surrogate materials of this research are verified and validated using limited amount of available  $\text{PuO}_2$ .

The CAP and POP samples have been sintered under identical conditions and thermal property investigations are performed.

From the studies conducted on surrogate systems and actual  $(\text{Th,Pu})\text{O}_2$  system, it is concluded that heterogeneous distribution of plutonium observed in the CAP pellets does not significantly impact the thermal conductivity of the fuel and therefore should be able to meet the desired linear heat rating of the fuel. In fact, some features of these pellets should result in improved in-reactor behavior of the fuel due to reduced fission gas release and reduced pellet clad mechanical interaction.

Coated agglomerate pelletization process is a potential technique for fabrication of nuclear fuel bearing high specific radioactivity such as  $\text{U}^{233}\text{O}_2$  and  $\text{PuO}_2$ . It not only offers various advantages like reduced man-rem problems, increased production rate, reduced radioactive liquid waste generation and improved safety, but also suffices the fuel property requirement. Hence, this research confirms that the CAP process is definitely a viable and beneficial technique for the fabrication of highly radioactive  $(\text{Th,Pu})\text{O}_2$  and  $(\text{Th,U}^{233})\text{O}_2$  fuel pellets.

## Table of Contents

---

List of Figures .....	xxii
<i>List of Tables</i> .....	xxvi
CHAPTER 1. INTRODUCTION .....	1
1.1 Preamble .....	1
1.2 Background .....	1
1.3 Motivation and methodology of present work .....	9
1.4 Objectives.....	11
1.5 Structure of the thesis .....	12
CHAPTER 2. LITERATURE SURVEY .....	14
2.1 Preamble .....	14
2.2 Thoria based systems.....	14
2.3 ThO <sub>2</sub> -CeO <sub>2</sub> system .....	22
2.4 ThO <sub>2</sub> -PuO <sub>2</sub> system .....	24
CHAPTER 3. EXPERIMENTAL METHODOLOGY .....	28
3.1 Experimental details.....	28
3.1.1 Feed Material.....	28
3.1.2 Preparation of green pellets .....	34
3.1.3 Fabrication of Sintered compacts .....	37
3.1.4 Fabrication of pins.....	39
3.2 Characterization Techniques .....	39
3.2.1 Density .....	39
3.2.2 Oxygen to metal ratio by Thermo gravimetric (TG) analysis .....	39
3.2.3 XRD studies .....	40
3.2.4 Microstructure .....	40
3.2.5 Chemical analysis (Heavy metal content and Total impurity) .....	41
3.2.6 Alpha- Autoradiography.....	41

3.2.7	Transport property (Ionic conductivity).....	42
3.2.8	Thermal Expansion.....	42
3.2.9	Thermal diffusivity .....	45
3.2.10	Thermal conductivity .....	46
3.2.11	Passive Gamma Scanning.....	46
3.2.12	Specific Heat (Cp) .....	47
CHAPTER 4. CHARACTERIZATION STUDIES ON (Th,Ce)O <sub>2</sub> SYSTEM.....		49
4.1	Introduction .....	49
4.2	Shrinkage behavior POP and CAP pellets.....	49
4.3	Sintering of actual pellets .....	62
4.4	Microstructure and homogeneity.....	63
4.5	Formation of (Th,Ce)O <sub>2</sub> solid-solutions.....	74
4.6	Ionic conductivity.....	76
4.7	Stoichiometry (O/M) .....	84
4.8	Specific heat (C <sub>p</sub> ) .....	86
4.9	Thermal properties .....	89
4.9.1	Theoretical Methodology.....	89
4.9.1.1	Interatomic potential function for pure oxides and MOX.....	89
4.9.1.2	Empirical potential .....	90
4.9.1.3	MD simulation details .....	90
4.9.1.4	Theoretical Calculations (Coulomb-Buckingham-Morse-many-body potential) .....	91
4.10	Thermal expansion.....	92
4.11	Thermal Diffusivity .....	97
4.12	Thermal conductivity .....	99
4.13	Microstructure effects on fuel behavior – current knowledge .....	105
4.14	Summary .....	107
CHAPTER 5. CHARACTERIZATION STUDIES ON (Th,Pu)O <sub>2</sub> SYSTEM.....		109

5.1	Introduction .....	109
5.2	Density .....	111
5.3	Alpha autoradiography studies.....	111
5.3.1	Optimization of etching using UV spectroscopy .....	115
5.3.2	Compositional characterization .....	119
5.3.3	Homogeneity studies.....	124
5.4	Microstructure .....	129
5.5	X-Ray Diffraction .....	129
5.6	Passive Gamma Scanning (PGS) .....	136
5.7	Thermal Properties .....	138
5.7.1	Thermal Expansion.....	139
5.7.2	Thermal diffusivity and Thermal Conductivity.....	144
5.8	Summary .....	151
CHAPTER 6. CHARACTERIZATION STUDIES ON (Th,U)O <sub>2</sub> SYSTEM .....		153
6.1	Introduction .....	153
6.2	Pellets fabricated using pure oxide powders.....	154
6.2.1	Micro homogeneity.....	157
6.2.2	Microstructure and homogeneity.....	158
6.2.3	XRD.....	161
6.2.4	Chemical analysis .....	163
6.2.5	Thermal property evaluation .....	168
6.3	Characterization of pellets fabricated using co-precipitated powders.....	178
6.3.1	Density .....	178
6.3.2	Microstructure .....	179
6.3.3	Uranium distribution.....	181
6.3.4	XRD.....	184
6.4	Summary .....	187

CHAPTER 7. CONCLUSIONS .....	189
7.1 Main Conclusions .....	189
7.2 Novel Techniques Developed .....	195
7.3 POP versus CAP .....	196
7.4 Recommendations for Future Work .....	197
References .....	199

## List of Figures

---

<i>Figure 1.1 : (a) AHWR fuel cluster showing configuration and fixtures for assembling the fuel pins [10] and (b) Schematic diagram of a typical AHWR (Th,1%Pu)O<sub>2</sub> fuel pin filled helium gas and loaded with fuel pellets and hardware [11].</i>	2
<i>Figure 1.2 : Flowsheet showing various operations involved in powder processing and pelletization (POP) process.</i>	4
<i>Figure 1.3 : Flowsheet of coated agglomerate pelletization (CAP) process.</i>	6
<i>Figure 2.1 : Phase diagram of ThO<sub>2</sub>-UO<sub>2</sub> system [25].</i>	18
<i>Figure 2.2 : Phase diagram of ThO<sub>2</sub>-PuO<sub>2</sub> system [74].</i>	25
<i>Figure 3.1: SEM photographs showing morphology of ThO<sub>2</sub> powder (a) before milling, (b) after milling, (c) CeO<sub>2</sub> powder and (d) U<sub>3</sub>O<sub>8</sub> powder.</i>	30
<i>Figure 3.2 : (a) Thoria extrudes and (b) Thoria spheroids.</i>	31
<i>Figure 3.3 : XRD patterns of ThO<sub>2</sub>-50%UO<sub>2</sub> powder made by co-precipitation process.</i>	32
<i>Figure 3.4: XRD patterns of ThO<sub>2</sub>-50%UO<sub>2</sub> powder at higher angles for the determination of lattice parameters.</i>	32
<i>Figure 3.5: (a) Thoria extrudes coated with U<sub>3</sub>O<sub>8</sub> (b) Green CAP pellets.</i>	36
<i>Figure 3.6: ThO<sub>2</sub>-5%CeO<sub>2</sub> green pellet fabricated by CAP process.</i>	37
<i>Figure 3.7: Sintering profile temperature with respect to time.</i>	38
<i>Figure 3.8 : Comparison of experimental percentage thermal expansion data of Tungsten 737, the NIST Standard Reference Material (SRM 737), against reported data.</i>	44
<i>Figure 3.9: Phase transformation temperatures for uranium metal as observed in dilatometer.</i>	45
<i>Figure 3.10: Schematic of annular counting set up.</i>	47
<i>Figure 4.1 : Densification plots of ThO<sub>2</sub>-CeO<sub>2</sub> POP green pellets and CAP green pellets under air and Ar atmosphere with respect to temperature.</i>	51
<i>Figure 4.2 : Shrinkage rate plots of ThO<sub>2</sub>-CeO<sub>2</sub> POP green pellets and CAP green pellets under air and Ar atmosphere.</i>	51
<i>Figure 4.3 : Schematic representation of sintering of POP samples (a) in air and (b) Ar atmospheres.</i>	56
<i>Figure 4.4 : Schematic representation of sintering of CAP samples (a) in air and (b) Ar atmospheres.</i>	58
<i>Figure 4.5 : Microstructure of the (a) CAP and (b) POP pellets sintered in air atmosphere (SEM images).</i>	63

<i>Figure 4.6: Microstructure of the (a) POP and (b) CAP pellets sintered in Ar–H<sub>2</sub> atmosphere (SEM images).....</i>	<i>64</i>
<i>Figure 4.7: (a) EPMA image of CAP pellet sintered in Ar–H<sub>2</sub> atmosphere (b) Ce elemental mapping of area shown in figure (a), (c) Th mapping of area shown in figure (a), (d) EPMA image of POP pellet sintered in Ar–H<sub>2</sub> atmosphere and (e) Th and Ce combined mapping of area shown in figure (d).....</i>	<i>65</i>
<i>Figure 4.8: (a) EPMA image of CAP pellet sintered in air atmosphere (b) Ce elemental mapping of area shown in figure (a), (c) Th mapping of area shown in figure (a), (d) EPMA image of POP pellet sintered in air atmosphere and (e) Th and Ce combined mapping of area shown in figure (d). .....</i>	<i>66</i>
<i>Figure 4.9 : XRD patterns of ThO<sub>2</sub> and ThO<sub>2</sub>–5%CeO<sub>2</sub> POP and CAP pellets sintered in air atmosphere at 1823 K for 4 h and Ar–H<sub>2</sub> atmosphere at 1923 K for 4 h. ....</i>	<i>75</i>
<i>Figure 4.10 : Expanded view (expanded around 27.5°) of XRD patterns of pellets sintered in (a) Ar–H<sub>2</sub> atmosphere at 1923 K for 4 h and (b) Air atmosphere at 1823 K for 4 h. ....</i>	<i>76</i>
<i>Figure 4.11: (a–d) The impedance plots for ThO<sub>2</sub>–5 wt. % CeO<sub>2</sub> of POP and CAP pellets sintered in air and Ar–H<sub>2</sub> atmospheres at different temperatures and (e) impedance plot measured at 600°C for ThO<sub>2</sub>–5 wt. % CeO<sub>2</sub> pellets of POP and CAP sintered in air and Ar–H<sub>2</sub> atmospheres.....</i>	<i>80</i>
<i>Figure 4.12 : Thermogravimetric plot of CAP and POP pellets under moist Ar–8%H<sub>2</sub> atmosphere. .....</i>	<i>85</i>
<i>Figure 4.13 : DSC measured temperature variation of C<sub>p</sub> values of ThO<sub>2</sub>–5 wt. % CeO<sub>2</sub> POP and CAP pellets sintered in air and Ar–H<sub>2</sub> atmospheres along with Neumann–Kopp (N–K) values. ThO<sub>2</sub> (a) and ThO<sub>2</sub> (b) represents experimentally measured C<sub>p</sub> values of ThO<sub>2</sub> taken from reference [69] and [146], respectively.....</i>	<i>86</i>
<i>Figure 4.14 : (a) Thermal expansion of ThO<sub>2</sub> measured by dilatometer and polynomial fitted curve compared with polynomial equation described by Touloukian et al [75] and (b) Thermal expansion of (Th,5%Ce)O<sub>2</sub> POP and CAP pellets sintered in different atmospheres. ....</i>	<i>93</i>
<i>Figure 4.15: (a) Experimentally measured thermal diffusivity of ThO<sub>2</sub> and ThO<sub>2</sub>–5% CeO<sub>2</sub> (POP and CAP pellets) sintered in air and (b) ThO<sub>2</sub>–5% CeO<sub>2</sub> (POP and CAP pellets) sintered in Ar–H<sub>2</sub> atmosphere. ....</i>	<i>98</i>
<i>Figure 4.16 : Experimentally measured thermal conductivity of ThO<sub>2</sub> and ThO<sub>2</sub>–5% CeO<sub>2</sub> fabricated by conventional route (POP) and CAP route sintered in Ar–H<sub>2</sub> and air atmospheres. Solid lines are polynomial fitting of experimentally obtained data points to determine constants A and B of equation 14. ....</i>	<i>101</i>
<i>Figure 4.17 : Comparison of Thermal conductivity calculated by MD simulations as a function of temperature for ThO<sub>2</sub> and Th<sub>0.9275</sub>Ce<sub>0.0625</sub>O<sub>2</sub> with experimental values of ThO<sub>2</sub> and ThO<sub>2</sub>–5wt% CeO<sub>2</sub> for POP as well as CAP pellets sintered in Ar–H<sub>2</sub> and Air atmosphere (95 % T.D). Solid lines are only for visual guidance. ....</i>	<i>104</i>

<i>Figure 5.1 : (a) Alpha autoradiograph image of <math>\text{ThO}_2</math>–1%<math>\text{PuO}_2</math> pellets fabricated by CAP process (b) Enlarged view of region of lowest track density region of (a) and (c) Enlarged view of region of highest track density region of (a).</i>	114
<i>Figure 5.2 : Alpha autoradiograph image of <math>(\text{Th},1\% \text{Pu})\text{O}_2</math> pellet fabricated by POP process showing uniform track density.</i>	115
<i>Figure 5.3 : UV absorbance spectra of the three films etched for different durations.</i>	117
<i>Figure 5.4: Images of the alpha autoradiographs of plancheted plutonium source etched for (a) 60mins, (b) 90mins and (c) 120mins showing change in size of the tracks.</i>	118
<i>Figure 5.5: Alpha autoradiographs of <math>(\text{Th},\text{Pu})\text{O}_2</math> POP pellets having (a)1% <math>\text{PuO}_2</math>, (b) 6% <math>\text{PuO}_2</math> and(c) 8% <math>\text{PuO}_2</math>.</i>	120
<i>Figure 5.6: Binary images of Alpha autoradiograph of <math>(\text{Th},\text{Pu})\text{O}_2</math> POP pellets shown in Figure 5.5 having (a) 1% <math>\text{PuO}_2</math>, (b) 6% <math>\text{PuO}_2</math> and (c) 8% <math>\text{PuO}_2</math>.</i>	121
<i>Figure 5.7: % Irradiated area as a function of <math>\text{PuO}_2</math> content.</i>	122
<i>Figure 5.8: UV Absorbance spectra of different alpha autoradiographs.</i>	123
<i>Figure 5.9: Absorbance as a function of %<math>\text{PuO}_2</math>.</i>	124
<i>Figure 5.10 : Alpha autoradiographs of <math>(\text{Th},1\%\text{Pu})\text{O}_2</math> pellets and blank portion for comparison.</i>	126
<i>Figure 5.11: UV absorption spectra of autoradiographs of POP, CAP and blank sample</i>	126
<i>Figure 5.12: UV–Vis spectro photometric responses of different portions of the alpha autoradiographs of POP and CAP sample using mini focus aperture.</i>	127
<i>Figure 5.13 : Microstructure of <math>\text{ThO}_2</math>–1% <math>\text{PuO}_2</math> (a) CAP pellet and (b) POP pellet.</i>	129
<i>Figure 5.14: XRD patterns of <math>\text{ThO}_2</math>, <math>\text{ThO}_2</math>–1%<math>\text{PuO}_2</math> (POP and CAP pellets) and <math>\text{ThO}_2</math>–6%<math>\text{PuO}_2</math> (POP pellets).</i>	130
<i>Figure 5.15: Expanded view of peak positions of XRD patterns of <math>(\text{Th},1\%\text{Pu})\text{O}_2</math> pellets and <math>\text{ThO}_2</math> sintered in reducing atmosphere.</i>	131
<i>Figure 5.16: Gamma scan of experimental pin containing <math>\text{ThO}_2</math>–1%<math>\text{PuO}_2</math> POP pellets.</i>	136
<i>Figure 5.17: Gamma scan of experimental pin containing <math>\text{ThO}_2</math>–1%<math>\text{PuO}_2</math> CAP pellets.</i>	136
<i>Figure 5.18: Thermal Expansion plots for <math>\text{ThO}_2</math>–1%<math>\text{PuO}_2</math> (sintered pellets fabricated by CAP and POP process) and <math>\text{ThO}_2</math>–6%<math>\text{PuO}_2</math> POP pellet measured experimentally using dilatometer.</i>	140
<i>Figure 5.19: Thermal diffusivity plots for <math>\text{ThO}_2</math>, <math>\text{ThO}_2</math>–1%<math>\text{PuO}_2</math> sintered pellets fabricated by CAP and POP process and <math>\text{ThO}_2</math>–6%<math>\text{PuO}_2</math> POP pellets.</i>	145
<i>Figure 5.20: Thermal conductivity plots for <math>\text{ThO}_2</math>, <math>\text{ThO}_2</math>–1%<math>\text{PuO}_2</math> sintered pellets fabricated by CAP and POP process and <math>\text{ThO}_2</math>–6%<math>\text{PuO}_2</math> POP pellet.</i>	145

<i>Figure 5.21 : Thermal conductivity calculated by MD simulations as a function of temperature for <math>\text{ThO}_2</math> and <math>\text{Th}_{0.9275}\text{Pu}_{0.0625}\text{O}_2</math> compared with our experimental values of <math>\text{ThO}_2</math> and <math>\text{ThO}_2</math>-6 wt% <math>\text{PuO}_2</math> POP pellet (95% T.D). These values are also compared with reported values of <math>\text{ThO}_2</math>, <math>\text{ThO}_2</math>-3 wt% and <math>\text{ThO}_2</math>-8 wt% <math>\text{PuO}_2</math> by Cozzo et al [127]. Solid lines are only for visual guidance. ....</i>	<i>146</i>
<i>Figure 6.1: Alpha autoradiograph of <math>\text{ThO}_2</math>- 6% <math>\text{UO}_2</math> (a) POP pellet and (b) CAP pellet.....</i>	<i>158</i>
<i>Figure 6.2 : SEM Microstructure of <math>\text{ThO}_2</math>-6wt.%<math>\text{UO}_2</math> CAP pellet sintered in Ar-8%<math>\text{H}_2</math> atmosphere. ....</i>	<i>159</i>
<i>Figure 6.3 : EDS spectrum taken from the area shown in Figure 6.2 showing the presence of three elements, i.e., Th, U and O. ....</i>	<i>159</i>
<i>Figure 6.4: (a) Microstructure of <math>\text{ThO}_2</math>-6%<math>\text{UO}_2</math> showing <math>\text{U}_3\text{O}_8</math> coating site (dark) and the initial <math>\text{ThO}_2</math> granules (b) elemental mapping of 'Th' coming from Th (M<math>\alpha</math>), (c) elemental mapping of O coming from O(K<math>\alpha</math>) and (d) elemental mapping of U coming from U(M<math>\alpha</math>). All the elemental mappings were done on the same area as shown in (a).....</i>	<i>160</i>
<i>Figure 6.5 : XRD patterns of <math>\text{ThO}_2</math>- x wt.% <math>\text{UO}_2</math> (x = 0 &amp; 6) at room temperature. Peaks at 40.47° and 47.12° are due to Pt-Rh sample carrier. ....</i>	<i>162</i>
<i>Figure 6.6 : Expanded view of XRD plot between 31° and 33° . ....</i>	<i>163</i>
<i>Figure 6.7 : Percentage thermal expansion data as a function of temperature for <math>\text{ThO}_2</math> and <math>\text{ThO}_2</math>-6%<math>\text{UO}_2</math> (CAP and POP pellets) as measured using dilatometer.....</i>	<i>169</i>
<i>Figure 6.8 : Thermal diffusivity plots of <math>\text{ThO}_2</math> and <math>\text{ThO}_2</math>-6%<math>\text{UO}_2</math> (POP and CAP pellet) between temperature range of 873 K and 1873 K. ....</i>	<i>171</i>
<i>Figure 6.9 : Thermal conductivity as calculated by MD simulations as a function of temperature for <math>\text{ThO}_2</math> and <math>\text{Th}_{0.9375}\text{U}_{0.0625}\text{O}_2</math> compared with our experimental values of <math>\text{ThO}_2</math> and <math>\text{ThO}_2</math>-6wt% <math>\text{UO}_2</math> (POP and CAP) pellet (both corrected to 95 %T.D). Reported values of Pillai et al [90] and Kutty et al [25] are also plotted for comparison.....</i>	<i>172</i>
<i>Figure 6.10 : SEM photograph of <math>\text{ThO}_2</math>-4%<math>\text{UO}_2</math> pellet made by CAP co-precipitated powder and sintered in air at 1400°C for 6 h showing non-uniform grain structure. ....</i>	<i>179</i>
<i>Figure 6.11: SEM photograph of <math>\text{ThO}_2</math>-4%<math>\text{UO}_2</math> pellet made by CAP co-precipitated powder and sintered in Ar-8%<math>\text{H}_2</math> (1650°C, 6 h).....</i>	<i>180</i>
<i>Figure 6.12 : X-ray line scan for Th M<math>\alpha</math>, U M<math>\alpha</math> and O K<math>\alpha</math> across the grain structure of <math>\text{ThO}_2</math>-4%<math>\text{UO}_2</math> pellet sintered in air (1400°C, 6 h).....</i>	<i>181</i>
<i>Figure 6.13 : X-ray line scan for Th M<math>\alpha</math>, U M<math>\alpha</math> and O K<math>\alpha</math> across the grain structure of <math>\text{ThO}_2</math>-4%<math>\text{UO}_2</math> pellet sintered in Ar-8%<math>\text{H}_2</math> (1650°C, 6 h). ....</i>	<i>182</i>
<i>Figure 6.14 : XRD patterns of <math>\text{ThO}_2</math> and <math>\text{ThO}_2</math>-50%<math>\text{UO}_2</math> powders used along with <math>\text{ThO}_2</math>-4%<math>\text{UO}_2</math> sintered pellet (1400 °C in air for 6 h). ....</i>	<i>185</i>

## List of Tables

---

<i>Table 1.1: Comparison between different routes for the fabrication of Th based MOX fuel.</i> .....	8
<i>Table 1.2: Physiochemical properties of cerium oxide and plutonium oxide powders (chemically prepared through oxalate route) [2, 14].</i> .....	10
<i>Table 3.1: Characteristics of feed powders used in various experiments.</i> .....	28
<i>Table 3.2: Density of ThO<sub>2</sub> powder before and after milling.</i> .....	29
<i>Table 3.3 : Chemical analysis for co-precipitated (Th-U)O<sub>2</sub> powder.</i> .....	33
<i>Table 3.4 : Impurities in the (Th,U)O<sub>2</sub> powder made by co-precipitation.</i> .....	33
<i>Table 3.5: Lattice parameter, O/M ratio and the amount of U<sub>3</sub>O<sub>8</sub> in co-precipitated (Th,U)O<sub>2</sub> powder after heating in air at 973K for 3 h.</i> .....	34
<i>Table 3.6: Density of ThO<sub>2</sub>-U<sub>3</sub>O<sub>8</sub> granules and spheroids.</i> .....	36
<i>Table 4.1 : Onset of sintering temperature for the pellets and the corresponding sintering conditions.</i> .....	52
<i>Table 4.2 : Characteristics of ThO<sub>2</sub>-5 wt.% CeO<sub>2</sub> experimental POP and CAP sintered pellets.</i> .....	62
<i>Table 4.3 : Experimentally measured (by dilatometer) and MD calculated thermal expansion coefficients of ThO<sub>2</sub> and (Th,Ce)O<sub>2</sub> MOX compared with available experimental data in the literature.</i> .....	95
<i>Table 4.4: Constants A and B of the equation 14, <math>1/\kappa = A+BT</math>, for ThO<sub>2</sub> and (Th,Ce)O<sub>2</sub> MOX calculated from experimental measurements and MD simulations.</i> .....	102
<i>Table 5.1: Characteristics of (Th,Pu)O<sub>2</sub> experimental sintered pellets.</i> .....	111
<i>Table 5.2 : Result of Irradiated area estimation by image analysis</i> .....	122
<i>Table 5.3 : Results of Alpha autoradiography image analysis of (Th,1% Pu)O<sub>2</sub> samples.</i> .....	125
<i>Table 5.4: UV-Vis spectrophotometry analysis for PuO<sub>2</sub> content of (Th,1% Pu)O<sub>2</sub> samples.</i> .....	127
<i>Table 5.5 : UV-Vis spectrophotometry analysis using mini focus aperture of (Th,1% Pu)O<sub>2</sub> samples.</i> .....	128
<i>Table 5.6 : Characteristics of (Th,Pu)O<sub>2</sub> experimental sintered pellets.</i> .....	138
<i>Table 5.7 : Experimentally measured thermal expansion coefficients (Th,Pu)O<sub>2</sub> MOX</i> .....	141
<i>Table 5.8 : MD calculated and experimentally measured thermal expansion coefficients of (Th,Pu)O<sub>2</sub> Experimentally measured thermal expansion coefficients (Th,Pu)O<sub>2</sub> MOX compared with available experimental data in the literature.</i> .....	142

<i>Table 5.9 : Constants A and B of the equation 14, <math>1/k = A+BT</math>, for <math>ThO_2</math> and <math>(Th,Pu)O_2</math> MOX calculated from MD simulations and experimental measurements.....</i>	<i>146</i>
<i>Table 6.1: Characteristics of experimental <math>ThO_2-6\%UO_2</math> pellets used for thermal property studies .....</i>	<i>156</i>
<i>Table 6.2 : Quantitative analysis of 'Th', 'U' and 'O' elements as obtained from EDS of <math>ThO_2-6\%UO_2</math> CAP pellet.....</i>	<i>161</i>
<i>Table 6.3 : Characteristics of experimental <math>ThO_2-6\%UO_2</math> sample pellets used for thermal property studies.....</i>	<i>169</i>
<i>Table 6.4 : Experimentally measured thermal expansion coefficients of <math>ThO_2</math> and <math>(Th,U)O_2</math> MOX compared with MD Calculated and data in the literature.....</i>	<i>170</i>
<i>Table 6.5 : Constants A and B of the equation 14, <math>1/\kappa = A+BT</math>, for <math>ThO_2</math>, <math>(Th,U)O_2</math> MOX calculated from MD simulations and experimental measurements.....</i>	<i>177</i>
<i>Table 6.6 : Composition, density and O/M ratio of <math>ThO_2-4\%UO_2</math> CAP pellets fabricated using co-precipitated powder.....</i>	<i>179</i>
<i>Table 6.7 : Phase, Lattice parameter and O/M ratio of <math>ThO_2-4\%UO_2</math> sintered pellets.....</i>	<i>184</i>

## List of Abbreviations

---

AHWR	Advanced Heavy Water Reactor
ASTM	American Society for Testing and Materials
BARC	Bhabha Atomic Research Centre
BMM model	Buckingham Morse Many model
CAP	Coated agglomerate Pelletization
Ce	Cerium
CTE	Coefficient of Thermal Expansion
CR	Computed Radiography
POP	Conventional powder processing and Pelletization
DFT	Density Functional Theory
DTG	Differential Thermo gravimetry
EPMA	Electron Probe micro analysis
EDTA	Ethylene di amine tetra acetic Acid
FRD	Fuel Reprocessing Division
GK formalism	Green Kubo formalism
HTGR	High Temperature Gas Cooled Reactors
HTXRD	High Temperature X-Ray Diffraction
ICP-AES	Inductively coupled plasma atomic emission spectroscopy
IAEA	International Atomic Energy Agency
LWR	Light water reactor
LMFBR	Liquid Metal cooled Fast Breeder Reactors
MOX	Metal oxide
MD	Molecular dynamics
MSBR	Molten Salt Breeder Reactors
NIST	National Institutes of Standards and Technology
NPT	Constant pressure-constant temperature for constant number of particles ensemble
O/M ratio	Oxygen to Metal ratio
%T.D	Percentage theoretical density
PGS	Passive Gamma Scanning
PHWR	Pressurized Heavy Water Reactors
PTFE	Polytetrafluoroethylene
Pu	Plutonium
RCS	Rate Controlled Sintering

SEM	Scanning electron microscope
SSNTD	Solid state nuclear track detector
SQS	Special quasirandom structures
T.D	Theoretical Density
TGA– SDTA	Thermo Gravimetry Analysis Simultaneous Differential thermal analysis
TG	Thermo gravimetry
TIG	Tungsten Inert gas
Th	Thorium
U	Uranium
UV	Ultra violet
XRD	X–ray diffraction

## List of Symbols

---

<b>C<sub>p</sub></b>	Specific heat capacity
<b>ρ</b>	Density
<b>β</b>	Coefficient of Thermal Expansion
<b>L</b>	Length
<b>T</b>	Temperature
<b>α</b>	Thermal diffusivity
<b>W</b>	Function of the relative heat loss
<b>κ</b>	Thermal conductivity
<b>p</b>	Porosity
<b>V<sub>o</sub><sup>••</sup></b>	Vacant oxygen site
<b>Ce<sub>Ce</sub><sup>x</sup></b>	Ce <sup>+4</sup> ion in location of Ce <sup>+4</sup> location , charge neutral
<b>O<sub>O</sub><sup>x</sup></b>	Oxygen atom in oxygen atom location , charge neutral
<b>O<sub>2</sub></b>	Oxygen molecule
<b>Ce<sub>Ce</sub><sup>'</sup></b>	Ce <sup>+3</sup> ion in location of Ce <sup>+4</sup> location , 1 -ve charge
<b>a<sub>s</sub></b>	Radius of solute ion
<b>a</b>	Radius of host ion
<b>Δa</b>	Difference between radii of solute and host ions (misfit in the lattice)
<b>B<sub>s</sub></b>	Bulk modulus of the solute
<b>μ<sub>h</sub></b>	Shear modulus of the host crystal
<b>U<sub>o</sub></b>	Strain energy
<b>λ<sub>max</sub></b>	Maximum permissible linear rating
<b>P</b>	Partial pressure of H <sub>2</sub>
<b>R</b>	Gas constant
<b>A</b>	Specific surface area of the powder

# **CHAPTER 1. INTRODUCTION**

## **1.1 Preamble**

This chapter deals with the newly developed Coated Agglomerate Pelletization (CAP) process for the fabrication of thorium based fuel of AHWR. The details and benefits of CAP process in comparison with other techniques and basis for its selection for fuel property investigations have been presented. The motivation for adopting this research work, objectives of the present study and methodology for evaluating CAP process have been described in this chapter.

## **1.2 Background**

Thorium fuel programme is fast gaining centre stage in nuclear power programme globally because of its potential capability to suffice the demands of increased energy requirements, environmentally clean and safe fuel. The advantage of adopting thorium for future programme is long term sustenance because of availability of vast resources for utilization [1]. Favorable neutronic characteristics and better fuel properties compared to uranium make thorium a good fuel material for reactor operations [2–6]. Thorium has been used in many reactors and sufficient experience has been generated. Its applicability in various reactors such as HTGR, LWR, PHWR, LMFBR and molten salt breeder reactors (MSBR) has already been demonstrated [2, 5]. The major concern arising regarding its fabrication and re-fabrication has also been adequately addressed by development of various techniques. Thorium fuel fabrication has been successfully demonstrated on lab scale like Co-precipitation and pelletization technique, Sol-Gel Microsphere Pelletization (SGMP),

Pellet/gel Impregnation; and on industrial scale by Powder processing and pelletization route (POP) and Coated Agglomerate Pelletization (CAP) [7–9].

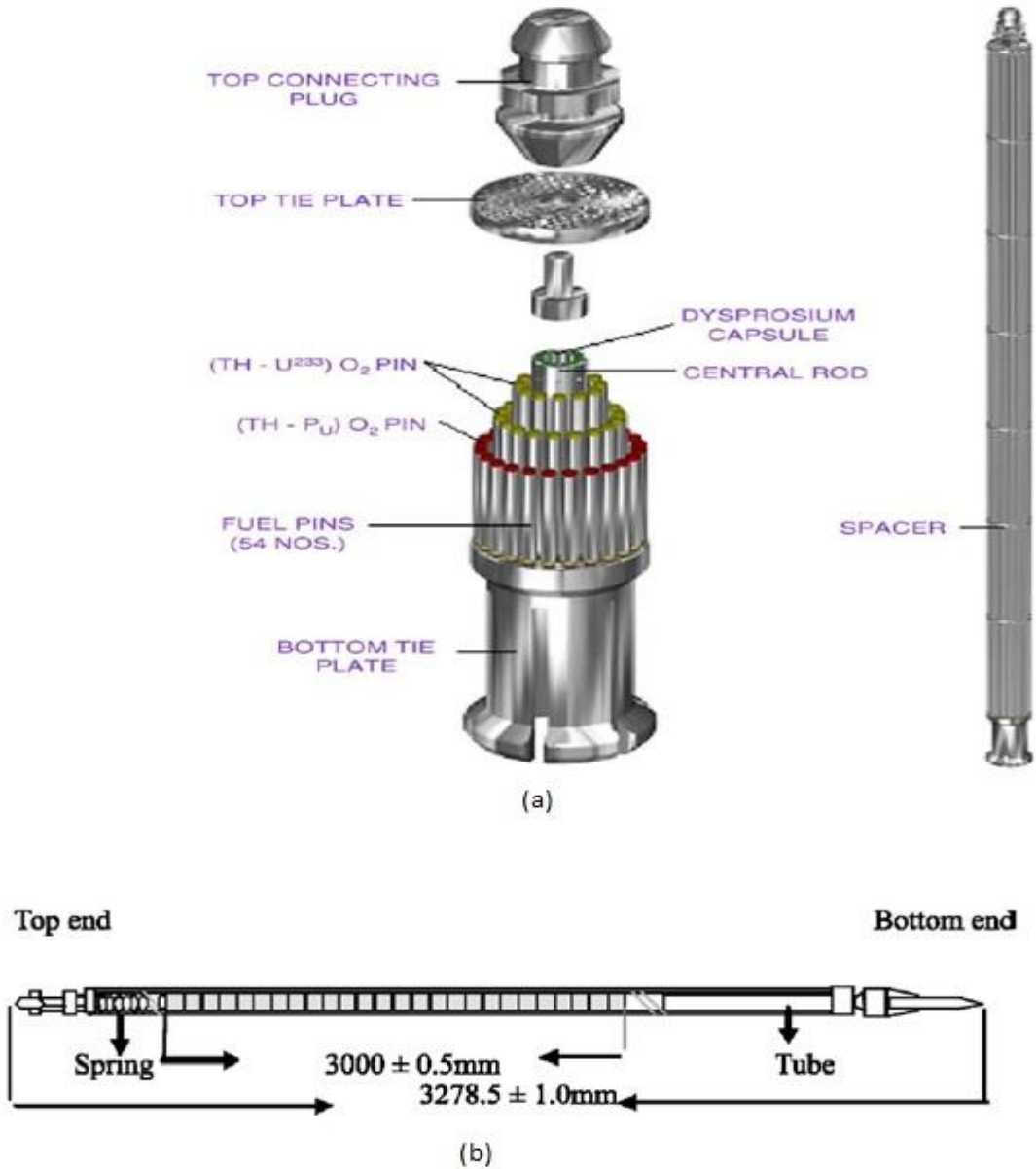


**Figure 1.1 : (a) AHWR fuel cluster showing configuration and fixtures for assembling the fuel pins [10] and (b) Schematic diagram of a typical AHWR (Th,1%Pu)O<sub>2</sub> fuel pin filled helium gas and loaded with fuel pellets and hardware [11].**

With the aim of utilizing thorium for power generation, advanced heavy water reactor (AHWR) is fuelled with thoria enriched with fissile ( $U^{233}O_2$  and  $PuO_2$ ) contents separately. Fig 1.1(a) shows a typical AHWR fuel cluster with different fuel compositions and Figure 1.1(b) shows schematic diagram of AHWR type  $(Th,1\%Pu)O_2$  fuel pin.

For the good performance of nuclear fuel during the operation of the reactor, it is required to meet the following desired criteria like good dimensional stability, good irradiation stability, chemical compatibility with coolant and clad, high melting point, low chemical impurities, good thermal properties, good fabricability and easy reprocessing. In order to meet these criteria the fuel should possess good characteristics or properties such as

- i. Density (thermal reactor  $\sim 95 \pm 2$  %T.D; fast reactor  $\sim 87 \pm 2$  %T.D).

(T.D=Mass/volume of the unit cell of the material)

(A fast reactor fuel has to remain inside a reactor for a longer duration for higher burnup as compared to a thermal reactor. Due to this, more fission gases get released during the life of the fuel inside the reactor. To accommodate higher fission gases released and also to prevent swelling due to that, the density of the fuel of the fast reactor is kept lower.)

- ii. O/M ratio (stoichiometry).

Oxides having stoichiometric O/M ratio (i.e. 2) are known to have highest thermal conductivity. Therefore, O/M ratio as close to 2 as possible is desirable in the fuel. Besides, subsequent to nuclear fission reactions, some oxygen atoms do get released due to the lower valency of the fission products. These oxygen atoms migrate to the

clad and deleteriously interact with it. This oxygen is also responsible for dilution of cover gas (helium) resulting in lowering its thermal conductivity.

- iii. Homogeneity (uniform).
- iv. Chemical composition (with in specification).
- v. Thermal conductivity (with respect to specification).
- vi. Desired microstructure (with respect to specification).

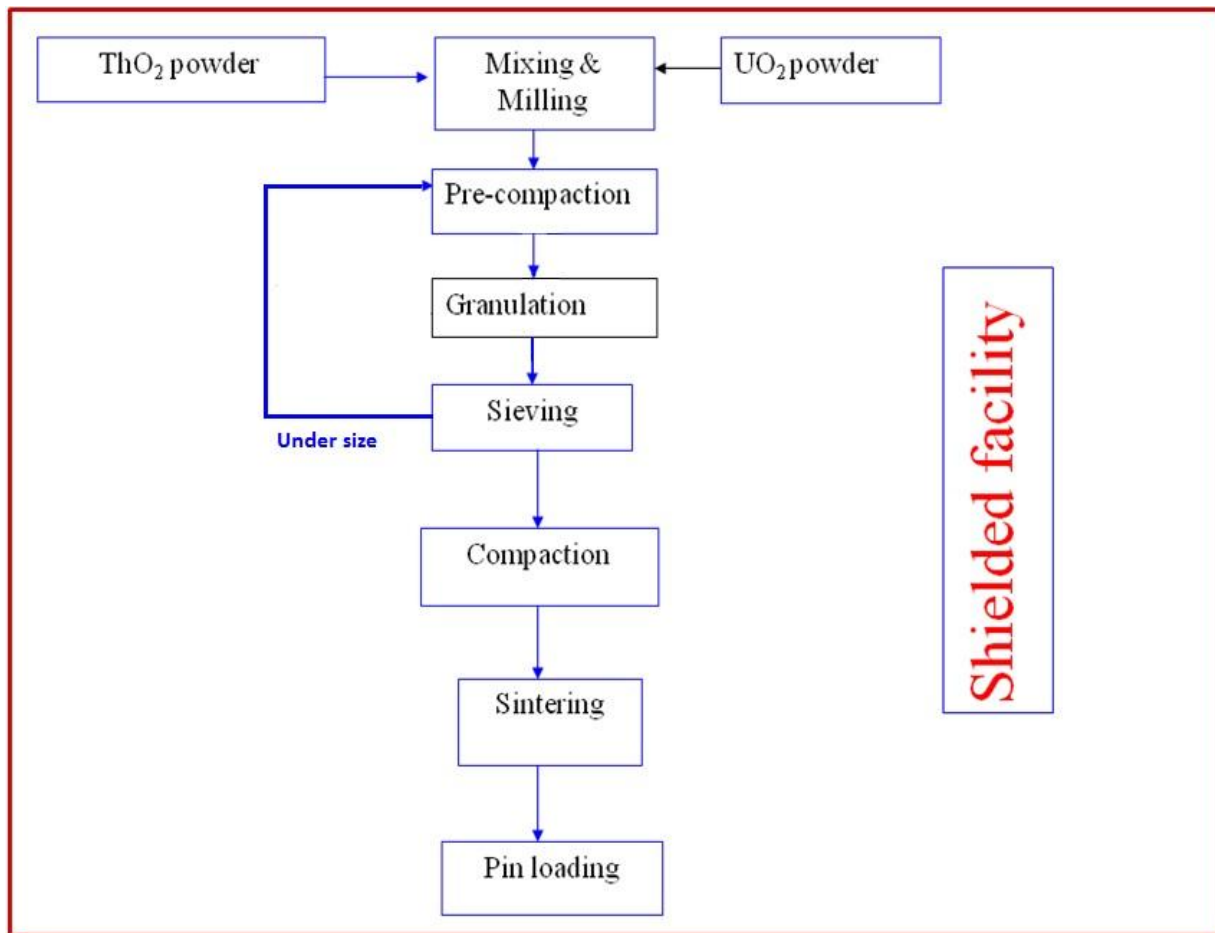


**Figure 1.2 : Flowsheet showing various operations involved in powder processing and pelletization (POP) process.**

Presently, most widely employed and standardized route of fabrication of ceramic nuclear fuel in large scale is powder processing and pelletization (POP) process. The flowsheet showing various processing steps involved in powder processing and pelletization (POP) process is given in Figure 1.2.

However, if the fissile materials such as  $U^{233}$  and  $Pu^{239}$  produced by transmutation of fertile elements  $Th^{232}$  and  $U^{238}$  respectively during reactor use, are to be used as fuel the present technique of fabrication (POP process) is not compatible, as these materials are associated with high radiation hazards due to higher number of processing steps, low production rate and difficulty in automation and remotization of process, thereby, resulting in radiation exposure to operator. To meet with the increasingly stringent safety standards, newer techniques as alternate to POP process such as sol-gel microsphere pelletization (SGMP), pellet / gel impregnation, and co-precipitation have been developed and investigated. The alternative routes being wet processes (involving handling of fissile material in liquid form) had key issues regarding liquid waste generation and criticality concerns.

In order to address these above mentioned issues related with POP as well as alternate techniques, novel and innovative dry fabrication technique process, known as coated agglomerate pelletization (CAP) process, was developed indigenously [12]. The CAP process was proposed as an alternative to conventional powder metallurgy process for nuclear fuel fabrication and could adequately address all the fabrication related issues encountered in the POP process [13]. The flow sheet of coated agglomerate pelletization route of fabrication is given in Figure 1.3.

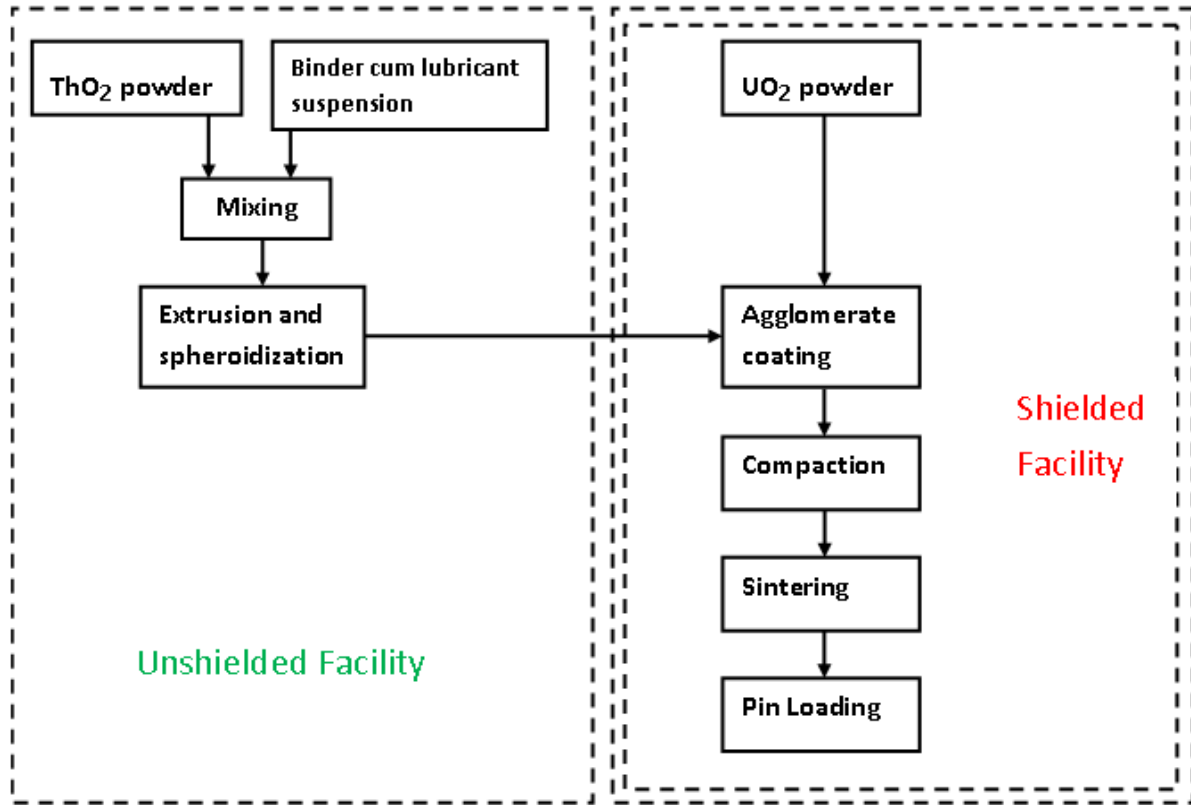


**Figure 1.3 : Flowsheet of coated agglomerate pelletization (CAP) process.**

Upon comparing Figure 1.2 and Figure 1.3 some of the main benefits of CAP technique of fuel fabrication could be summarized as:

- Reduced radiation dose to operators (exposure of operator to radiation). Unlike POP process, where radioactive  $\text{UO}_2$  is added in the beginning of the process exposing an operator to possible radiation doses, in CAP process basic steps required to treat  $\text{ThO}_2$  are taken prior to mixing with radioactive  $\text{UO}_2$ . This minimizes dusty operations and reduces process steps required for shielded operation.
- As shown in Figure 1.3, only  $\text{ThO}_2$  is handled and all its operations are carried out in a normal alpha tight glove-box facility. The operations carried out under shielding

are post coating of ThO<sub>2</sub> agglomerates with desired amount of U<sup>233</sup> oxide such as Compaction, Sintering , Pellet loading and encapsulation into fuel rods. Thus, number of operations to be carried out in shielded atmosphere is reduced significantly compared to POP process. This helps in easy maintainability, robust and simple machine handling and reduces the production time.

- To make free flowing agglomerates in the extrusion route, ThO<sub>2</sub> powder is mixed with an organic binder cum lubricant suspension and extruded through perforated rollers. The organic binder cum lubricant suspension used for agglomeration consists of 10% water, 1.2% polyethylene glycol (liquid, binder, Molecular weight – 380 g/mol.) and 0.8% oleic acid (liquid, lubricant, Molecular weight – 280 g/mol.) and is mixed with ThO<sub>2</sub> powder thoroughly and extruded. This suspension present on the surface of ThO<sub>2</sub> agglomerate (increased wetness) improves the binding property and helps in adhesion of UO<sub>2</sub>, CeO<sub>2</sub> or PuO<sub>2</sub> powder particles. This new agglomeration process results onto higher production rate.
- The agglomerate shape and simple design of equipments makes the system amenable to automation and remotization.
- The unextruded powder generated can be easily and immediately recycled back into the agglomeration process, thus minimizing the solid waste and thereby increasing the agglomerate production yield.

Table 1.1 provides a comparison between different routes for important criteria relevant for the fabrication of Th based MOX fuel.

**Table 1.1: Comparison between different routes for the fabrication of Th based MOX fuel.**

	<b>POP Route</b>	<b>SGMP</b>	<b>Impregnation</b>	<b>Co-precipitation process</b>	<b>CAP Process</b>
Radiation dose to operators	Highest	Medium	Medium	Medium	Low
Uranium/Plutonium Distribution in starting product	Uniform	Uniform	For pellet impregnation: Higher U / Pu concentration at periphery For gel impregnation: Uniform	Uniform	Varying U/Pu concentration in ThO <sub>2</sub> granules. Better distribution with premixed powders
Insitu Adjustment of Composition	Possible	Not Possible	Not Possible	Not Possible	Possible
Grain size	Uniform	Uniform	Uniform	Uniform	Duplex
Waste	Solid waste	Liquid waste, organic waste	Less Liquid waste	Liquid waste	Less waste
For Pu fuel (Criticality issue)	Low	High	High	High	Low

It may be noticed from the Table 1.1, as compared to other processes CAP process provides maximum flexibility, minimum radiation exposure and minimum waste. Also criticality issues inherited on account of handling plutonium are less as compared to the other

routes for fabrication of the thorium based fuels. CAP process, therefore, seems to be amongst the most optimum processes for fabrication of nuclear fuel involving handling of highly radioactive materials.

### **1.3 Motivation and methodology of present work**

ThO<sub>2</sub>-PuO<sub>2</sub> fuel is being actively considered for reactor use in PWRs as substitute to conventional UO<sub>2</sub> fuel from point of faster disposition and incineration of plutonium along with increased proliferation resistance. ThO<sub>2</sub>-PuO<sub>2</sub> fuel utilization is precursor to (Th,U<sup>233</sup>)O<sub>2</sub> utilization programme. It along with (Th,U<sup>233</sup>)O<sub>2</sub> is the proposed equilibrium core fuel of AHWR designed for thorium utilization. The choice of ThO<sub>2</sub>-PuO<sub>2</sub> fuel for reactor application is seriously impeded by two major issues (i) reductions in reprocessing and fuel fabrication costs and (ii) very limited investigations of fuel properties. It is very important to adopt a process amenable and flexible for the fabrication of any thorium based fuel without requiring major parametric alterations to reduce huge investment costs.

The present study will, therefore, be focused on the ThO<sub>2</sub>-PuO<sub>2</sub> pellets fabricated by CAP process. Characterization of the ThO<sub>2</sub>-PuO<sub>2</sub> fuel fabricated by CAP process has not been attempted previously and to the best of our knowledge no report exists in open literature. The fuel properties being important for reactor performance dictate whether a process is suitable for adopting it for large scale fabrication. Therefore, it is necessary to thoroughly investigate the fuel and draw a comparison between the fuels fabricated by CAP with those produced using the present process (POP process) employed. The assessment of fuel fabricated via different processes would provide necessary insight into the property changes affected. For this purpose, fuel pellets will be fabricated by both

POP and CAP routes and various physical and thermal properties will be compared. Because of the difficulties involved in handling of plutonium, requirement of special facilities, contamination and lack of characterization equipment in the glove boxes and various limitations associated, in the present study CeO<sub>2</sub> will be used as a surrogate for PuO<sub>2</sub> because of their similar physicochemical properties as shown in Table 1.2.

**Table 1.2: Physiochemical properties of cerium oxide and plutonium oxide powders (chemically prepared through oxalate route) [2, 14].**

Sl. No:	Characteristics	CeO <sub>2</sub>	PuO <sub>2</sub>
1	Crystal structure	Cubic (Fluorite)	Cubic (Fluorite)
2	Melting point	2400 °C	2390 °C
3	Specific heat	390 J/kg/K	344J/kg/K
4	Lattice parameter	0.5410 nm	0.5396 nm
5	O/M	≤ 2	≤ 2
6	Ionic radius	1.0 Å	1.0 Å
7	Typical specific surface area	15–25 m <sup>2</sup> /g	15–25 m <sup>2</sup> /g
8	Thermal conductivity	2.5 W/(m.K)	2.85 W/(m.K)
9	Theoretical density (T.D)	7.215 g/cm <sup>3</sup>	11.5 g /cm <sup>3</sup>
10	Typical average particle size (µm)	≤ 2	≤ 2

The study will also be conducted using U<sub>3</sub>O<sub>8</sub> powder to simulate density similar to PuO<sub>2</sub> powder and its effect on achievable composition besides being relevant for ThO<sub>2</sub>–U<sup>233</sup>O<sub>2</sub> fuel pellets. The present study also includes experimental simulation using co-precipitated powder of (Th,U)O<sub>2</sub> to study the effects on homogeneity and microstructure. Subsequent to the surrogate studies, characterization studies on ThO<sub>2</sub>–PuO<sub>2</sub> fuel will be attempted with available and alternate techniques for verification. Thermal properties of the

pellets fabricated by both processes will be evaluated experimentally and verified by theoretical studies using molecular dynamics for similar compositions.

The main motivation for conducting the present research studies was to address the following key aspects:

- Investigate suitability and assess potential of CAP technique for nuclear fuel fabrication.
- Evaluate implication of homogeneity variation in the fuel pellets on their thermal properties.
- Investigate fuel characteristics of CAP fuel pellet and compare with POP pellet for predicting fuel performance.
- Develop theoretical understanding of thermal behavior of Thorium based MOX fuels of relevant compositions using MD simulations

The studies are expected to bring out salient features of CAP process and help in assessing the feasibility of fabrication of AHWR fuel by CAP process.

#### **1.4 Objectives**

The coated agglomerate pelletization (CAP) process offers benefits in fabrication of fuel over POP process. However, the desired fuel characteristics, such as physical, chemical, microstructure, oxygen to heavy metal ratio (O/M) and thermal properties, govern the basis of selection of fabrication route as these properties affect the performance of the fuel in the reactor.

In CAP process, the fissile material distribution in the starting product (agglomerate) is different from that of conventional method. This might result in deviation from the desired characteristics and properties. The extent and effect of deviation in characteristics and properties need to be investigated thoroughly.

Therefore, the main objectives of the present research work are as follows:

- i. Comparing properties of CAP pellets with respect to conventional POP pellets such as microstructure, homogeneity and other characteristics,
- ii. Investigate thermo physical properties of CAP pellets for predicting the in-reactor fuel behavior and performance ,
- iii. Extrapolation of experimentally measured thermal properties to higher temperatures and for different compositions through Molecular Dynamic Simulation and develop methodology for application on other fuel systems.

## **1.5 Structure of the thesis**

The thesis comprises of eight chapters. Chapter 1 describes the importance of CAP process and relevance of investigations of pellets fabricated through this route, the overall objectives of the doctoral research work to be carried out and plan of study and its presentation. Chapter 2 presents detailed literature review conducted on thorium fuel systems, fuel properties and their fabrication relevant for systems adopted for investigations in this doctoral work. In Chapter 3, experimental details related to fabrication processes, sample preparation and its characterization are presented. Chapters 4 to 6 will deal independently with  $\text{ThO}_2\text{-CeO}_2$ ,  $\text{ThO}_2\text{-UO}_2$  and  $\text{ThO}_2\text{-PuO}_2$  systems selected for the study

respectively, their experimental findings and analyses towards realizing each of the defined research objectives. Chapter 7 summarizes the outcome of the research work with respect to objectives and any novel approaches implemented.

## **CHAPTER 2. LITERATURE SURVEY**

### **2.1 Preamble**

This chapter encompasses detailed literature survey conducted on the investigated  $\text{ThO}_2\text{-CeO}_2$ ,  $\text{ThO}_2\text{-UO}_2$  and  $\text{ThO}_2\text{-PuO}_2$  fuel systems. The literature survey presented in this chapter has relevance with the characterization carried out on pellets of these systems with emphasis on thermal property studied previously. The literature survey was beneficial in identification of areas to be addressed during research. Additionally, conclusions derived from previous studies are mentioned in this chapter.

### **2.2 Thoria based systems**

Thoria based fuels investigations have long been pursued for their utilization in nuclear fuel cycle because of the various advantages offered by them. Extensive studies have been carried out primarily on pure  $\text{ThO}_2$  and  $\text{ThO}_2\text{-UO}_2$  systems.  $\text{ThO}_2\text{-UO}_2$  has been of particular interest as substitute for  $\text{UO}_2\text{-PuO}_2$  fuel system arising due to utilization of abundant resources available and to take advantage of better neutronic characteristics of thorium.

The powders of  $\text{ThO}_2$ ,  $\text{UO}_2$  and  $\text{PuO}_2$  being ceramic in nature are processed via powder metallurgy route for nuclear fuel fabrication [15, 16]. The conventional route involves powder processing, compaction and sintering at high temperature. In the sintering process usually two mechanisms dominate, i.e., densification and non densification [17–23]. Non densification mechanisms occur at the early stages of sintering process and densification mechanisms takes place at later stages of sintering. The non –densification mechanisms are

vapor transport i.e., evaporation/condensation, surface diffusion and lattice diffusion which are surface related phenomena, whereas in densification mechanisms such as grain boundary diffusion, lattice diffusion from the grain boundary and plastic flow are bulk phenomena.

Previous studies show that thorium dioxide (Thoria) is a highly stable compound as thorium is a single valent element and exhibits very little non-stoichiometry. Hence the sintering kinetics of thoria is very slow and necessitate requirement of high temperatures of sintering ( $> 1400^{\circ}\text{C}$ ) for appreciable changes in the pellet characteristics. It has been shown that  $\text{ThO}_2$  could be sintered in atmosphere such as air, hydrogen, argon or vacuum; however, sintering temperature should be above  $2000^{\circ}\text{C}$  for attaining about 80%T.D without additives [24–35].

The sintering temperature of the mixed oxide system, however, could be lowered either by utilizing appropriate atmosphere or by the addition of suitable dopant. Matzke et al and Lidiard et al [36–38] studied the point defect model which has been used to explain many observed features of diffusion in non-stoichiometric fluorite type oxide fuels. They derived a relation for the temperature dependence of the concentration of vacancies and interstitials in both the oxygen and metal sub lattices by solving the anion Frenkel, Schottky and cation Frenkel products. In studies of Balakrishna et al [39] and Radford et al [40] it has been observed that when the range of compositions near stoichiometry are large as in  $\text{UO}_2$ , advantage could be taken by introducing oxygen pressure in the sintering atmosphere. For uranium dioxide, oxidizing atmosphere has been used for lowering sintering temperature from  $1700^{\circ}\text{C}$  to  $1300^{\circ}\text{C}$ . When the range of compositions near stoichiometry is narrow as is the case in  $\text{ThO}_2$ , advantage is taken by introducing additives. In the case of thorium dioxide,

dopants have been successfully used to lower the temperature of sintering from 1700°C to 1200°C.

It was experimented that higher densities at still lower temperatures can be achieved with certain dopants. In correlation to the same, Balakrishna et al [39] have demonstrated that thoria could be sintered to densities greater than 97.6% T.D. at 1150°C by doping with 0.25 mol% Nb<sub>2</sub>O<sub>5</sub>. The effect of the addition of aliovalent cations has been found to accelerate the sintering of thoria and could be carried out at a temperature as low as 1150°C in air. Similar studies were carried out by Ananthasivan et al [41], with the addition of V, Nb and Ta fabricated pellets with densities as high as 98 %T.D at temperature of 1273 K and 97 %T.D at 1523 K respectively. He concurred that niobia accelerates the sintering process in thoria; however, thoria had to be doped with 0.5 mol% niobia and sintered at 1423 K to obtain a density of 97 %T.D. This concentration of niobia is higher than the concentration used by Balakrishna [39]. Addition of vanadia and tantala were also found to reproduce similar behavior of accelerated sintering in thoria. Dopant addition of 0.5 mol% of vanadia and 0.5 mol% tantala to thoria has yielded the similar effects on sintering behavior which depends mainly on its valency. These studies have also stated that an additive may assist sintering by one of the two possible mechanisms. Firstly, additive may create point defects in the ThO<sub>2</sub> lattice and thereby increase the diffusion of Th<sup>+4</sup> ions by many orders of magnitude. Secondly, an additive may significantly retard grain growth so that pores are linked to the grain boundaries. This mechanism is observed in the case of CaO/MgO in ThO<sub>2</sub>. Among the pentavalent dopants, concentration of 0.5mol% niobia is most effective in bringing about accelerated sintering in thoria. Several other dopant studies have been conducted by Kutty et al [24–27] where the effects of dopants, like CaO and Nb<sub>2</sub>O<sub>5</sub>, on shrinkage of ThO<sub>2</sub> and

ThO<sub>2</sub>-PuO<sub>2</sub> compositions have been studied in detail. The addition of a lower valency additive like CaO to ThO<sub>2</sub> is expected to create vacant oxygen sites in ThO<sub>2</sub> lattice. The same effect may also be achieved by providing a reducing atmosphere. Similarly, the addition of higher valency additive like Nb<sub>2</sub>O<sub>5</sub> is expected to create oxygen interstitials in ThO<sub>2</sub>. The same effect may also be achieved by providing oxidizing atmosphere. Thus either a lower valency additive in a reducing atmosphere or a higher valency additive in an oxidizing atmosphere may be expected to cause activated sintering. Therefore, out of the two dopants studied, CaO was found to be a better dopant for all the composition covered in their study.

Apart from the above discussed dopants, several studies were also conducted to evaluate the significance of U<sub>3</sub>O<sub>8</sub> addition for enhancing sintering, especially in UO<sub>2</sub>. The main objective was to eliminate the chemical impurities contribution arising out of extraneous additions and unwanted non volatile elements in the thoria pellet. U<sub>3</sub>O<sub>8</sub> is one of the most thermodynamically stable forms of uranium [42, 43]. Although U<sub>3</sub>O<sub>8</sub> is a stable oxide of uranium at room temperature, it dissociates into UO<sub>2</sub> above 1100°C when heated in air or inert atmosphere like Ar. Chevrel et al [44] have reported that the composition of UO<sub>2.25</sub> appeared to be the most appropriate form for the low temperature sintering which is obtained by the addition of U<sub>3</sub>O<sub>8</sub> powder to UO<sub>2</sub>. However, it is reported by Paul et al and Kutty et al [45, 46] that in solid state the solubility of U<sub>3</sub>O<sub>8</sub> in ThO<sub>2</sub> is negligible. Therefore reduction of U<sub>3</sub>O<sub>8</sub> to lower oxide during the heat treatment process of sintering either by use of reducing atmosphere or at sintering at elevated temperatures would be advantageous as UO<sub>2</sub> has excellent solubility in thoria as shown in Figure 2.1.

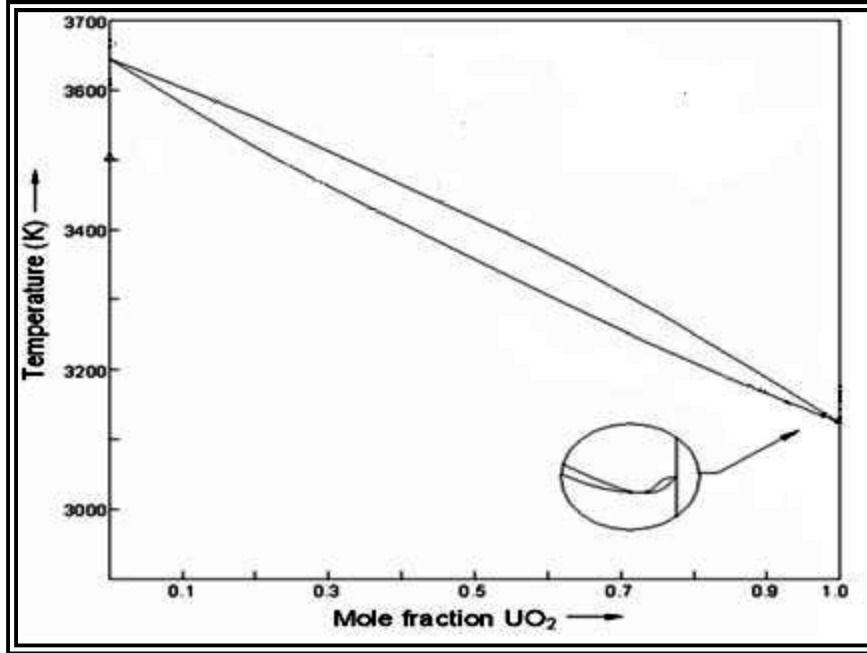


**Figure 2.1 : Phase diagram of ThO<sub>2</sub>-UO<sub>2</sub> system [25].**

Kutty et al have made green pellets using CAP process, of ThO<sub>2</sub>-4%UO<sub>2</sub> and ThO<sub>2</sub>-20%UO<sub>2</sub> from ThO<sub>2</sub> agglomerates and U<sub>3</sub>O<sub>8</sub> powder without the addition of any dopants or sintering aids. The green density of the compacts was in the range of 62–67%T.D of the theoretical density [24, 25]. For ThO<sub>2</sub>-4%UO<sub>2</sub> pellets, sintering under oxidizing condition yields a density of around 95% T.D at around 1550°C. In the reducing atmosphere, however, for same chemical composition a higher temperature of 1600°C was needed even to attain 90% T.D. ThO<sub>2</sub>-20%UO<sub>2</sub> pellets have inferior sintering behavior which could be attributed to net effect of decrease in the oxygen potential of Th<sub>1-y</sub>U<sub>y</sub>O<sub>2+x</sub> solid solution and increase in uranium concentration (y) even though it increases with the oxygen excess (x).

Diffusion of thorium and uranium during sintering in thoria has been reported by several authors [17, 19, 21, 47–53]. Results on the diffusion reported show an unusually large

scatter. Matzke [50] has reported the value of  $D_U$  in  $\text{ThO}_2$  at 1673 K and 1823 K as  $2 \times 10^{-14} \text{ cm}^2/\text{s}$  and  $3 \times 10^{-13} \text{ cm}^2/\text{s}$ , respectively. Olander [49] determined the volume and grain boundary diffusion coefficients in  $\text{ThO}_2\text{-UO}_{2+x}$  mixed oxides, which were deduced from the concentration distributions established by preferential evaporation of  $\text{UO}_3$  during air-annealing of a specimen at 1923 K. The volume diffusion coefficients for  $\text{U}_{0.1}\text{Th}_{0.9}\text{O}_{2.05}$  and  $\text{U}_{0.25}\text{Th}_{0.75}\text{O}_{2.125}$  have been found to be  $3 \times 10^{-14} \text{ cm}^2/\text{s}$  and  $8 \times 10^{-13} \text{ cm}^2/\text{s}$  respectively. The substantial reduction (by a factor of  $\sim 25$ ) in the volume diffusion coefficient of uranium in the  $\text{U}_{0.1}\text{Th}_{0.9}\text{O}_{2.05}$  oxide was attributed to the effect of deviations from stoichiometry on the cation vacancy concentration, which controls cation mobility. Matzke [50] have also studied the diffusion of U in  $\text{ThO}_2$  by conducting very extensive diffusion anneals using both polycrystals and single crystals in a broad temperature range and reported that volume diffusion is less predominant below  $0.6 T_m$  for  $\text{ThO}_2$  and was found to be of the order of  $\sim 10^{-18} \text{ cm}^2/\text{s}$  at 1873 K. Dominant grain boundary diffusion coefficients for  $\text{ThO}_2$  are  $10^{-10} \text{ cm}^2/\text{s}$  to  $10^{-9} \text{ cm}^2/\text{s}$  at 1673 K to 1773 K, which are of the order of  $10^{-7} \text{ cm}^2/\text{s}$  to  $10^{-6} \text{ cm}^2/\text{s}$  i.e; 100 times higher at 2273 K.

The activation energy for the diffusion in  $\text{ThO}_2\text{-UO}_2$  system has also been measured by many authors [50–53]. Hawkins et al [51] have estimated activation energy of 2.55 eV for polycrystalline thoria, whereas King [47] and Matzke [50] reported much higher values of 6.48 eV and 6.5 eV, respectively. A constant rate of heating (CRH) method for the estimation of activation energy of sintering of thoria–urania was proposed by Young and Cutler [41] and Wang and Raj [55]. Wang and Raj have assumed that grain boundary diffusion is the dominant sintering mechanism and estimated activation energy for sintering. Other techniques such as Master sintering curve approach for the estimation of activation energy of

sintering [55], ratio method [56], rate controlled sintering (RCS) [57, 58] and Dorn method [59] are also available in literature. Aiybers [53] has studied the first-stage sintering of  $(U_{0.8}Th_{0.2})O_{2+x}$ ,  $(U_{0.05},Th_{0.95})O_{2+x}$  using a dilatometer and showed that both the atmosphere and the composition affected the activation energy of sintering. He has reported that in  $CO_2$  atmosphere, U atoms diffuse approximately 1000 times faster than in reducing atmospheres.

Schram [60] used defect model and thermochemical model to assess oxygen potential of  $(Th,U)O_{2+x}$ . It was observed that the oxygen potential of  $(Th_{1-y}U_y)O_{2+x}$  increases with increase in temperature and increase in 'x'. Though oxygen potential of thoria is lower than that of urania, but in thoria-urania, oxygen potential increases with increase in thorium content. This is due to increase in uranium valency in the solid solution with increase in 'Th' content to accommodate the same amount of 'O'. The specific heats of  $ThO_2$ ,  $UO_2$  and  $ThO_2-UO_2$  solid solutions [ $(Th_yU_{1-y})O_2$  where  $0 < y \leq 1$ ] have been reported in literature by many researchers [59, 61, 62–73]. In these reported data, wide variation was observed in the compositions, analysis techniques and temperatures investigated. The literature data shows considerable scatter which can be attributed to the different methods of preparation of samples which ultimately lead to samples of different stoichiometry, density and impurity contents. Hence, it is imperative for a fuel designer to measure the specific heat of the samples prepared by his proposed methods.

Thermal expansion studies on  $(Th,U)O_2$  system have widely been carried out and reported in literature [75, 56, 75–81]. Momin et al [82] measured lattice thermal expansion of  $(Th,U)O_2$  system by X-ray diffraction method and obtained coefficient of expansion data for pure  $ThO_2$  and  $(Th_{0.8}U_{0.2})O_2$  to be  $9.5 \times 10^{-6} K^{-1}$  and  $7.1 \times 10^{-6} K^{-1}$ , respectively in the

temperature range 298–1600 K. It was observed CTE (coefficient of thermal expansion) values reported by different authors varied widely and could not be correlated due to lack of sufficient information. Bakker et al [74] concluded that thermal expansion of the solid solutions of  $(\text{Th}_{1-y}\text{U}_y)\text{O}_2$  could be reasonably approximated at various temperatures by taking linear interpolated expansion data of  $\text{ThO}_2$  and  $\text{UO}_2$  as per their weight fraction.

High temperature lattice parameter measurements have been used for  $(\text{Th,U})\text{O}_2$  system to estimate its density and its variance with temperature and average coefficient of linear thermal expansion in the temperature range 298–1600 K as a function of  $\text{UO}_2$  content and have been reported in the literature [35, 56, 61, 74, 82–86]. Effects of differential thermal expansion between the fuel and the cladding have been reported in literature [76].

Berman et al [87] made a systematic attempt to correlate thermal conductivity, temperature, and composition for  $\text{ThO}_2\text{--UO}_2$  system in the early 1970s. They also updated the thermal conductivity correlation to 3400 K by making use of the enthalpy data. Thermal conductivity studies on thoria–urania system have been reported by many authors [87–93]. The studies were carried out on varied compositions and in different temperature ranges. The investigations showed decrease in the thermal conductivity values with addition of uranium. Pillai et al [90] reported significantly low thermal conductivity values for  $(\text{Th}_{0.8}\text{U}_{0.2})\text{O}_2$  which might be due to errors of measurement as studies were conducted in steady state or due to low density of pellets.

Thermal conductivity of  $\text{ThO}_2$  and  $\text{ThO}_2\text{--UO}_2$  compositions was measured by Jacobs [94] during the reactor irradiation and reported no statistically significant difference between in reactor and unirradiated values for  $\text{ThO}_2$  and  $\text{ThO}_2\text{--}9.8$  mol%  $\text{UO}_2$  below 1273 K.

Matolich and Storhok [95] determined post-irradiation thermal conductivity of irradiated  $\text{ThO}_2$ -3% $\text{UO}_2$ ,  $\text{ThO}_2$ -9.8% $\text{UO}_2$ , and  $\text{ThO}_2$ -14.8% $\text{UO}_2$  (composition in mol%). They could not find any significant differences between irradiated and unirradiated measurements for  $\text{ThO}_2$ -3%  $\text{UO}_2$ . Based on this observation they concluded that due high temperature (1173 K) lattice damages created by irradiation were annealed out. This annealing of defects has restored the thermal conductivity of fuel to unirradiated state. Bhagat et al [96] conducted studies on pellet simulated for in reactor fuel compositions including fission products (SIMFUEL) postulated at different burn ups. Lattice parameter for  $\text{ThO}_2$ -3.45%  $\text{UO}_2$  and SIMFUEL corresponding to 28000 and 43000 MWD/T were calculated from XRD patterns as 0.55947 nm, 0.55880 nm and 0.55873 nm, respectively. It could also be noticed that lattice parameter estimated by SIMFUEL was lower than the experimentally determined parameter for  $\text{ThO}_2$ -3.45%  $\text{UO}_2$  and decreases with burn-up. Also, there is a systematic increase in the average thermal expansion coefficient of simulated fuel with burn-up compared to  $\text{ThO}_2$ -3.45%  $\text{UO}_2$ .

### **2.3 $\text{ThO}_2$ - $\text{CeO}_2$ system**

$\text{CeO}_2$  has been used as surrogate compound in place of  $\text{PuO}_2$  because of its similar physicochemical properties viz., ionic radii in octahedral and cubic coordination, melting points, standard enthalpy of formation and specific heat etc. Applicability of  $\text{CeO}_2$  as a surrogate material for  $\text{PuO}_2$  has been reported by different researchers [97-100]. Most of the studies using  $\text{CeO}_2$  as a surrogate are conducted on uranium based MOX fuels and very few on thorium based MOX fuel. A comparison of some physicochemical properties is given in Table 1.2.

Chen et al [101] describe an effective procedure for mixing and conditioning of ThO<sub>2</sub> and CeO<sub>2</sub> powders suited for pressing and sintering into high density (Th<sub>0.9</sub>,Ce<sub>0.1</sub>)O<sub>2</sub> ceramic pellets. Wet ball milling with an organic dispersant aided the powder dispersing process by reducing the agglomeration of very small oxide particles. They have reported a homogeneous elemental distribution within the calcined powder mixture. Heat treatments were carried out on calcined ThO<sub>2</sub>/CeO<sub>2</sub> mix to study phase transformations. They have reported that solid solution formation commences at around 1300°C and goes to completion at a temperature of 1500°C.

ThO<sub>2</sub> forms a homogeneous solid solution with the cubic fluorite structure when doped with Ce in the entire compositional range and measurements of the thermal expansion and crystallization behavior of Th<sub>1-x</sub>Ce<sub>x</sub>O<sub>2</sub> systems have been reported previously by Yildiz et al and Bukaemskiy et al [102, 103] Studies on same system have also been reported by Mathews et al and Grover et al [104, 105]. However, phase diagram exhibiting complete solubility between ThO<sub>2</sub> and CeO<sub>2</sub> could not be located in the available literature.

The thermal expansion behavior of thoria doped with CeO<sub>2</sub> (y = 0.0, 0.04, 0.08 and 1.0) from room temperature to 1123 K and to 1473 K using high temperature X-ray diffraction (HTXRD) and dilatometer, respectively, have been reported by Mathews et al [98].

From data available in literature, it could be observed that CeO<sub>2</sub> has higher thermal expansion coefficient than ThO<sub>2</sub> and (Th,U)O<sub>2</sub>. Studies showed increase in average coefficient of linear thermal expansion of thoria on addition of CeO<sub>2</sub>. Grover and Tyagi [105] have observed that coefficient of linear thermal expansion of (Th,Ce,Zr)O<sub>2</sub> is higher than

ThO<sub>2</sub> and increases with increase of cerium and zirconium content. Electron probe microanalysis (EPMA) investigations on CeO<sub>2</sub>–ThO<sub>2</sub>–ZrO<sub>2</sub> system have also been reported by Grover et al [106].

Murbayashi [107] tried to simulate the thermal conductivity as a function of temperature and CeO<sub>2</sub> up to 10 wt% using Laser flash method. Nelson et al [108] have extensively evaluated thermophysical properties of stoichiometric CeO<sub>2</sub> and compared with UO<sub>2</sub> and PuO<sub>2</sub>.

Modeling studies using first–principles calculations have been undertaken to investigate various properties of this system [109–112]. The mixing energetics of the ThO<sub>2</sub> doped with CeO<sub>2</sub> were measured by high temperature oxide melt solution calorimetry and supported by a computational density–functional–theory (DFT) study [113]. Experimental studies on thermal conductivity of (Th,Ce)O<sub>2</sub> system and validated by classical molecular dynamics have recently been reported by Ghosh et al [114].

## **2.4 ThO<sub>2</sub>–PuO<sub>2</sub> system**

The experimental data on the phase diagram of thoria–plutonia system is very scarce. Though, absence of hyper–stoichiometry in this system is known, ThO<sub>2</sub>–PuO<sub>2</sub> system is known to exhibit reasonable hypo–stoichiometry. Paprocki et al [115] found that sintering of PuO<sub>2</sub> and ThO<sub>2</sub> mixtures in Ar at around 1700°C results in solid solution. But sintering in hydrogen resulted in the reduction of PuO<sub>2</sub> to Pu<sub>2</sub>O<sub>3</sub>, thus preventing the formation of a homogeneous solid solution. As this hypo–stoichiometry is due to the presence of lower oxidation states of ‘Pu’, it is strongly linked to the fraction of ‘Pu’ in ThO<sub>2</sub>–PuO<sub>2</sub> solid

solution. Freshley and Mattys [116, 117] have shown that  $\text{ThO}_2$  and  $\text{PuO}_2$  form a complete solid solution in the whole composition range and is given in Figure 2.2. A complete solid solution formation of  $\text{ThO}_2$  is reported with various amounts of  $\text{PuO}_2$  in helium at  $1650^\circ\text{C}$  for 6 hours. Freshly and Mattys [116] also reported a linear decrease in lattice parameter with increase in  $\text{PuO}_2$  content of the mixture. XRD pattern of  $\text{PuO}_2$  rich pellets sintered in helium revealed the traces of  $\alpha\text{-Pu}_2\text{O}_3$ .

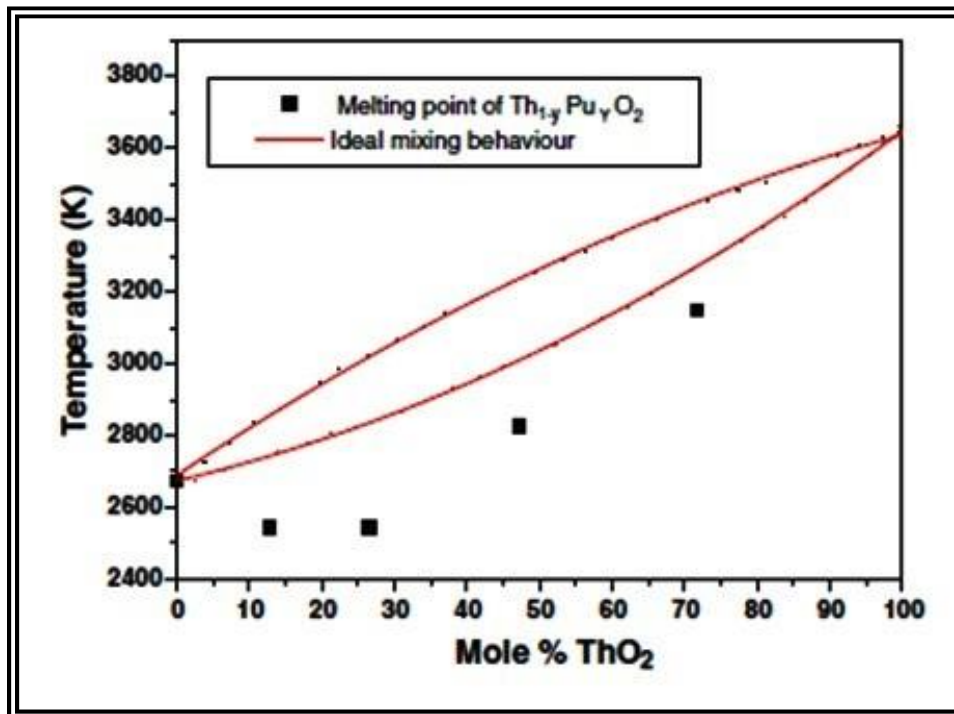


**Figure 2.2 : Phase diagram of  $\text{ThO}_2\text{-PuO}_2$  system [74].**

A low intensity peak corresponding to  $\alpha\text{-Pu}_2\text{O}_3$  was also recorded. Sintering studies showed that the sintered density of  $(\text{Th,Pu})\text{O}_2$  compacts increases with increase in  $\text{PuO}_2$  content between 2 and 50 at.%  $\text{PuO}_2$  [118, 119]. Small additions of  $\text{PuO}_2$  enhance the sinterability of  $\text{ThO}_2$  in the same way as do small addition of  $\text{CaO}$ . A sintered density of 96 %T.D was obtained at  $1600^\circ\text{C}$  in hydrogen atmosphere for  $\text{ThO}_2$  containing 2 to 18% of

PuO<sub>2</sub>. Kutty et al [46] studied the shrinkage behavior of ThO<sub>2</sub>, ThO<sub>2</sub>-30%PuO<sub>2</sub>, ThO<sub>2</sub>-50%PuO<sub>2</sub> and ThO<sub>2</sub>-75%PuO<sub>2</sub> pellets using a dilatometer in inert (Ar) and reducing atmospheres (Ar-8%H<sub>2</sub>). The effects of dopants like CaO and Nb<sub>2</sub>O<sub>5</sub> on shrinkage of the above compositions were also evaluated. Out of the two dopants studied, CaO was found to be a better dopant for all the composition covered in their study. They reported that shrinkage was marginally superior in Ar-8%H<sub>2</sub> than Ar atmosphere. They also observed that addition of PuO<sub>2</sub> to ThO<sub>2</sub> enhanced sintering rate.

A continuous series of solid solution has also been reported by Mulford and Ellinger [120] who reported only a single fluorite structure by X-ray diffraction (XRD) and also showed that the lattice parameter of the solid solution varied linearly with composition. The lattice parameter of fluorite type cubic phase was found to decrease regularly from 0.5597 nm for ThO<sub>2</sub> to 0.5396 nm for pure PuO<sub>2</sub> [121]. The lattice parameter of (Th<sub>1-y</sub>Pu<sub>y</sub>)O<sub>2</sub> decreases linearly from pure ThO<sub>2</sub> to pure PuO<sub>2</sub> [122].

Fabrication of (Th,Pu)O<sub>2</sub> pellets have been very scarcely reported in open literature. Few reports available belong to Indian fuel fabrication facilities. The conventional route have been adopted for fabrication of fuel pellets of (Th,Pu)O<sub>2</sub> with varying compositions for densification studies, microstructure investigations and thermal expansion studies [123-127]. The only reported data on oxygen potential of ThO<sub>2</sub>-PuO<sub>2</sub> is the one determined in Hanford Engineering Development Laboratory [128], measured by thermogravimetry. The data is available only for Pu/(Th + Pu) = 0.25 and 0.35, at 1273, 1373 and 1473 K, up to hypo-stoichiometry region of its stability. Unlike in the case of (Th,U)O<sub>2+x</sub>, where oxygen potential

increases with decreasing 'U' content, in (Th,Pu)O<sub>2-x</sub> system, oxygen potential decreases with decrease in 'Pu' content.

Although thorium-based fuels have been studied extensively in the past, namely in the 1970s, very little open literature is available for (Th,Pu)O<sub>2</sub> [123,124]. Only a few measurements of thermal conductivity have been made for ThO<sub>2</sub>-PuO<sub>2</sub> fuel. Bakker et al have evaluated the thermal properties of ThO<sub>2</sub>, Th<sub>1-y</sub>U<sub>y</sub>O<sub>2</sub> and the literature data on ThO<sub>2</sub>-PuO<sub>2</sub> system [74]. Jeffs [125, 126] determined the integral thermal conductivity of irradiated (Th<sub>1-y</sub>Pu<sub>y</sub>)O<sub>2</sub> containing 1.10, 1.75, and 2.72 wt% of PuO<sub>2</sub> using a steady state method.

The thermal conductivity of a mixture of ThO<sub>2</sub> and 4 wt% PuO<sub>2</sub> was also measured by Basak et al [124] using the laser flash technique for the temperature range of 950–1800 K. Recently, Cozzo et al [127] reported that at 500 K the thermal diffusivity of the Th-MOX can be down to 50 % of that of its pure oxide components ThO<sub>2</sub> and PuO<sub>2</sub>. The thermal conductivity, **k**, of (Th<sub>1-y</sub>Pu<sub>y</sub>)O<sub>2</sub> as a function of temperature and PuO<sub>2</sub> content is reported by IAEA study [2]. Thermal conductivity data of ThO<sub>2</sub>-20%PuO<sub>2</sub>, ThO<sub>2</sub>-30%PuO<sub>2</sub> and ThO<sub>2</sub>-70 % PuO<sub>2</sub> with CaO or Nb<sub>2</sub>O<sub>5</sub> as dopant have been reported in the literature [128]. ThO<sub>2</sub>-70 % PuO<sub>2</sub> showed the least thermal conductivity among these samples.

## CHAPTER 3. EXPERIMENTAL METHODOLOGY

### 3.1 Experimental details

#### 3.1.1 Feed Material

The feed powders of ThO<sub>2</sub>, UO<sub>2</sub>, U<sub>3</sub>O<sub>8</sub>, CeO<sub>2</sub>, PuO<sub>2</sub> and co-precipitated (Th,U)O<sub>2</sub> by oxalate route [7] were used for preparation of experimental sample pellets. The important characteristics of starting ThO<sub>2</sub>, UO<sub>2</sub>, U<sub>3</sub>O<sub>8</sub>, CeO<sub>2</sub>, PuO<sub>2</sub> and co-precipitated (Th,U)O<sub>2</sub> powders used in the studies are given in Table 3.1.

*Table 3.1: Characteristics of feed powders used in various experiments.*

Property	ThO <sub>2</sub>	CeO <sub>2</sub>	UO <sub>2</sub>	U <sub>3</sub> O <sub>8</sub>	PuO <sub>2</sub>	Co-precipitated (Th,50%U)O <sub>2</sub>
Apparent density (g/cc)	0.7	0.3	1.3	0.9	1.6	0.9
Specific Surface Area (m <sup>2</sup> /g)	1.53–2.98	20	3	2.15	20–30	7.16
Theoretical density (g/cc)	10	7.2	10.96	8.34	11.46	10.48 [26]
O/M ratio	2	2	2.18	2.66	1.99	2.301
Total Impurities (ppm)	< 1200	< 500	< 700	< 700	< 2500	< 2500

It could be observed that the UO<sub>2</sub> and CeO<sub>2</sub> powder characteristics are similar to PuO<sub>2</sub> powder from density and specific surface area aspects respectively. The density and specific surface area of the powder are important criteria which govern the extent of coating on spheroids during fabrication vide CAP process. U<sub>3</sub>O<sub>8</sub> powder was obtained by heating of the

UO<sub>2</sub> powder at 873K for 4h. The total chemical impurities of the feed powders were analyzed and determined by techniques described in subsequent Section 3.2.5.

The thoria powder used in the studies exhibited platelet morphology as shown in Figure 3.1(a). The as-received ThO<sub>2</sub> powder was milled in a planetary ball mill for 3 h to break its platelet morphology. A typical SEM picture of milled ThO<sub>2</sub>, CeO<sub>2</sub> and U<sub>3</sub>O<sub>8</sub> powders used for experimental studies are shown in Figures 3.1(b), 3.1(c) and 3.1(d) respectively. The values of apparent and tap densities of ThO<sub>2</sub> powder before and after milling are given in Table 3.2. Resultant change in powder morphology due to milling operation reflected as improved powder density characteristics due to reduced mechanical interlocking of the particles.

***Table 3.2: Density of ThO<sub>2</sub> powder before and after milling.***

<b>Density (g/cc)</b>	<b>ThO<sub>2</sub> (as received)</b>	<b>ThO<sub>2</sub> ( milled)</b>
Apparent	0.973	2.143
Tap	1.219	3.00

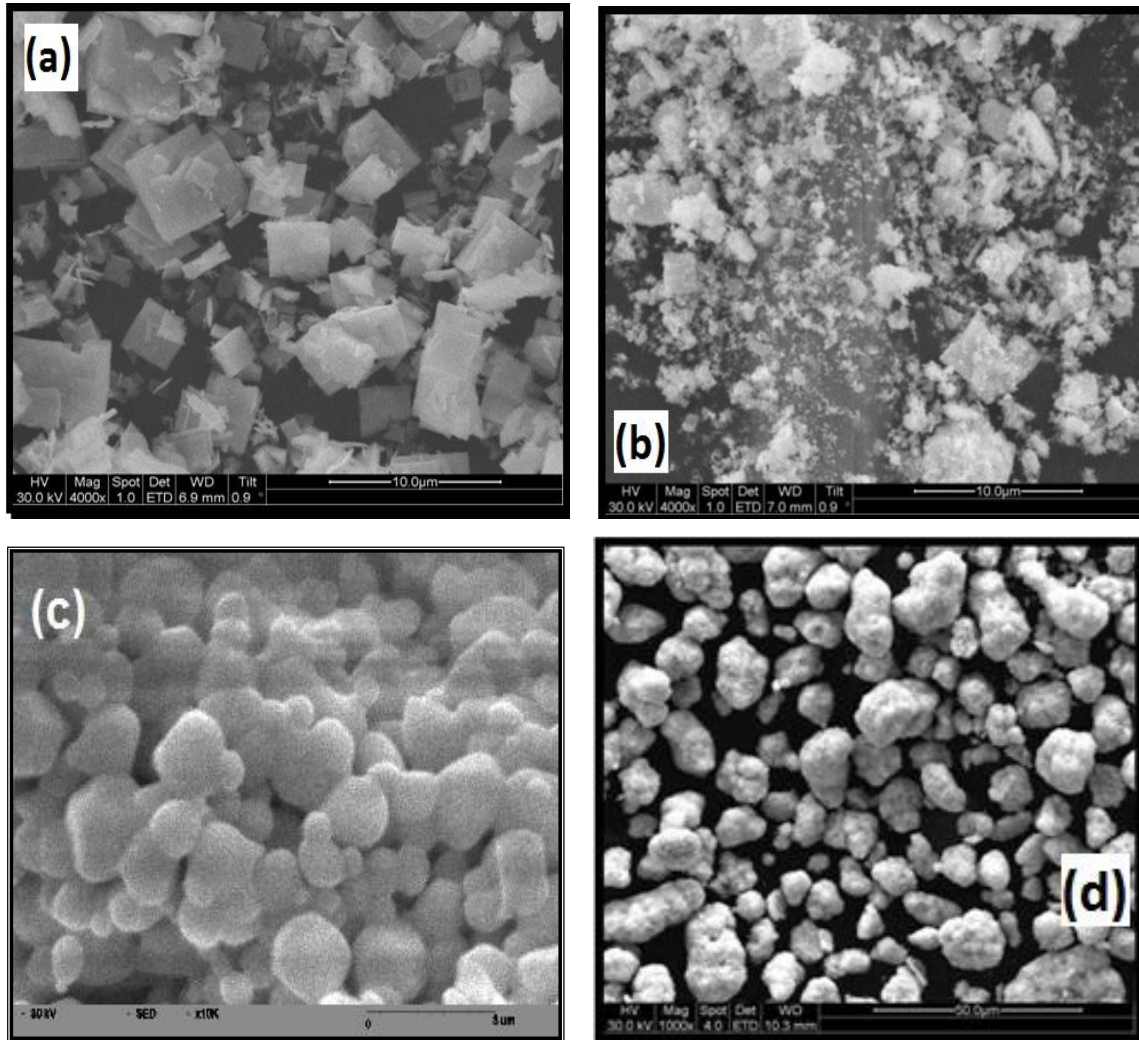


*Figure 3.1: SEM photographs showing morphology of ThO<sub>2</sub> powder (a) before milling, (b) after milling, (c) CeO<sub>2</sub> powder and (d) U<sub>3</sub>O<sub>8</sub> powder.*

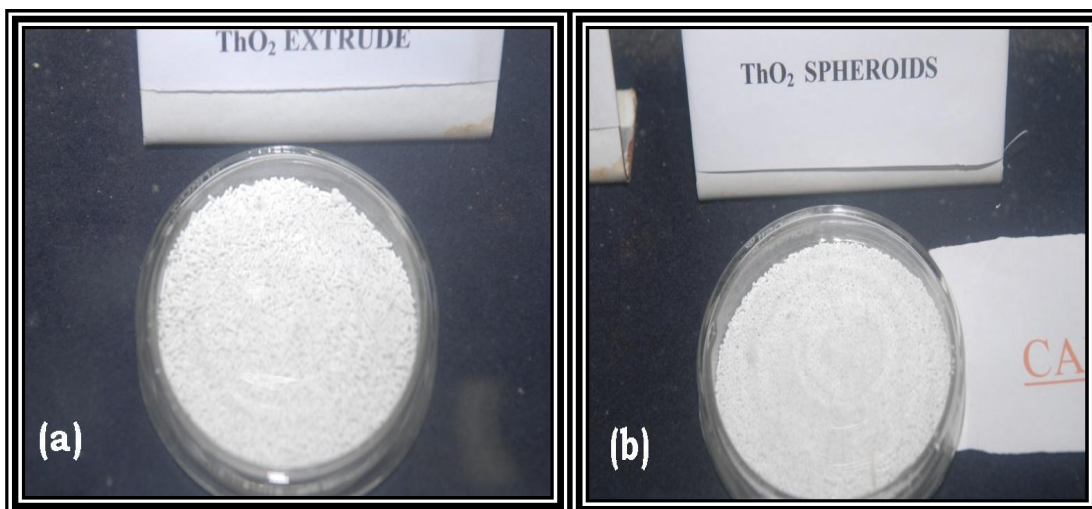


**Figure 3.2 :** (a) *Thoria extrudes* and (b) *Thoria spheroids*.

As mentioned in Section 1.2, the powder is extruded and subsequently spheroidized in CAP process. Figures 3.2(a) and 3.2(b) show the thoria extrudes and spheroids fabricated by CAP process respectively. The co-precipitated (Th,U)O<sub>2</sub> powders obtained from FRD, BARC were analyzed for phases by XRD, O/M and chemical composition. The XRD pattern is shown in Figure 3.3 and at higher angles in Figure 3.4. The chemical analysis of co-precipitated powder was carried out using techniques described in subsequent Section 3.2.5. The ratio of heavy metal content and the impurities of the co-precipitated powder are given in Tables 3.3 and 3.4 respectively.

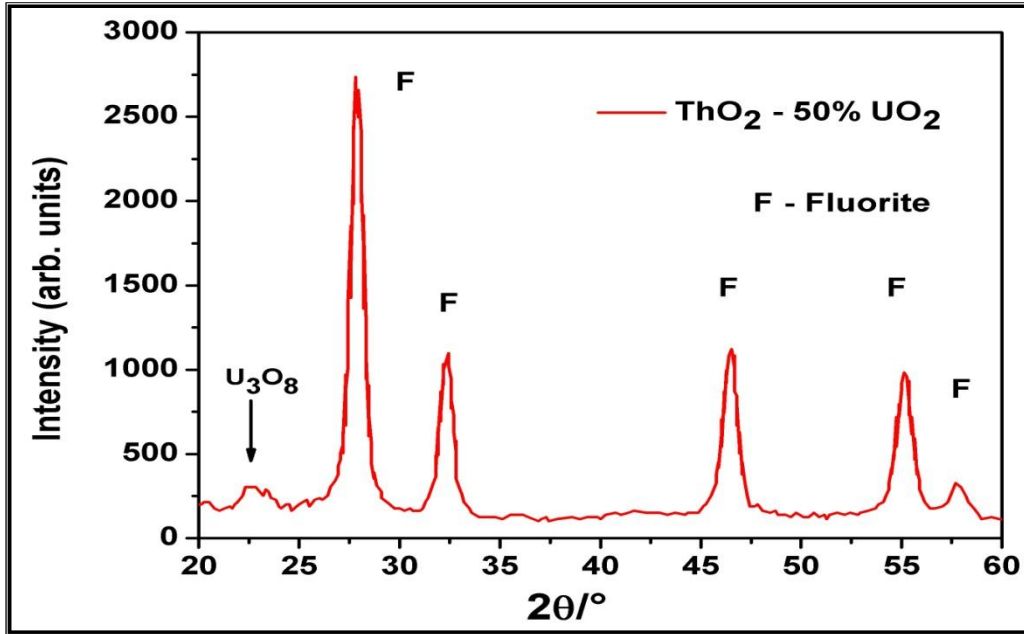


Figure 3.3 : XRD patterns of  $\text{ThO}_2$ -50% $\text{UO}_2$  powder made by co-precipitation process.

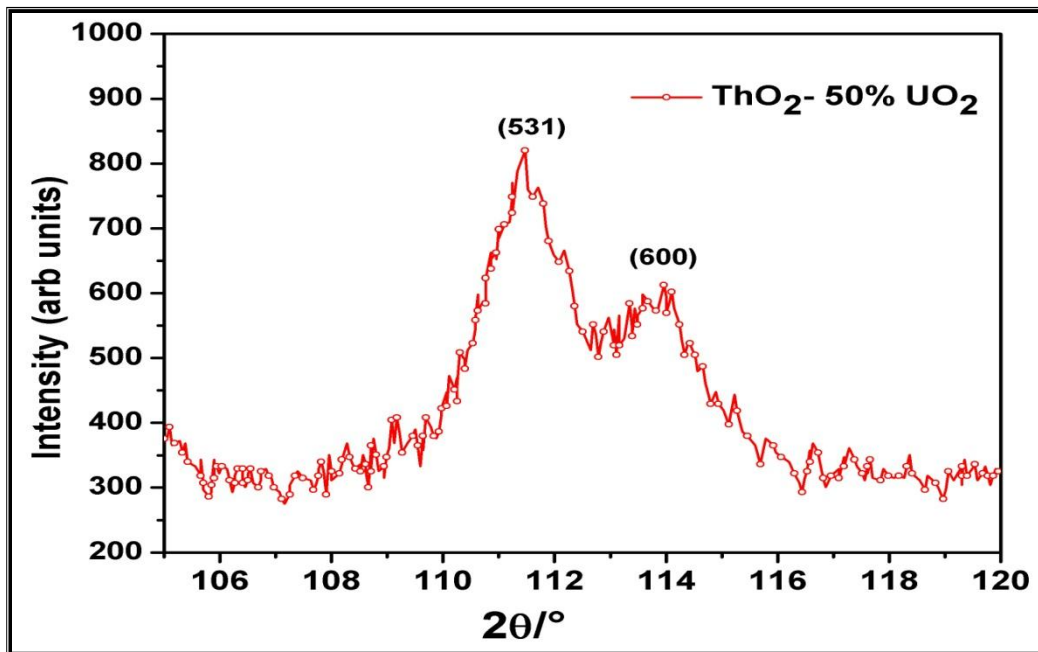


Figure 3.4: XRD patterns of  $\text{ThO}_2$ -50% $\text{UO}_2$  powder at higher angles for the determination of lattice parameters.

**Table 3.3 : Chemical analysis for co-precipitated (Th-U)O<sub>2</sub> powder.**

<b>Composition</b>	<b>Ratio of Th:U (wt.%)</b>
ThO <sub>2</sub> -50%UO <sub>2</sub>	50.1:49.9

**Table 3.4 : Impurities in the (Th,U)O<sub>2</sub> powder made by co-precipitation.**

<b>Element</b>	<b>ThO<sub>2</sub>-50%UO<sub>2</sub> (ppm)</b>	<b>Element</b>	<b>ThO<sub>2</sub>-50%UO<sub>2</sub> (ppm)</b>
B	0.1	W	<40
Cd	<0.1	Cr	<5
Co	<5	Pb	9.1
Ca	<5	Mo	19.6
Fe	<10	Ni	20.5
Si	<40	Na	<5
Al	43.4	V	<5
Mn	<2	Zn	<10

Table 3.5 shows the lattice parameters and phases present in the co-precipitated powder of ThO<sub>2</sub>-50%UO<sub>2</sub> composition. From the O/M ratios and the lattice parameter data, the amount of U<sub>3</sub>O<sub>8</sub> present in the above powders was estimated. The estimation was made from the assumption that for high O/M values, ThO<sub>2</sub> forms a solid solution with UO<sub>2.25</sub>. The remaining UO<sub>2</sub> is assumed to exist as U<sub>3</sub>O<sub>8</sub>. The amount of U<sub>3</sub>O<sub>8</sub> present in ThO<sub>2</sub>-50%UO<sub>2</sub> powders was calculated and found to be 14.19 mol%.

**Table 3.5: Lattice parameter, O/M ratio and the amount of  $U_3O_8$  in co-precipitated (Th,U) $O_2$  powder after heating in air at 973K for 3 h.**

<b>Material</b>	<b>Lattice parameter (nm)</b>	<b>O/M</b>	<b>y in <math>(Th_{1-y}U_y)O_{2+x}</math></b>	<b>Mol% <math>U_3O_8</math></b>
ThO <sub>2</sub> -50%UO <sub>2</sub>	0.55205	2.301	0.4781	14.19

### **3.1.2 Preparation of green pellets**

The green pellets were fabricated by both conventional powder metallurgical and coated agglomerate pelletization routes.

#### **3.1.2.1 POP Route**

The steps involved for the fabrication of ThO<sub>2</sub> MOX green pellets using conventional powder metallurgy route of POP consists of the following:

1. Weighing of as received ThO<sub>2</sub> and U<sub>3</sub>O<sub>8</sub>/CeO<sub>2</sub>/PuO<sub>2</sub>/Co-precipitated powder for required composition of study,
2. Mixing and milling of the powders in an high energy ball mill along with 1.2% polyethylene glycol (liq.) and 0.8% oleic acid (liq.) as binder cum lubricant ,
3. Pre-compaction of the above prepared mixtures at 105–120 MPa,
4. Granulation of the pre-compacts in an oscillatory granulator,
5. Sieving of granules using – 40 mesh,
6. Double Pre-compaction of the above prepared mixtures at 105–120 MPa,
7. Granulation of the pre-compacts in an oscillatory granulator,
8. Sieving of granules using – 40 mesh, and

9. Final cold compaction of the granules at 270–300 MPa into green pellets

All the above and subsequent operations were carried out in alpha leak tight and shielded glove boxes (refer Figure 1.2).

### **3.1.2.2 CAP Route**

The steps involved for the fabrication of ThO<sub>2</sub> based MOX green pellets using newly proposed and developed coated agglomerate pelletization (CAP) technique are described below:

1. Milling of the as received ThO<sub>2</sub> powder in an high energy ball mill,
2. Mixing of milled ThO<sub>2</sub> powder with 10% water, 1.2% polyethyelene glycol (liquid, binder) and 0.8% oleic acid (liquid, lubricant) in a planetary mixer for 30 minutes,
3. Extrusion of mixed ThO<sub>2</sub> powder in an extruder with perforated roller with 1mm holes,
4. Spheroidisation of ThO<sub>2</sub> extrudes in a spheroidiser,
5. Sieving using –40 mesh,
6. Drying of spheroids in an oven at 343 K for 1 h,
7. Coating of ThO<sub>2</sub> spheroids with weighed quantity of U<sub>3</sub>O<sub>8</sub> / CeO<sub>2</sub> / PuO<sub>2</sub> / co-precipitated powder admixed with binder in an universal mixer, and
8. Final compaction of the coated spheroids at 270–300 MPa into green pellets

Only operations 7 onwards (refer Figure 1.3) required to be carried out in alpha leak tight as well as shielded glove boxes. The apparent and tap densities of granules of conventional powder metallurgical (POP) route and spheroids of newly developed CAP process made by using ThO<sub>2</sub> and U<sub>3</sub>O<sub>8</sub> were measured and are given Table 3.6.

**Table 3.6: Density of  $\text{ThO}_2\text{-U}_3\text{O}_8$  granules and spheroids.**

Density (g/cc)	Granules	Spheroids
Apparent	2.54	2.972
Tap	3.386	3.442

The green densities of the compacts made by either POP route or CAP process were maintained in the range of 65–67% of the theoretical density. Figure 3.5 (a) and Figure 3.5 (b) show thoria extrudes coated with  $\text{U}_3\text{O}_8$  and green CAP pellets of  $\text{ThO}_2\text{-U}_3\text{O}_8$  respectively. Figure 3.6 shows green pellet fabricated by CAP process of composition  $\text{ThO}_2\text{-5%CeO}_2$ .

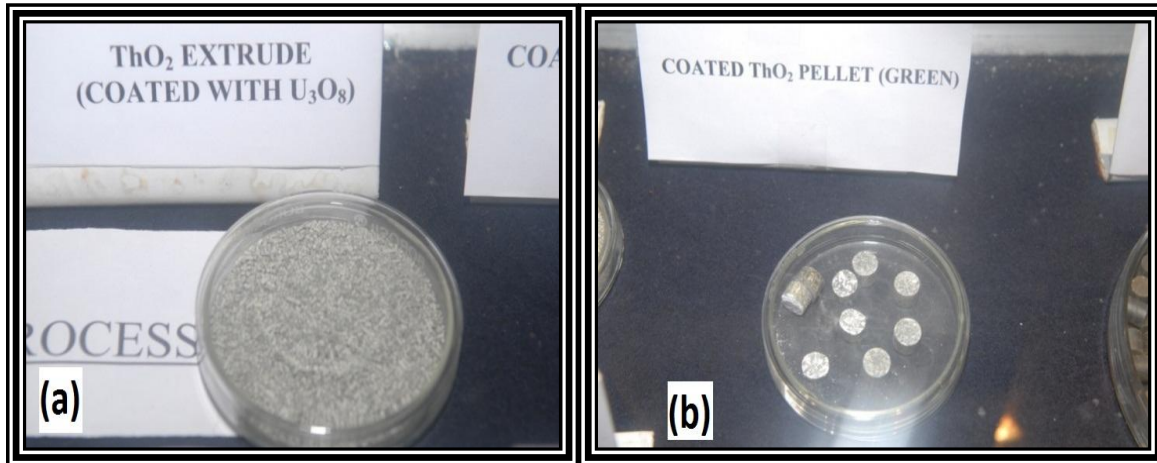


**Figure 3.5: (a) Thoria extrudes coated with  $\text{U}_3\text{O}_8$  (b) Green CAP pellets.**



**Figure 3.6:** *ThO<sub>2</sub>-5%CeO<sub>2</sub> green pellet fabricated by CAP process.*

### **3.1.3 Fabrication of Sintered compacts**

The green compacts of different compositions and enrichments were fabricated by POP and CAP routes and were sintered together in a resistance heating batch furnace. The sintering of pellets in oxidizing conditions was carried out in furnace with moly di silicide (MoSi<sub>2</sub>) heating elements in Air atmosphere at 1823 K ± 25 K for 4 h, whereas, for sintering in reducing conditions was carried out in furnace with molybdenum (Mo) heating elements in Ar-H<sub>2</sub> at 1923 K ± 25 K for 4 h.

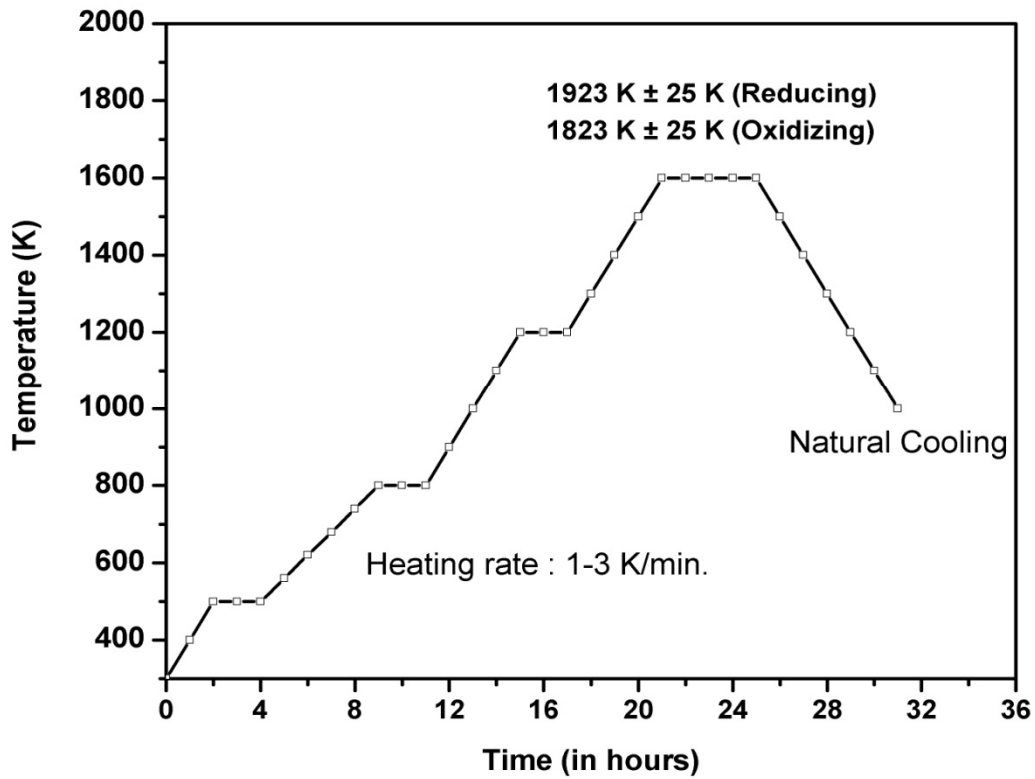


**Figure 3.7: Sintering profile temperature with respect to time.**

ThO<sub>2</sub> reference pellets were also prepared using POP route and sintered in oxidizing atmosphere for comparison during thermal expansion and diffusivity studies. Similarly (Th,Pu)O<sub>2</sub> reference POP pellets for the studies were prepared in reducing atmosphere conditions. Figure 3.7 shows the standard sintering profile along with the soaking times used for sintering of the samples for studies. Presently employed sintering profile for fabrication of good quality and acceptable pellets has been adopted for the present studies.

### **3.1.4 Fabrication of pins**

The metrological accepted sintered pellets of  $\text{ThO}_2 - 1\% \text{PuO}_2$  made by POP and CAP process were visually inspected, degassed and separately loaded into stainless steel clad tubes for encapsulation. The end plugs were welded by TIG welding. These sealed tubes containing fuel pellets are known as fuel pins. The pins were decontaminated to avoid radiation hazard to persons handling the fuel pins. These pins were gamma scanned.

## **3.2 Characterization Techniques**

### **3.2.1 Density**

The pellet density was determined by geometrical methods as per ASTM standards C 776–83. The green density of the pellet was measured by geometric method using micrometer and weighing balance. The density of the sintered pellet was measured by geometric method and Archimedes method.

### **3.2.2 Oxygen to metal ratio by Thermo gravimetric (TG) analysis**

Oxygen to metal (O/M) ratio of the sintered pellet was determined by thermogravimetry (TG) method. Thermo–gravimetric study on the sintered pellet was carried out in Setsys Evolution 24 TG–DTA/DSC equipment having provision of moisture control of the gas. The pellet was pulverized and sample powder ~ 2 g was loaded in TG and heated upto 1273 K and held isothermally for 4 h in a flowing  $\text{Ar}-8\% \text{H}_2$  gas (flow rate: 20 cc/min) with a heating rate of 2 K/min over saturated moisture ( $\text{H}_2\text{O}$ ) content with defined oxygen potential ( $-100 \text{ kcal/mol}$ ) which ensures the perfect oxygen stoichiometry to 2.0. The change in weight of the sample was noted continuously as it was heated. Thus the change in weights

(gain/loss) before and after the experiment measured by TG corresponds to the extent of hypo-/hyper-stoichiometry from which the O/M ratio was calculated. The accuracy of the measurement in weight was within  $\pm 1 \mu\text{g}$ .

### **3.2.3 XRD studies**

X-ray diffraction studies of the sintered pellets were carried out using STOE diffractometer (Diano XRD-8760) using Cu K $\alpha$  radiation and graphite monochromator. The XRD patterns were recorded at a  $2\theta$  scan rate of  $1^\circ/\text{min}$  from  $20^\circ$  to  $70^\circ$ . Accuracy of this equipment for phase analysis is typically  $\pm 2\%$ .

### **3.2.4 Microstructure**

For microstructure investigation, the sintered pellet was mounted in Araldite cement and ground using emery papers of increasing grit size. The final polishing was carried out using diamond paste as polished structure was observed under optical microscope for pore size evaluation and their distribution. The pellets were removed from the mount by dissolving the Araldite cement in acetone and then etched thermally at 1873 K for 4 h. The etched samples were examined under optical microscope (model: Leica make: model DM ILM).

The grain size of the sintered pellet was measured by linear intercept method. The etched samples of pellet were mounted in Bakelite, silver coated and were examined in SEM (Model: Quanta 200)/ SEM (Philips make, Model: XL- 30) using tungsten filament for microstructure evaluation. The elemental distribution of area scan or line scan was determined by X-ray mapping with the help of EPMA (Cameca, Model Sx-100).

### **3.2.5 Chemical analysis (Heavy metal content and Total impurity)**

The sintered pellet was analyzed chemically for the heavy metal content by dissolution method in Microwave setup. The pellet was pulverized and powdered sample (100 –200 mg) was dissolved using 16 M HNO<sub>3</sub> and 0.05 M HF in PTFE pressure vessel. The time taken for complete dissolution of sample was 1 h. For the determination of Th content, complexometric EDTA titration was carried out at 2–3 pH with xylenol orange indicator. U/Pu was titrated separately using electro analytical technique like Davies and Gray method. The chemical impurity analysis of the sintered pellets was carried out by ICP–AES analysis.

### **3.2.6 Alpha– Autoradiography**

The sample preparation of sintered pellets of POP and CAP route for alpha autoradiography was using conventional metallography sample preparation techniques. The surface of the pellet was ground using emery papers of different grit sizes. The ground pellet surface was polished by using polishing papers and finally by diamond paste smeared on polishing cloth. The pellet surface was cleaned ultrasonically to remove any loose particles. The polished samples were placed on the alpha sensitive polymer film (CR–39) covered with aluminum mylar of thickness 11 µm. For avoiding any experimental errors, both the samples of CAP and POP were mounted in araldite. The mount was placed on a single film and exposed for an identical period (30s). A load of 350 g was kept on the mount during exposure to ensure proper contact between the samples and the film. The irradiated film was decontaminated and chemically etched to reveal the alpha tracks using 6N KOH at 343 K for 90 minutes and examined under a microscope. The microscopic image of each of the alpha

autoradiographs was analyzed using an image analysis software (Metal power image analyzer version 3.0.0.9) for the measurement of alpha tracks /cm<sup>2</sup> (track density) of various sections of the sample. Higher specific activity element rich areas could be estimated by the increased  $\alpha$  track density in the region. The samples of (Th,Ce)O<sub>2</sub>, (Th,U)O<sub>2</sub> and (Th,Pu)O<sub>2</sub> were prepared using similar methods and alpha autoradiography was carried out. The alpha autoradiographs were further analyzed using different techniques.

### **3.2.7 Transport property (Ionic conductivity)**

Ionic conductivity measurements were carried out on pellets of (Th,5%Ce)O<sub>2</sub> fabricated by both CAP and POP routes and sintered in air and Ar-H<sub>2</sub> atmospheres. Platinum conductive paste was coated on both faces of the sample sintered pellet and allowed to dry. The coated pellet was heated to 950°C at a constant heating rate of 300°C/h to bake out the organic matters present in the paste. Electrical measurements were carried out in a SOLARTRON (Model: 1260) frequency response analyser in the frequency range 1 Hz to 10 MHz and in the temperature range 400 – 700°C. PROBOSTAT sample holder (Norwegian Ceramic Society, Norway) was employed for measurement.

### **3.2.8 Thermal Expansion**

#### **3.2.8.1 Dilatometry**

The thermal expansion studies were carried out using a Setaram (model) vertical dilatometer. The sintered pellets were heated at a heating rate of 2 K/min up to 1773 K in high purity argon atmosphere at a flow rate of 20 cc/min. The accuracy of the measurement of change in length was within  $\pm 0.1 \mu\text{m}$ . The coefficient of thermal expansion (CTE) was

calculated by a software package attached to the dilatometer. Data correction was made using the standard sample (poco graphite – NIST). The coefficient of thermal expansion (CTE) between two temperatures  $T_1$  and  $T_2$  can be calculated using the equation 1.

$$\text{CTE}_{T_2-T_1} = \left[ \frac{(L_2-L_1)}{L_1} \right] \left[ \frac{1}{(T_2-T_1)} \right] \quad (1)$$

where,  $L_1$  and  $L_2$  are the lengths at temperatures  $T_1$  and  $T_2$  respectively.

### **Calibration of Dilatometer:**

A blank heating was carried out in similar experimental condition where actual samples were heated, called the ‘standard run’ to find the expansion of sample holder, push rod etc which accounted for the expansion of the system. This expansion data of the ‘standard run’ was subtracted for all subsequent experimental data. Dilatometer was calibrated with respect to both expansion value as well as temperature. The calibration for expansion was carried out with the standard reference material, Tungsten. The comparison of reported [129] and experimental thermal expansion data for Tungsten NBS SRM (Standard Reference Material) 737 is shown in Figure 3.8. The temperature calibration of dilatometer was done using uranium metal sample whose phase transformation temperatures are known. From room temperature to its  $\alpha$  (orthorhombic)  $\rightarrow$   $\beta$  (tetragonal) at 942 K and  $\beta$  (tetragonal)  $\rightarrow$   $\gamma$  (bcc) at 1045 K. Slope changes at these phase transformation temperatures were observed in the thermal expansion vs. temperature plot in dilatometer for uranium metal and were noted. The experiment was repeated to check the reproducibility of the data.

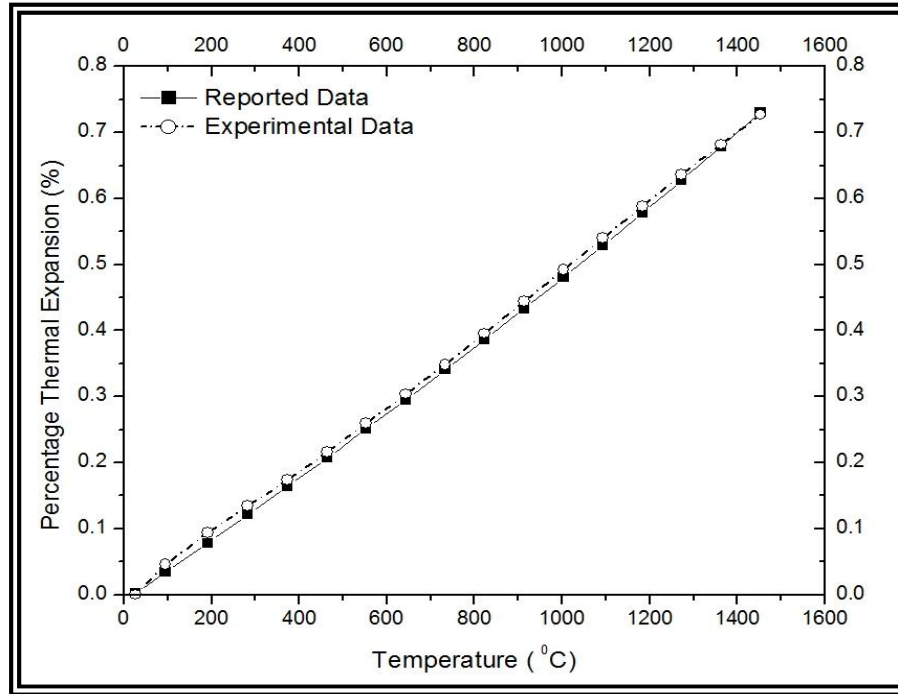


***Figure 3.8 : Comparison of experimental percentage thermal expansion data of Tungsten 737, the NIST Standard Reference Material (SRM 737), against reported data.***

The reproducibility of the data from dilatometer was also found to be well within the acceptable limit. The transition temperatures observed were compared with the corresponding phase transformation temperature of uranium as reported in the literature and were found to be in close agreement with each other. This is shown in Figure 3.9. The alpha to beta phase transformation temperature was found to be 941 K as against reported temperature of 942 K [96]. The beta to gamma transformation temperature was found to be the same as reported temperature of 1045 K [96].

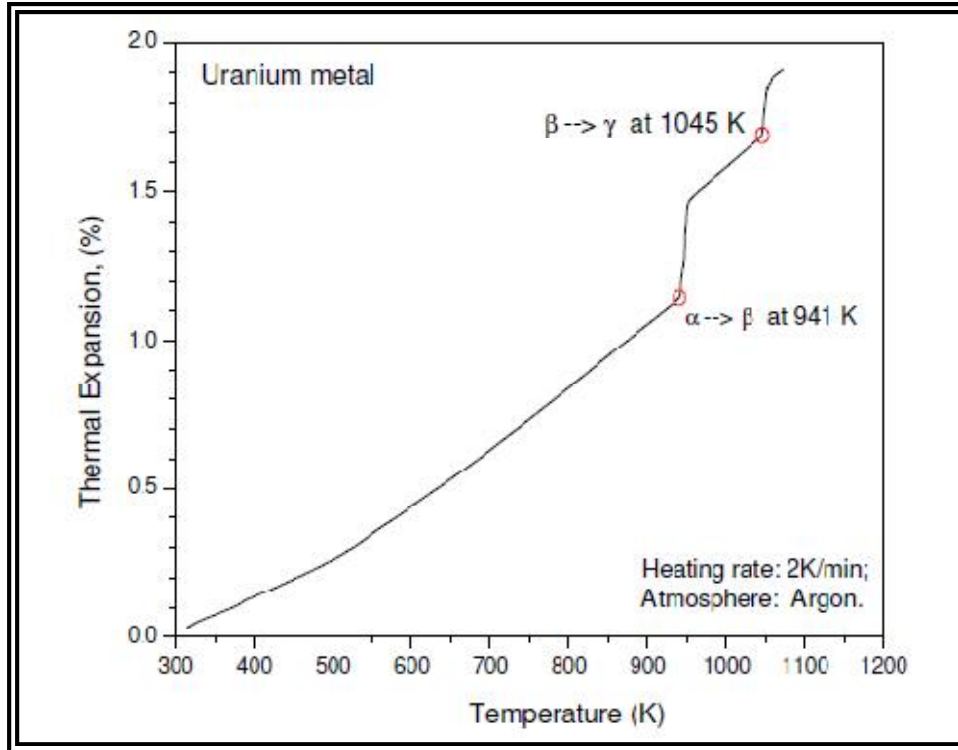


*Figure 3.9: Phase transformation temperatures for uranium metal as observed in dilatometer.*

### 3.2.9 Thermal diffusivity

The thermal diffusivity measurements of the samples of  $\text{ThO}_2-(\text{CeO}_2/\text{UO}_2/\text{PuO}_2)$  were done by laser flash method (Ulvac, Sinku-Riko, Japan). The thermal diffusivity ( $\alpha$ ) was calculated from the equation 2.

$$W L^2 / \pi t_{1/2} \quad (2)$$

where,  $t_{1/2}$  is the time required in seconds to reach half of the maximum temperature rise at the rear surface of the sample and L is the sample thickness in millimeter and W is a dimensionless parameter which is a function of the relative heat loss from the sample during the measurement.

### 3.2.10 Thermal conductivity

The thermal conductivity was deduced from the experimental values of thermal diffusivity, specific heat and density of the sample using the following equation 3:

$$\kappa_m = \alpha * C_p * \rho \quad (3)$$

where,  $\kappa_m$  is measured thermal conductivity in W/mK,  $\alpha$  is the thermal diffusivity in  $\text{cm}^2/\text{s}$ ,  $C_p$  is the specific heat in J/g K and  $\rho$  is the density of the sample in g/ cc.

### 3.2.11 Passive Gamma Scanning

Passive gamma scanning of welded and decontaminated fuel pins loaded with the accepted pellets of  $\text{ThO}_2 - 1\% \text{PuO}_2$  fabricated through CAP and POP routes was carried out using the gamma scanning set up to study the homogeneity of Pu distribution across the length of fuel stack. This technique indirectly gives an idea of fissile heavy metal content variation in the pellets within a batch.

The gamma scanner set up consists of a fully automated pin movement system in synchronization with the counting system. The counting system consists of annular NaI (TI) detector coupled with a single channel analyzer based counting electronics. An annular counting system was chosen for this study as it was more sensitive and suitable for this composition [130].

The signature gamma complex peak of  $\text{Pu}^{239}$  centered at 384keV was selected for the assay [131] and the full pin was assayed in virtually divided segments. The counts obtained from the segments were statistically analyzed to understand the fissile material distribution.

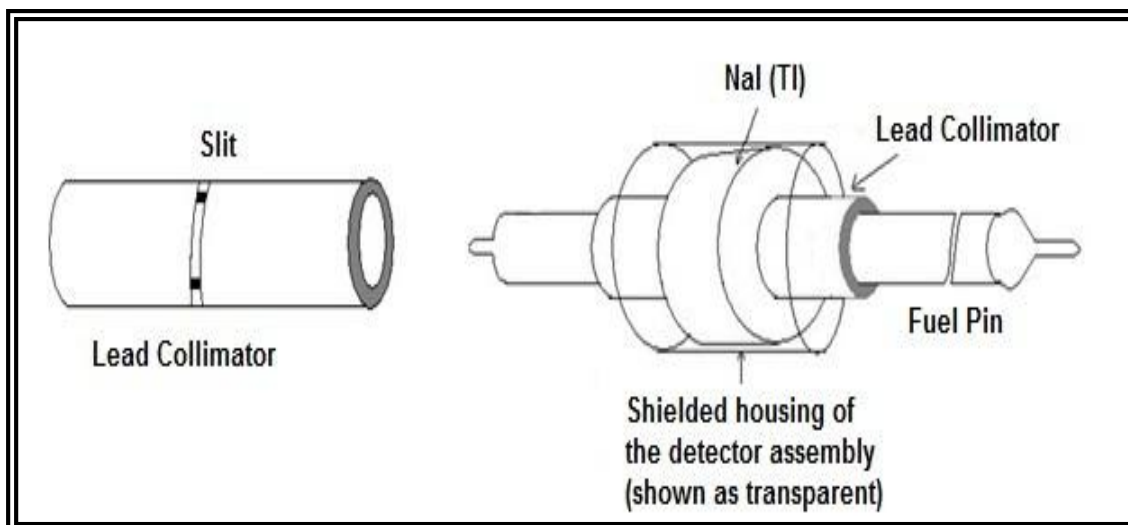


**Figure 3.10: Schematic of annular counting set up.**

The detector was externally shielded with lead sandwiched stainless steel housing and collimated internally with a pipe shaped lead collimator with slit size 8mm. The counting system was calibrated for energy window and counting error with standard sources and a counting error of < 1% of the average counts were achieved under the scanning conditions. The pin was made to pass through the collimator so that the fuel pin was virtually divided into segments of width 8 mm each for assay as shown in Figure 3.10. Every segment of the pin was assayed for constant time by enabling the pin movement in steps with a speed of 8mm/s.

### **3.2.12 Specific Heat (Cp)**

Differential scanning calorimeters of heat flux type was used for the measurement of heat capacities of thoria–ceria samples. In the low temperature range (300 to 760 K) DSC–131 was used whereas MHTC–96 was used for the measurement of heat capacity in the high temperature range (700 to 1650 K). The sintered pellet were crushed into powder under inert

atmosphere in a glove box and loaded into the measuring crucible of MHTC which was further annealed in the high pure argon atmosphere at the highest temperature of measurement. The crucible was filled successively with the powder and the annealing procedure was repeated to ensure firm contact between the sample and the crucible wall. This method ensures good thermal contact between the sample and the crucible wall.

## **CHAPTER 4. CHARACTERIZATION STUDIES ON (Th,Ce)O<sub>2</sub> SYSTEM**

### **4.1 Introduction**

Studies on material like PuO<sub>2</sub> are subjected to restrictions due to stringent safety and strategic requirements and only few characterization equipments are adaptable in the glove boxes, therefore, studies require to be conducted with substitute material having similar characteristics of PuO<sub>2</sub>. As discussed earlier in Section 1.2, CeO<sub>2</sub> has such properties and has been used in the study.

This chapter deals with the experimental studies conducted on (Th,Ce)O<sub>2</sub> system wherein CeO<sub>2</sub> has been used as surrogate for PuO<sub>2</sub> because of their similar physicochemical properties. The studies aim to address the characterization of pellets for their physical, metallurgical, chemical and thermal properties which otherwise are difficult to be performed on actual (Th,Pu)O<sub>2</sub> pellets. The studies will draw a parallel comparison of characteristics of the pellets fabricated by coated agglomerate pelletization process (CAP) viz a viz with pellets made by conventional powder processing and pelletization process (POP). The thermal properties evaluated by experimental techniques will be verified by molecular dynamics approach for better understanding.

### **4.2 Shrinkage behavior POP and CAP pellets**

The physical properties of the final pellet depend substantially on sintered density. The shrinkage studies are therefore, important for determining the optimum parameters for achieving such characteristics in the pellet. These also help in understanding the mechanisms operating during sintering. The shrinkage behavior of the green pellets of

(Th,5%Ce)O<sub>2</sub> fabricated by both CAP and POP routes was studied in both air and argon (Ar) atmospheres by dilatometry. The densification plots of ThO<sub>2</sub>-CeO<sub>2</sub> POP green pellets and CAP green pellets under air and Ar atmosphere with respect to temperature at 10K/min are shown in Figure 4.1. The rate of shrinkage dY/dT, (where,  $Y = \Delta L/L_0$ ) for all the powder compacts were evaluated and plotted as a function of heat treatment temperature in Figure 4.2.

The shrinkage behavior of both POP and CAP samples was observed to be different. Moreover, sintering atmosphere was found to influence the sintering behavior. The maximum extent of shrinkage was found in POP sample sintered in air and minimum in the CAP sample sintered in argon atmosphere. It was also observed from the dilatometric plots that the samples of CAP and POP sintered in air had higher shrinkage as compared to the samples sintered in argon. A comparison of densification values (in %) of the pellets at maximum temperature of study are presented in Table 4.1. Although the pressed densities of all these powders were very close to each other (65–67% T.D), the extra shrinkage in the air sintered samples over the samples sintered in argon was an indication of attainment of better sintered density by the former. The shrinkage behavior was not different when CAP pellets were sintered in air and in argon (Ar). The onset temperature of shrinkage between the CAP pellets were sintered in air and in argon (Ar) was only ~ 50 K, whereas, the difference was appreciable ~200 K in the case of POP pellets (Figure 4.1 and Figure 4.2). A comparison of CAP and POP samples also showed that at elevated temperatures shrinkage in POP samples was more than that of CAP samples, irrespective of the sintering atmosphere.

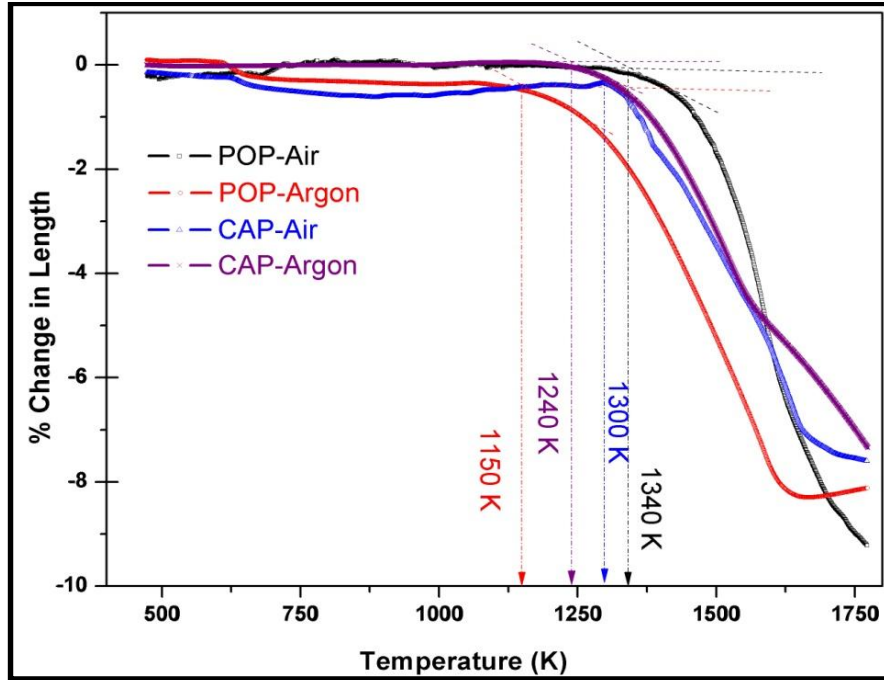


Figure 4.1 : Densification plots of  $\text{ThO}_2\text{-CeO}_2$  POP green pellets and CAP green pellets under air and Ar atmosphere with respect to temperature.

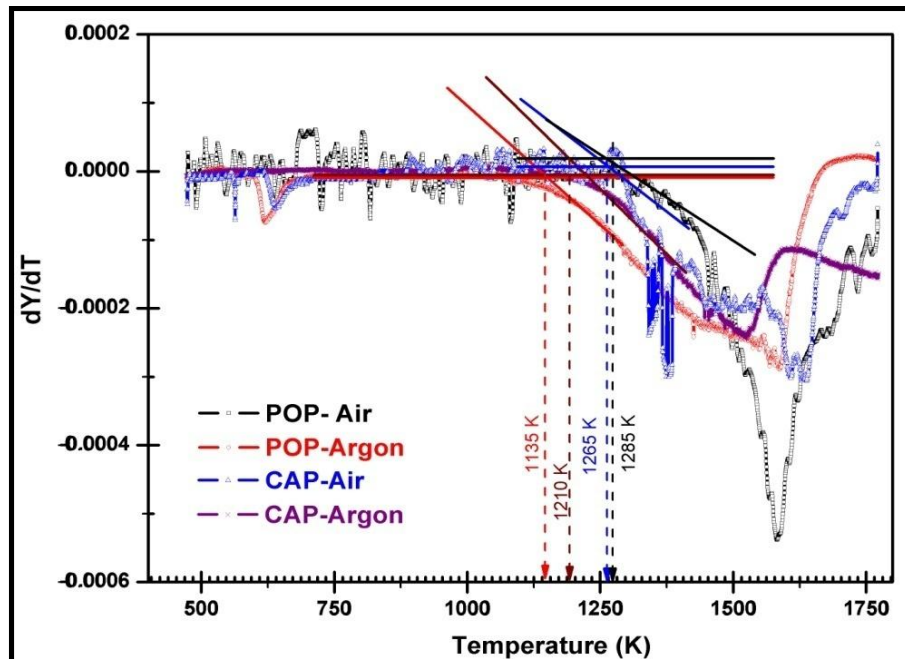


Figure 4.2 : Shrinkage rate plots of  $\text{ThO}_2\text{-CeO}_2$  POP green pellets and CAP green pellets under air and Ar atmosphere.

Generally rate of shrinkage is expressed as,  $dY/dT$ . At constant rate of heating,  $dT/dt$  is a constant, where  $t$  is time. Therefore,  $dY/dt$  can be expressed as,  $dY/dT \times \text{Constant}$ . In the densification and shrinkage rate plots, there exist two important temperatures, viz the temperature at which the shrinkage has commenced i.e.  $Y < 0$  and the temperature at which the shrinkage rate becomes negative i.e.  $dY/dT < 0$ . All these temperatures have been listed in the Table 4.1.

**Table 4.1 : Onset of sintering temperature for the pellets and the corresponding sintering conditions.**

<b>Pellet details</b>	<b>Sintering atmosphere</b>	<b>Onset of sintering temperature (K) (<math>Y &lt; 0</math>)</b>	<b>Onset of shrinkage temperature (K) (<math>dY/dT &lt; 0</math>)</b>	<b>% Shrinkage at 1773 K</b>
(Th,5%Ce)O <sub>2</sub> POP	Air	1340	1285	9.25
Th,5%Ce)O <sub>2</sub> CAP	Air	1300	1265	7.6
Th,5%Ce)O <sub>2</sub> POP	Argon	1150	1135	8.2
Th,5%Ce)O <sub>2</sub> CAP	Argon	1240	1210	7.5

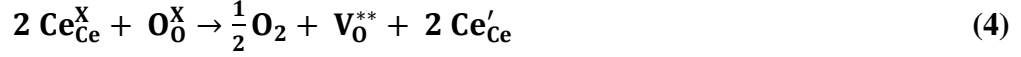
It clearly shows that the temperature corresponding to ( $dY/dT < 0$ ) for air sintered samples of POP and CAP were relatively close to each other (1285 K and 1265 K respectively) as compared to the samples sintered in argon. Argon sintered POP sample had the minimum temperature corresponding to ( $dY/dT < 0$ ) at 1150 K and for CAP sample it was 1240 K. Another interesting feature that can be observed in the Figure 4.2 was the vast difference in the nature of behavior of the shrinkage rate curve. Except for air sintered POP

sample, no other samples had shown a single temperature corresponding to maximum rate of shrinkage. Both argon sintered POP and CAP had anisotropic maximum shrinkage rate peak whereas air sintered CAP had shown multiple maxima rates of shrinkage over a wide temperature range (1300–1635 K).

From the dilatometry plots obtained for the shrinkage of pellets, it could be observed that under different atmospheric conditions the shrinkage % and rates varied with temperature. It could be seen that the onset of sintering temperatures for pellets varied with the sintering conditions. As the green pellets were fabricated under similar conditions, the sintering kinetics might have affected starting homogeneity in the pellets and by the extent of different mechanism in play at the sintering temperatures and conditions.

During initial stages of sintering in air,  $\text{Th}^{+4}$  ions remain unaffected, so do most of the Ce remains as  $\text{Ce}^{+4}$  ions. Both the species being stoichiometric are responsible for very low defect contribution. Therefore, initial stages of sintering are very slow and rate is subdued. Analyzing together the shrinkage behavior exhibited by POP and CAP pellets as shown in Figure 4.1 and Figure 4.2, it was observed that up to the temperature of 1200 K (during initial stages) due to the presence of very low level of defect concentration surface diffusion phenomenon will be prominent and responsible only for inter-particle neck formation and does not contribute towards shrinkage in the sample [54]. This was also evident from the horizontal profile of the shrinkage plots extending up to onset of sintering temperatures. Beyond the onset of shrinkage temperatures, indicated in Table 4.1, for respective pellets in different sintering conditions the grain boundary diffusion starts controlling the shrinkage behavior (densification).

In the case of POP and CAP pellet under air sintering, cerium is in  $Ce^{+4}$  valence state which is retained up to temperature of 1200K [132]. Beyond this temperature  $Ce^{+4}$  reduces to  $Ce^{+3}$ . The Kroger Vink Notation for this reaction is given below in equation 4:



where,  $Ce'_{Ce}$  represents  $Ce^{+3}$  ion in location of  $Ce^{+4}$ ,  $Ce_{Ce}^X$  represents  $Ce^{+4}$  ion in location of  $Ce^{+4}$  location,  $V_0^{**}$  represents vacant oxygen site,  $O_2$  represents oxygen molecule and  $O_0^X$  represents oxygen atom in oxygen atom location.

The substitution of  $Ce^{+4}$  with  $Ce^{+3}$  induces elastic strain in the lattice as the ionic size of  $Ce^{+3}$  (1.07Å) is larger than compared to  $Ce^{+4}$  (0.97Å) [133]. The elastic strain energy induced due to misfit generated in the lattice is given by the following relations:

$$\frac{\Delta a}{a} = \frac{a_s - a}{a} \quad (5)$$

$$U_o = \frac{6\pi a^3 B_s \left(\frac{\Delta a}{a}\right)^2}{1 + 3B_s/4\mu_h} \quad (6)$$

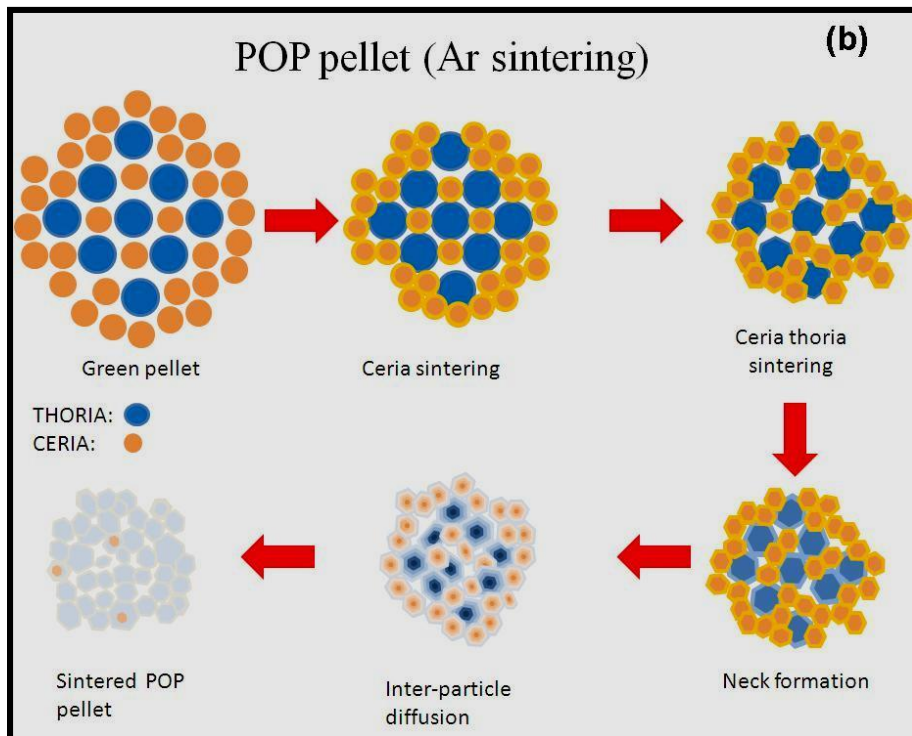
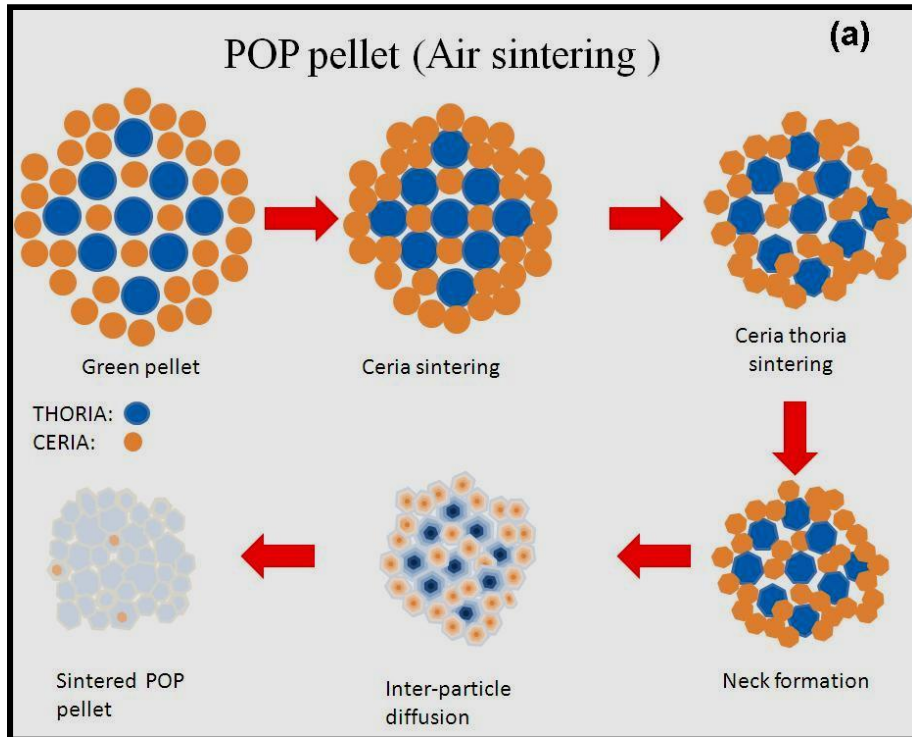
where,  $a_s$  and  $a$  are radii of solute and host ions respectively,  $\Delta a$  is the misfit in the lattice,  $B_s$  is the bulk modulus of the solute,  $\mu_h$  is the shear modulus of the host crystal and  $U_o$  is the strain energy [134].

From the relation it can be seen that the strain energy is proportional to the square of the misfit. This strain induced in the lattice is relieved during sintering and provides a driving force for densification [135]. This may be the reason of close proximity of sintering initiation temperatures in POP and CAP pellets in air atmosphere. From this analysis, we can correlate

that the behavior of the POP and CAP pellets during bulk sintering in air around 1300–1350 K is quite similar as sufficient strain is induced in the ceria region which activates the diffusion and thereby the densification process. Defect induced strain energy controls the segregation of cations to the grain boundary (solute segregation) and thereby affects sintering and grain growth. Rahaman and Zhou have reported in their study on sintering of ultrafine ceria that on addition of additive such as Y, Sc, Nd cations with larger ionic radii than that of host cation ( $\text{Ce}^{+4}$  in their study) caused a shift in densification curves to higher temperature and achieved nearly full density compared to undoped ceria [136].

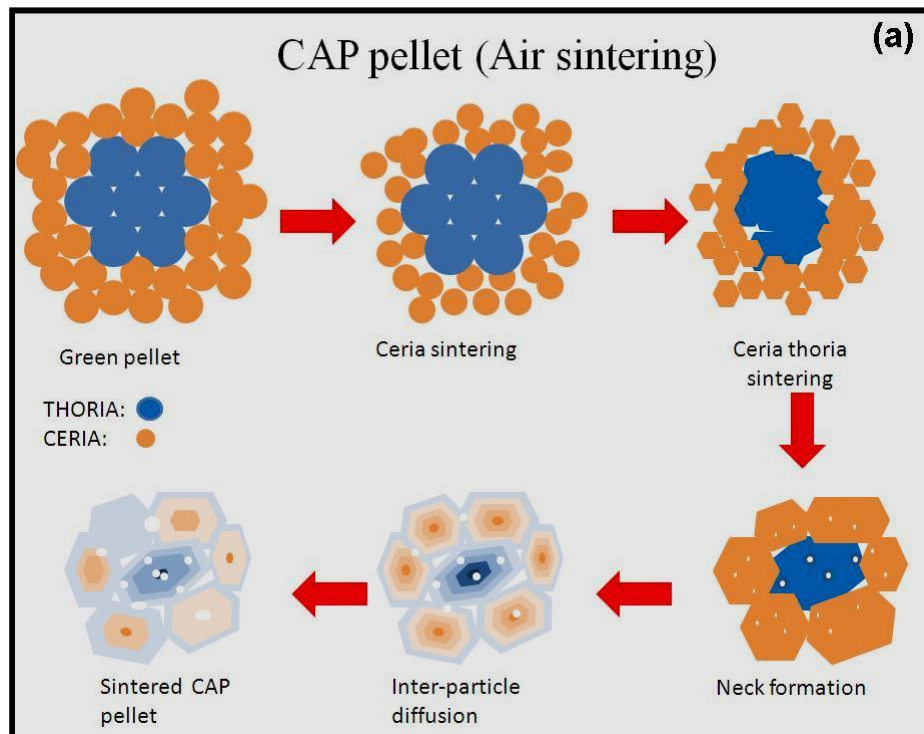
It is striking to note here that due to uniform distribution of ceria particles in the case of POP pellets, the infinitesimal effect on microscopic scale occur over the entire pellet and accelerate with time and temperature due to increase in defect concentration. The maximum densification rate was reflected at around 1600 K. From 1600 K to 1773 K, as the specific surface area of the particles and induced lattice strain had considerably reduced, and therefore the mass movement was retarded resulting in lowering of densification rate. POP pellet sintered in air exhibits better densification as apparent by peak in Figure 4.2. The peak observed for POP air sample shows that POP pellet being a well mixed powder compact and during air sintering at around 1250 K due to reduction of  $\text{Ce}^{+4}$  to  $\text{Ce}^{+3}$ , results in good inter diffusion of cerium and thorium uniformly throughout the pellet at temperatures beyond 1285 K up to 1600 K.

A schematic representation of sintering of the POP pellets in air and Ar atmospheres with the undergoing processes is shown in Figure 4.3(a) and Figure 4.3(b) respectively.



*Figure 4.3 : Schematic representation of sintering of POP samples (a) in air and (b) Ar atmospheres.*

In the case of CAP pellets due to physical difference of Thoria agglomerate and Ceria coating, the conglomerated particles of the ceria began to sinter at around 1200 K in air and the elastic strain was generated in the ceria lattice due to  $Ce^{+4}$  reduction to  $Ce^{+3}$ . Due to higher strain on the adjacent interface region interdiffusion of Th and Ce ions is prominently undergoing phenomenon. The densification of pellet is extended between the temperature ranges of 1300 K to 1600 K as it is affected at different regions simultaneously. As it is known that thoria sinters at higher temperatures, the same is reflected in the CAP pellet where the agglomerate sintering is active with diffusion of Ce species in to the lattice through the interface region. As a consequence, the maximum rate of shrinkage in Thoria rich region occurred  $\sim 1625$  K. A schematic representation of sintering of the CAP pellets in air with the undergoing processes is shown in Figure 4.4 (a) and Figure 4.4 (b) respectively.



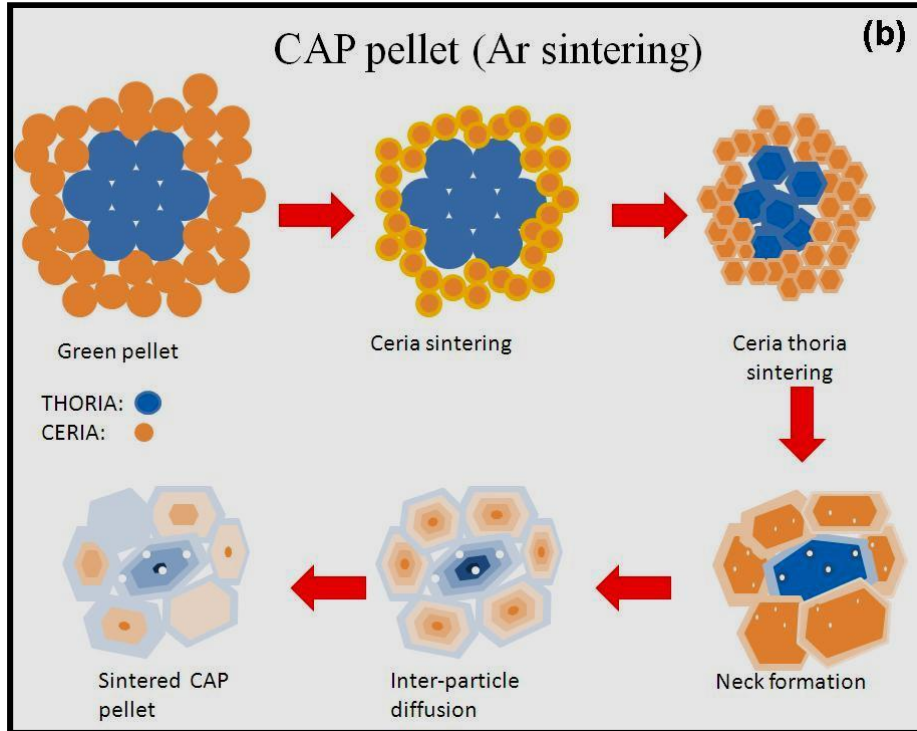


**Figure 4.4 : Schematic representation of sintering of CAP samples (a) in air and (b) Ar atmospheres.**

In the case of sintering in Ar atmosphere, early onset of shrinkage temperature was observed in the case of POP pellet at 1135 K and in CAP pellet at 1210 K. Since the partial pressure of oxygen in this system is low, the reduction of  $\text{CeO}_2$  to  $\text{Ce}_2\text{O}_3$  initiates at lower temperatures. Subsequently at temperatures around 1210 K with increased availability of  $\text{Ce}^{+3}$  and the diffusion kinetics progressing at the interface, smooth and steady shrinkage rate was observed. It is interesting to note that, unlike air sintered POP and CAP; the argon sintered sample had already reached a sintering plateau at elevated temperature. This may cause higher shrinkage in the ceria rich region.

During sintering of agglomerated ceramic powder, it was observed that the sintering within agglomerates that initiates at lower temperatures, caused crack like void formation

due to differential shrinkage in agglomerates and the matrix [137, 138]. Corollary can be drawn in the present case, where earlier sintering in ceria rich particles would result in the similar kind of void formation leading to inhibition of sintering. The effect of this differential sintering is more prevalent in CAP pellets because of close proximity of ceria particles during coating process as compared to POP pellets where the ceria particles were uniformly distributed in thoria. At this temperature of  $\sim 1200$  K, thoria particles remain almost intact and do not show any shrinkage effect. Hence, a lower shrinkage was observed in the reducing atmosphere.

In CAP pellets, densification in the coated ceria regions because of lower sintering temperature of ceria might have initiated earlier compared to thoria agglomerates. The localized micro sintering of the coated regions across the pellet appears to be responsible for lowering of onset temperature of sintering. With further increase in temperature, in POP pellets interdiffusion of  $\text{Th}^{+4}$  and  $\text{Ce}^{+4}$  ions was enhanced due to similar ionic sizes of  $\text{Th}^{+4}$  ( $1.05\text{\AA}$ ) and  $\text{Ce}^{+4}$  ( $0.97\text{\AA}$ ). This results in good densification and homogeneity in the pellet. As the defect concentration was very low and the slow diffusion of  $\text{Th}^{+4}$  ions being the rate determining step, the sintering kinetics were slow. However due to higher mobility of Ce ions especially at higher temperatures, the densification rate gets accelerated. In the CAP pellets, it was observed that due to preferential sintering of ceria particles in coated region must have generated voids in interface of thoria agglomerate and coated region.

Lange [137] stated in his observations on powder processing of ceramics, heterogeneity persist even during further processing or develop into a new heterogeneity during densification and microstructural development. Agglomerates with different bulk

densities can persist during powder consolidation to form crack like voids during densification because of their different shrinkage rates relative to the surrounding powder [139]. Agglomerates may not uniformly deform to fill inter agglomerate void space during compaction [140]. They will leave irregular voids that persist after densification. Agglomerates also limit densification [138, 141]. These voids create discontinuities between the thoria agglomerate and surrounding ceria sintered agglomerates. With increasing sintering temperature, however, progressive sintering occurs but cationic inter diffusion is affected due to reduced contact areas. Because of this, though the pellet exhibits good density, it will have inhomogeneous distribution of Ce. Subsequently, in CAP pellets further shrinkage at elevated temperatures gets inhibited which could be due to stabilization of the pores and voids attaining critical size and their removal is very difficult.

Based on our studies, it is evident from the densification values exhibited by the pellets under different atmospheres at 1750 K as given in Table 4.1 that the POP pellets will possess higher densities compared to CAP pellets. The CAP pellets are expected to possess higher porosity and inhomogeneity compared to POP pellets. Extrapolating our studies on to reducing environment, the POP pellets shall exhibit better homogeneity as compared to CAP pellets and also higher densities.

The main findings of the shrinkage studies on  $\text{ThO}_2$ -5wt.%  $\text{CeO}_2$  pellets under different atmospheres are following:

1. Previous studies on sintering of pure  $\text{ThO}_2$  showed requirement of temperature  $2000^\circ\text{C}$  to attain about 80 %T.D without any additive [31]. It can be seen from our studies that  $\text{ThO}_2$ - $\text{CeO}_2$  pellets exhibit better sintering

behavior compared to pure  $\text{ThO}_2$  in air as densification occurred at much lower temperatures.

2. The sintering behavior of the pellets was highly influenced by the homogeneity of the powders in the green pellets.
3. Resultant homogeneity of solute (Ce) in the host matrix (Th) was better in POP pellets as compared to CAP pellets.
4. At temperature of 1723 K, POP pellet sintered in air exhibited shrinkage of ~ 10% compared to pellet sintered in Ar atmosphere (~ 8.2%). The studies clearly showed that densification phenomenon was highly influenced by sintering temperature. Therefore, to achieve higher pellet densities further increase in sintering temperatures will be helpful.
5. At temperature of 1723 K, CAP pellets densities were independent of sintering atmospheres used in the study and showed densities lower by 13–18% compared to POP pellets.
6. Employing reducing atmosphere of  $\text{Ar-H}_2$ /  $\text{N}_2\text{-H}_2$  instead of Ar, will be highly helpful in accelerating the kinetics of reduction reaction of  $\text{CeO}_2$  or hypo-stoichiometric materials and assist in the diffusion mechanisms.
7. At temperatures higher than that used in the present study, the pellet densities and densification rate will be considerably higher than achieved in the experiment.

### 4.3 Sintering of actual pellets

Based on our key observations in dilatometric shrinkage studies in different atmospheres, the actual sintering of ThO<sub>2</sub>-5 wt.% CeO<sub>2</sub> pellets of POP and CAP were conducted in air and Ar-H<sub>2</sub> atmospheres at 1823 K and 1923 K respectively. The sintered pellets were characterized for density and O/M ratio. The characteristics of ThO<sub>2</sub>-5 wt.% CeO<sub>2</sub> POP and CAP sintered pellets are given in the Table 4.2.

**Table 4.2 : Characteristics of ThO<sub>2</sub>-5 wt.% CeO<sub>2</sub> experimental POP and CAP sintered pellets.**

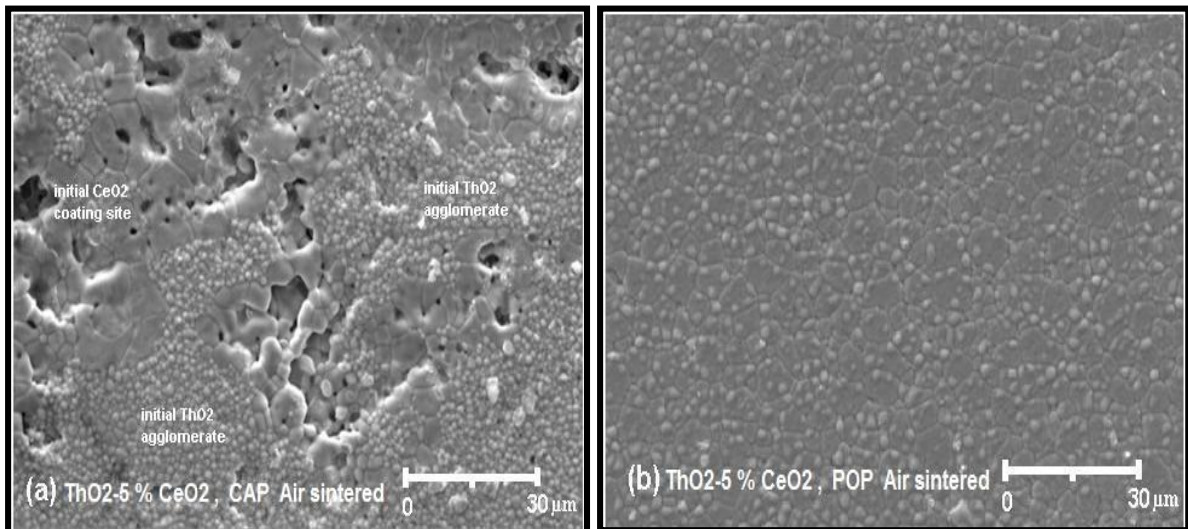
Process	Sintering atmosphere / Temperature	Density (%T.D)	O/M	Porosity range (% T.D)
POP	Air /1823 K	95 – 96	2.00 ± 0.003	4 – 5
CAP	Air/1823 K	93 – 94	2.00 ± 0.003	6 – 7
POP	Ar-H <sub>2</sub> /1923 K	93 – 94	1.98 ± 0.003	6 – 7
CAP	Ar-H <sub>2</sub> /1923 K	91 – 93	1.99 ± 0.003	7 – 9

Better densities were obtained in the pellets under air sintering compared to sintering in Ar-H<sub>2</sub> atmosphere as predicted by shrinkage studies and are given in Table 4.2. Improved densities could be attributed to reduction of CeO<sub>2</sub> to Ce<sub>2</sub>O<sub>3</sub> in Ar-H<sub>2</sub> atmosphere leading to high concentration of Ce<sup>+3</sup> in the pellets compared to the pellets when sintered in air. Ionic size of Ce<sup>+3</sup> (1.07Å) is quite close to Th<sup>+4</sup> (1.05Å). Consequentially the strain generated is lower and densification is affected.

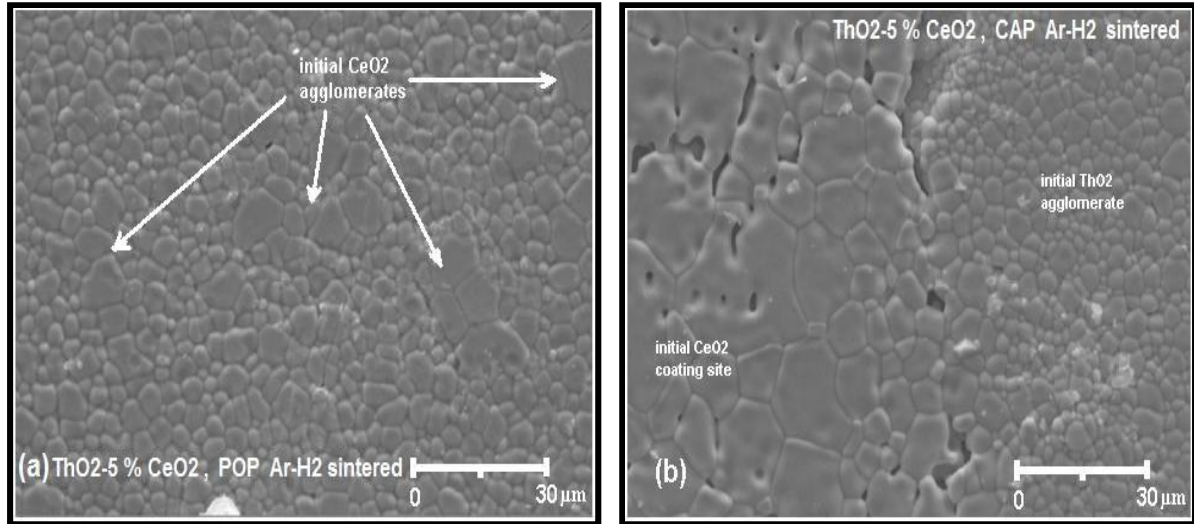
But on other hand, Ar-H<sub>2</sub> atmosphere sintered pellets due to high concentration of Ce<sup>+3</sup> will undergo higher interdiffusion and result in better homogeneity compared to pellets sintered in air.

#### 4.4 Microstructure and homogeneity

The microstructure of the POP pellets and CAP pellets sintered in air atmosphere are given in Figures 4.5 (a) and 4.5 (b), respectively. The microstructure of POP pellets and CAP pellets sintered in reducing atmosphere are shown in Figures 4.6 (a) and 4.6 (b).

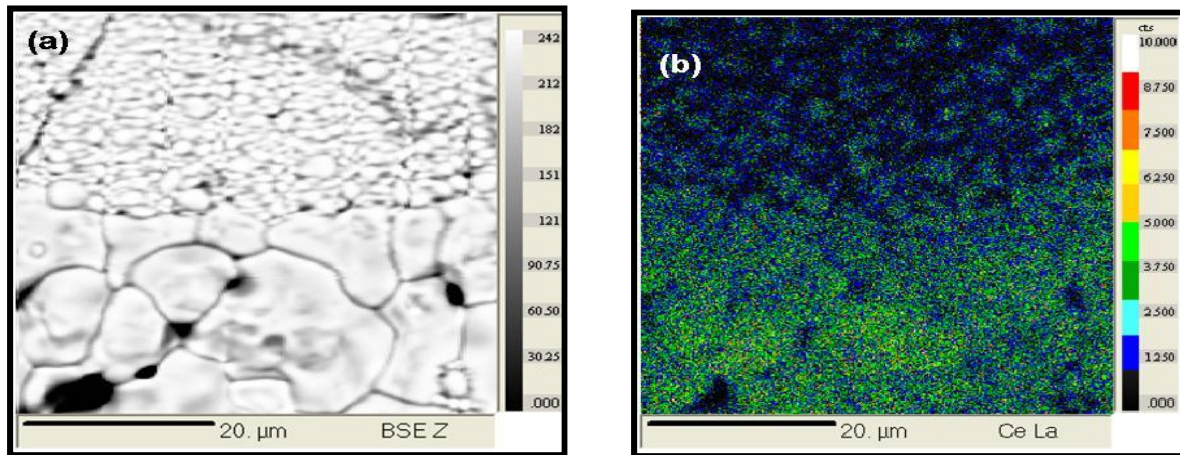


**Figure 4.5 : Microstructure of the (a) CAP and (b) POP pellets sintered in air atmosphere (SEM images).**



**Figure 4.6:** Microstructure of the (a) POP and (b) CAP pellets sintered in Ar-H<sub>2</sub> atmosphere (SEM images).

The EPMA analysis of CAP pellets and POP pellets sintered in atmospheres of Ar-H<sub>2</sub> and air are shown in Figures 4.7 and 4.8 respectively.



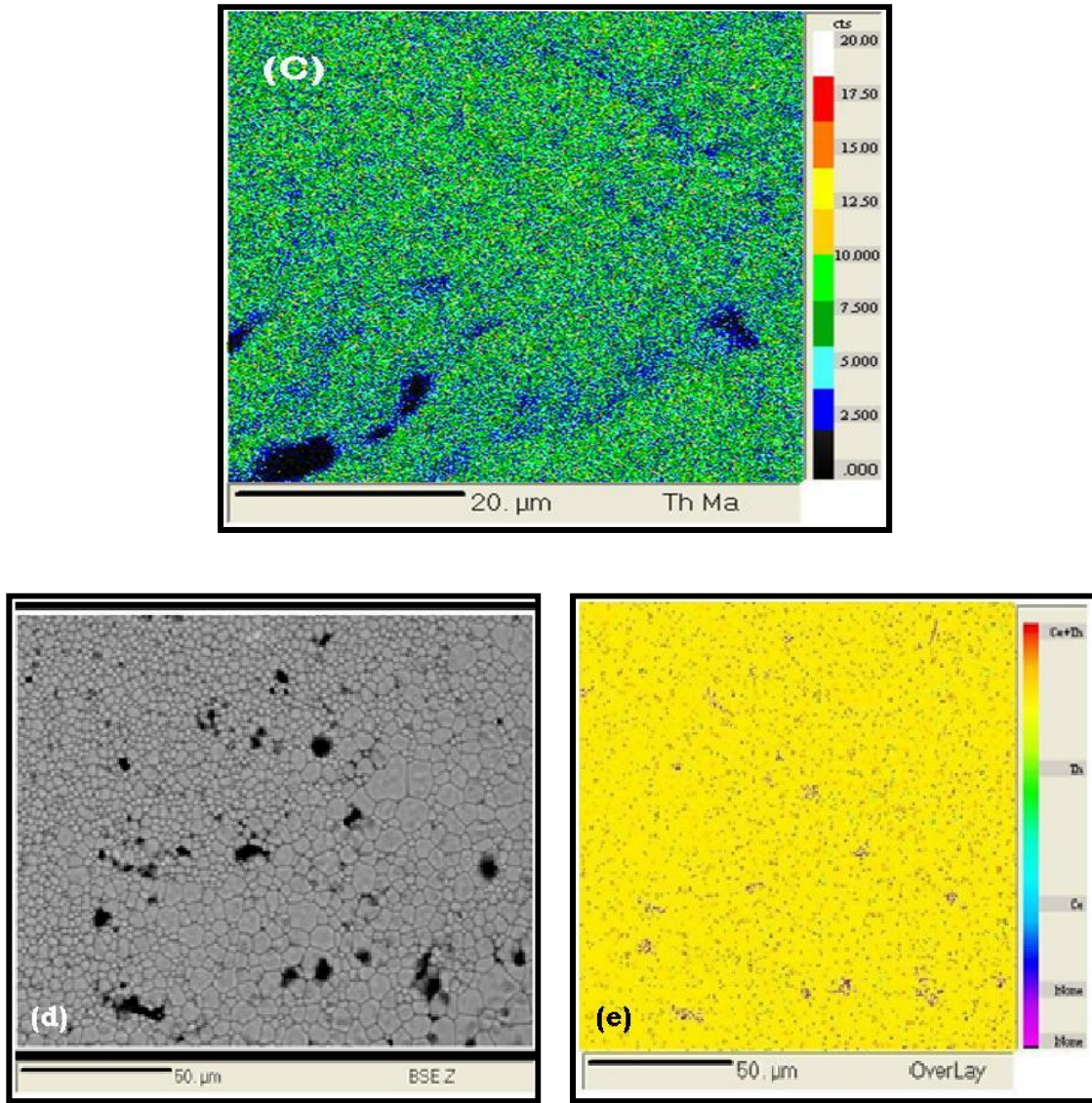


*Figure 4.7: (a) EPMA image of CAP pellet sintered in Ar-H<sub>2</sub> atmosphere (b) Ce elemental mapping of area shown in figure (a), (c) Th mapping of area shown in figure (a), (d) EPMA image of POP pellet sintered in Ar-H<sub>2</sub> atmosphere and (e) Th and Ce combined mapping of area shown in figure (d).*

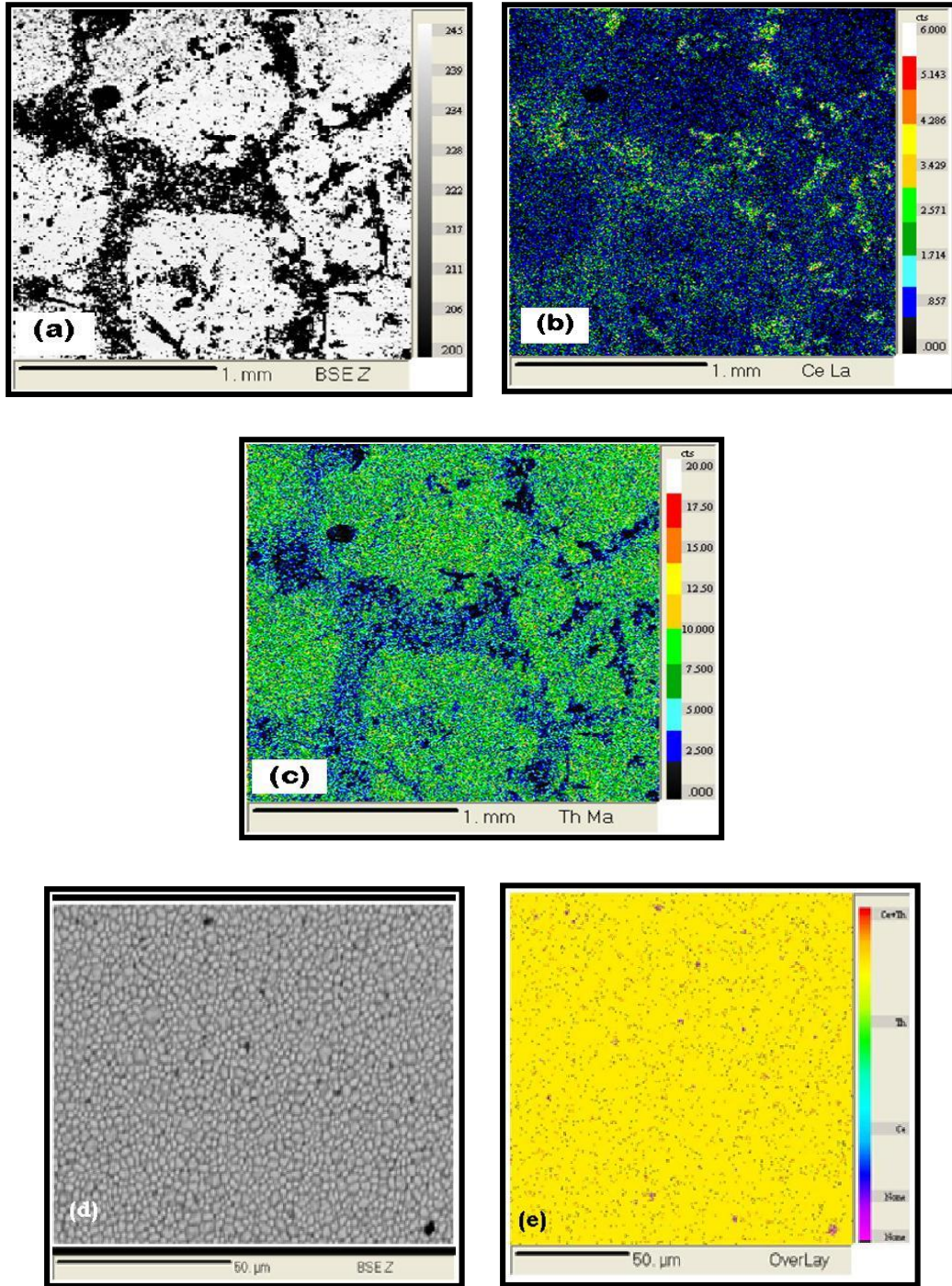


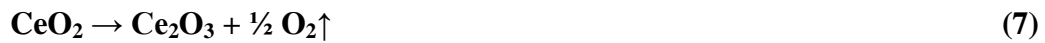
*Figure 4.8: (a) EPMA image of CAP pellet sintered in air atmosphere (b) Ce elemental mapping of area shown in figure (a), (c) Th mapping of area shown in figure (a), (d) EPMA image of POP pellet sintered in air atmosphere and (e) Th and Ce combined mapping of area shown in figure (d).*

It could be observed that the CAP pellets (air sintered) showed large grains (size  $\sim 10 \mu\text{m}$ ) surrounding the regions of fine grains (size  $\sim 4 \mu\text{m}$ ). The pores were found to be preferentially located at large grain regions and average pore size was  $\sim 8 \mu\text{m}$ . The presence of pores in fine grain packets was found to be scarce but did show presence at trigranular junctions. The sintered POP pellets (air sintered) showed uniform grain structure and the average size of grain was  $\sim 6 \mu\text{m}$ . The POP pellets sintered in Ar-H<sub>2</sub> atmosphere also showed bimodal grain size distribution. The POP pellets (Ar-H<sub>2</sub> sintered) showed uniform grain structure in the matrix with the grain size between 4 – 6  $\mu\text{m}$  and also bigger grains of size between 10–12  $\mu\text{m}$  could be seen. The CAP pellets showed larger grains ( $\sim 26 \mu\text{m}$ ) surrounding the fine grains ( $\sim 5 \mu\text{m}$ ). On comparing Figure 4.7 (a) and Figure 4.7 (b), it could be seen that in regions of large grains Ce concentration was relatively higher compared to that at small grain regions. Similarly, comparison of Figure 4.7 (a) and Figure 4.7(c) shows that the thorium was more or less uniformly distributed across the matrix excepting at regions of porosity.

From the studies conducted on microstructure for grain characterization and homogeneity, it was evident that the developed microstructure (grain size and its distribution, porosity) and Ce distribution (homogeneity) in the pellets were matching with the predictions of sintering studies given in Section 4.2.

The POP pellets when sintered in different atmospheres exhibited grossly similar grain size and distribution (uniform) across the pellet matrix. But close examination brought out difference between the two microstructures. In POP (air sintered) during initial stages up to temperature of 1300 K as mentioned earlier only non-densification mechanism like

surface diffusion was operational for neck formation and growth. Therefore, during initial stages of sintering there exists good inter diffusion of  $\text{Ce}^{+4}$  and  $\text{Th}^{+4}$  ions between the powder particles. The cationic exchange aggravated with rise in temperature and resulted in formation of solid solution. However for temperatures  $> 1200$  K,  $\text{CeO}_2$  exhibits tendency to form  $\text{Ce}_2\text{O}_3$ . This conversion of  $\text{CeO}_2$  to  $\text{Ce}_2\text{O}_3$  is accompanied with release of oxygen as given in the equation below:



With the concentration of  $\text{Ce}^{+3}$  being low, the kinetics of shrinkage is not very high ( $\sim 1300$  K). Subsequently at further higher temperature  $> 1300$  K due to increased concentration of  $\text{Ce}^{+3}$  and inter diffusion of cations introduces sufficient lattice strain and uniform defect structure in the matrix. This leads to improved kinetics of shrinkage and pellet underwent uniform densification. This has been reflected as higher shrinkage rate in sintering study in Figure 4.2. As the temperature of sintering was  $\sim 1823$  K only, the grain growth kinetics was slow owing to slowest diffusion by  $\text{Th}^{4+}$  ion in this temperature regime. This resulted in pellet with smaller grains uniformly present in the entire microstructure, as shown in Figure 4.6 (a). The sintering studies revealed that POP pellets possessed highest densities. The polished samples under microscopic examination showed distribution of fine pores in the pellet.

Considering POP pellets sintered in reducing atmosphere show grains slightly lower in size than POP pellets sintered in air and uniformly present in the matrix along with some larger grains. In this case the reducing atmosphere is responsible for the reduction of  $\text{Ce}^{+4}$  to  $\text{Ce}^{+3}$  in ceria particles. The kinetics of this reduction reaction was favorable even at low

temperature of 1000 K. Hence sintering and reduction are simultaneously affected. Subsequently, at the temperatures around 1210 K the diffusion kinetics are more predominant because of increased availability of  $Ce^{+3}$ . Diffusion of  $Ce^{+3}$  into  $Th^{+4}$  sites does not introduce sufficient strain in the lattice because of similar ionic sizes. This suggests that  $Ce^{+3}$  would in fact lead to inhibition of sintering rather than contributing positively. The same has been reflected in shrinkage rate profile in Figure 4.2 wherein it can be seen that in POP pellet showed early onset of sintering but the rate was gradual. Whereas in the case of air sintering, shrinkage rate was quite steep, even though, the onset was delayed. Further as discussed earlier sintering was mainly affected due to temperature which was responsible for increasing the mobility of ions and reduction of surface area of particles. At temperature similar to air the POP pellet under reducing atmosphere would have exhibited lower densification but due to high sintering temperature of  $\sim 1923$  K pellets experience thermally activated sintering and attain high densities. Under the same circumstances as mentioned earlier the interface of particle wherein high diffusion occurred and was concentrated region of  $Ce^{+3}$  shows grain growth at temperature  $> 1873$  K as densification was nearing completion. Therefore we observe presence of bigger grains in the matrix. The pores in the pellet were eliminated gradually at lowered rate as shrinkage was gradual; this led to rounding and stabilizing of pores in the matrix. Only at higher temperature thermodynamically instable fine pores shall get eliminated through the grain boundaries. Summarizing the observation the POP pellets sintered in  $Ar-H_2$  atmosphere show bimodal grain distribution whereas pellets sintered in air show mono modal grain size distribution as seen in Figure 4.7 (d) and Figure 4.8 (d) respectively. EPMA studies on POP samples as seen

in Figure 4.7 (e) and Figure 4.8 (e) sintered in either atmospheres of Ar-H<sub>2</sub> and air respectively exhibit good homogeneity across the matrix.

This study provided conclusive evidence that sintering temperature and atmosphere have considerable influence on shrinkage mechanisms and their kinetics, homogeneity and grain structure in the pellet.

Considering the CAP pellets sintered in air, referring to Figure 4.1, Figure 4.2 and Figure 4.4, similar to POP pellets clearly indicated < 1200 K the densifications were in play especially in ceria coated region because of lower sintering temperatures. At this high temperature Ce<sup>+4</sup> is converted to Ce<sup>+3</sup>. This is preferentially at the surface of globules which due to shrinkage had formed void around them. This leads to dilation of lattice and establishing contact with the thoria agglomerates and enhancing inter diffusion of Ce<sup>+3</sup> and Th<sup>+4</sup> ions across this interface. Inter diffusion plays a key role in shrinkage, as diffusion of Th<sup>+4</sup> into the ceria lattice created sufficient strain. Ionic size of Th<sup>+4</sup> was bigger than Ce<sup>+4</sup>. Lange et al [137–139] had proposed knife like voids at regions of agglomerates in their studies, similar development could also be observed in the microstructure. At ~1550 K thoria agglomerate densification occurred at a very slow rate. Hence due to delayed densification which ended at high temperature grain growth at regions having lower cerium content was not affected. As thoria agglomerate shrinkage was at high temperatures and slow process, the pores were eliminated to the nearby void region. Therefore in the microstructure we find large grains in ceria coated regions and fine grains in the thoria agglomerate regions. As discussed above the thoria region were devoid of any pores. The voids/pores were predominantly present in the interface of ceria and thoria agglomerate interface. The ceria

large grains strikingly exhibited pores at the trigranular junctions. Batista et al [142] reported in their studies on sintering of gadolinia-doped ceria in air that the formation of intergranular pores indicated that gaseous species might have been trapped along the boundaries, possibly due to a low solubility of these species in the matrix or due to some reaction of the gaseous species with impurities at the boundary region.

Similar feature was observed in this study in CAP pellets sintered in air. As these pores must have been formed at later stages of sintering of ceria cluster, they help in accommodating the oxygen released due to the reaction given in equation 7 which occurs at higher temperatures. The oxygen formed in the grains migrates to the grain boundary and coalesce to form a pore. This additional pore generation leads to further lowering of densities. Hence in CAP pellet sintered in air presence of large grains with pores in the grain boundaries and voids at the interface region could be observed along with dense fine grains in the matrix.

Evaluating the microstructure of CAP pellet sintered in Ar-H<sub>2</sub>, due to simultaneous reduction and shrinkage occurring in ceria coated region from early stages of sintering process, the oxygen evolved due to reduction escapes out due to lower density off the pellet. Similar to CAP pellet sintered in air, pellets sintered in Ar-H<sub>2</sub> also exhibited early preferential sintering of ceria particles. This was due to strains sufficiently the cerium lattice due its larger ionic size. The high Ce<sup>+3</sup> concentrations at cerium globule surface (interface) leads to increased diffusion into the thoria agglomerate and Th<sup>+4</sup> into ceria globule. The increased kinetics around this interface resulted in development of diffusion zone due to high cationic concentrations. The diffusion zone or band is a high defect ion concentration region

due to exchange mechanisms exhibited grain growth which occurred prematurely at ~ 1400 K. And at around 1500 K thoria agglomerate sintering occurs but due very low concentration of cerium does not exhibit any grain growth thereby retaining very fine grain size. A very low concentration of cerium in thoria agglomerate centre was because of large migration lengths for cerium ions to reach centre of thoria agglomerate. Further as per Fick's law, diffusion rate is dependent on the concentration of diffusing species which decreases with increasing diffusion length. Hence a diffusion gradient of cerium content was observed from periphery to centre of agglomerate. During the latter stages of sintering at temperatures beyond 1600 K excessive grain growth occurred in diffusion zone due to temperature effect. Hence in microstructure of CAP pellets sintered in Ar-H<sub>2</sub> large grains with large voids surrounding the fine grains could be observed. The fine grain colonies were densely packed. No pores could be detected within the large grain region.

As mentioned earlier, in the case of CAP pellets sintered in air wherein the ceria globule sintering occurred prior to bulk sintering and subsequently the diffusion occurred. In this case both the phenomena occurred simultaneously. This led to delayed onset of shrinkage compared to POP pellets which was due to poor contribution of Ce<sup>+3</sup> towards sintering of cerium particles to form globules.

So in the analysis, microstructure evolved in the pellets could be well correlated with the shrinkage studies. The EPMA studies conducted on the CAP pellets also corroborate with the analysis and confirmed higher cerium content in the bigger grains as discussed. The densities of the pellets also were in agreement with the microstructure displayed.

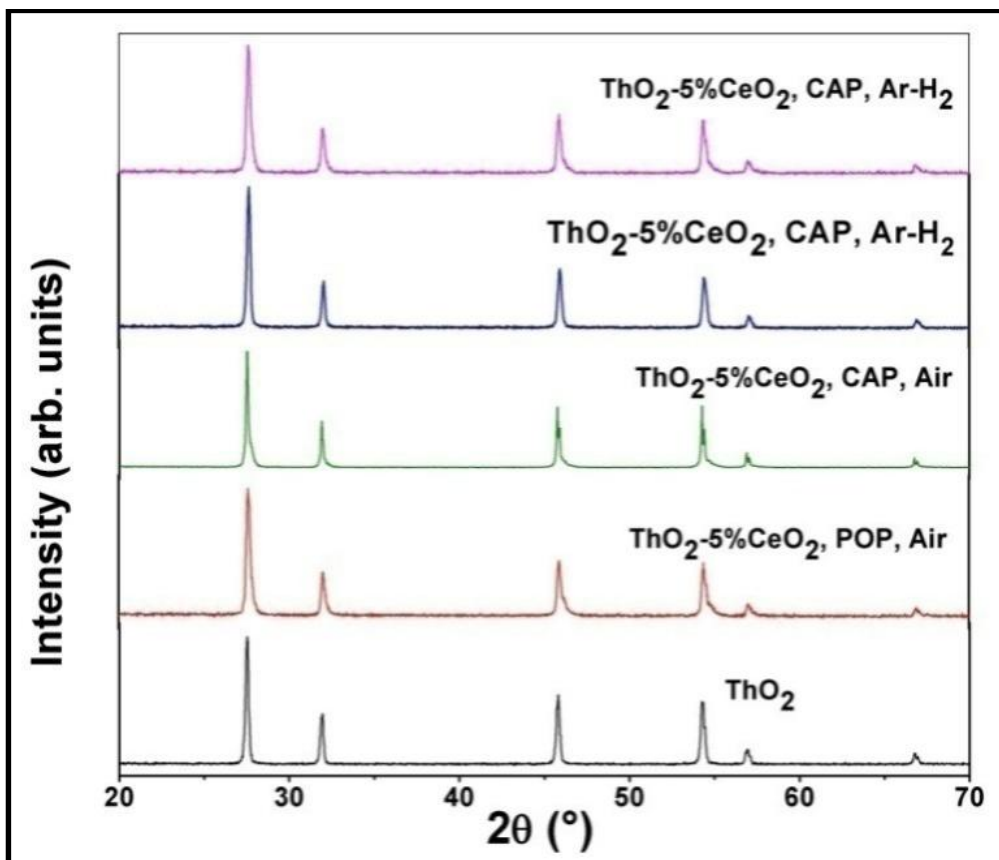
The following conclusions were derived from microstructure and related EPMA studies in correlation with sintering studies:

1. POP pellets sintered in air possessed dense microstructure with good homogeneity. The grain sizes were uniform in the matrix with average size of  $\sim 6 \mu\text{m}$ .
2. POP pellets sintered in reducing atmosphere possessed microstructure with good homogeneity. The fine grains of size  $4\text{--}6 \mu\text{m}$  were uniform in the matrix along with some grains of higher size ranging between  $(12\text{--}15 \mu\text{m})$ . The volume percentage of larger grains was quite low.
3. CAP pellets (air sintered) showed large grains (size  $\sim 10 \mu\text{m}$ ) surrounding the regions of fine grains (size  $\sim 4 \mu\text{m}$ ). The pores were found to be preferentially located at large grain regions and average pore size was  $\sim 8 \mu\text{m}$ . The pores in fine grain packets were found to be scarce but at junction of large grain boundaries pores of size  $(1\text{--}3 \mu\text{m})$  was observed.
4. CAP pellets sintered in reducing atmosphere, higher concentration of defects generated due to Ce in the coating sites and higher sintering temperature had assisted in grain growth. The larger grains ( $\sim 26 \mu\text{m}$ ) show higher cerium concentration compared to the fine grains ( $\sim 5 \mu\text{m}$ ).
5. The EPMA images showed variation in cerium richness especially in the CAP pellets.
6. Large variation was observed between the POP and CAP pellets with respect to homogeneity and density in the case of air sintering compared to sintering in reducing atmosphere.

- Pellets sintered in reducing atmosphere at high temperatures possessed optimal combination of desired properties such density, homogeneity, grain size and porosity.

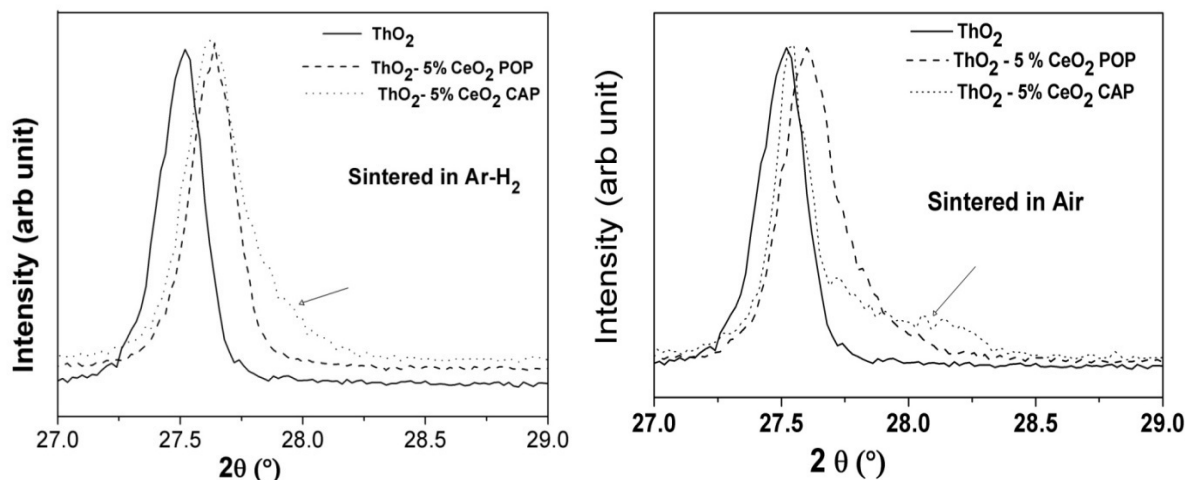
#### **4.5 Formation of (Th,Ce)O<sub>2</sub> solid-solutions**

Figure 4.9 shows X-ray diffraction (XRD) patterns of ThO<sub>2</sub> and ThO<sub>2</sub>-5%CeO<sub>2</sub> (POP and CAP) pellets sintered in air and Ar-H<sub>2</sub> atmospheres. The XRD pattern of most intense peak, i.e., at 27.5° have been expanded for pure ThO<sub>2</sub> and ThO<sub>2</sub>-5%CeO<sub>2</sub> sintered in Ar-H<sub>2</sub> and air atmospheres have been shown in Figures 4.10 (a) and 4.10 (b), respectively. Evidently the XRD patterns of sample from POP pellets shows complete solid solution formation when sintered in Ar-H<sub>2</sub> but in the case of CAP samples, higher angle fluctuations (Shoulder formation- indicated by arrows in the figures) were observed in Figure 4.10 (a). XRD of above pellets when sintered in air showed much broader shoulder (Figure 4.10 (b)) for CAP and a small shoulder for POP pellets. The above results are in agreement with dilatometric curves shown in Section 4.2 which depicts inferior shrinkage behavior for pellets when they were sintered in air especially for POP pellets.



**Figure 4.9 :** XRD patterns of  $\text{ThO}_2$  and  $\text{ThO}_2\text{-5\%CeO}_2$  POP and CAP pellets sintered in air atmosphere at 1823 K for 4 h and Ar- $\text{H}_2$  atmosphere at 1923 K for 4 h.

The inhomogeneity of Ce distribution across the pellet might have possibly resulted in the formation of solid solutions with higher cerium concentration locally which manifest itself in terms of shoulder formation in the XRD patterns. These Ce rich regions were original sites of  $\text{CeO}_2$  coating on agglomerates which have not completely diffused and equilibrated with the matrix. Slower inter diffusion of Th and Ce cations, larger diffusion lengths (bigger agglomerate size) and insufficient sintering time for completion of diffusion process are responsible for inhomogeneity of cerium distribution in the matrix.



**Figure 4.10 :** Expanded view (expanded around 27.5°) of XRD patterns of pellets sintered in (a) Ar-H<sub>2</sub> atmosphere at 1923 K for 4 h and (b) Air atmosphere at 1823 K for 4 h.

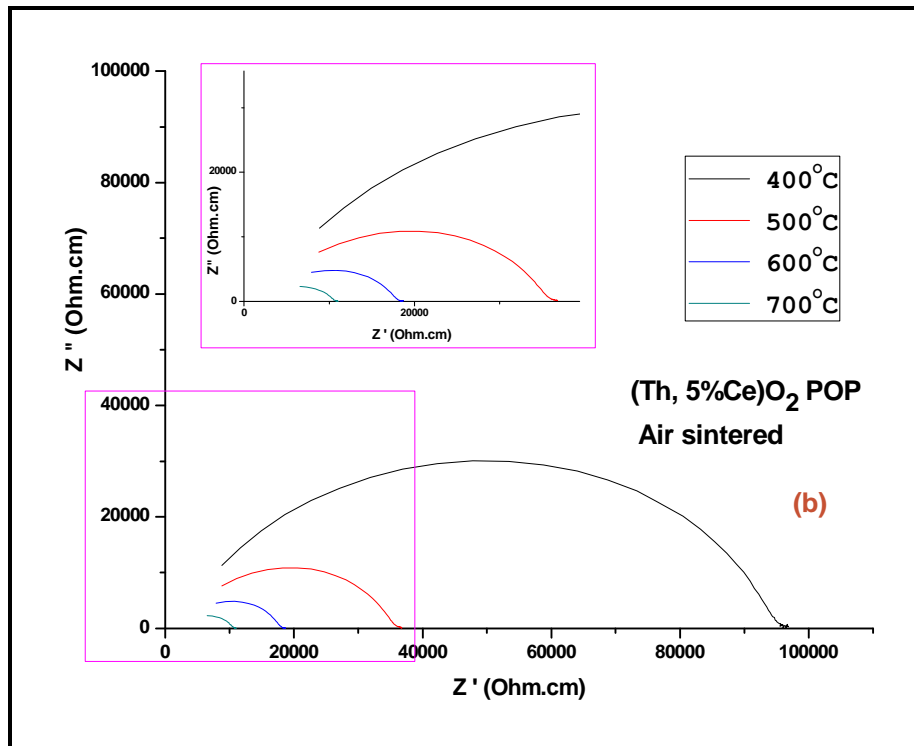
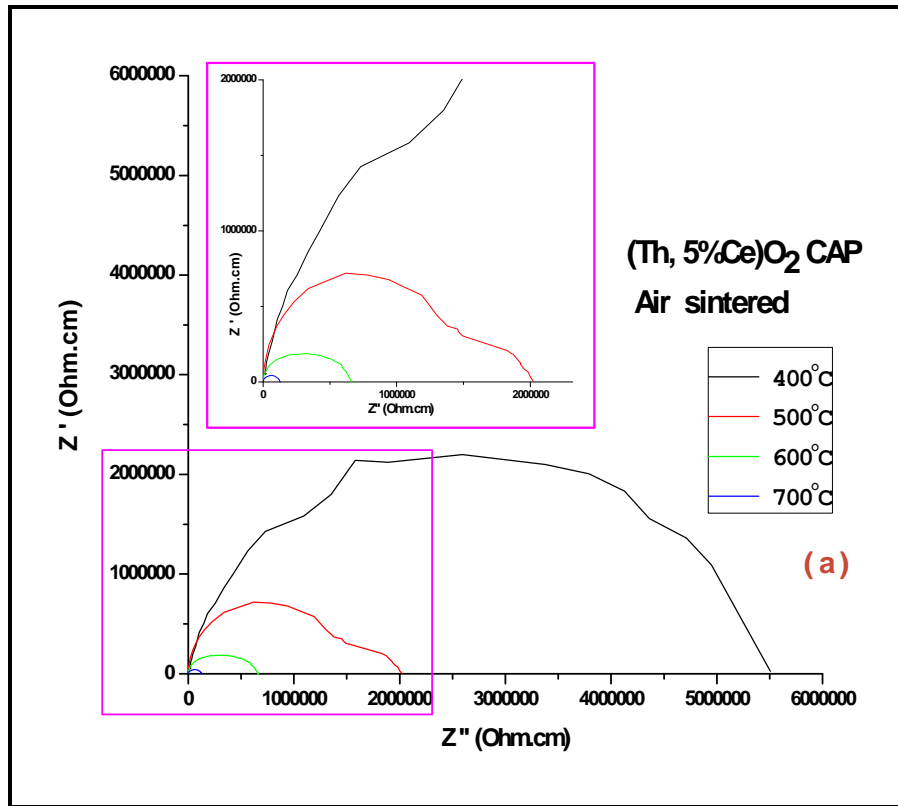
The XRD analysis of sintered samples did not indicate presence of any Ce<sub>2</sub>O<sub>3</sub> or CeO<sub>2</sub> phases. Another striking observation is that the peaks shift toward higher diffraction angles suggesting the lattice parameter reducing with ceria diffusing into thoria lattice, which may be attributed to lower ionic radii of Ce<sup>4+</sup> (0.97Å) than that of Th<sup>4+</sup> (1.05Å).

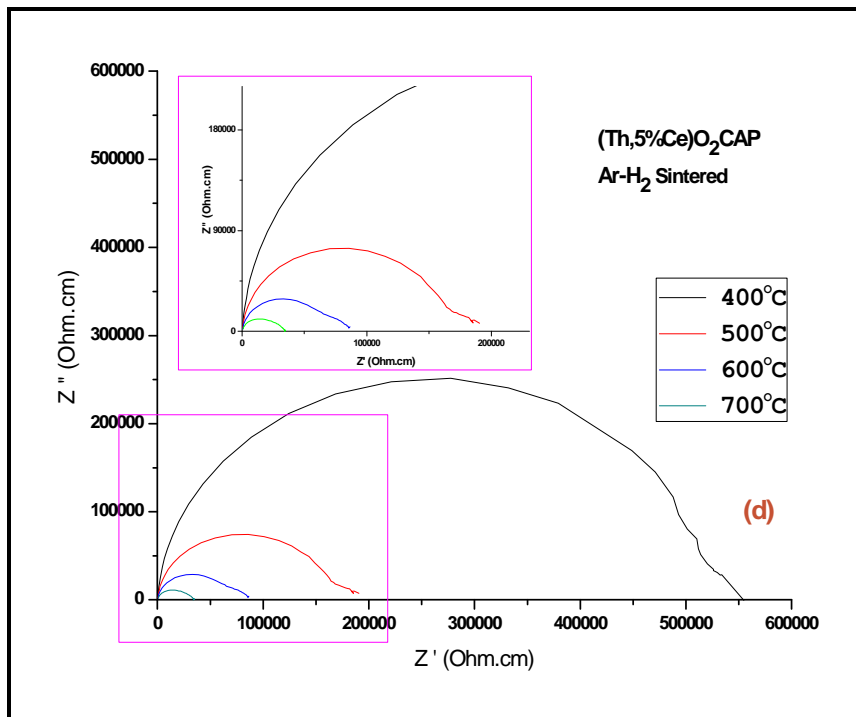
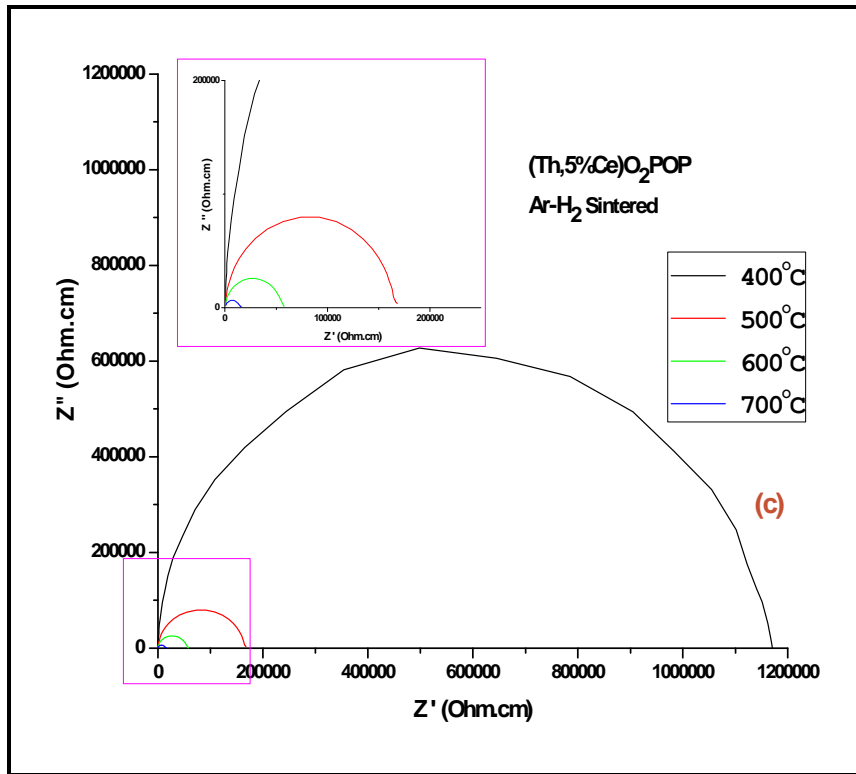
#### 4.6 Ionic conductivity

Impedance spectroscopy is a powerful tool to obtain ionic and electronic response from the samples. Mostly this technique is used to separate grain and grain boundary contribution coming from ceramic sample as well as to analyze electrode response. Therefore, the nature of grain boundary can be predicted using this technique [143]. However very few studies have been carried out on pseudo composite materials like insitu reaction sintered ThO<sub>2</sub>-CeO<sub>2</sub> system, which is the main focus of the present investigation.

As mentioned in Section 3.2.7, the samples were subjected to heat treatment up to 950°C in air for drying of platinum conductive paste applied on sample surfaces which was a pre-requisite for conducting the ionic conductivity studies on the sample pellets. During this treatment, from our thermogravimetric studies carried out on these samples for determination of O/M ratio (as given in Section 4.5), it can be considered that all the samples irrespective of their post-sintered O/M ratio must have got converted to stoichiometry (O/M=2.00) value. Hence in the present impedance spectroscopy study, the effect of multiple valency of Ce will be not of any significance.

For the analysis of electrical behavior of the samples, real impedance ( $Z'$ ) and imaginary impedance ( $Z''$ ) data were used. The data were presented in the form of impedance plot ( $-Z''$  vs.  $Z'$ ) to extract information on the ionic conductivity. The impedance values used in the plots were normalized to account for variations in diameter and thickness of the samples. The impedance plots were fitted in semicircles and from their intercepts on real impedance axis the resistances were determined. The impedance plot for ThO<sub>2</sub>-5 wt.% CeO<sub>2</sub> of POP and CAP pellets sintered in air and Ar-H<sub>2</sub> atmospheres measured at various temperatures are given in Figures 4.11(a-d). The impedance plot measured at 600°C for ThO<sub>2</sub>-5 wt.% CeO<sub>2</sub> pellets of POP and CAP sintered in air and Ar-H<sub>2</sub> atmospheres is given in Figure 4.11 (e).





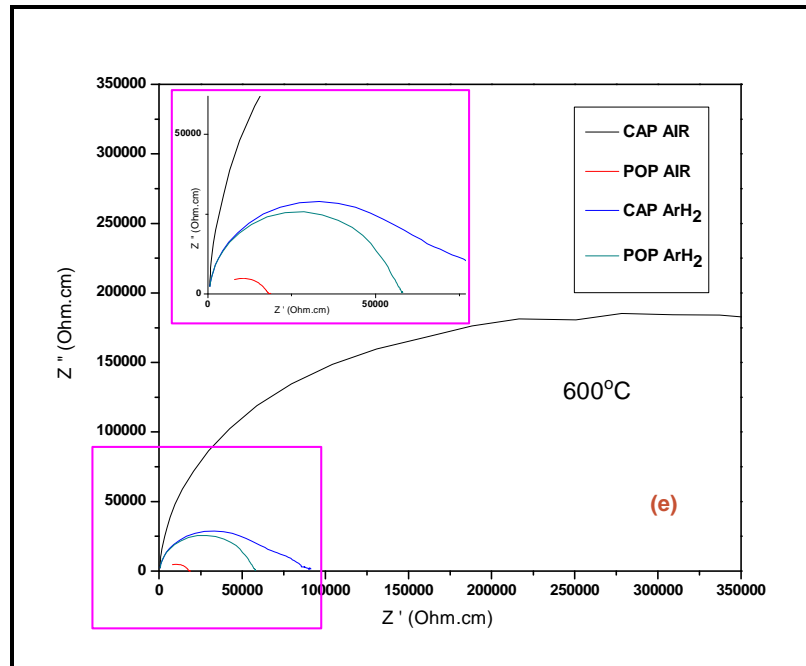


**Figure 4.11:** (a–d) The impedance plots for  $\text{ThO}_2$ –5 wt.%  $\text{CeO}_2$  of POP and CAP pellets sintered in air and  $\text{Ar-H}_2$  atmospheres at different temperatures and (e) impedance plot measured at  $600^\circ\text{C}$  for  $\text{ThO}_2$ –5 wt.%  $\text{CeO}_2$  pellets of POP and CAP sintered in air and  $\text{Ar-H}_2$  atmospheres.

From the impedance spectra shown in Figure 4.11, it could be observed that with temperature, the conductivity of all the samples, irrespective of their sintering conditions, has increased. This was mainly due to the enhanced diffusivity of  $\text{O}^{2-}$  ions with temperature. The conductivity of POP samples is higher than samples of CAP. CAP samples sintered in  $\text{Ar-H}_2$  show significant improvement in the conductivity as compared to samples sintered in air. The different impedance spectra reflected in the studies could be analyzed in the terms of microstructure and inhomogeneity present in the pellets.

At a particular temperature of  $600^\circ\text{C}$ , conductivity of the POP sample sintered in air was found to be highest whereas the CAP sample sintered in the same atmosphere exhibited the lowest conductivity. In the case of CAP and POP samples sintered in  $\text{Ar-H}_2$  atmosphere,

impedance data showed that conductivity was better in POP in comparison to CAP even though difference in their densities was negligible (within 2%). This shows that inhomogeneity present in the sample has effect on the impedance behavior.

When the samples were sintered at lower temperature of 1823 K, POP sample pellets had attained highest density and since in case of POP sample the homogeneity of distribution of Th and Ce was much better (as discussed in Section 4.4), the combined effect was reflected in the impedance spectroscopy data.

In the case of CAP samples sintered in air, the inter-diffusion of Th and Ce was restricted, resulting in higher inhomogeneity as could be observed in Figure 4.8. The CAP pellets also exhibited lower densities comparatively. This combination of inhomogeneity along with lower density of the CAP pellets cumulatively resulted in very high resistivity which could be observed in the Figure 4.11.

On comparison of CAP samples sintered in Ar-H<sub>2</sub> with CAP samples sintered in air, it could be clearly seen that there is significant improvement in conductivity in the CAP sample sintered in Ar-H<sub>2</sub>. This could be attributed to the fact that CAP pellet was sintered at higher temperature of 1923 K in Ar-H<sub>2</sub> compared to 1823 K when sintered in air. Though this did not significantly change the densification of the samples (difference in density ~1–2% T.D), the interdiffusion of ions of Th and Ce was found to be much better when sintering occurs at higher temperatures. This has caused a significant decrease in grain boundary resistivity owing to better homogeneity obtained at 1923 K (higher temperature).

From the study it was evident that the impedance values were strongly dependant on the processing and sintering conditions as they were responsible for the manifestation of density and microstructural features in the pellets. From the Figure 4.11 (e) it is very clear that the CAP sample sintered in air exhibited higher resistivity compared to CAP pellet sintered in Ar-H<sub>2</sub>. But in the case of POP samples, pellets sintered in Ar-H<sub>2</sub> exhibited higher resistivity compared to pellets sintered in air. Further, EPMA studies conducted on CAP samples refer section 4.4, confirmed that the homogeneity of Ce distribution was inferior in the CAP pellets sintered in air as compared to the samples of pellets sintered in Ar-H<sub>2</sub>. As the density difference between the two was marginal, it could be inferred that inhomogeneity of Ce distribution across the interfacial diffusion zone has resulted in very high impedance value in the case of CAP sample sintered in air.

Analyzing the samples sintered in Ar-H<sub>2</sub>, it could be observed that POP sample had better conductivity than the CAP sample. Since the POP sample had higher density and better homogeneity compared to CAP sample, it was obvious that these two factors were responsible for POP samples exhibiting very high conductivity. Further the microstructure reveals that grain to grain contact was also better compared to CAP sample.

The POP sample sintered in air, as mentioned earlier, showed lowest resistance as it had highest density. As in POP samples good intermixing of powders was ensured during initial stages of fabrication, it could be considered that the level of homogeneity in POP samples sintered in different atmospheres will be comparable. Considering the microstructure study conducted and given in Figure 4.5 and Figure 4.6, it was evident that the POP air sample had more uniform grains compared to POP Ar-H<sub>2</sub> sample. The grain size distribution

in POP Ar-H<sub>2</sub> sample was comparatively wider with some large grains surrounded by smaller grains. This sort of microstructure (higher specific grain boundary area) leads to higher grain boundary resistance towards O<sup>-2</sup> ion movement from one grain to another owing to increased number of grain boundaries in contact. Hence as a consequence the electrical resistivity in this kind of system (POP air sample) is expected to be higher than CAP air sample. However it was noted that the CAP air sample had lower density compared to POP air sample, thereby, having higher porosities (discontinuities), resulting in higher electrical resistivity.

Dijk and Burggraaf [144] conducted studies on Grain Boundary Effects on Ionic Conductivity in ceramic Gd<sub>x</sub>Zr<sub>1-x</sub>O<sub>2-(x/2)</sub> solid solution and observed that the smaller grain size alkoxide sample has a larger  $\sigma_{g,b}$  than the larger grain size alkoxide. Radford and Bratton reported that both grain bulk and grain boundary conductivities are decreased by adding impurities, frequently used as sintering aids in their study on zirconia electrolyte cells [145]. Mechanisms proposed to account for these effects are dissolution of impurities in the grains, segregation of them in the grain boundaries and, if present in higher concentrations, the formation of thin continuous or discontinuous layers of a second phase.

In CAP pellets our investigations also show that second phase ceria is inhomogeneously distributed and regions rich in cerium concentration exist. Therefore CAP pellets though have lesser specific grain boundary area exhibit higher resistivity. Our finding corroborates with the reported observations.

Impedance spectroscopy provided the information on possible route of ionic diffusion which will be dominant during irradiation. Secondly, the effect of density along with the microstructure and homogeneity were well understood for diffusion mechanisms. Thirdly,

between the samples the effect of processing conditions could be well resolved which would help the fuel fabricator to tailoring the microstructure as desired.

#### 4.7 Stoichiometry (O/M)

Oxygen to metal (O/M) ratio in the pellets was determined by thermogravimetry (TG) method and is shown in Figure 4.12. The weight changes observed during TG analysis were converted to O/M ratio for plotting. The pellets of  $\text{ThO}_2\text{-5\%CeO}_2$  sintered in air fabricated by POP and CAP routes showed O/M ratio of 2.00. During thermogravimetry in dry air, the samples exhibited only buoyancy effect. Under moist  $\text{Ar-8\% H}_2$ , it was observed that CAP pellets showed higher O/M ratio compared to POP pellets. The O/M ratio was within the range of 1.96–1.98 for the sintered pellets fabricated by conventional route whereas the pellets made by CAP route showed in range of 1.98–1.992.

Figure 4.12 also shows differential thermogravimetry (DTG) curves during heating in moist  $\text{Ar-8\% H}_2$  atmosphere for the samples. The DTG curve is a derivative of thermogravimetry (TG) with respect to unit rise of temperature. Hence, a small change in TG steps can be clearly observed in the DTG curve. Figure 4.12 clearly shows that the oxidation of  $(\text{Th}_{0.95}, \text{Ce}_{0.05})\text{O}_{2-x}$  to  $(\text{Th}_{0.95}, \text{Ce}_{0.05})\text{O}_{2.00}$  by moist  $\text{Ar-8\%H}_2$  is comparatively fast for CAP pellet as compared to POP pellet. The symmetric DTG plots for oxidation of CAP and POP pellet show single step oxidation indicating presence of single phase solid solution in the pellets. The presence of two component system would have shown fluctuations or multimodal DTG plot. Hence the study indicates presence of only single phase of  $\text{ThO}_2\text{-CeO}_{2-x}$  i.e; solid solution in the pellets. This was further confirmed from the XRD patterns of these samples which showed formation of solid solution.

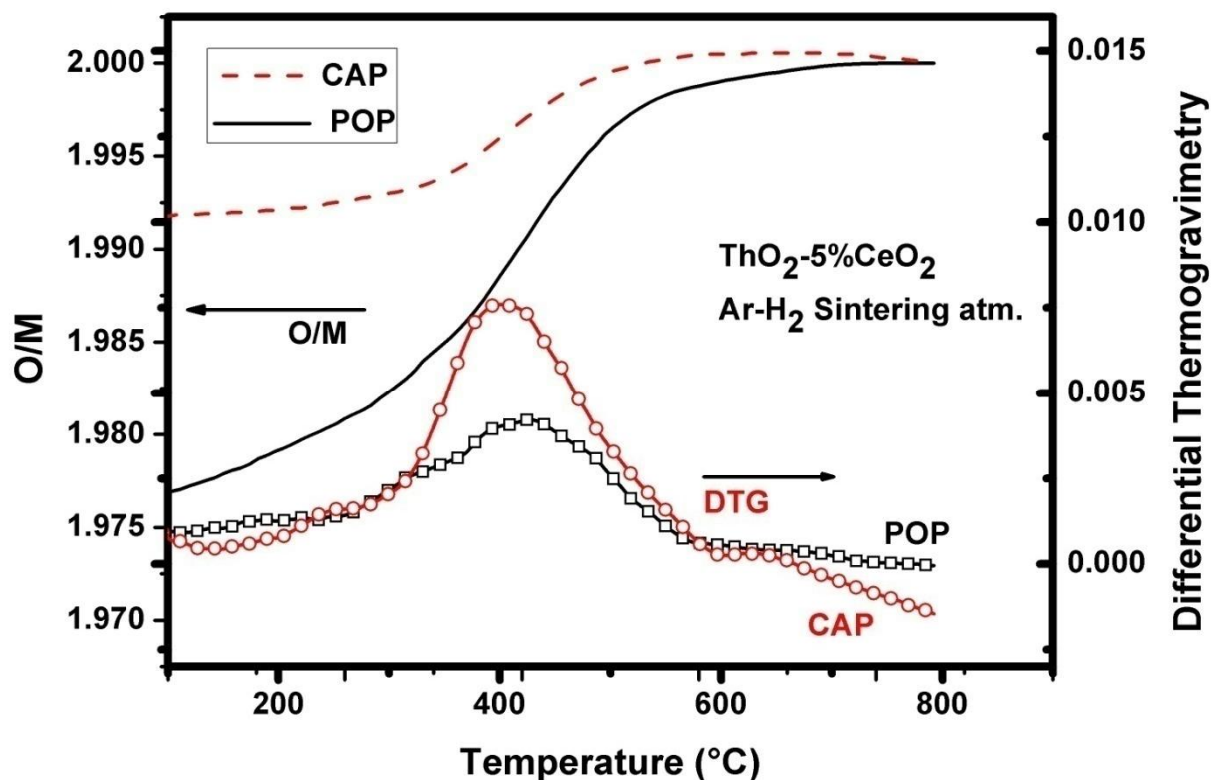


*Figure 4.12 : Thermogravimetric plot of CAP and POP pellets under moist Ar-8% $H_2$  atmosphere.*

The difference in hypo-stoichiometry exhibited by sintered pellets of CAP and POP under reducing conditions was due to better homogeneity in the powder mixture because of mixing and milling operation in POP process. This has resulted in uniform reduction of CeO<sub>2</sub> particles during initial stages of sintering. Whereas in CAP pellets, the coated CeO<sub>2</sub> material showed preferential sintering due to its lower melting point and higher surface area densified prior to bulk sintering. This localized micro-sintering phenomenon was responsible for closure of pores present in CeO<sub>2</sub> coated regions and decrease in specific surface area for reduction. The reducing gas permeation in to these densified particles is hindered and only surface reduction of consolidated CeO<sub>2</sub> powder particles (agglomerates) might have

occurred. Hence in CAP pellets, the O/M ratio was observed to be comparatively higher than POP pellets.

#### 4.8 Specific heat ( $C_p$ )

The specific heat measurements of  $\text{ThO}_2$ -5% $\text{CeO}_2$  POP and CAP pellets sintered in air and  $\text{Ar-H}_2$  atmosphere were conducted using differential scanning calorimeter from ambient temperature to 763 K. The measured  $C_p$  values of POP and CAP pellets (sintered in air and  $\text{Ar-H}_2$  atmosphere) have been plotted in Figure 4.13 along with the values of pure  $\text{ThO}_2$  reported in literature [63,146].

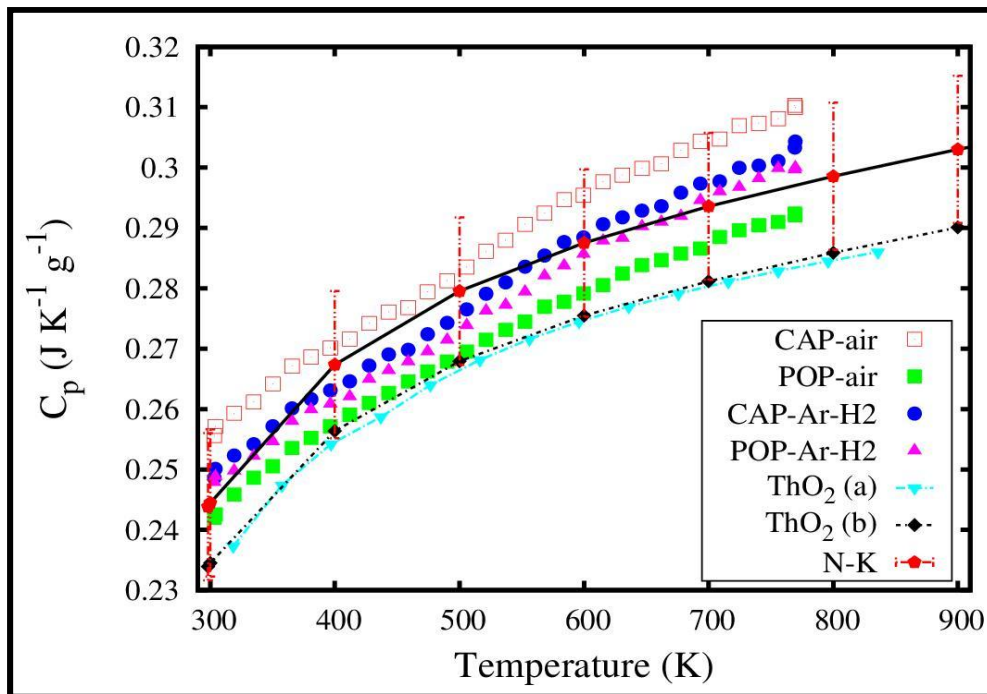


**Figure 4.13 :** DSC measured temperature variation of  $C_p$  values of  $\text{ThO}_2$ -5 wt.%  $\text{CeO}_2$  POP and CAP pellets sintered in air and  $\text{Ar-H}_2$  atmospheres along with Neumann-Kopp (N-K) values.  $\text{ThO}_2$  (a) and  $\text{ThO}_2$  (b) represents experimentally measured  $C_p$  values of  $\text{ThO}_2$  taken from reference [69] and [146], respectively.

Heat capacity values measured on different samples are shown in Figure 4.13, are best least squares fitted into the following equations:

$$C_p (\text{JK}^{-1}\text{g}^{-1}) = 0.215106 + 1.04295 \times 10^{-4} (T^{-1}) + 0.993843(T^{-2}) \quad (\text{POP Air}) \quad (8)$$

$$C_p (\text{JK}^{-1}\text{g}^{-1}) = 0.224394 + 1.15070 \times 10^{-4} (T^{-1}) + 0.995227(T^{-2}) \quad (\text{CAP Air}) \quad (9)$$

$$C_p (\text{JK}^{-1}\text{g}^{-1}) = 0.215921 + 1.12310 \times 10^{-4} (T^{-1}) + 0.996421(T^{-2}) \quad (\text{POP Ar-H}_2) \quad (10)$$

$$C_p (\text{JK}^{-1}\text{g}^{-1}) = 0.217192 + 1.15525 \times 10^{-4} (T^{-1}) + 0.995396(T^{-2}) \quad (\text{CAP Ar-H}_2) \quad (11)$$

From the Figure 4.13, it is evident that  $C_p$  values of  $\text{ThO}_2$ -5% $\text{CeO}_2$  MOX are higher than the pure  $\text{ThO}_2$  values over the whole temperature range. This could be attributed to higher value of  $C_p$  of  $\text{CeO}_2$  in that temperature range.  $C_p$  values of  $\text{ThO}_2$ -5% $\text{CeO}_2$  MOX derived by Neumann-Kopp's method are also plotted for reference in Figure 4.13 using  $C_p$  values of pure  $\text{ThO}_2$  and  $\text{CeO}_2$  at different temperature from available data[146].

Xiao et al [147] in their studies investigated the heat capacity of  $(\text{Th,Ce})\text{O}_2$  solid solutions based on their thermal expansion coefficients. They found isochoric and isobaric heat capacities for  $(\text{Th,Ce})\text{O}_2$  of different compositions are lower than those for pure  $\text{ThO}_2$  and  $\text{CeO}_2$  suggesting that the heat capacity of  $(\text{Th}_{1-x},\text{Ce}_x)\text{O}_2$  is not a simple function of Ce content. Kandan et al [148] reported calorimetric studies on  $(\text{Th}_{1-x},\text{U}_x)\text{O}_2$  and reported increase of heat capacities with U content which is consistent with the applicability of the Neumann-Kopp's law. The same was disputed by Springer et al [85] for  $(\text{Th}_{1-x},\text{U}_x)\text{O}_2$  in their studies by enthalpy drop method. They observed deviation in Neumann-Kopp's rule over entire temperature range. Agarwal et al [149] conducted studies on enthalpy increments and heat capacities of  $\text{ThO}_2$  and  $(\text{Th}_{1-x},\text{U}_x)\text{O}_2$  experimentally. They calculated thermal

conductivity of MOX compositions using experimental values and Neumann–Kopp’s heat capacity values and observed a maximum deviation of  $\pm 5\%$ . They suggested that in absence of experimental heat capacity values, Neumann–kopp’s estimated values could be used to obtain reasonably reliable thermal conductivity values.

As proposed by Xiao [147], the  $C_p$  values of  $CeO_2$  being quite close to  $C_p$  of  $ThO_2$  the variation from Neumann–Kopp rule is very small. Their studies also indicate that free energies for mixed oxides of  $(Th_{1-x}, Ce_x)O_2$  ( $0 < x < 1$ ) are less dependent on temperature than individual components and energy changes with temperature variations are also smaller.

It can be observed that the measured values of  $ThO_2$ –5% $CeO_2$  POP and CAP pellets (sintered in air and Ar– $H_2$  atmosphere) were within  $\pm 5\%$  deviation of Neumann–Kopp’s values over the whole temperature range. Hence our studies confirm applicability of Neumann–Kopp’s values for  $(Th,Pu)O_2$  MOX system. The study reveals that in reducing atmosphere because of good interdiffusion of the constituent materials and better homogenization compared to that in pellets sintered in oxidizing atmosphere, the specific heat capacity were quite close and deviation was minimal. It was also revealed that under reducing atmosphere sintering the specific heat values of CAP pellets were similar to POP pellets.

## 4.9 Thermal properties

### 4.9.1 Theoretical Methodology

#### 4.9.1.1 Interatomic potential function for pure oxides and MOX

The interatomic potential functions for ThO<sub>2</sub>, CeO<sub>2</sub>, UO<sub>2</sub>, PuO<sub>2</sub> and their MOX used in this study were having Buckingham (Buck) [150, 151] and Buckingham–Morse–Many–body (BMM) functional form [150, 151]. Born model of ionic solid, where the ions within the system are considered to be a series of charged interacting particle with a partial ionic charge, was used. The Buckingham potential model was used to study thermal properties of ThO<sub>2</sub> and (Th,Ce)O<sub>2</sub> MOX. For the Buckingham potential model, the potential parameters of Th–O and Ce–O was determined by reducing the difference between calculated and measured thermal expansion and bulk modulus [152, 153]. The potential parameters of O–O were obtained from the previous work [154, 155]. In this functional form upper cut–off of the Buckingham potential used was 12 Å.

In BMM potential model, the pair interaction potential between two particles in this system consists of long–range Coulomb interaction and short range interaction given by combining Morse and Buckingham forms. In this functional form upper cut–off of the Buckingham, Morse and many–body potential used was 11 Å. Embedded atom model was used to introduce subtle many–body term in combination with Morse and Buckingham forms. Using BMM potential model thermal properties of (Th,U)O<sub>2</sub> and (Th,Pu)O<sub>2</sub> MOX was evaluated. The Buck model and BMM model was compared by evaluating thermal properties of (Th,Ce)O<sub>2</sub> MOX.

#### ***4.9.1.2 Empirical potential***

The most recent empirical potential (reported or developed) for pure oxides (such as ThO<sub>2</sub> [147], CeO<sub>2</sub> [148], UO<sub>2</sub> or PuO<sub>2</sub>) or MOX system were employed as it combines a pair-wise and a many body interaction term.

The pair interaction potential between two particles in this system consists of long-range Coulomb interaction and short range interaction given by combining Morse and Buckingham forms. Special quasirandom structures (SQS) were employed to establish solid solution configurations [156]. In the present study, the determination of thermal expansion and thermal conductivities of Th<sub>1-x</sub>M<sub>x</sub>O<sub>2</sub> with x = 0, 1/16, 2/16, 3/16, 4/16 and or 5/16, where M=U/Ce/Pu, were performed using a supercell of 96 atom SQS generated from face centered cubic SQS [156].

#### ***4.9.1.3 MD simulation details***

Special quasirandom structures (SQS) were employed to establish solid solution configurations of MOX [156].

MD simulations for thermal expansion and thermal conductivity were carried out using the MD code LAMMPS [157]. Coulombic interactions were calculated using the Ewald method [158] with the particle-particle particle-mesh (PPPM) implementation of the method within MD calculations to improve computational efficiency [157]. In the present study, the MD supercell was constructed having 4000 cations and 8000 anions by an array of 10x10x10 unit cells for ThO<sub>2</sub> and 5x5x5 supercell of 96 atom SQS for (Th, M)O<sub>2</sub> MOX. These structures are equilibrated with 1 fs time step in the temperature range between 300 K and 3000 K (100 K interval) with the NPT ensemble (constant number of particles N,

constant pressure P, constant temperature T) at zero external pressure using the Berendsen barostat with a time constant of 5 ps and Nose-Hoover thermostat with a time constant of 1 ps. Each simulation of thermal expansion was carried out initially for 200 ps for equilibration (at desired temperature) and then for another 50 ps to get average values of the thermodynamic quantities.

Green-Kubo (GK) formalism was employed to calculate thermal conductivity using MD simulations where an estimate of a transport coefficient relies on the integral of an accurate time-correlation of the equilibrium fluctuations of the corresponding heat flux in the system.

#### ***4.9.1.4 Theoretical Calculations (Coulomb-Buckingham-Morse-many-body potential)***

The philosophy of adding pair-wise interaction (Coulomb-Morse-Buckingham potential) with many-body potential was to reproduce experimentally reported thermal and mechanical properties of AO<sub>2</sub> compounds (A= Ce, Th, U, Np, Pu, Am and Cm) simultaneously. This potential is referred as Coulomb-Buckingham-Morse-many-body (BMM) potential. One of the primary goals of this study is to compare the predictive potential for thermal properties (thermal expansion and thermal conductivity) of ThO<sub>2</sub> and (Th,Ce)O<sub>2</sub> MOX at low composition range of CeO<sub>2</sub>.

To calculate the temperature dependent elastic constants, C<sub>11</sub>, C<sub>12</sub> and C<sub>44</sub>, a simple stress-strain method was applied in the stress-strain method, positive and negative box displacements (deformation) were given in all the symmetry directions and the resultant changes in stress is computed to determine elements of the elastic stiffness tensor. Poly-

crystalline Young and shear moduli were calculated using Voight–Reuss–Hill approximations [159–161].

MD calculations were performed using buck model and BMM model [150, 151] for predicting thermal expansion and thermal conductivity of ThO<sub>2</sub> and (Th,Ce)O<sub>2</sub> MOX ((Th<sub>0.9375</sub>Ce<sub>0.0625</sub>)O<sub>2</sub> and (Th<sub>0.875</sub>Ce<sub>0.125</sub>)O<sub>2</sub>) are compared with experimentally determined thermal expansion and conductivity values [114] as well as with those available in the literature and investigated.

#### **4.10 Thermal expansion**

The pellets of (Th,5%Ce)O<sub>2</sub> MOX fabricated by different processes and sintered in different atmospheres were characterized for their density and O/M ratio to estimate the extent of their influence on thermal properties. The details of samples used for studies are given in Table 4.2 in Section 4.3.

The typical variation of linear thermal expansion (%) as a function of temperature (298–1773 K) measured by dilatometer for ThO<sub>2</sub> and (Th,5%Ce)O<sub>2</sub> MOX are shown in Figure 4.14 (a) and Figure 4.14 (b) respectively.

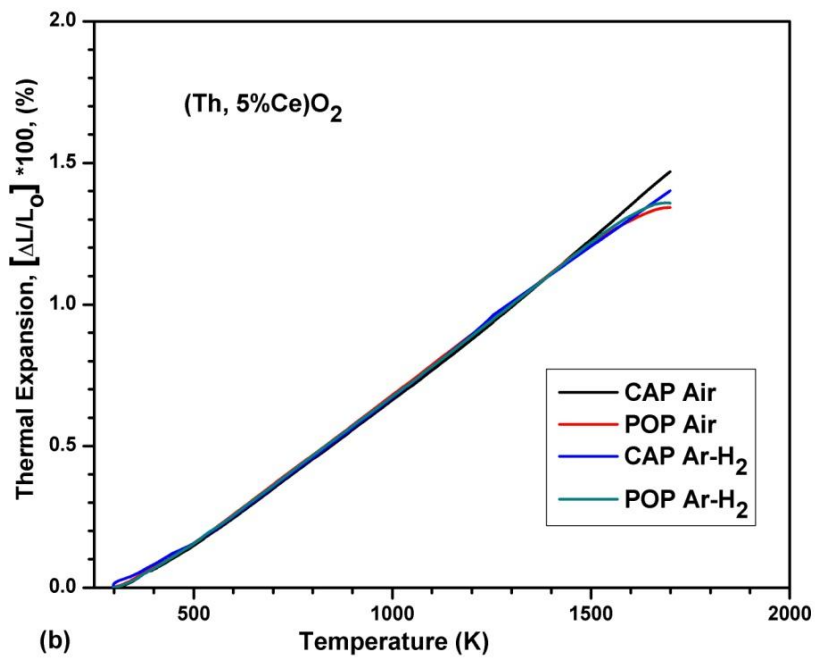
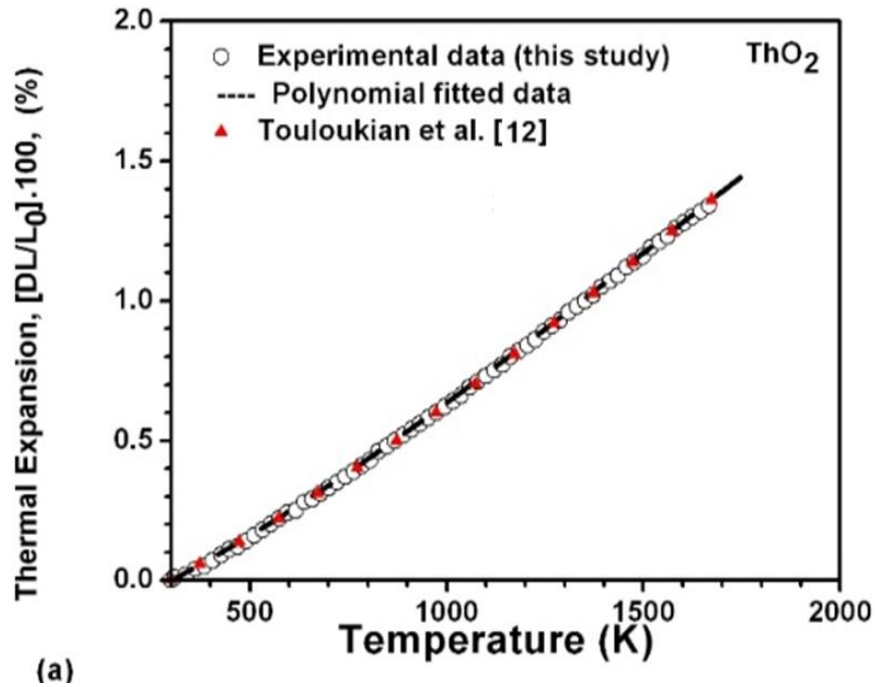


*Figure 4.14 : (a) Thermal expansion of  $\text{ThO}_2$  measured by dilatometer and polynomial fitted curve compared with polynomial equation described by Touloukian et al [75] and (b) Thermal expansion of  $(\text{Th}, 5\% \text{Ce})\text{O}_2$  POP and CAP pellets sintered in different atmospheres.*

The thermal expansion of ThO<sub>2</sub> is well established and is widely reported in the literature. Touloukian et al [75] list more than 34 different experimental determinations which are in excellent agreement and recommended the following equation (150–2000 K):

$$(\Delta L/L_0) \times 100\% = -0.179 + 5.097 \times 10^{-4} \times T + 3.732 \times T^2 - 7.594 \times 10^{-11} \times T^3 \quad (12)$$

Our predicted  $(\Delta L/L_0) \times 100\%$  third order polynomial equation for ThO<sub>2</sub> almost reproduces the above relation (within  $\pm 10\%$  range of the coefficients) as can be observed in Figure 4.14 (a). The experimental thermal expansion data of (Th,5%Ce)O<sub>2</sub> samples shown in Figure 4.14 (b) was least squares fitted to a third degree polynomial equation for each sample. The fitting errors for all these compositions were within  $\pm 1\%$ .

Experimentally measured (Th,5%Ce)O<sub>2</sub> (POP and CAP pellets) and MD calculated thermal expansion coefficients ( $\alpha$ ) values deduced between 298–1773 K [114] with other literature data [162] are given in Table 4.3.

**Table 4.3 : Experimentally measured (by dilatometer) and MD calculated thermal expansion coefficients of ThO<sub>2</sub> and (Th,Ce)O<sub>2</sub> MOX compared with available experimental data in the literature.**

<b>Thermal expansion coefficients (<math>10^{-6}K^{-1}</math>)</b>	<b>Remarks</b>
ThO <sub>2</sub>	
10.29 (300–1800 K)	MD (BMM model)
10.61 (300–1800 K)	MD (Buck model) [114]
9.99 (300–1773 K)	Dilatometry, [114]
9.04 (293–1123 K)	Dilatometry, 96% T.D [162]
9.54 (293–1173 K)	HTXRD [162]
ThO <sub>2</sub> –5%CeO <sub>2</sub>	
10.42 (300–1800 K)	MD, Th <sub>0.9375</sub> Ce <sub>0.0625</sub> O <sub>2</sub> (BMM model)
10.57 (300–1800 K)	MD, Th <sub>0.875</sub> Ce <sub>0.125</sub> O <sub>2</sub> (BMM model)
10.78 (300–1800 K)	MD, Th <sub>0.9375</sub> Ce <sub>0.0625</sub> O <sub>2</sub> (Buck model) [114]
10.93 (300–1800 K)	MD, Th <sub>0.875</sub> Ce <sub>0.125</sub> O <sub>2</sub> (Buck model) [114]
10.35 (873–1773 K)	Dilatometry, POP, ThO <sub>2</sub> –5wt% CeO <sub>2</sub> (Air) [114]
10.44 (873–1773 K)	Dilatometry, POP, ThO <sub>2</sub> –5wt% CeO <sub>2</sub> (Ar–H <sub>2</sub> ) [114]
10.56 (873–1773 K)	Dilatometry, CAP, ThO <sub>2</sub> –5wt% CeO <sub>2</sub> (Air) [114]
10.65 (873–1773 K)	Dilatometry, CAP, ThO <sub>2</sub> –5wt% CeO <sub>2</sub> (Ar–H <sub>2</sub> ) [114]
9.35 (293–1123 K)	Th <sub>0.96</sub> Ce <sub>0.04</sub> O <sub>2</sub> , Dilatometry, 83% T.D [159]
9.76 (293–1173 K)	Th <sub>0.96</sub> Ce <sub>0.04</sub> O <sub>2</sub> , HTXRD [159]
9.49 (293–1123 K)	Th <sub>0.92</sub> Ce <sub>0.08</sub> O <sub>2</sub> , Dilatometry, 83% T.D [159]
9.96 (293–1173 K)	Th <sub>0.92</sub> Ce <sub>0.08</sub> O <sub>2</sub> , HTXRD [159]

Experimental studies using dilatometry indicated that the thermal expansion coefficient of (Th,Ce)O<sub>2</sub> increases with incorporation of CeO<sub>2</sub> due to higher thermal expansion coefficient of CeO<sub>2</sub> arising from its lower melting point compared to that of ThO<sub>2</sub>

[114]. Similar observations have been largely reported on (Th,Ce)O<sub>2</sub> system [162–164] and other MOX systems [123]. Mathews et al [162] measured thermal expansion coefficient of CeO<sub>2</sub> and ThO<sub>2</sub> using dilatometer and HTXRD in the temperature range of 293–1173 K and found CTE values of CeO<sub>2</sub> to be higher than ThO<sub>2</sub>. The CTE values obtained in their studies by HTXRD were slightly higher than obtained by dilatometric experiments. The deviation in CTE values was due to the difference in the heat treatment during fabrication and extent of homogeneity in the samples.

Xiao et al [144] in their studies based on first principles calculations with quasi-harmonic approximations for calculating thermodynamic properties of (Th,Ce)O<sub>2</sub> solid solutions reported similar observation of increase in CTE of ThO<sub>2</sub> with the substitution of CeO<sub>2</sub>. Lower melting point and cohesive energy of CeO<sub>2</sub> was considered to reflect in stronger thermal response of lattice thermal vibrations and a higher thermal expansion in their studies. Uiter et al [165] have suggested a relationship between the linear thermal expansion coefficient and the melting point for fluorite type oxides, i.e.  $\alpha_l \times T_m = 0.03$ . It was also observed that the pellets fabricated by CAP process exhibited slightly higher expansion as compared to pellets fabricated by conventional route. However, the difference between the CTE values of pellets fabricated by different routes was not very significant and that can clearly be observed in Figure 4.14 (b). The CTE values observed in the present study showed deviation on the higher side compared to the extrapolated values for similar compositions in the study conducted by Tyagi et al [164].

The deviation in CTE values might be due to difference in fabrication methods and conditions as it influences the porosity content, O/M ratio and the extent of homogeneity in

the samples. It was observed that the MD calculated thermal expansion coefficients ( $\alpha$ ) values were higher than the experimentally measured  $\alpha$  values as MD calculations were performed on a model system with homogeneous distribution of CeO<sub>2</sub> in ThO<sub>2</sub> matrix with no incorporation of porosity effects, impurity effects, etc.

The comparison of CTE values of POP and CAP samples show that the difference was quite negligible and both the pellets were expected to exhibit similar thermal expansion behavior during the reactor operation. The difference as could be seen from the Table 4.3 at an temperature of ~1000 K between the two samples would be <5% (~ 3.0  $\mu$ m) whereas the design criteria for accommodation of expansion is much higher (100–150  $\mu$ m). Therefore, from the fuel design point of view, the thermal expansion behavior of CAP pellet will be equivalent to that of POP pellet.

#### **4.11 Thermal Diffusivity**

The thermal diffusivity studies were conducted on samples from the pellets of ThO<sub>2</sub> and ThO<sub>2</sub>–5wt.%CeO<sub>2</sub> made by two different processes (POP and CAP) and sintered under different sintering atmospheres (air and Ar–H<sub>2</sub>) which had been used for the thermal expansions studies. The technique employed for thermal diffusivity studies have been described in Section 3.2.9. The results of thermal diffusivity measurements of samples sintered in air and Ar–H<sub>2</sub> are plotted in Figures 4.15 (a) and 4.15 (b) respectively. The thermal diffusivity of the pellets was observed to decrease with increase in temperature. The trend observed in the MOX samples might be due to the addition of ceria. The scattered values could be attributed to the porosity present in the samples which are responsible for high scattering of the phonons in the matrix.

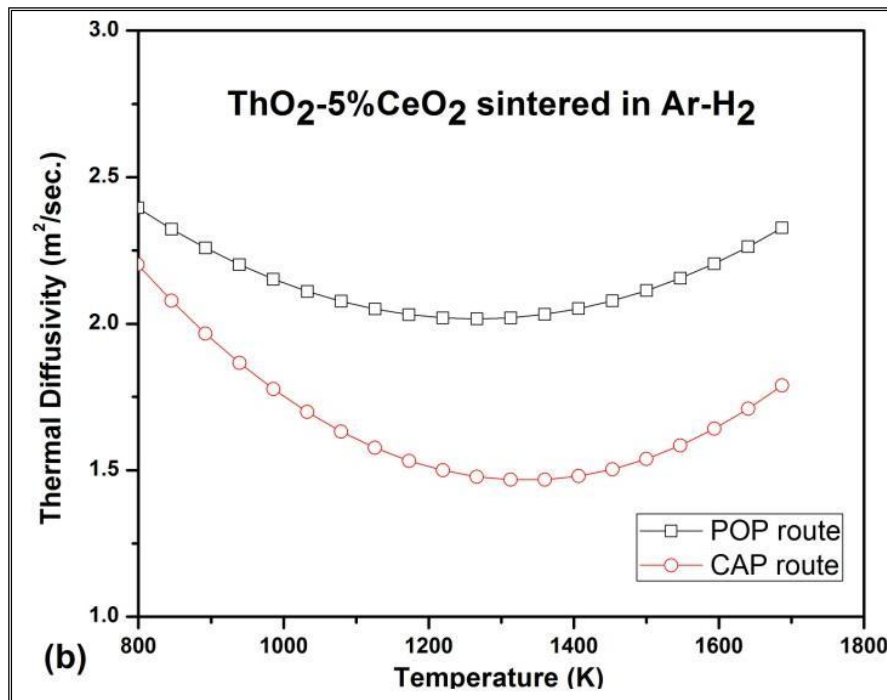
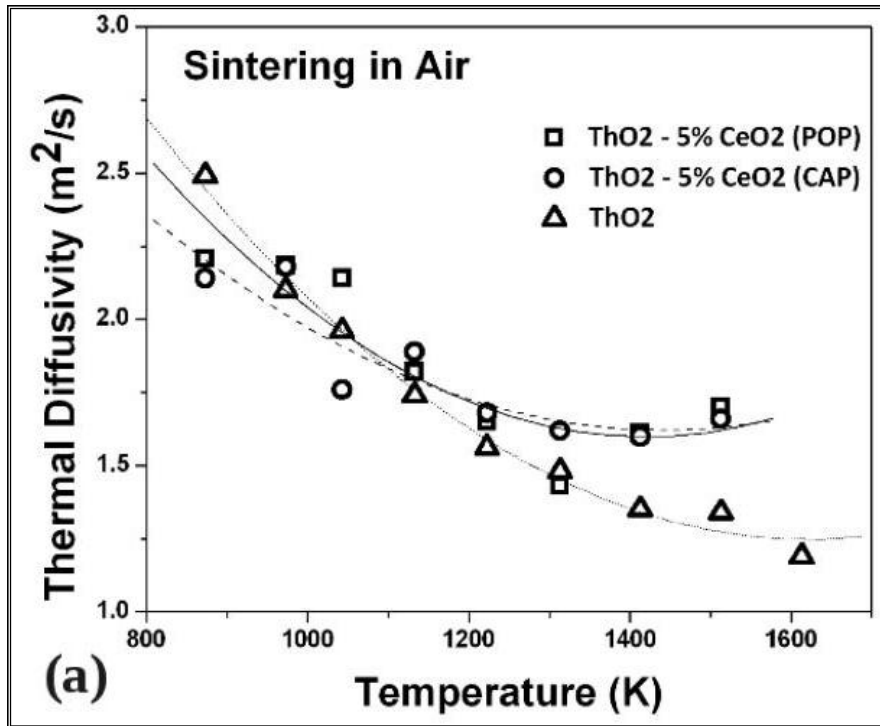


Figure 4.15: (a) Experimentally measured thermal diffusivity of ThO<sub>2</sub> and ThO<sub>2</sub>-5% CeO<sub>2</sub> (POP and CAP pellets) sintered in air and (b) ThO<sub>2</sub>-5% CeO<sub>2</sub> (POP and CAP pellets) sintered in Ar-H<sub>2</sub> atmosphere.

The pellets fabricated by CAP process exhibited lower thermal diffusivity compared to POP pellets. The CAP pellets possess thoria rich and ceria rich solid solutions in the matrix which might have affected the material property and thereby, the thermal diffusivity. The thermal diffusivity of the samples with  $\text{ThO}_2$ -5% $\text{CeO}_2$  (sintered in air both POP and CAP) was almost equal to that of  $\text{ThO}_2$  at temperature around 1000K. The samples of  $\text{ThO}_2$ -5%  $\text{CeO}_2$  (both POP and CAP sintered in  $\text{Ar-H}_2$ ) exhibited higher thermal diffusivity compared to  $\text{ThO}_2$  samples and  $\text{ThO}_2$ -5%  $\text{CeO}_2$  (POP and CAP) samples sintered in air. This could be attributed to O/M ratio of pellet. In the MOX samples due to reduction of  $\text{Ce}^{+4}$  to  $\text{Ce}^{+3}$ , higher  $\text{V}_\text{O}^{\bullet\bullet}$  sites are generated compared to  $\text{ThO}_2$  which is a very stable oxide. This resulted in high mobility of  $\text{O}^{-2}$  ions at high temperatures and thereby assisted in thermal transport mechanisms.

#### 4.12 Thermal conductivity

The thermal conductivity values of  $\text{ThO}_2$  and  $\text{ThO}_2$ -5% $\text{CeO}_2$  POP and CAP pellets (sintered in air and  $\text{Ar-H}_2$ ) were calculated from the measured values of thermal diffusivity and density along with the specific heat values by Neuman-kopp's equation (validated) in the 873–1613 K temperature range. Figure 4.16 shows experimentally measured thermal conductivity of  $\text{ThO}_2$  and  $\text{ThO}_2$ -5%  $\text{CeO}_2$  fabricated by conventional route (POP) and CAP route sintered in  $\text{Ar-H}_2$  and air atmospheres as function of temperature.

The lattice thermal conductivity of  $\text{ThO}_2$  was calculated using a supercell comprising 8x8x8 fluorite unit cells using Green-Kubo formalism [166, 167]. The calculated thermal conductivities of  $\text{ThO}_2$  and  $\text{CeO}_2$  as a function of temperature (300–2000 K range) decreases with an increase of temperature, which reflects lowering of thermal conductivity by the

phonon–phonon scattering. In order to compare with the reported experimental data, a density (porosity) correction was applied to the MD calculated values as these were obtained for 100% T.D. The porosity effect incorporated thermal conductivity ( $\kappa$ ) is related to the 100% T.D thermal conductivity ( $\kappa_0$ ) by Maxwell–Eucken equation:

$$\kappa = \kappa_0 \frac{1-p}{1-\beta p} \quad (13)$$

where  $\beta = 0.5$  and  $p$  is the porosity ( $p = 0.05$  for this study)[168].

For ceramic oxide systems, the behavior of thermal conductivity with temperature is governed by two factors: (i) the phonon–phonon interaction and (ii) the density of defects (phonon scattering centers) in the lattice. For temperatures below 1900 K, the contribution of the free electrons on the thermal conductivity can be neglected for electronically insulator materials [74,169]. The thermal conductivity data was fitted to the standard relation of phonon conduction as given in equation 14.

$$\kappa = \frac{1}{(A+BT)} \quad (14)$$

where,  $A$  represents scattering due to the presence of impurity and is independent of temperature and  $B$  represents scattering due to phonon and is a function of temperature. The first term,  $A$ , in above relation represents the defect thermal resistivity. The influence of substituted impurities on the thermal conductivity is described by the increase of the parameter  $A$ . This results from the phonon interactions with lattice imperfections, impurities, isotopic, or other mass differences as well as bulk defects such as grain boundaries in the sample. Parameter ‘ $B$ ’ remains constant theoretically and the second term, namely  $B*T$ ,

represents the intrinsic lattice thermal resistivity caused by phonon–phonon scattering. As the temperature increases, this term becomes predominant. By polynomial fitting of the thermal resistivity versus temperature data constants  $A$  and  $B$  can be obtained for each composition of solid solution.

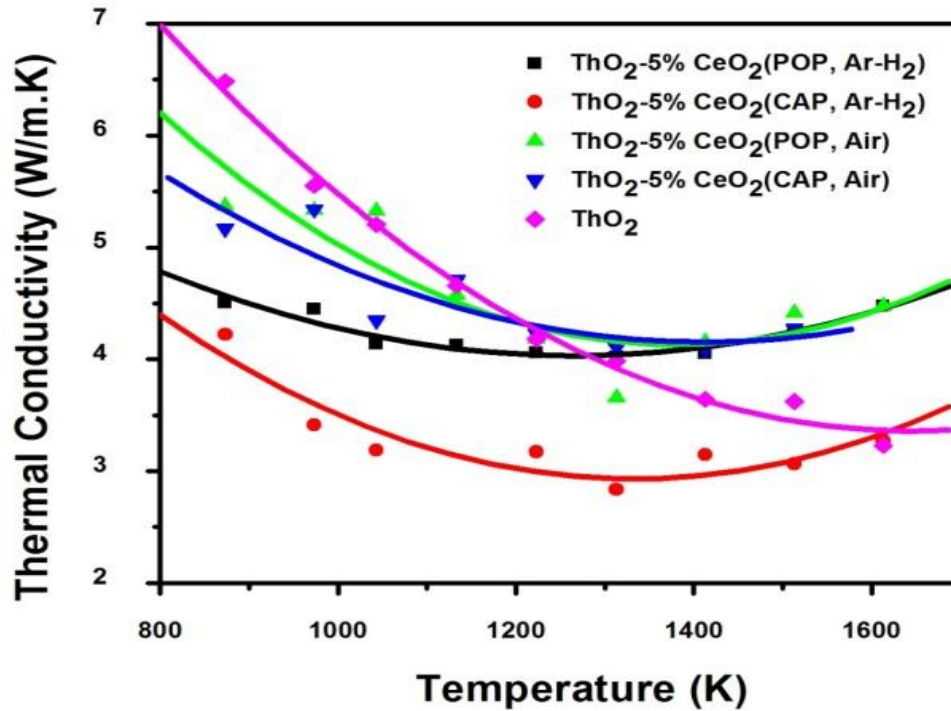


*Figure 4.16 : Experimentally measured thermal conductivity of  $\text{ThO}_2$  and  $\text{ThO}_2$ -5%  $\text{CeO}_2$  fabricated by conventional route (POP) and CAP route sintered in  $\text{Ar-H}_2$  and air atmospheres. Solid lines are polynomial fitting of experimentally obtained data points to determine constants  $A$  and  $B$  of equation 14.*

The parameters  $A$  and  $B$  were obtained for each composition of solid solution by polynomial fitting of the thermal resistivity versus temperature data. Table 4.4 shows the determined values of  $A$  and  $B$  constants for  $k$  values of experimentally measured and the MD

calculated using Coulomb–Buckingham–Morse–many–body potential (BMM) and also Coulomb–Buckingham (Buck) potential [150, 151].

As shown in Figure 4.17, the MD calculated thermal conductivities were in good agreement with the experimental data within  $\pm 1 \text{ W m}^{-1} \text{ K}^{-1}$  for temperatures greater than 750 K and slightly overestimated at temperature below 750K.

**Table 4.4: Constants A and B of the equation 14,  $1/\kappa = A+BT$ , for  $\text{ThO}_2$  and  $(\text{Th,Ce})\text{O}_2$  MOX calculated from experimental measurements and MD simulations.**

<i>Sample</i>	<i>A(m.K/W)</i>	<i>B(m/W)<math>\times 10^{-4}</math></i>
ThO <sub>2</sub> , MD (BMM model)	0.00315	1.88
Th <sub>0.9375</sub> Ce <sub>0.0625</sub> O <sub>2</sub> , MD (BMM model)	0.00794	2.05
ThO <sub>2</sub> , MD (Buck model) [114]	0.00254	2.44
Th <sub>0.9375</sub> Ce <sub>0.0625</sub> O <sub>2</sub> , MD (Buck model) [ 114]	0.00825	2.41
ThO <sub>2</sub> , Experiment [ 114]	0.02000	1.34
ThO <sub>2</sub> –5wt%CeO <sub>2</sub> (POP) Ar–H <sub>2</sub> , Experiment [114]	0.20519	0.08
ThO <sub>2</sub> –5wt%CeO <sub>2</sub> (CAP) Ar–H <sub>2</sub> , Experiment [114]	0.22145	1.00
ThO <sub>2</sub> –5wt%CeO <sub>2</sub> (CAP) Air, Experiment [114]	0.07449	0.90
ThO <sub>2</sub> –5wt%CeO <sub>2</sub> (POP) Air, Experiment [114]	0.08605	0.90

Experimental observations on thermal conductivity studies show that the pellets fabricated by CAP process exhibited lower thermal diffusivity and conductivity compared to pellets fabricated by conventional route (POP) under similar conditions. Thermal conductivity of pellets sintered in oxidizing atmosphere showed decreasing trend with

increasing temperature. With increasing temperature, the difference in thermal conductivity was reducing between pellets made by different processes.

Correlating the thermal conductivity studies with the microstructure investigations of the present study, the CAP pellets with higher average pore size and preferentially located at large grain regions with some interconnectivity as compared to the small pores uniformly dispersed in the POP pellets, suggested porosity in the pellets affected the thermal conductivity. The pore distribution and morphology influence the extent of porosity effect on the thermal properties.

The pore characteristics (bigger pore sizes, higher porosity fraction, pore concentration along the grain boundaries and inter-connectivity of pores) typical of CAP pellets [24, 25] and inhomogeneity in the pellet could be collectively responsible for observed decrease in thermal diffusivity and conductivity compared to POP pellets which possess smaller pores uniformly distributed in the matrix and uniform distribution of Ce in the pellet. However, the variation between thermal conductivity of POP pellets and CAP pellets expected to be large was not observed. In the CAP pellets, specific grain boundary area was lower compared to POP pellets due to presence of large grains. These grain boundaries being defect structures are phonon scattering sites and influence the thermal properties. The reduced phonon scattering sites in CAP pellets due to grain boundary area reduction could have positively affected the thermal conductivity and compensated the deleterious effect.

It was evident from Table 4.4 that MD calculated constant  $A$  increases with  $\text{CeO}_2$  incorporation in agreement with the experimental trend which could be attributed to the

scattering of the phonons occurring due to mass and size difference between substituted and host atoms.

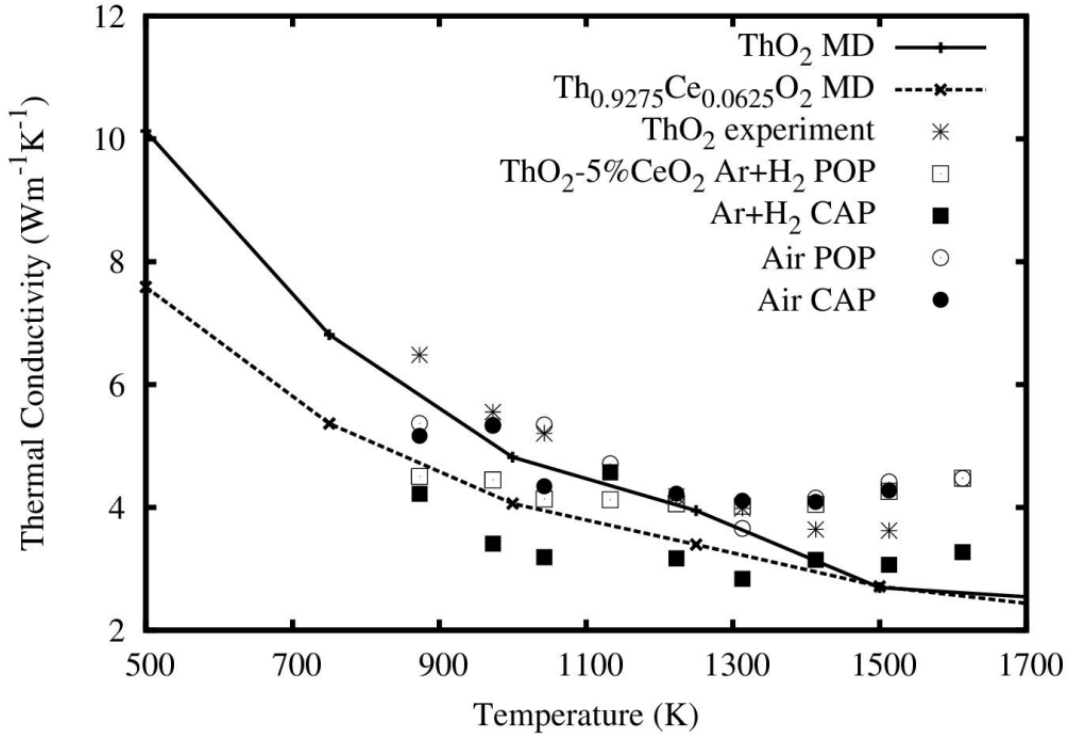


**Figure 4.17 :** Comparison of Thermal conductivity calculated by MD simulations as a function of temperature for  $\text{ThO}_2$  and  $\text{Th}_{0.9275}\text{Ce}_{0.0625}\text{O}_2$  with experimental values of  $\text{ThO}_2$  and  $\text{ThO}_2$ -5wt%  $\text{CeO}_2$  for POP as well as CAP pellets sintered in  $\text{Ar-H}_2$  and Air atmosphere (95 % T.D). Solid lines are only for visual guidance.

The experimental observations on conductivity studies show that the pellets fabricated by CAP-process exhibited slightly lower thermal conductivity compared to pellets fabricated by conventional route (POP).

Considering the experimental thermal conductivity values for pellet of size 10 mm operating at a particular linear heat rating and with centre line temperature of pellet in normal operation of 1773 K. The change in centre line temperature will be 200–300 K (maximum).

Therefore, the effect of replacing CAP pellet instead POP pellet of  $(\text{Th},5\%\text{Ce})\text{O}_2$  will be negligible as its effect will be 20% of the design margin of operation.

Further extrapolating, the effective change in the centerline temperature of the pellet fabricated by POP with CAP pellet will be further lowered due to higher thermal conductivity of  $\text{PuO}_2$  compared to  $\text{CeO}_2$ . Therefore, the CAP pellets during reactor operation are expected to meet the designed criteria of heat dissipation similar to POP pellets without any substantial increase in centerline temperature of the pellet.

#### **4.13 Microstructure effects on fuel behavior – current knowledge**

The effect of initial grain size on fission gas release and swelling has been studied by various authors and based on their irradiation studies have recommended use of large grained fuel for higher burn up achievements [170–173]. Une et al.[170] showed that fission gas release and swelling caused by high temperature annealing up to 1800°C for  $\text{UO}_2$  fuels irradiated to 23GWD/T, were reduced to about 1/3–1/2 with increasing grain size from 16 to 43mm. They reported that the FGR and the swelling were determined by the release rate of the fission gas to the grain boundaries and the smaller grain size the higher the release rate to the grain boundaries and the higher the FGR and the swelling. Turnbull [172] showed a significant reduction of fission gas release and swelling with increasing grain size (7 and 40mm) during irradiation at a constant temperature of 1750°C up to 4GWD/T. Hastings [173] showed that  $\text{UO}_2$  fuel with grain sizes from 8 to 80mm was irradiated to 3GWD/T at linear heat rating of 50kW/m, and the reduction in FGR was about 1/3 for absolute FGRs of 1.2 and 0.4%, respectively. Irradiation experiments using  $\text{UO}_2$  pellets possessing normal grain size (~8  $\mu\text{m}$ ) with fine pores as formed of sizes (< 5  $\mu\text{m}$ ) and large grains ranging from (23–80

$\mu\text{m}$  ) with large pores of sizes ( $> 10 \mu\text{m}$  ) have been conducted by various and reported [174]. Harada and Doi conclude from their irradiation experiments that fission gas release was inversely proportional to the average grain size. The presence of large pore was contributing in reduction of fission gas release and swelling of pellet. The effect of pore structure on the densification mechanism has studied by various authors [175–177]. They also reported that in–pile and out–of–pile densification of the large grain pellets were smaller than those of the normal pellets by measuring the internal pressure of the fuel rod. They found that density change during resintering (out–of–pile test) was one fifth of normal grained fuel rod. They attributed in–pile and out–of–pile densification occur owing to the disappearance of fine pores  $< 5 \mu\text{m}$  diameter. The creep rate of the large grain pellet was found to be lower than that of the normal one in the low stress region. In their study on thermal expansion behavior, they observed that the thermal expansion is independent of the differences in the microstructure of the two pellets.

From our studies, we could observe that CAP pellets and POP pellets possessed similar microstructure characteristics used for experimental irradiation studies in earlier reported studies. Referring to above evidences, it could be reasonably correlated and concluded that the microstructure characteristics of CAP pellet being duplex (fine grains and large grains) will also exhibit similar behavior of higher fission gas retention due to larger grains with higher fissile content along with co–located porosity, which in turn might be helpful in reduced dilution of cover gas (helium) in the fuel pin and thereby maintaining the thermal conductivity of the cover gas effectively compared to POP pellets especially relevant for thermal reactor operation. Further due to the presence of fine grains, CAP pellets will possess good creep properties. The small grains shall imbibe plasticity to the pellets and shall

help in reducing pellet clad mechanical interaction. Summarily, from nuclear fuel performance aspect, the CAP pellet appeared to possess properties comparable to POP pellets when sintered in reducing atmosphere.

#### 4.14 Summary

From the extensive experimental studies and MD simulations conducted on (Th,Ce)O<sub>2</sub> MOX pellets for characterization of physical, metallurgical, homogeneity and thermal properties, following were drawn:

- i) The pellets fabricated by CAP process showed microstructure with fine grain colonies surrounded by large grains. Average grain size of pellets sintered in reducing atmosphere was comparatively larger than pellets sintered in oxidizing atmosphere.
- ii) The POP pellets sintered in reduced atmosphere showed lower O/M ratio compared to CAP pellets.
- iii) Ionic conductivity of POP pellets was observed to be higher compared to CAP pellets due to better homogeneity (outcome of good cationic inter diffusion between Ce and Th cations) and due to better densities (lesser discontinuities).
- iv) The specific heat capacity of the pellets (both CAP and POP) measured using DSC in the temperature range 300–763 K were in good agreement with Neumann–Kopp’s values within 5% deviation.
- v) The CAP pellets exhibited lower thermal conductivity compared to POP pellets because of higher scattering of phonon due to cumulative effect of porosity and lower O/M ratio compared to the POP pellets sintered in same atmosphere.

- vi) The effect of inhomogeneity on thermal expansion and thermal conductivity was not very pronounced compared to that of porosity and O/M (stoichiometry) of the MOX pellets.
- vii) The differences observed in thermal conductivity values of (Th,Ce)O<sub>2</sub> pellets fabricated by different processing routes (due to different pellet characteristics) became insignificant at higher temperatures.
- viii) Coulomb–Buckingham type potential model developed and used in the thermal property study could predict precisely the lattice parameters as a function of temperature for MOX solid solutions and were in good agreement with experimental measurements on (Th,Ce)O<sub>2</sub>.
- ix) MD simulations using Coulomb–Buckingham–Morse–many–body (BMM) potential could evaluate mechanical and thermal properties of ThO<sub>2</sub> and (Th,Ce)O<sub>2</sub> MOX .
- x) Coulomb–Buckingham–Morse–many–body potential as well as Coulomb–Buckingham type potential model are useful for predicting thermal expansion and thermal conductivity values of ThO<sub>2</sub> and (Th,Ce)O<sub>2</sub> MOX.

Overall from the study on (Th,Ce)O<sub>2</sub> MOX system, it is expected that the thermal property of CAP pellets should be quite similar to POP pellets and would exhibit similar thermal performance in the reactor.

## CHAPTER 5. CHARACTERIZATION STUDIES ON (Th,Pu)O<sub>2</sub> SYSTEM

### 5.1 Introduction

In the previous chapter, some important experimental studies which were not feasible to be conducted on (Th,Pu)O<sub>2</sub> system and required for comparative evaluation of the two different techniques of fabrication were carried out on (Th,Ce)O<sub>2</sub> system. From these surrogate studies, important findings will be reflected in this study on (Th,Pu)O<sub>2</sub> system to bring out the comparison between characteristics of CAP pellets and POP pellets more effectively. Sintering studies conducted on (Th,Ce)O<sub>2</sub> system under different atmospheres were highly significant. The sintering behavior and resultant characteristics of the pellets were considered to be applicable to (Th,Pu)O<sub>2</sub> pellets. The (Th,Ce)O<sub>2</sub> pellets (POP and CAP) sintered in oxidizing atmosphere showed wide variance in the densities, homogeneity, ionic conductivity and also specific heat capacity ( $C_p$ ). Studies using EPMA had confirmed that the CAP pellets possessed better homogeneity when sintered in reducing atmosphere than in oxidizing atmosphere (air) atmosphere. Microstructure studies showed that CAP pellets had bimodal grain size distribution in the pellet compared to that unimodal grain size distribution in POP pellets. Further properties of CAP pellet were comparable to those of POP pellets when sintered in reducing atmosphere. Importantly EPMA studies revealed higher cerium concentrated regions exhibited higher grain growth forming larger grains and the same will be assumed in this study. From the surrogate study, as it was evident that sintering of (Th,Pu)O<sub>2</sub> pellets in reducing atmosphere would be highly favorable and it was adopted for fabrication of samples for further studies and investigations. Reported studies suggest mainly recommend evaluation of specific heat capacities of the system under study. Reported literature gave contrary views on applicability of Neumann–kopp method for determining the

$C_p$  of the system. As  $C_p$  is sensitive to material composition, applicability of Neumann–kopp method for determining specific heat of  $(\text{Th,Ce})\text{O}_2$  was investigated. The study was very significant as pellets were fabricated by different routes, in different conditions and with different homogeneity were investigated for the first time. The experimental study confirmed applicability of Neumann–kopp method for determining specific heat of  $(\text{Th,Ce})\text{O}_2$  and the same was adopted for  $(\text{Th,Pu})\text{O}_2$  study for thermal conductivity calculations.

The present chapter represents the study carried out on  $(\text{Th,Pu})\text{O}_2$  with 1 wt.%  $\text{PuO}_2$  addition and in conditions similar to that proposed for in–reactor investigation purposes with POP route. Pellets with 6% and 8%  $\text{PuO}_2$  compositions have been used only for reference purposes in some of the studies.

Extensive investigation using alpha autoradiography alongwith image analysis and UV–Vis spectrophotometry were performed to develop as a potential techniques for estimation of the fissile element content and to quantify the fissile element distribution as an alternate to expensive, elaborate, and slow and operator dependent chemical analytical techniques.

The chapter will present the comparative evaluation of  $(\text{Th,1\%Pu})\text{O}_2$  CAP pellets and POP pellets for their characteristics and properties.

## 5.2 Density

*Table 5.1: Characteristics of (Th,Pu)O<sub>2</sub> experimental sintered pellets.*

<b>Pellet composition</b>	<b>Fabrication Process</b>	<b>Density (%T.D)</b>	<b>Porosity (%T.D)</b>	<b>O/M</b>	<b>Th (%)</b>	<b>Pu (%)</b>	<b>Chemical Impurities (ppm)</b>
ThO <sub>2</sub> -1%PuO <sub>2</sub>	POP	91-94	6-9	1.978-1.998	86	0.97	< 1200
ThO <sub>2</sub> -1%PuO <sub>2</sub>	CAP	90-93	7-10	1.997-1.999	86	0.96	< 1200
ThO <sub>2</sub> -6%PuO <sub>2</sub>	POP	90-94	6-10	1.978	81.7	5.88	< 1200

The (Th,1%Pu)O<sub>2</sub> pellets were fabricated by both routes namely, POP and CAP. The pellets were sintered under reducing atmosphere. The details of the process followed are given in Chapter 3. The pellets fabricated by both the routes were characterized for their physical, chemical (impurities and heavy metal content) and O/M ratio. The characteristics of (Th,Pu)O<sub>2</sub> experimental sintered pellets obtained are given in Table 5.1.

## 5.3 Alpha autoradiography studies

Composition and homogeneous fissile nuclide distribution are important characteristics of nuclear fuels. Homogeneity evaluation of (Th,Pu)O<sub>2</sub> using standard techniques such as EPMA and SEM could not be conducted due to safety related issues. Therefore, alpha autoradiography of (Th,Pu)O<sub>2</sub> fuel compacts have been carried out to explore feasibility of homogeneity evaluation in the fuel pellets.

For uranium based MOX fuels, composition and homogeneity is estimated by chemical dissolution studies. However, in thoria based system, this approach proves to be ineffective because of thoria based system is highly chemically stable and inert having poor solubility in HNO<sub>3</sub> thereby, necessitating use of strong acids like HF (hydrofluoric) for long time durations [178]. Further the chemical dissolution technique does not provide necessary information on size, richness or any other detail pertaining to inhomogeneity. Previous attempts have been made to characterize the pellets for homogeneity by different methods of analyses and have been reported [179].

Alpha Autoradiography has been in use to verify homogeneity of Pu in the fuel and to check the presence of PuO<sub>2</sub> agglomerates in the fuel. The specific activity of plutonium (0.06 Ci/g) being significantly higher than that of thorium ( $1.1 \times 10^{-7}$  Ci/g), the effect on the film could be attributed to alpha irradiation from plutonium. This makes the technique capable of monitoring the distribution of plutonium in the fuel matrix. The image frames of alpha autoradiographs grabbed through an optical microscope is evaluated to obtain detailed information.

Usually image analysis of auto radiograph images is done by either counting of tracks or measuring the track density of the image. Image analysis of Alpha autoradiography using CR-39 films were earlier explored for compositional characterization of (Th,U)O<sub>2</sub> MOX fuel with large range of composition [180]. A linear correlation between track density and thorium content could be established using different compositions. However, this approach is not feasible for plutonium bearing fuels due to very high specific radioactivity of plutonium. It results in misinterpretations and erratic information especially when track densities are

significantly high and overlapping even with minimum practically possible exposures because of either high plutonium composition in the pellet or longer exposures of the film.

Considering the limitations of previous techniques and approaches adopted for investigating the homogeneity in plutonium bearing pellets, two alternate and fast analytical novel techniques based on alpha autoradiography coupled with image analysis with different approach and UV–Vis spectrophotometry were studied on nuclear fuels for the first time. Studies using these two techniques were conducted to address the important aspect of plutonium content and the plutonium distribution (micro homogeneity) in the pellets for correlating its effect on other characteristics and behavior of pellet in absence of suitable, accurate and effective techniques presently. In order to overcome the limitations of present approach of image analysis, different approach of area fraction estimation method was applied. Different MOX fuel samples were analyzed using both the techniques for compositional and homogeneity characterizations.

The optical absorption of CR39 films in UV–Vis region and changes in its optical properties due to alpha irradiation has been studied earlier [181]. It has been reported that alpha fluence with which the film has been irradiated has noticeable effect on its absorbance due to variation in thickness of the film as well as the structural changes in the polymer due to the irradiation. In this study, the changes in spectro photometric response of CR39 film due to alpha irradiation from different MOX fuel samples have been analyzed to correlate the change in optical properties of the film with the characteristics of the fuel samples.

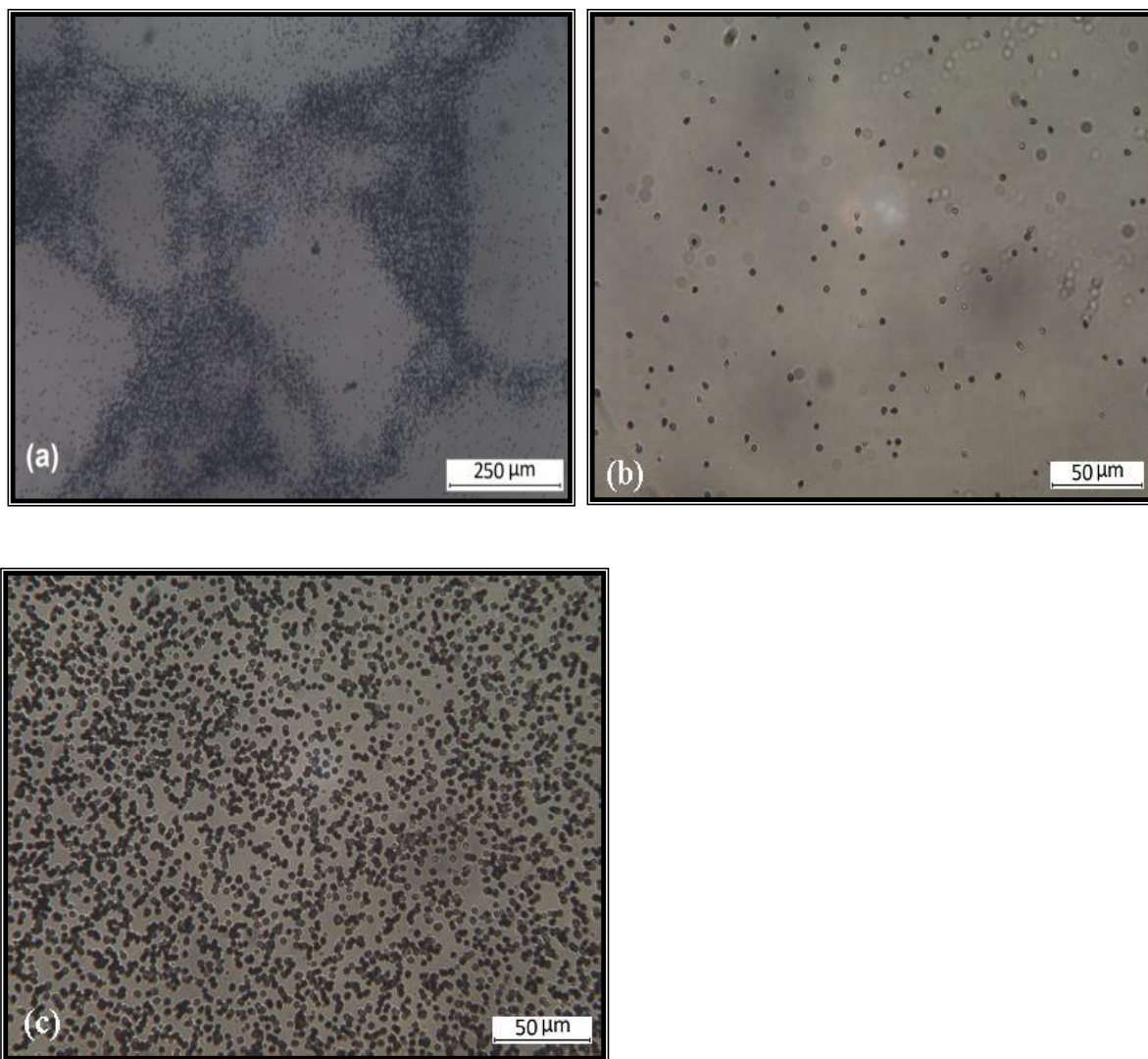


***Figure 5.1 : (a) Alpha autoradiograph image of  $\text{ThO}_2$  –1% $\text{PuO}_2$  pellets fabricated by CAP process (b) Enlarged view of region of lowest track density region of (a) and (c) Enlarged view of region of highest track density region of (a).***

In this study, the alpha autographs showed the tracks generated by 5.4 MeV alphas emitted from plutonium. The alpha autoradiograph of  $\text{ThO}_2$  –1% $\text{PuO}_2$  pellets made by CAP process revealed alternate regions with high and low densities of alpha tracks as shown in Figure 5.1 (a). The regions of highest and lowest track densities are enlarged and shown in Figures 5.1 (b) and 5.1 (c) respectively. The alpha autoradiograph of  $\text{ThO}_2$  –1% $\text{PuO}_2$  pellets

made by POP process is shown in Figure 5.2. The alpha track density was more or less uniform across the matrix of POP pellet. However, there were some regions of higher track density indicating presence of plutonium rich agglomerates (darker spots) in the alpha autograph.

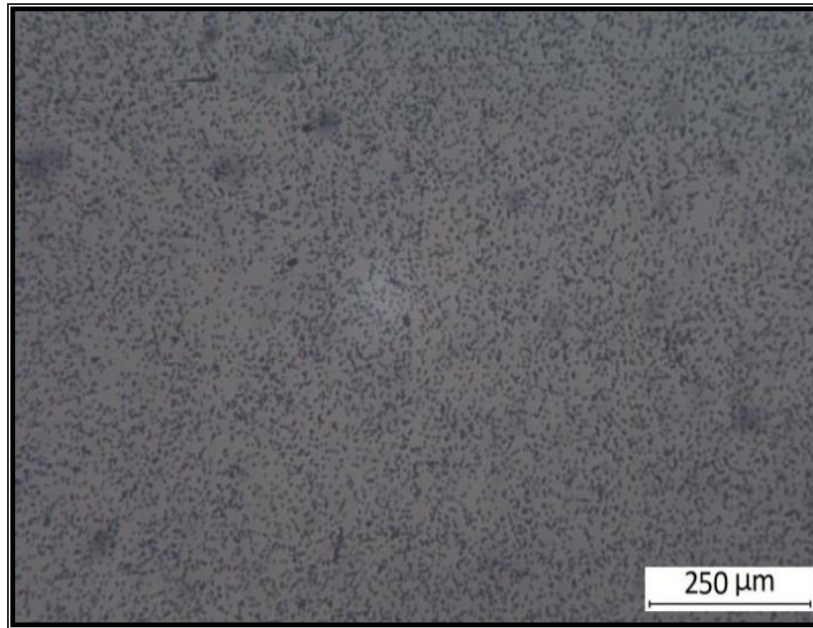


*Figure 5.2 : Alpha autoradiograph image of (Th,1% Pu)O<sub>2</sub> pellet fabricated by POP process showing uniform track density.*

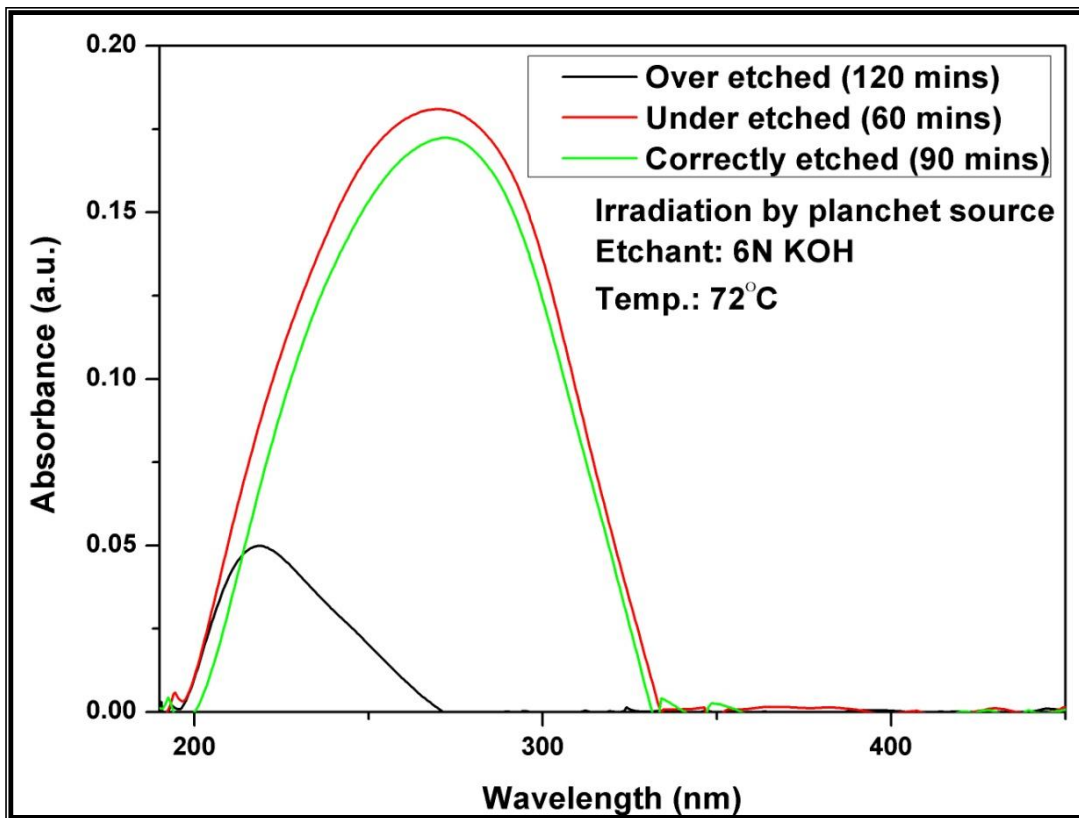
### **5.3.1 Optimization of etching using UV spectroscopy**

The standardization of parameters was important as investigations on nuclear fuel for characterization using UV–Vis spectroscopy had not been conducted and reported previously. It was necessary to ensure that all the autoradiographs were subjected to equivalent etching conditions for sake of uniform comparison. As the conditions such as exposure time, usage of mylar film, etchant concentration, etchant temperature and etching

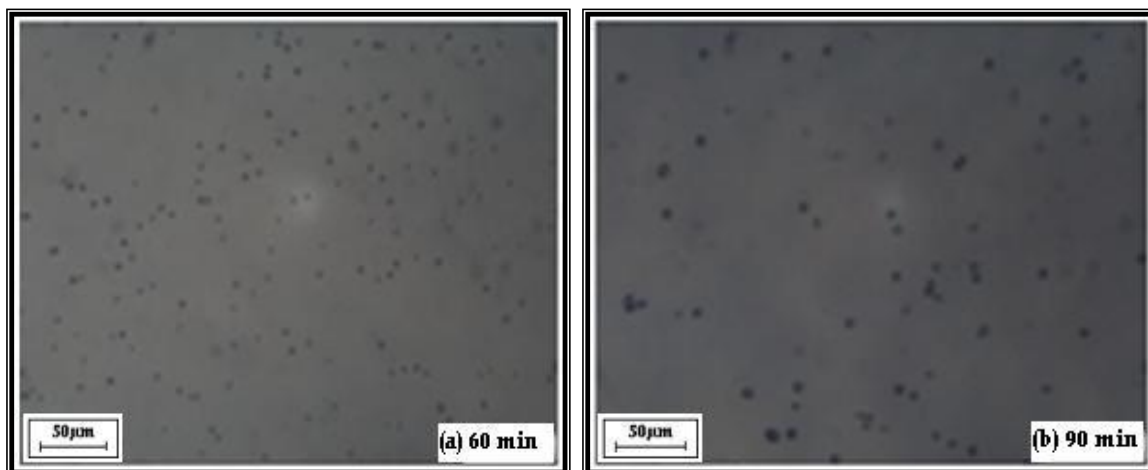
time are all operator dependant, any uncertainty or human error in the process would lead to erroneous results and interpretations.

Exposure time and etching conditions jointly dictate the extent of etching which is crucial for the enhancement of alpha tracks and thereby influence the accuracy of the analyzed results. It is very difficult to estimate the extent of etching using only microscopic observation of the autoradiograph which may lead to erratic comparison of results. Therefore, experiments for estimating the optimal etching conditions using UV–Visible spectro photometry was carried out prior to the actual studies. The same would be suitable for image analysis interpretation.

Three SSNTDs (CR–39 films) were topped with 11 $\mu$ m thickness of aluminium mylar and exposed to alphas from plutonium plancheted source (13320 dpm ) for a period of 30sec. The films were etched with KOH solutions under different conditions. The first film was etched for 60minutes, second one for 90 minutes and the third one for 120 minutes. The optical properties of the films were evaluated using spectro photometry in UV–Visible range using JASCO V 650 spectrophotometer. It was observed that the intensity and the peak maxima (absorbed wavelength) were sensitive to etching conditions. Figure 5.3 shows the UV absorbance spectra of the three films which indicate three different extents of etching. Images of the alpha autoradiographs etched for 60 mins, 90 mins and 120 mins are shown in Figures 5.4 (a), (b) and (c) respectively. The spectral studies provide valuable indication of suitability and effect of etching conditions/parameters for comparative studies on alpha autoradiographs.



*Figure 5.3 : UV absorbance spectra of the three films etched for different durations.*



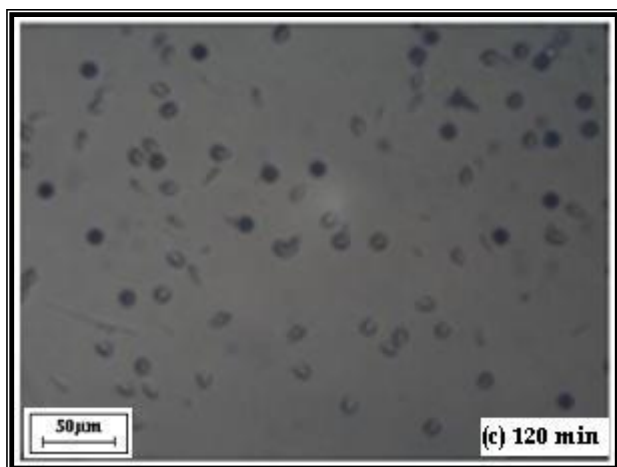


***Figure 5.4: Images of the alpha autoradiographs of plancheted plutonium source etched for (a) 60mins, (b) 90mins and (c) 120mins showing change in size of the tracks.***

While analyzing the images shown in Figure 5.4, it was observed that Figure 5.4 (b) gave the most optimal results whereas in Figure 5.4 (a) tracks were not fully revealed. In the case of image shown in Figure 5.4 (c) it was evident that diameter and depth of the tracks had increased and overlapped on to nearby tracks. The CR-39 structure is in the form of poly allyl chains connected by diethylene glycol dicarbonate link. The monomer is containing three functional groups; these are: Allyl group ( $\text{CH}_2=\text{CHACH}_2\text{A}$ ), ether group ( $-\text{CH}_2-\text{O}-\text{CH}_2-$ ), and carbonyl group ( $\text{C}=\text{O}$ ). However, these functional groups are responsible for the modifications in physicochemical properties upon exposure to any kind of radiation. In principle, the deposited energy by 5 MeV  $\alpha$ -particles is sufficient to dissociate all bonds in the CR-39 detector, even the strongest one  $-\text{C}=\text{C}-$  of dissociation energy 6.4 eV. Modifications in structure lead to preferential local chemical reaction during etching. Extent of etching depends both on radiation exposure as well as etching parameters. The duration of  $\alpha$  irradiation being maintained same for all the three films, different resultant thickness of the film is affected by the extent of etching. It can be seen that excess etching leads to change in

the peak maxima (220 nm) as compared to the correctly etched (270 nm). The excess etching of irradiated CR-39 resulted in complete removal of layers along with the changes in the groups present leading to shift in peak position as well as peak value. Maintaining the temperature and etchant concentration are very crucial parameters which have pronounced effect on etching with slight variations. Alpha autoradiographs of nuclear fuel could be compared for peak matching as an indication of equivalence of etching before detailed interpretation of the optical images. Based on comparative analysis of UV-Vis spectrophotometry and visual inspection of the images, the auto radiograph film development conditions were standardized to 6N KOH etchant maintained at constant temperature of 72°C for 90 mins for further experimental investigations.

### **5.3.2 Compositional characterization**

Alpha autoradiography of (Th,Pu)O<sub>2</sub> POP pellets containing 1%, 6% and 8% PuO<sub>2</sub> were carried out. To ensure uniform conditions of investigations, all the three samples pellets were fixed in a single mount of araldite and prepared. Film was exposed to all the three samples under exactly same conditions for accurate correlation of their images with alpha fluence. The images of alpha autoradiographs corresponding to MOX pellets containing 1, 6 & 8% PuO<sub>2</sub> were analyzed for compositional characterization of the fuel pellets using image analysis and UV-Vis spectroscopy. The specific activity of plutonium is significantly higher than that of thorium, therefore, the alpha fluence on the film could be considered to be from the plutonium present in the samples.

### 5.3.2.1 Image analysis

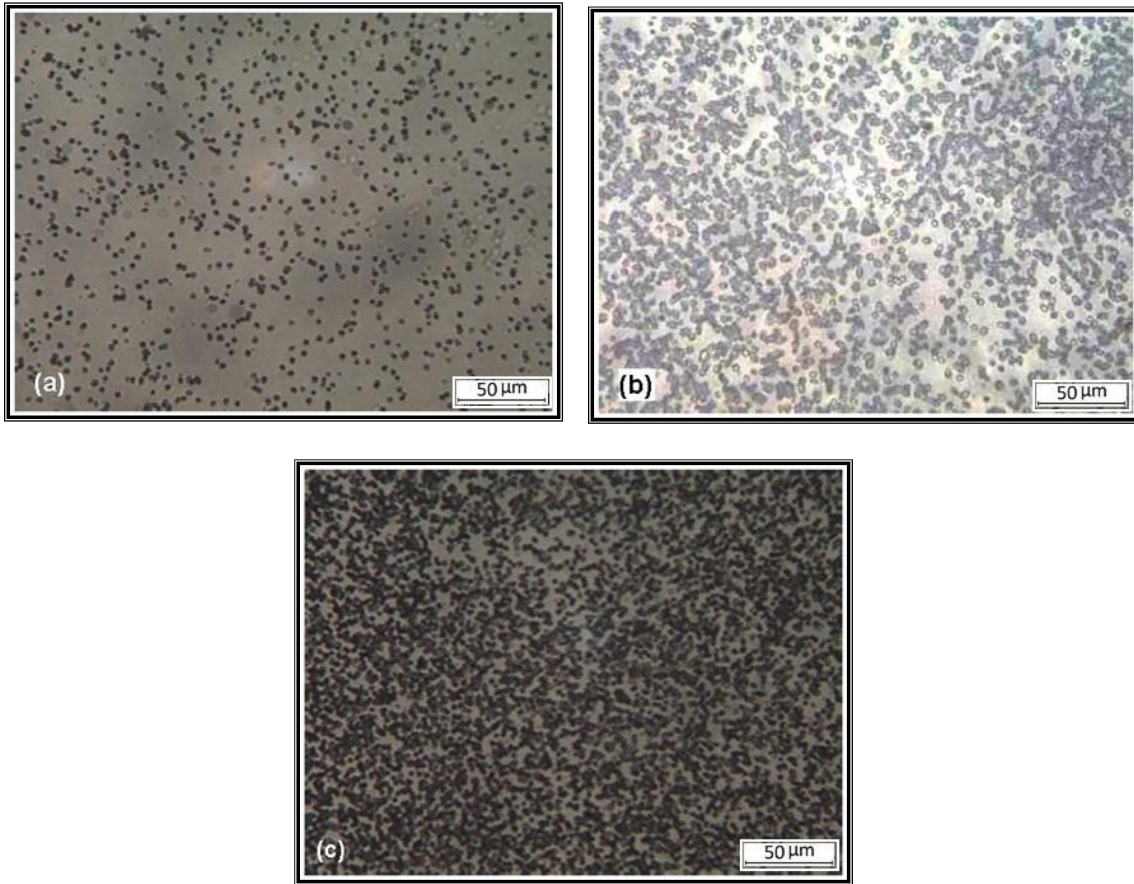


***Figure 5.5: Alpha autoradiographs of (Th,Pu)O<sub>2</sub> POP pellets having (a)1% PuO<sub>2</sub>, (b) 6% PuO<sub>2</sub> and(c) 8% PuO<sub>2</sub>.***

The autoradiographs of (Th,Pu)O<sub>2</sub> POP pellets containing 1, 6 & 8% PuO<sub>2</sub> are shown in Figures 5.5 (a), 5.5 (b) and 5.5 (c) respectively. The corresponding threshold binary images are shown in Figures 5.6 (a), 5.6 (b) and 5.6 (c) respectively. Plutonium being an element with high specific activity, it was difficult to accurately estimate the track density optically, more so especially with samples of 6 and 8% PuO<sub>2</sub>, wherein the partial overlapping of tracks could not be resolved and results in counting errors. Multiple frames were grabbed from the autoradiograph and converted into binary images by thresholding them with

appropriate grey levels. The total irradiated area fraction of each image was estimated using the software. The area fraction estimated from images using Metal power image analyzer version 3.0.0.9 are given in Table 5.2. Results from multiple frames of each of the images were estimated and the average value corresponding to each of the sample was calculated. The effect of variation in isotopic composition was eliminated by selecting the pellet samples made using only a single  $\text{PuO}_2$  powder lot.

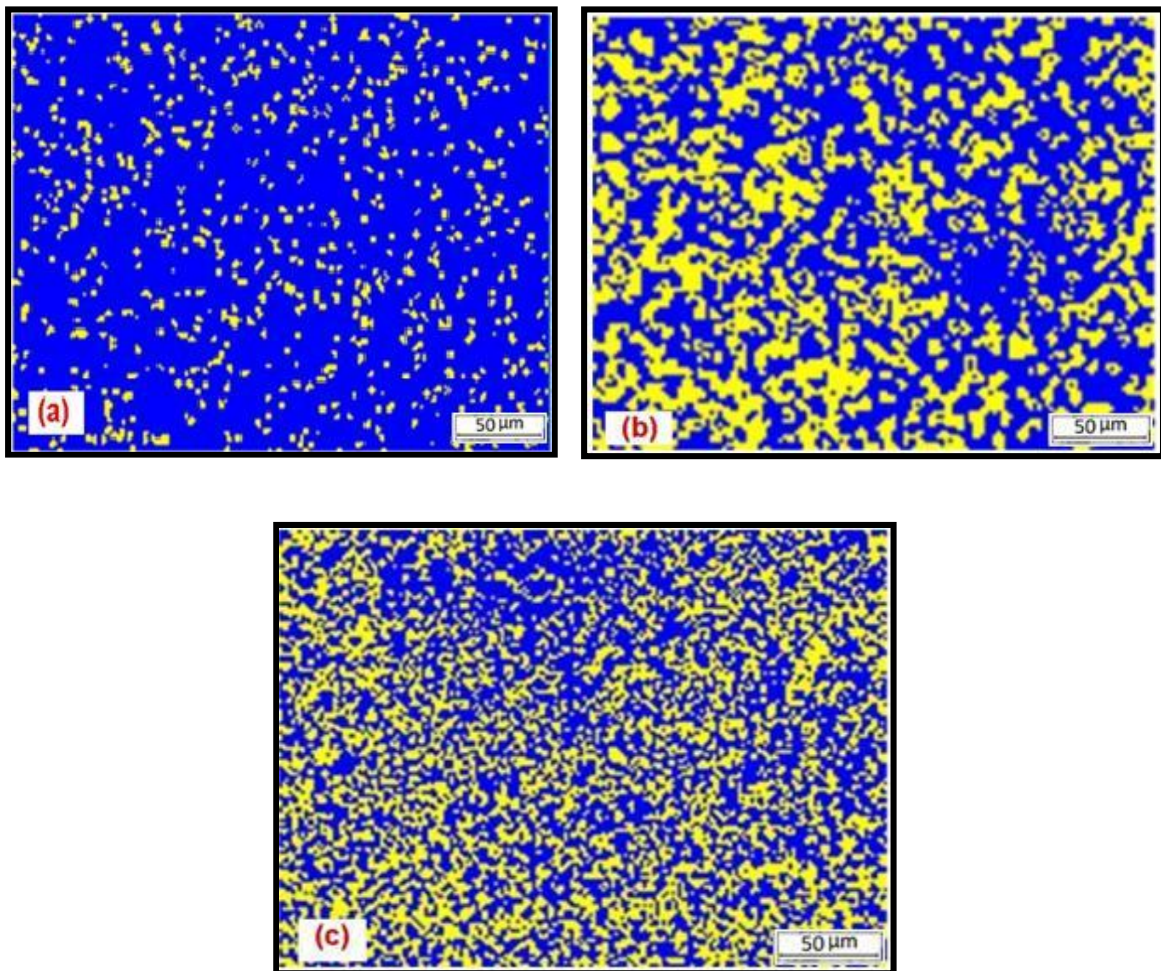


**Figure 5.6: Binary images of Alpha autoradiograph of  $(\text{Th,Pu})\text{O}_2$  POP pellets shown in Figure 5.5 having (a) 1%  $\text{PuO}_2$ , (b) 6%  $\text{PuO}_2$  and (c) 8%  $\text{PuO}_2$ .**

**Table 5.2 : Result of Irradiated area estimation by image analysis**

<b>PuO<sub>2</sub> % in the pellet</b>	<b>% Area Irradiated</b>
1	10.947
6	39.439
8	43.797

It could be seen from the result of image analysis given in Table 5.2 that the fraction of irradiated area was increasing with increasing PuO<sub>2</sub> content. The average irradiated area corresponding to each sample was plotted and a linear correlation was established with the PuO<sub>2</sub> content in the sample as shown in Figure 5.7. The best fit linear correlation is given in equation (15) with a correlation coefficient of 0.975.

$$\% \text{ Irradiated area} = (4.88623 * \text{PuO}_2\%) + 6.96318 \quad (15)$$

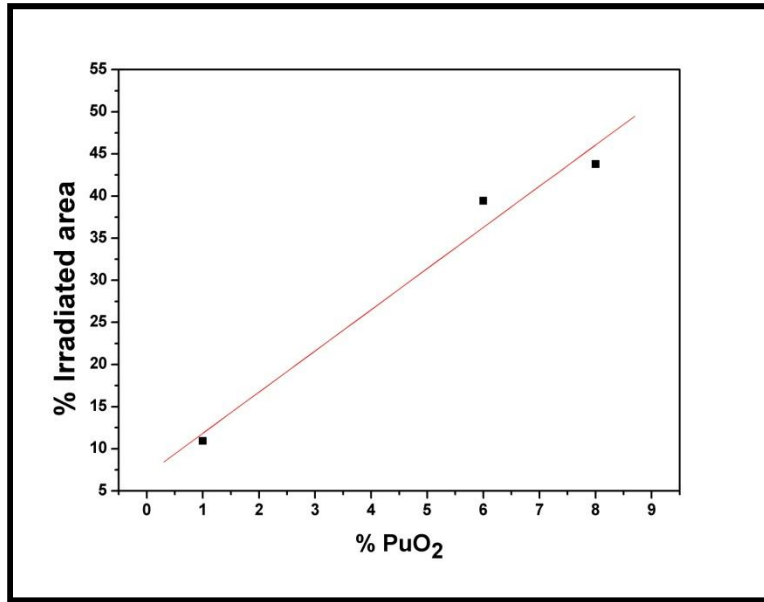


**Figure 5.7: % Irradiated area as a function of PuO<sub>2</sub> content.**

### 5.3.2.2 UV–Vis Spectrophotometry

CR–39 films were irradiated with these three samples under similar conditions and etched along with pristine film under same conditions to eliminate any uncertainty. The UV absorption spectra of the samples with all the three compositions superimposed with that of a pristine film are shown in Figure 5.8. The irradiated films showed a decrease in the peak intensity in the absorption spectra as compared to pristine CR–39 sample. It was observed that an increase in the alpha fluence resulted in a decrease of the intensity of the peak. The decrease in intensity could be attributed to the reduction in the thickness of the film through chemical etching assisted by alpha exposure. Higher the plutonium content in the pellet higher is the alpha irradiation on the film which leads to removal of more material on etching thereby reducing the film thickness and subsequent decrease in absorption of UV radiation.

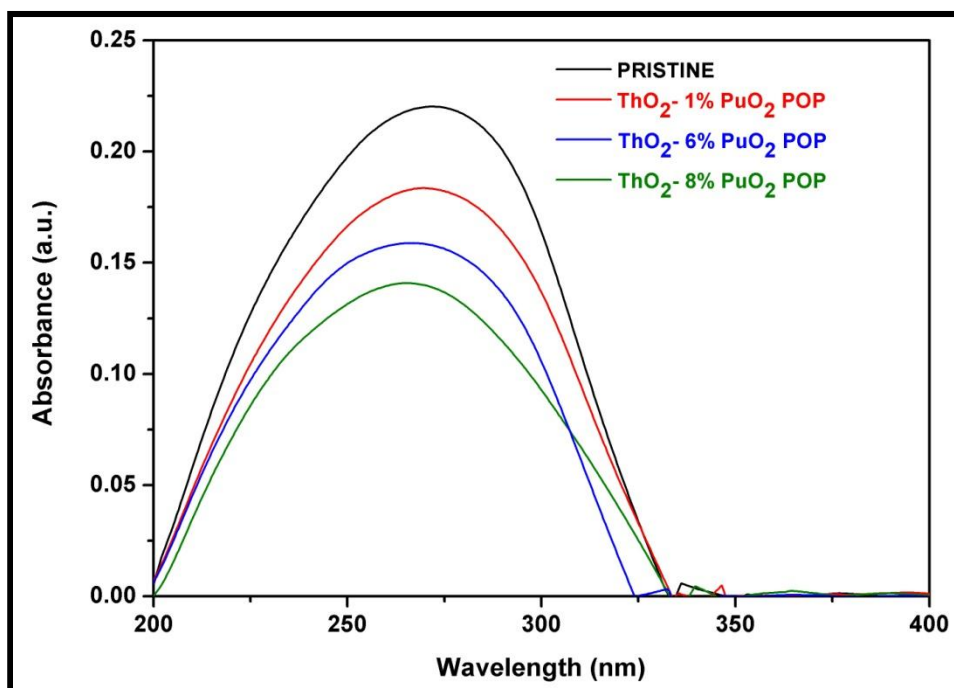


*Figure 5.8: UV Absorbance spectra of different alpha autoradiographs.*

A linear correlation between the peak intensity and the PuO<sub>2</sub> content of the pellet sample could be established. The linear correlation between absorbance values and %PuO<sub>2</sub> was plotted in Figure 5.9 and the best fit derived linear correlation is given in equation (16). The correlation coefficient of the equation was 0.9921.

$$\text{Absorbance} = (-0.008 * \% \text{PuO}_2) + 0.209 \quad (16)$$

Hence this technique could be used for compositional characterization of plutonium bearing fuels within the studied range of plutonium content.

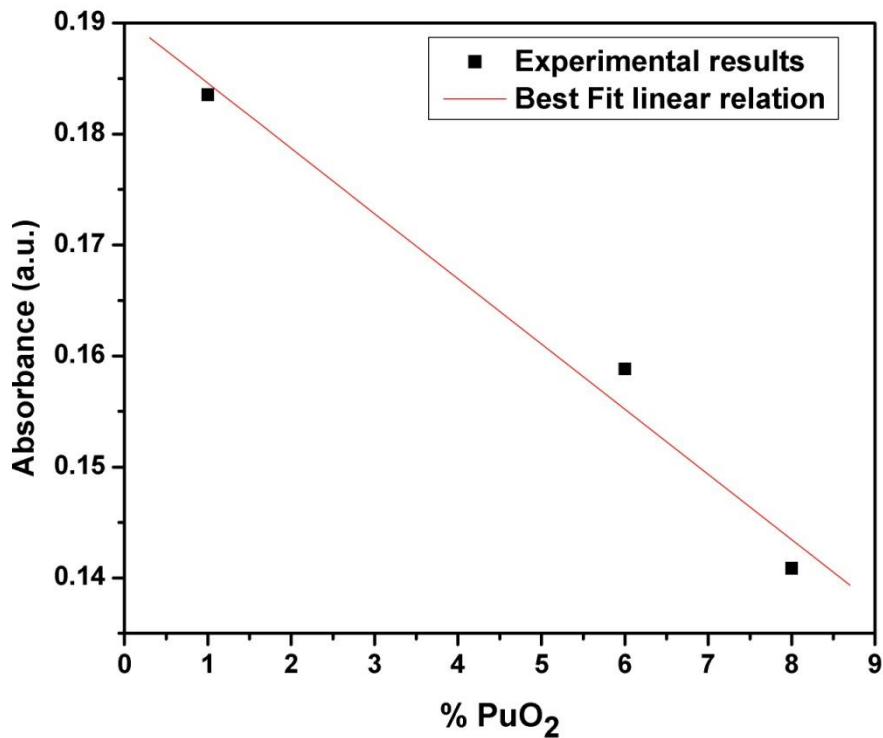


*Figure 5.9: Absorbance as a function of %PuO<sub>2</sub>.*

### 5.3.3 Homogeneity studies

(Th,Pu)O<sub>2</sub> MOX pellets of 1% PuO<sub>2</sub> fabricated through two different routes viz; Coated Agglomerate Pelletisation (CAP) and Powder Pellet route (POP) were analysed for

plutonium homogeneity by image analysis and UV–Vis spectroscopy. As both samples were confirmed to have same PuO<sub>2</sub> content by chemical analysis, their alpha track registration could be compared with each other for assessing homogeneity.

### 5.3.3.1 Image analysis

The alpha autoradiograph images of (Th,1% Pu)O<sub>2</sub> CAP pellets exhibit adjacent regions with high as well as low densities of alpha tracks as shown in Figure 5.1 (a) indicating Pu rich and depleted zones respectively. Images showing the lowest and highest track densities are shown in Figures 5.1 (b) and 5.1(c) respectively. Figure 5.2 shows image of POP pellet. Images of CAP pellet showing different track densities were compared with that of POP pellet. Images was divided into multiple frames, converted into binary images by appropriate thresholding of grey levels and analyzed.

The results of irradiated area percentage of the image data is shown in Table 5.3. Table 5.3 also gives corresponding P% uO<sub>2</sub> calculated by using equation (15).

**Table 5.3 : Results of Alpha autoradiography image analysis of (Th,1% Pu)O<sub>2</sub> samples.**

Type	% Irradiated area	Estimated %PuO <sub>2</sub> (eqn. 15)
CAP dense	24.83	3.876
CAP less dense	1.421	< MDL
POP	10.947	0.815

### 5.3.3.2 UV–Vis Spectrophotometry

Homogeneity studies were carried out on the autoradiograph shown in Figure 5.10 using UV–Vis spectrometry by exposing them to UV light through a mini aperture. The alpha autoradiographs of (Th,Pu)O<sub>2</sub> MOX pellets from POP and CAP process along with a

blank portion (for comparison) is shown in Figure 5.10. The responses of each autoradiograph covering the full circular image are shown in Figure 5.11

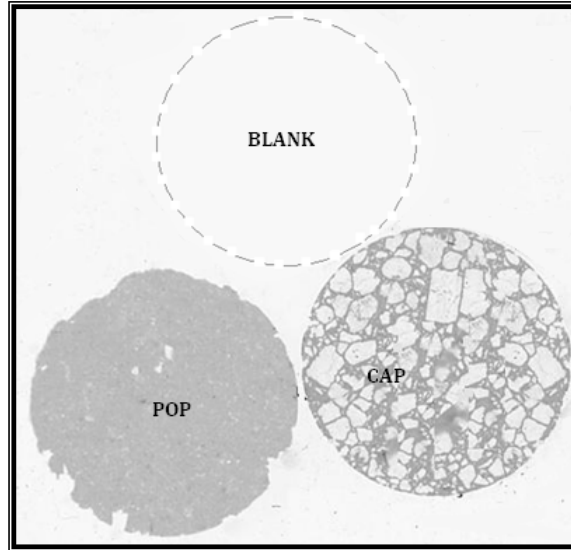


*Figure 5.10 : Alpha autoradiographs of (Th,1%Pu)O<sub>2</sub> pellets and blank portion for comparison.*

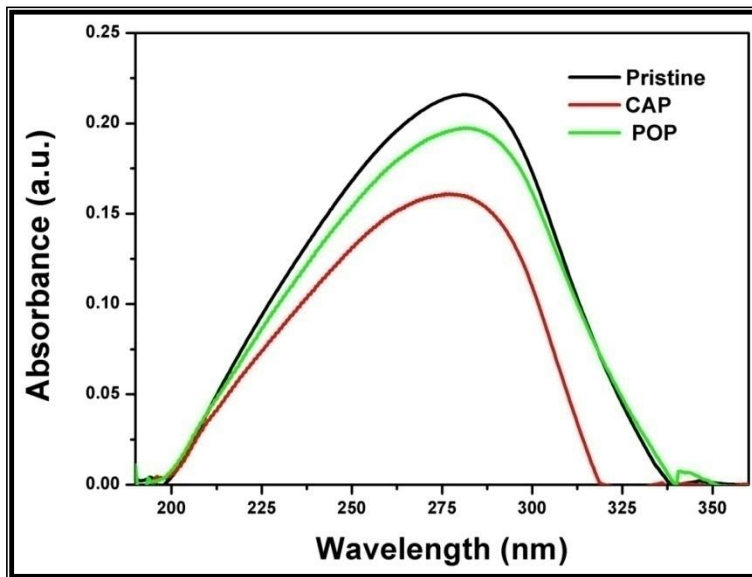


*Figure 5.11: UV absorption spectra of autoradiographs of POP, CAP and blank sample*

. The corresponding PuO<sub>2</sub> % for POP and CAP pellets using equation 16 has been given in Table 5.4.

**Table 5.4: UV-Vis spectrophotometry analysis for PuO<sub>2</sub> content of (Th,1% Pu)O<sub>2</sub> samples.**

Type	Absorbance at Peak Maxima	Estimated %PuO <sub>2</sub>
POP	0.198	1.375
CAP	0.161	6.000

The responses from different portions of the same autoradiograph were acquired for homogeneity through a mini aperture as shown in Figure 5.12. It could be seen that the responses from different portions of the autoradiograph of POP sample were overlapping with each other indicating same optical response of the regions

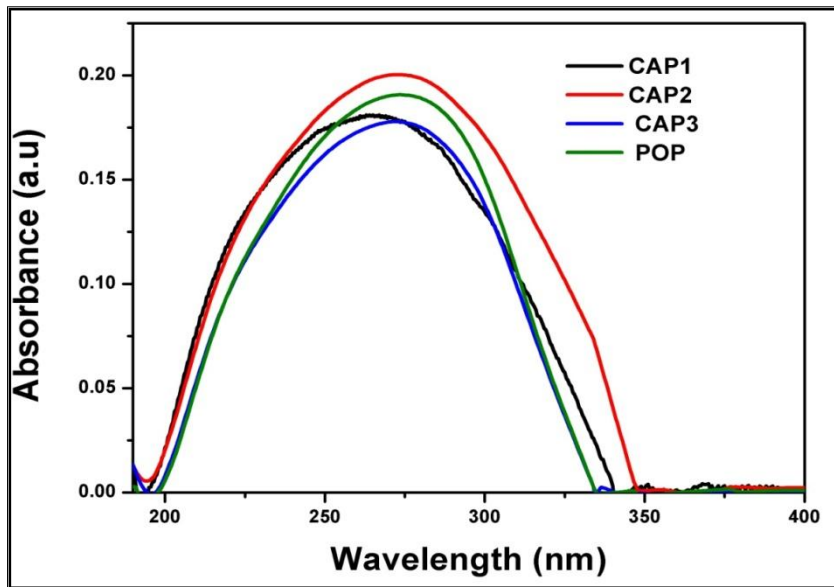


**Figure 5.12: UV-Vis spectro photometric responses of different portions of the alpha autoradiographs of POP and CAP sample using mini focus aperture.**

. The response of different portions of CAP sample was significantly different from each other as well as from that of POP sample as shown in Table 5.5. This indicated that plutonium concentration in the pellet was varying in different parts of the CAP sample. The UV absorption response of CAP autoradiograph revealed regions of higher PuO<sub>2</sub> content as well as lower PuO<sub>2</sub> content with respect to that of the POP sample which was in concurrence with the results of optical image analysis.

**Table 5.5 : UV-Vis spectrophotometry analysis using mini focus aperture of (Th,1% Pu)O<sub>2</sub> samples.**

<b>Type</b>	<b>Absorbance at Peak Maxima</b>	<b>Estimated %PuO<sub>2</sub></b>
CAP – 1	0.1808	3.525
CAP – 2	0.201	1
CAP – 3	0.178	3.875
POP	0.197	1.5

Investigations have revealed that these techniques, image analysis and UV-Vis spectrophotometry have considerable potential to characterize the pellets for homogeneity.

## 5.4 Microstructure

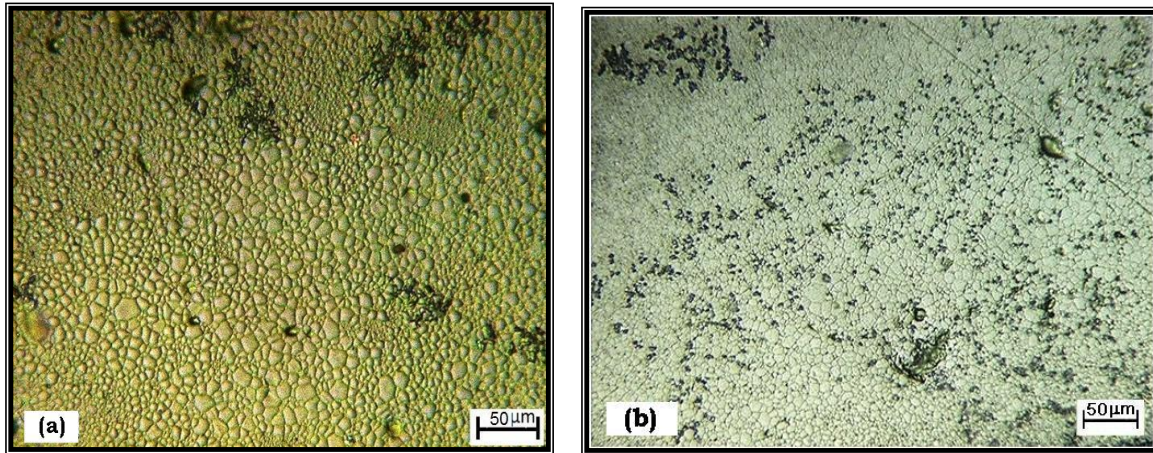


**Figure 5.13 : Microstructure of  $\text{ThO}_2-1\% \text{PuO}_2$  (a) CAP pellet and (b) POP pellet.**

The microstructures of thermally etched sintered pellets fabricated by POP and CAP processes were observed under optical microscope. The microstructures of  $\text{ThO}_2-1\% \text{PuO}_2$  CAP pellet and POP pellet are shown in Figures 5.13 (a) and 5.13 (b) respectively. In POP pellets, the grains were uniformly distributed and the average grain size was found to be  $\sim 6\mu\text{m}$ . Microstructure of CAP pellets showed duplex grain structure consisting of fine grains and large grains distributed in the matrix. The average size of these fine grains ranged between  $2 - 4 \mu\text{m}$  whereas the larger grains size varied between  $6 - 10 \mu\text{m}$ . This microstructure is similar to the microstructure observed in  $(\text{Th,Ce})\text{O}_2$  pellets synthesized by POP and CAP routes.

## 5.5 X-Ray Diffraction

The XRD patterns of  $\text{ThO}_2$ ,  $\text{ThO}_2-1\% \text{PuO}_2$  (POP and CAP) samples and  $\text{ThO}_2-6\% \text{PuO}_2$  (POP) are shown in Figure 5.14. No peak broadening or characteristic peaks of other phases was observed in XRD patterns of the samples fabricated by different processes

indicating the formation of complete solid solution of thoria– plutonia. However, a shift in peak positions of XRD plot of thoria– plutonia samples was noticed compared to that of pure  $\text{ThO}_2$  as shown in Figure 5.15. The shift in the peak position was similar to that observed during XRD analysis of  $(\text{Th,Ce})\text{O}_2$  samples.

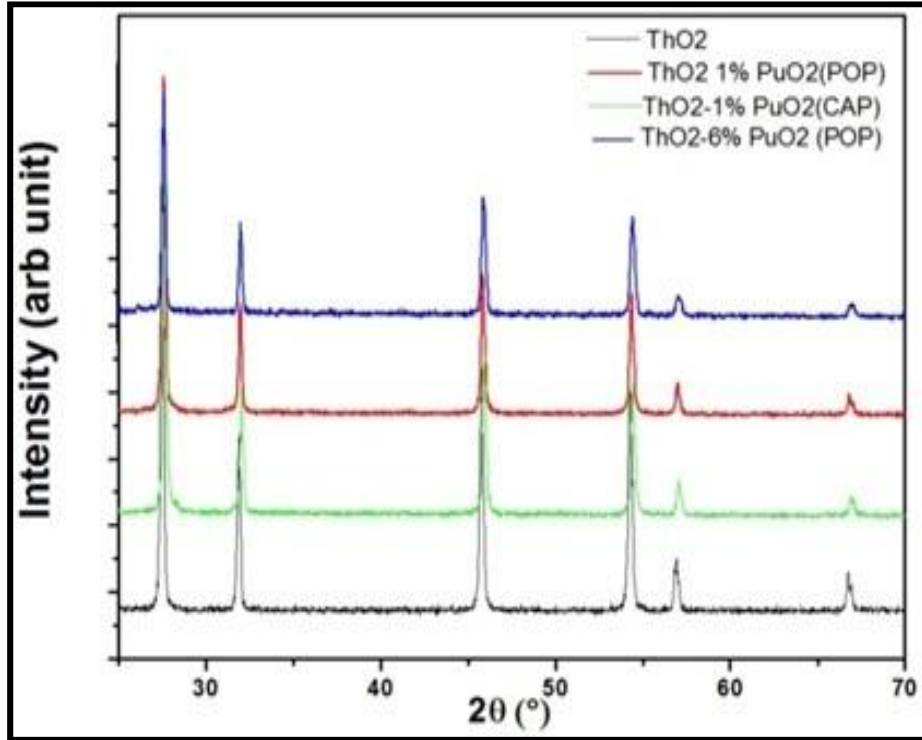


*Figure 5.14: XRD patterns of  $\text{ThO}_2$ ,  $\text{ThO}_2$ –1% $\text{PuO}_2$  (POP and CAP pellets) and  $\text{ThO}_2$ –6% $\text{PuO}_2$  (POP pellets).*

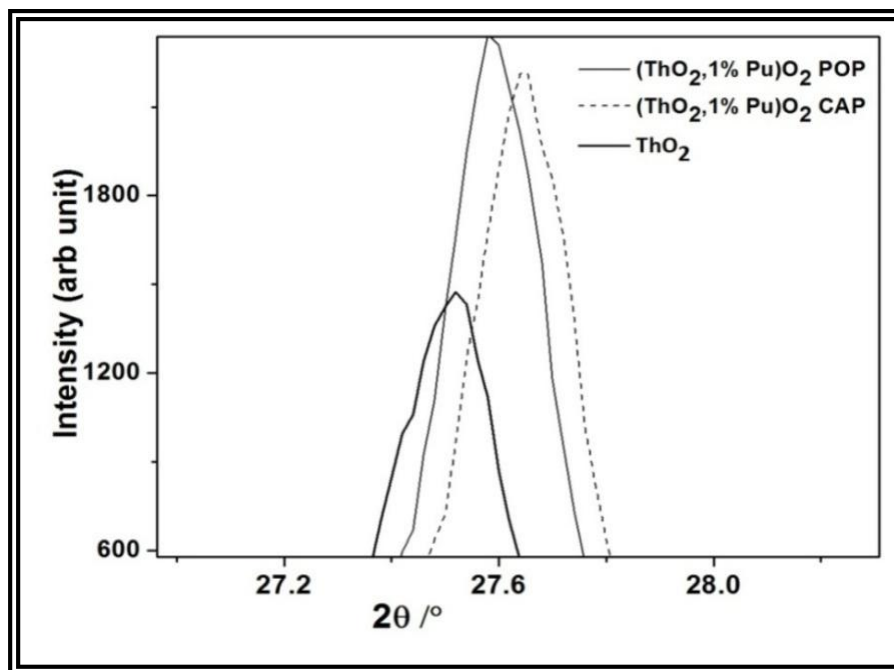


**Figure 5.15: Expanded view of peak positions of XRD patterns of  $(Th,1\%Pu)O_2$  pellets and  $ThO_2$  sintered in reducing atmosphere.**

The characteristic features observed in CAP pellets and POP pellets with respect to their microstructure and plutonium homogeneity are analyzed herein.  $ThO_2$  exhibits very little non stoichiometry compared to  $PuO_2$  [182,183]. Hence the defect concentrations in pure  $ThO_2$  are comparatively less and most are thermally induced at high temperatures compared to oxides of elements which exhibit multiple valencies such as  $PuO_2$ ,  $UO_2$  and  $CeO_2$ . As described in Chapter 2, sintering conditions play an important role during sintering processes as the effect of defect concentrations present in the material could be enhanced or nullified. Therefore,  $PuO_2$  having tendency to be hypo-stoichiometric sinters better in reducing atmosphere than in oxidizing atmospheres. The superior sintering behavior of  $PuO_2$  bearing mixed oxides in reducing atmosphere may be associated with the generation of defect structure as  $PuO_2$  gets reduced to  $Pu_2O_3$ . The deviation from stoichiometry is accompanied

by the formation of Frenkel defects in the oxygen ion sublattice of the crystal [184–189]. The migration energies of  $\text{Pu}^{+3}$  and  $\text{Pu}^{+4}$  ions are 4.11 and 5.95 eV respectively. Hence  $\text{Pu}^{+3}$  ions can move faster than  $\text{Pu}^{+4}$  ions resulting in faster diffusion of the former [190,191]. As  $\text{PuO}_2$  powder has higher specific surface area compared to  $\text{ThO}_2$  powder it provides higher driving force for sintering. It has been established in reported studies that the addition of  $\text{PuO}_2$  aids in sintering of MOX fuel and is primarily responsible for increase in the size of the grains.

From the homogeneity studies carried out in this experimental investigations of  $(\text{Th,Pu})\text{O}_2$  pellets it was evident that alpha autoradiography of sintered pellet provided a clear picture of plutonium distribution in the sintered pellets. From the images of alpha autoradiographs of sintered pellet provides a clear picture of plutonium distribution in the sintered pellets. From the images of alpha autoradiographs of CAP pellet and POP pellet given in Figures 5.1 and 5.2 respectively, it can be seen that POP pellet exhibited homogenous distribution in the pellet as compared to that in CAP pellet. It was clearly evident that the green pellet features were still retained and have not been completely lost during sintering process. The inherent advantage of use of plutonium was it could be utilized as radiotracer species. Therefore, valuable information about extent of its diffusion and content both could be estimated.

The CAP pellets showed different track densities at different locations of the alpha autoradiograph as could be seen in Figure 5.1. The inhomogeneous mixing of starting material in CAP process seemed to have been retained in the pellets even after sintering. In studies on CAP pellets of  $(\text{Th,Ce})\text{O}_2$  (refer Section 4.1) similar result was observed in the microstructure and EPMA studies. It was discussed therein that diffusion of the  $\text{CeO}_2$  second

phase ( $\text{PuO}_2$  in this case) would be dependent on the initial concentration of the material as per Fick's First law of diffusion. The second phase concentration at a particular distance will be affected by the rate of diffusion and time. Therefore, the extent of variation of Pu in the CAP pellet observed in this study as compared to that in CAP pellets of  $(\text{Th,Ce})\text{O}_2$  was different. This was due to lower initial  $\text{PuO}_2$  content of the pellet (1% being coated over the agglomerates), lower diffusion coefficients of cations ( $\text{Th}^{+4}$ ,  $\text{Pu}^{+3}$ ) and insufficient high temperature soak.

The coated regions of  $\text{PuO}_2$  on reduction to  $\text{Pu}_2\text{O}_3$  generate higher defect concentration and diffuse into the adjacent thoria lattice. Concentration gradient of Pu over the diffusion length is understood to be responsible for varied grain growth as observed in the pellet. The plutonium concentration varying across the diffused regions in the pellet was reflected clearly as different track densities in the alpha autoradiographs. As already discussed in the previous above sections, in CAP pellets solid solution formation of varying enrichments of plutonium was present in the pellet matrix. In our studies on  $(\text{Th,Ce})\text{O}_2$  system.

The large grains formation was attributed to higher cerium content and fine grain regions richer in thorium from EPMA studies (refer Figures 4.6 and 4.7). extending the same analogy to  $(\text{Th,Pu})\text{O}_2$  system in this study, higher track density observed in the alpha autoradiograph because of higher Pu content were generated from large grained regions and lesser track density due to lesser Pu content were from fine grains. Therefore, the resultant microstructure of CAP pellet is duplex grain structure with presence of larger grains along with finer grains. Further, density measurements show higher porosity in the CAP pellets

similar to that in (Th,Ce)O<sub>2</sub> system given in Table 4.1. The O/M ratio of the CAP pellet was observed to be higher as compared to POP pellets. Similar observation in studies on (Th,Ce)O<sub>2</sub> system are given in Section 4.5. It could be assigned to the specific surface area of powders affected by the homogeneity in the pellet during sintering. O/M ratio of the pellet was also affected by the % Pu addition as could be observed from Table 5.1.

In POP pellet, good intermixing of thoria and plutonia initial particles ensured close contact between the particles subsequently resulted in good uniformity of plutonium distribution post sintering. This led to development of microstructure of grains with uniform size in the POP pellet. The alpha autoradiograph also showed uniform track density across the pellet as shown in Figure 5.2. In spite of good mixing of starting powders existence of small plutonium agglomerates in the pellet was revealed by alpha autoradiograph.

Preliminary investigation of the pellets for compositional and homogeneity analysis using two different techniques coupled with alpha autoradiography was explored. It could be seen from the Table 5.3 that compositional analysis by image analysis of CAP pellets revealed heterogeneous distribution of plutonium showing PuO<sub>2</sub> content up to 3.8% in some regions and below minimum detectable levels of this technique in some regions.

Image analysis estimated the average Pu composition of POP pellet to 0.815%. Image analysis of the agglomerates showed average composition of 13.26%. The size of these agglomerates being comparatively very small, the overall effect was normalized in analysis of gross sample. Image analysis showed variation of  $\pm 3\%$  of irradiated area in the POP sample indicating better homogeneity of plutonium concentration compared to CAP sample.

However, it could be observed from comparison of results given in Table 5.4 and Table 5.5, the gross pellet absorbance of POP image indicated average PuO<sub>2</sub> composition equivalent to 1.375% whereas sectional compositions indicated 2.25%, the variation was attributed to the Pu agglomerates present in the POP pellet discretely distributed.

Consequently, the X-ray Diffraction studies performed on the CAP and POP samples showed shift in peak maxima to higher angles compared to ThO<sub>2</sub> peak. The diffraction studies indicate contraction of lattice as the Th<sup>+4</sup> ions are substituted by Pu<sup>+4</sup> ions. The lattice parameter of pure thorium dioxide is 5.596 Å and that of pure plutonium dioxide is 5.396 Å. The diffraction peak at (111) of (Th,Pu)O<sub>2</sub> samples of POP and CAP shifted towards the higher diffraction angle proportional to the percentage of PuO<sub>2</sub> in the solid solution. Correlating with our studies on (Th,5%Ce)O<sub>2</sub> described in Section 4.3, similar observations were recorded in XRD investigations where in it was attributed to presence of regions with solid solution of higher Ce composition in the (Th,5%Ce)O<sub>2</sub> CAP pellets. Applying the same analogy in present case, peak shift towards higher angles in CAP sample, as compared to POP sample, shows presence of solid solution with higher plutonium concentration. Though, no secondary peaks characteristic of feed powders could be detected, their presence in the pellet could not also be ruled out.

## 5.6 Passive Gamma Scanning (PGS)

The scans of the experimental pins containing  $\text{ThO}_2$ -1% $\text{PuO}_2$  sintered pellets fabricated by POP and CAP processes are shown in Figures 5.16 and 5.17 respectively.

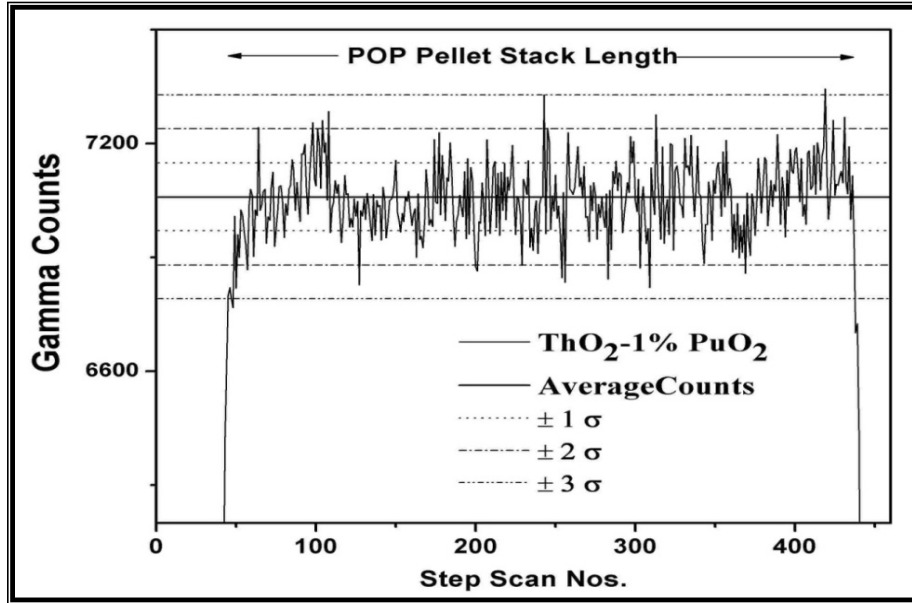


Figure 5.16: Gamma scan of experimental pin containing  $\text{ThO}_2$ -1% $\text{PuO}_2$  POP pellets.

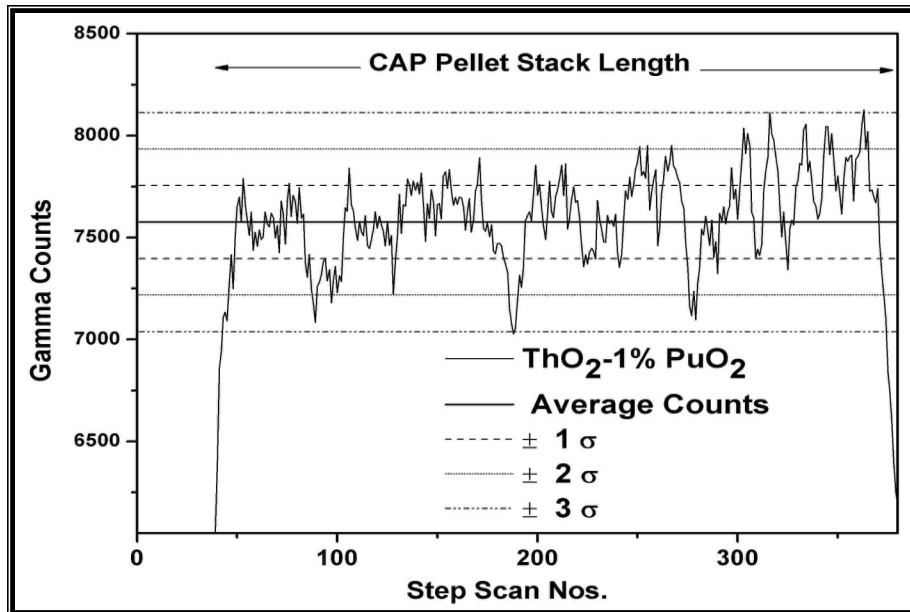


Figure 5.17: Gamma scan of experimental pin containing  $\text{ThO}_2$ -1% $\text{PuO}_2$  CAP pellets.

In the Figures 5.16 and 5.17, the gross gamma count corresponding to single pellet in each pin was recorded because of the slit width and step movement of the pin. The difference in average gamma counts obtained in experimental pins containing CAP pellets (7500) and POP pellets (7000) was due to difference in plutonium composition. The standard deviation of the scan in CAP pin was very high (179) as compared to the theoretically estimated value (87) whereas POP pin presented a scan with standard deviation 87 which was comparable to its theoretically estimated value (83).

All the data points (segmented counts) of CAP gamma scan were within a statistical fluctuation of three standard deviations ( $\pm 3\sigma$ ), whereas it was  $\pm 6\sigma$  for the POP fuel scan. This indicated considerable heterogeneity in the distribution of plutonium in the CAP fuel pin. However, there were data points exceeding the  $\pm 3\sigma$  limits in POP scan indicating presence of localized micro heterogeneity (Pu rich agglomerates) in the pellet. Vrinda Devi et al [192] had conducted studies on (U, Pu)O<sub>2</sub> fuel on wide range of plutonium compositions using similar PGS set up and reported detection of compositional variation within  $\pm 5\%$  and also agglomerates using annular set up. Passive gamma scanning studies revealed that the gross homogeneity in POP pellets was better compared to CAP pellets. The contribution of agglomerates in increasing the gross alpha counts of POP pellets ( $> +3\sigma$ ) in high background of gamma was detected.

From these investigations it could be observed on comparison that surrogate studies conducted on (Th,Ce)O<sub>2</sub> system were valid for (Th,Pu)O<sub>2</sub> system. The pellets of CAP and POP in both the systems showed similar characteristics with respect to O/M ratio, homogeneity (micro and macro) and microstructure.

## 5.7 Thermal Properties

The relevance of this study could be understood from the dependence of performance of a nuclear fuel on its thermophysical properties, especially their variation with temperature. Thermal expansivity of the fuel is responsible for the thermal stresses generated during irradiation due to reduction in fuel–clad gap and most importantly, affects the heat transport due to lowering of fuel density. Thermal diffusivity and thermal conductivity are important for understanding the heat transport characteristics of the fuel. They govern the fuel operating temperatures and have indirect influence on the centerline temperature of the fuel and fission gas release.

Thermal property investigation were carried out on sintered pellets of (Th,1%Pu)O<sub>2</sub> fabricated by CAP and POP routes and (Th,6%Pu)O<sub>2</sub> reference pellet made by POP route. The details of the sample pellets are given in Table 5.6.

*Table 5.6 : Characteristics of (Th,Pu)O<sub>2</sub> experimental sintered pellets.*

<b>Pellet composition</b>	<b>Process</b>	<b>Density (%T.D)</b>	<b>Porosity (%T.D)</b>	<b>O/M</b>	<b>Th (%)</b>	<b>Pu (%)</b>	<b>Chemical Impurities (ppm)</b>
ThO <sub>2</sub> –1%PuO <sub>2</sub>	POP	92.9	7.1	1.978–1.998	86	0.97	<1200
ThO <sub>2</sub> –1%PuO <sub>2</sub>	CAP	92.7	7.3	1.997–1.999	86	0.96	<1200
ThO <sub>2</sub> –6%PuO <sub>2</sub>	POP	93.2	6.8	1.978 –1.987	81.7	5.88	<1200

### **5.7.1 Thermal Expansion**

In nuclear reactors, some gap is kept between the fuel pellets and clad. The difference between the coefficients of thermal expansion of the fuel and the cladding determines whether the initial fuel–cladding gap decreases or increases when the fuel element is brought to power [2]. If the initial gap is small and the fuel expands more than the cladding, contact might be established between the fuel pellets and clad which may result in probable fuel failure. On the other hand, if the cladding expands more than the fuel and the gap is enlarged, heat conduction through the fuel–cladding gap will be low and the centre line temperature of the fuel will increase and the probability of fuel melting increases. Therefore it is important to generate thermal expansion data by dilatometer is required to decide the pellet clad gap during fuel design.

#### **5.7.1.1. Experimental by Dilatometry**

The thermal expansion of  $\text{ThO}_2\text{--}1\%\text{PuO}_2$  (POP and CAP) and  $\text{ThO}_2\text{--}6\%\text{PuO}_2$  (POP) reference pellets measured using dilatometry in the temperature range from room temperature to 1773 K are shown in Figure 5.18

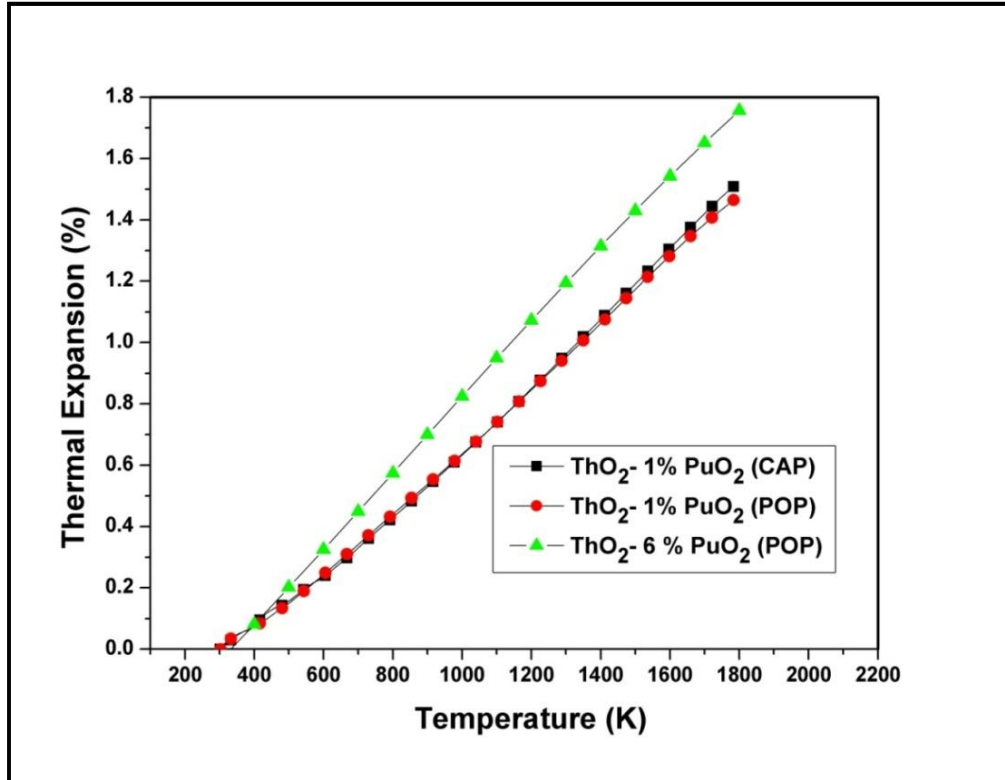


**Figure 5.18: Thermal Expansion plots for  $\text{ThO}_2\text{-1}\%\text{PuO}_2$  (sintered pellets fabricated by CAP and POP process) and  $\text{ThO}_2\text{-6}\%\text{PuO}_2$  POP pellet measured experimentally using dilatometer.**

The experimental thermal expansion data are least squares fitted to give a third degree polynomial equation for each sample. The fitting errors for all these compositions are within  $\pm 1\%$ . The recommended percentage thermal expansion data in the temperature range from 300 to 1773 K for CAP and POP pellets are given below (T in K):

$\text{ThO}_2\text{-1}\%\text{PuO}_2$  (POP):

$$(\Delta L/L_0) \times 100 (\%) = -0.1670 + 4.4503 \times 10^{-4} * T + 4.5139 \times 10^{-7} * T^2 - 9.6473 \times 10^{-11} * T^3 \quad (17)$$

$\text{ThO}_2\text{-1}\%\text{PuO}_2$  (CAP):

$$(\Delta L/L_0) \times 100 (\%) = -0.1909 + 5.1705 \times 10^{-4} * T + 4.0987 \times 10^{-7} * T^2 - 9.9212 \times 10^{-11} * T^3 \quad (18)$$

ThO<sub>2</sub>-6wt.%PuO<sub>2</sub> :

$$(\Delta L/L_0) \times 100 (\%) = -0.1819 + 5.6429 \times 10^{-4} * T + 3.5816 \times 10^{-7} * T^2 - 6.8467 \times 10^{-11} * T^3 \quad (19)$$

The experimentally measured thermal expansion coefficients of the sample pellets in the temperature range 300–1773 K are given in Table 5.7.

**Table 5.7 : Experimentally measured thermal expansion coefficients (Th,Pu)O<sub>2</sub> MOX .**

<i>Thermal expansion coefficients (10<sup>-6</sup> K<sup>-1</sup>)</i>	<i>Remarks</i>
10.17(300–1773 K)	Dilatometry, POP, experimental, ThO <sub>2</sub> -1wt%PuO <sub>2</sub>
10.28 (300–1773 K)	Dilatometry, CAP, experimental, ThO <sub>2</sub> -1wt%PuO <sub>2</sub>
11.99 (300–1773 K)	Dilatometry, POP, experimental, ThO <sub>2</sub> - 6wt%PuO <sub>2</sub>

### 5.7.1.2 Theoretical using MD Simulation

In order to further analyze the effect of defects on thermal expansion behavior of Th<sub>1-x</sub>Pu<sub>x</sub>O<sub>2</sub> MOX for similar composition was performed using MD studies in manner similar to as described in Section 4.8.

The experimentally measured and MD calculated thermal expansion coefficients ( $\alpha$ ) are listed in Table 5.8 along with other literature data.

**Table 5.8 : MD calculated and experimentally measured thermal expansion coefficients of (Th,Pu)O<sub>2</sub> Experimentally measured thermal expansion coefficients (Th,Pu)O<sub>2</sub> MOX compared with available experimental data in the literature.**

Thermal expansion coefficient (10 <sup>-6</sup> K <sup>-1</sup> )	Remarks
10.45 (300–1800 K)	MD , Th <sub>0.96875</sub> Pu <sub>0.03125</sub> O <sub>2</sub>
10.55 (300–1800 K)	MD , Th <sub>0.9375</sub> Pu <sub>0.0625</sub> O <sub>2</sub>
10.70 (300–1800 K)	MD , Th <sub>0.90675</sub> Pu <sub>0.093275</sub> O <sub>2</sub>
10.17 (300–1773 K)	Dilatometry, POP, ThO <sub>2</sub> –1wt%PuO <sub>2</sub>
10.28 (300–1773 K)	Dilatometry, CAP, ThO <sub>2</sub> –1wt%PuO <sub>2</sub>
11.99 (300–1773 K)	Dilatometry, POP, ThO <sub>2</sub> –6wt%PuO <sub>2</sub>
9.35 (293–1123 K)	Dilatometry, Th <sub>0.96</sub> Ce <sub>0.04</sub> O <sub>2</sub> , 83% T.D [156]
9.76 (293–1173 K)	Th <sub>0.96</sub> Ce <sub>0.04</sub> O <sub>2</sub> , HTXRD [156]
9.35 (293–1123 K)	Dilatometry, Th <sub>0.92</sub> Ce <sub>0.08</sub> O <sub>2</sub> , 83% T.D [156]
9.96 (293–1173 K)	Th <sub>0.92</sub> Ce <sub>0.08</sub> O <sub>2</sub> , HTXRD [156]

From the Table 5.7, it can be seen that the coefficient of thermal expansion for ThO<sub>2</sub> –1%PuO<sub>2</sub> pellets in the temperature range 300–1773 K were found to be 10.17 x 10<sup>-6</sup>/K and 10.28 x 10<sup>-6</sup>/K pellets made by POP and CAP process respectively whereas in same temperature range coefficient of thermal expansion for ThO<sub>2</sub> –6%PuO<sub>2</sub> was 11.99 x 10<sup>-6</sup>/K. The coefficient of thermal expansion of ThO<sub>2</sub> determined in our present study was found to be 9.99 x 10<sup>-6</sup>/K in the same temperature range (refer Table 4.4 in Chapter 4). From our MD

thermal expansion studies it was found that the thermal expansion coefficient of (Th,Pu)O<sub>2</sub> increases with an increasing PuO<sub>2</sub> content. With incorporation of PuO<sub>2</sub> which has higher thermal expansion coefficient and is also responsible for the decrease in the lattice parameter of the system causes increased interaction between the phonons and atoms. Due to this combined effect, the net resultant is increase in coefficient of thermal expansion of (Th,Pu)O<sub>2</sub>, the increase is dependent on the PuO<sub>2</sub> addition. Similar observations have been reported on (Th,Ce)O<sub>2</sub> system [193, 194].

The CAP pellet exhibited a deviation from this trend which could be attributed to higher porosity compared to POP pellet. In our previous analysis in preceding chapter on (Th,Ce)O<sub>2</sub>, it could be clearly observed that the CAP pellets possessed large pores which were closely located and also inhomogeneously distributed in the pellet might have been responsible for accommodating the expansion to some extent and thereby reducing the effect. The coefficients of thermal expansion for ThO<sub>2</sub>-6%PuO<sub>2</sub> pellets in the temperature range 300-1773K was found to be  $11.99 \times 10^{-6}/K$  whereas coefficient of thermal expansion for ThO<sub>2</sub> -6%UO<sub>2</sub> was  $10.098 \times 10^{-6}/K$  [156]. It could be seen that incorporation of U in Th lattice had lesser effect compared to Pu incorporation because of difference in coefficient of thermal expansion and higher lattice parameter. The MD calculated  $\alpha$  is always greater than the HTXRD and dilatometry measured  $\alpha$  value. This can be attributed to the fact that our MD calculations are performed on a model system with homogeneous distribution of PuO<sub>2</sub> in ThO<sub>2</sub> matrix and our calculations are not affected from porosity, impurity effects, etc.

In this context, it is relevant to mention that in our studies, the difference between the CTE values of (Th,Pu)O<sub>2</sub> pellets fabricated by different routes was not very significant and

that was clearly evident in Figure 5.18. To understand the effect of thermal expansion, considering a solid pellet of 10 mm diameter of  $(\text{Th},1\%\text{Pu})\text{O}_2$  in reactor at a high temperature of  $2000^\circ\text{C}$  will expand by 0.2034 mm in the case of POP pellet and 0.2056 mm in the case of CAP pellet. The difference in diametrical expansion of  $2.2\ \mu\text{m}$  between the two pellets is quite negligible and at lower temperatures the difference would be correspondingly smaller. From our studies, it could be affirmed that the inhomogeneity exhibited by the CAP pellets has inconsequential or negligible effect on contribution thermal expansion of pellet even at very high temperatures and for the purpose of fuel design could be considered same as POP pellet.

### **5.7.2 Thermal diffusivity and Thermal Conductivity**

The experimental thermal diffusivity data of  $\text{ThO}_2 - 1\%\text{PuO}_2$  pellets made by CAP and POP processes as a function of temperature is shown in Figure 5.19. The corresponding thermal conductivity of the above samples corrected for 95% T.D. are shown in Figure 5.20. The MD calculated thermal conductivity of pure  $\text{ThO}_2$  and  $\text{Th}_{0.9375}\text{Pu}_{0.0625}\text{O}_2$  MOX as a function of temperature (300–2000 K range) are shown in Figure 5.21 along with our experimentally measured values of  $\text{ThO}_2$  and  $\text{ThO}_2 - 6\%\text{PuO}_2$  MOX (873–1513 K temperature range) and previously reported experimental values by Cozzo et al [127].

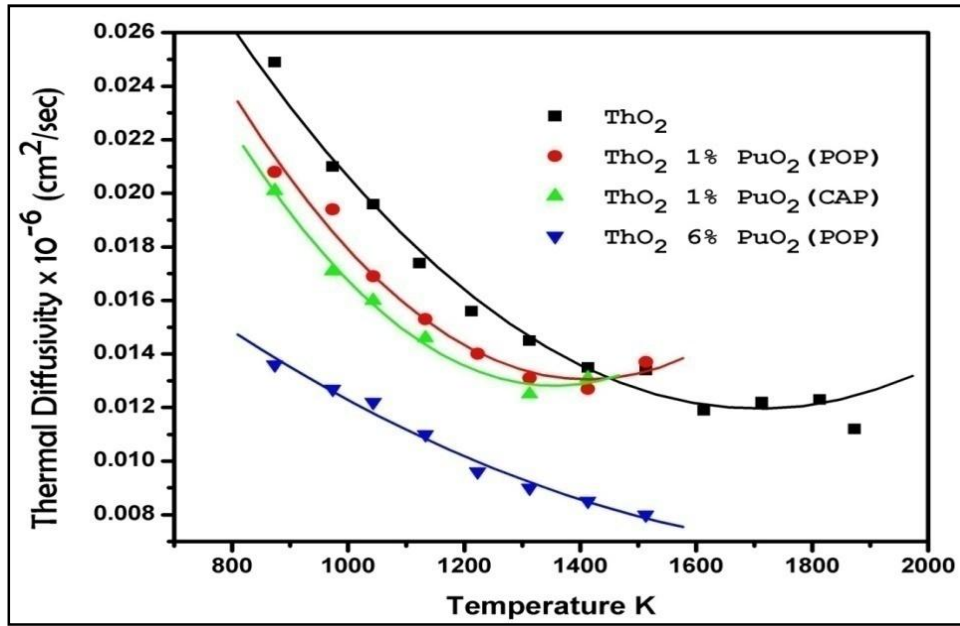


Figure 5.19: Thermal diffusivity plots for  $\text{ThO}_2$ ,  $\text{ThO}_2$ -1% $\text{PuO}_2$  sintered pellets fabricated by CAP and POP process and  $\text{ThO}_2$ -6% $\text{PuO}_2$  POP pellets.

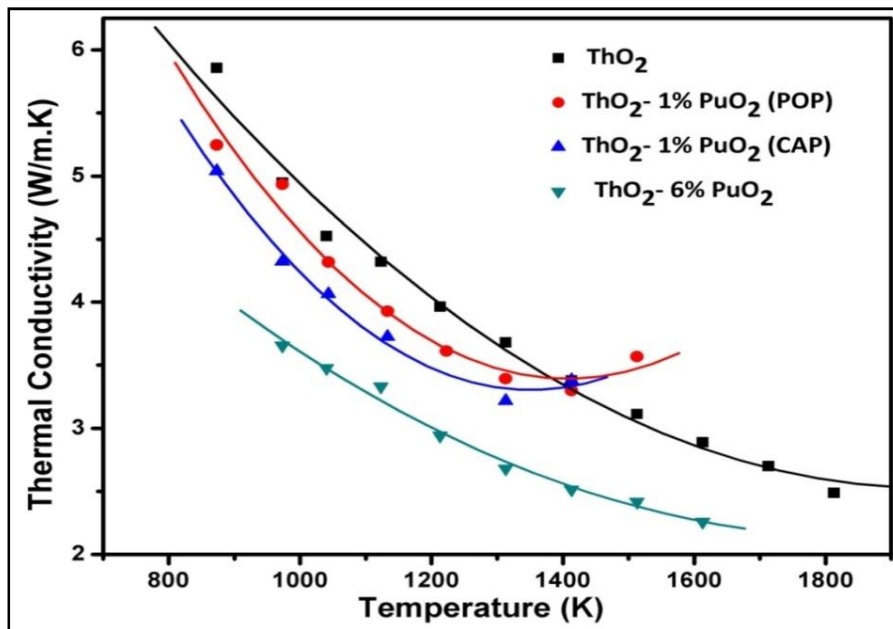
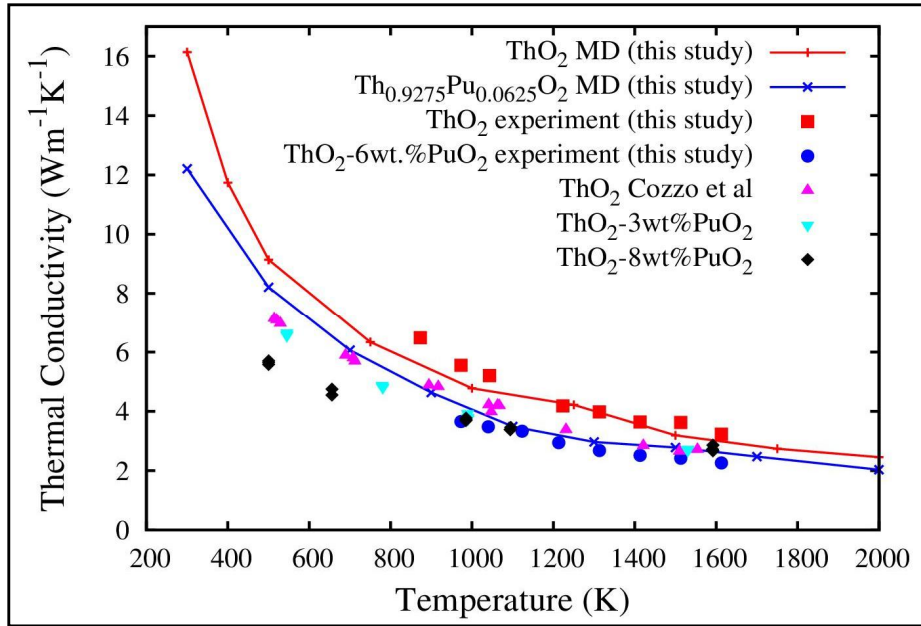


Figure 5.20: Thermal conductivity plots for  $\text{ThO}_2$ ,  $\text{ThO}_2$ -1% $\text{PuO}_2$  sintered pellets fabricated by CAP and POP process and  $\text{ThO}_2$ -6% $\text{PuO}_2$  POP pellet.



**Figure 5.21 :** Thermal conductivity calculated by MD simulations as a function of temperature for  $\text{ThO}_2$  and  $\text{Th}_{0.9275}\text{Pu}_{0.0625}\text{O}_2$  compared with our experimental values of  $\text{ThO}_2$  and  $\text{ThO}_2$ -6 wt%  $\text{PuO}_2$  POP pellet (95% T.D). These values are also compared with reported values of  $\text{ThO}_2$ ,  $\text{ThO}_2$ -3 wt% and  $\text{ThO}_2$ -8 wt%  $\text{PuO}_2$  by Cozzo et al [127]. Solid lines are only for visual guidance.

**Table 5.9 :** Constants A and B of the equation 14,  $1/k = A+BT$ , for  $\text{ThO}_2$  and  $(\text{Th,Pu})\text{O}_2$  MOX calculated from MD simulations and experimental measurements.

Sample	A(m.K/W)	B(m/W)x10 <sup>-4</sup>
$\text{ThO}_2$ , MD calculated	0.003152	1.88
$\text{Th}_{0.9375}\text{Ce}_{0.0625}\text{O}_2$ , MD calculated	0.004506	2.24
$\text{ThO}_2$ , Experimental	0.02	1.34
$\text{ThO}_2$ -1wt% $\text{PuO}_2$ (POP), Experimental	0.01728	2.00
$\text{ThO}_2$ -1wt% $\text{PuO}_2$ (CAP), Experimental	0.01541	2.20
$\text{ThO}_2$ -6wt% $\text{PuO}_2$ (POP), Experimental	0.00424	2.74
$\text{ThO}_2$ , Cozzo et al [127]	0.010	2.30
$\text{ThO}_2$ -3wt% $\text{PuO}_2$ , Cozzo et al [127]	0.035	2.20
$\text{ThO}_2$ -8wt% $\text{PuO}_2$ , Cozzo et al [127]	0.099	1.69

It was observed that both CAP and POP pellets exhibited similar thermal diffusivities and decreased with increasing temperatures. Experimental observations on conductivity studies show that the pellets fabricated by CAP process exhibited slightly lower thermal diffusivity and conductivity compared to pellets fabricated by conventional route (POP) in general. Pore characteristics (bigger pore sizes, distribution of pores along the grain boundaries and inter-connectivity of pores) typical of CAP pellets [24, 25] and inhomogeneity in the pellet could be responsible for observed decrease in thermal conductivity compared to POP pellets with uniform distribution of small pores and Pu.

Moreover, thermal diffusivity values of CAP pellet are 5% lower than POP pellets in the 873–1513 K temperature range even though porosity content and O/M ratio of the POP and CAP pellets are almost similar. The difference can be attributed to the inhomogeneous distribution of PuO<sub>2</sub> in the ThO<sub>2</sub> matrix. The reduction in thermal diffusivity values of ThO<sub>2</sub>–1%PuO<sub>2</sub> (POP pellets) compared to pure ThO<sub>2</sub> is 20% at temperature 873 K and 7% at 1413 K. Similarly, the reduction in thermal diffusivity values of ThO<sub>2</sub>–6%PuO<sub>2</sub> (POP pellets) compared to pure ThO<sub>2</sub> is 46% at temperature 873 K and 37% at 1413 K.

Maxwell–Eucken equation described in section 4.12 was used to incorporate porosity correction draw on MD calculated values obtained for 100% T.D and compare with the reported experimental data. It was found that 5% porosity incorporated MD calculated thermal conductivity ( $\kappa$ ) is lower compared to  $\kappa_0$  by  $(1 - 0.92683) \times 100\% = 7.32\%$  at all temperature. The MD calculated values decreases with an increase of temperature, which reflects lowering of thermal conductivity by the phonon–phonon scattering. Moreover, our MD calculated values for ThO<sub>2</sub> are overestimation of experimental results of Cozzo et al

[127] in the whole temperature range. These MD values are underestimation of our laser flash measured values in the 900–1100 K range but matches very well (with in  $\pm 1\%$ ) in the 1200–1600 K temperature range. Our MD calculated values for  $\text{Th}_{0.9375}\text{Pu}_{0.0625}\text{O}_2$  MOX overestimates experimental results of Cozzo et al [127] in the 500–900 K temperature range. But in the high temperature range ( $>1000$  K) MD calculated values matches very well (with in  $\pm 1\%$ ) with our laser–flash measured values for  $\text{ThO}_2$ –6% $\text{PuO}_2$  and previous experimental values for  $\text{ThO}_2$ –3% $\text{PuO}_2$  and  $\text{ThO}_2$ –8% $\text{PuO}_2$  [127]. Importantly, significant decrease in MD calculated thermal conductivity values as a result of Pu addition in  $\text{ThO}_2$  lattice, particularly at low temperatures, is due to phonon mean free path reduction from lattice–phonon scattering associated with non–uniform cation sublattice. However, at high temperature decrease in MD calculated values upon Pu addition is less as phonon mean free path at high temperatures is governed by the phonon–phonon scattering mechanism dominantly.

One pair of **A** and **B** constants of equation 17 can be obtained for each composition of solid solution by polynomial fitting of the thermal resistivity (inverse of thermal conductivity) versus temperature data. Table 5.9 shows the determined values of **A** and **B** constants from our MD calculated and experimentally measured thermal conductivity variation as a function of temperature along with those values as determined by Cozzo et al [127].

From the thermal property studies, it could be observed that  $\text{ThO}_2$ –1% $\text{PuO}_2$  showed higher thermal conductivity than  $\text{ThO}_2$  at temperatures greater than 1400K.

Previous reports on thermal conductivity of  $(\text{Th,Pu})\text{O}_2$  are very limited. Basak et al [124] studied thermal conductivity of  $\text{ThO}_2$ –4wt.%  $\text{PuO}_2$  over a temperature range between 923 K

and 1773 K. Cozzo et al [127] determined thermal diffusivity and conductivity of  $\text{Th}_{1-x}\text{Pu}_x\text{O}_2$  MOX ( $x = 0.0, 0.03, 0.08, 0.3$  and  $1.0$ ) over a temperature range between 500 K and 1600 K. Das and Bharadwaj [195] compared thermal conductivity data reported by Cozzo et al [127] and Basak et al [124] and it could be seen that they were in complete disagreement. Our experimental results are also in disagreement with values reported by Basak et al [124] as they were higher than even pure  $\text{ThO}_2$  and hence were not included in our evaluation and comparison. Our thermal conductivity studies on  $\text{ThO}_2 - 1\% \text{PuO}_2$  and  $\text{ThO}_2 - 6\% \text{PuO}_2$  were in good agreement with thermal conductivity values reported by Cozzo as evident from Table 5.9.

It is evident from Table 5.9 that our MD calculated  $B$  constants are almost independent of composition of solid solutions which is in accordance with experimental measurements of Cozzo et al [127]. On the other hand, the values of constant  $A$  continuously increase with  $\text{PuO}_2$  concentration in agreement with the experimental trend. This is attributed to the scattering of the phonons occurring due to mass and size difference between substituted and host atoms.

The thermal conductivity of CAP pellet and POP pellet at 873 K was  $5.03 \text{ Wm}^{-1}\text{K}^{-1}$  and  $5.24 \text{ Wm}^{-1}\text{K}^{-1}$  respectively. The difference between thermal conductivity of these two pellets was  $< 4\%$  was marginal and further reduced with increased temperature.

In this context it is very important to discuss the effect of increase in centerline temperature of the pellet due to decrease in thermal conductivity for same linear heat rating for design purposes. In normal conditions, thermal conductivity and linear power determine the peak fuel operating temperature. Under the accident conditions, the thermal conductivity

of the fuel determines the maximum permissible linear rating,  $\lambda_{\max}$ , if central melting is to be avoided. If the thermal conductivity is low, the temperature gradient in the radial direction of the fuel pellet is large causing high temperature at the central part of the fuel pin [74, 196, 197]. The correlation between thermal conductivity,  $\mathbf{k}$ , the centre temperature of fuel  $T_c$  and the surface temperature  $T_s$ , is given in equation 20.

$$\lambda = 4\pi \int_{T_s}^{T_c} \mathbf{k} \cdot dT \quad (20)$$

where,  $\lambda$ , is the linear rating.

Considering the thermal conductivity values obtained by ThO<sub>2</sub>-1%PuO<sub>2</sub> POP and CAP pellets in this study, the increase in centreline temperature can be predicted. For instance, a pellet of ThO<sub>2</sub>-1%PuO<sub>2</sub> POP with 10mm diameter having a surface temperature and centreline temperature of 500°C and 1500°C respectively for a particular linear heat rating, the change in centreline temperature by replacement of POP pellet with CAP pellet was calculated to be about 40°C. This shows that thermal performance of CAP pellet will be quite similar to that of POP pellet.

Considering the other aspects of thermal conductivity of nuclear fuel being an important parameter to understand the performance of the fuel pins under irradiation [124, 195] as it influences almost all important processes such as fission gas release, swelling, grain growth etc. and limits the linear power [198, 199] in regard to present study. It was evident from our studies that CAP pellets have pores preferentially located at the sites of large grains which are rich in fissile material (preferential sites of nuclear fissions). Due to close proximity of pores with fission sites, they will act as sinks during diffusion of the

fission gas atoms, thereby, accumulating them and reducing the fission gas release. Similarly during irradiation swelling of fuel pellets these pores will help in accommodating it to some extent [13, 25, 26].

Correlating the wide variance in Pu distribution and thermal conductivity, it could be inferred that heterogeneous distribution of plutonium observed in the CAP pellets did not significantly impact the thermal conductivity of the fuel and that phonon–phonon interaction (Umklapp process) is the major factor which influences the thermal conductivity of the material at higher temperatures.

Critical evaluation of the thermal properties of the pellets and extrapolation of their behavior at high temperature conditions indicate that the CAP pellets would exhibit better in–reactor behavior due to inherent characteristics of the pellets such as presence of large grain with pores as well as fine grains and higher O/M as compared to POP pellets.

## **5.8 Summary**

The conclusions drawn from validation studies on (Th,Pu)O<sub>2</sub> MOX system for their various properties are given below:

- i. Microhomogeneity of plutonium in ThO<sub>2</sub>–1%PuO<sub>2</sub> MOX fuel fabricated through CAP process was found to be much lower than that attained by POP process of fabrication.
- ii. Alpha autoradiography coupled with other techniques such as image analysis, UV–Vis and photoluminescence spectrophotometry could be used for compositional and homogeneity evaluations.

- iii. Passive Gamma Scanning revealed variation in count rates from CAP pellets was higher compared to that from POP process showing presence of higher compositions. PGS could also detect agglomerates in the POP pellets.
- iv. The coefficient of thermal expansion of  $\text{ThO}_2 - 1\% \text{PuO}_2$  pellets made by POP and CAP process was  $10.17 \times 10^{-6}/\text{K}$  and  $10.28 \times 10^{-6}/\text{K}$  pellets respectively in the temperature range 300–1773 K.
- v. Marginal difference of  $< 4\%$  was observed between the thermal conductivity of CAP pellet ( $5.03 \text{ Wm}^{-1}\text{K}^{-1}$ ) and POP pellet ( $5.24 \text{ Wm}^{-1}\text{K}^{-1}$ ) at 873 K which further reduced with increased temperature. Both experimental and MD studies conclude that heterogeneous distribution of plutonium observed in the CAP pellets did not significantly impact the thermal conductivity of the fuel.

From the studies and investigations carried out, it could be seen that the CAP pellets of  $(\text{Th,Pu})\text{O}_2$  MOX similar to  $(\text{Th,Ce})\text{O}_2$  MOX as mentioned in Section 4.12 possessed similar properties and characteristics and were comparable to POP pellets. Therefore, CAP and POP pellets of similar compositions and are expected to perform similarly during in reactor operation.

## CHAPTER 6. CHARACTERIZATION STUDIES ON (Th,U)O<sub>2</sub> SYSTEM

### 6.1 Introduction

In Chapter 4, cerium was used as surrogate for plutonium as their physical and chemical properties were matching. However, due to difference in their densities, study with CeO<sub>2</sub> will not exactly replicate the changes in the coating characteristics on the thoria agglomerates. This will lead to incorrect enrichment of the fuel. For this purpose UO<sub>2</sub>, which has powder density close to PuO<sub>2</sub> (refer Table 3.1) has been used in the present work for some of the studies. Hence experimental studies using UO<sub>2</sub> as surrogate for PuO<sub>2</sub> to simulate the specific gravity of PuO<sub>2</sub> powder were conducted. The study was envisaged using U<sub>3</sub>O<sub>8</sub> in place of UO<sub>2</sub> for controlling the O/M of the UO<sub>2</sub> powder which might be affected due to moisture pick up in storage conditions, useful as sintering aid and also to correlate with earlier studies. (Th,Pu)O<sub>2</sub> pellets have tendency of being hypo-stoichiometry (O/M ratio < 2) as observed from the previous study and sintering of such material in reducing atmosphere is favorable as previous reported studies using U<sub>3</sub>O<sub>8</sub> for (Th,U)O<sub>2</sub> pellets by sintering in air concluded that the pellets possessed hyper-stoichiometry (O/M > 2) because of incomplete decomposition even at high temperatures Therefore it would be relevant to conduct the present study in reducing atmosphere as an extension to the present research work to investigate any major deviations from present observations and also address the unresolved issues of previous reported studies. This study has two pronged approach, firstly, for estimating the maximum achievable plutonium or uranium enrichment by CAP process (similar powder densities) and corresponding homogeneity in the pellet and secondly,

relevant for fabrication of pellets with material having hyper-stoichiometric tendency such as  $U^{233}O_2$ .

This chapter is mainly divided into two sections. The first section deals with study on pellets fabricated using pure oxide powders by both POP and CAP routes and sintered in reducing atmosphere. The pellets were evaluated for their physical, metallurgical, chemical and thermal properties at maximum loading for comparison. The study shall focus on the CAP pellet characteristics investigation and compared to previously studies on POP pellets of relevant compositions.

The second section deals with the studies conducted using  $ThO_2$  powder with co-precipitated  $(Th,U)O_2$  mixed oxide powder. The details of the co-precipitated powder are given in Chapter 3. As the co-precipitated powder of 50% $UO_2$  composition containing around ~ 14 mol% in form of  $U_3O_8$ , it will also simulate for powder density and cater  $U_3O_8$  requirement. Therefore, co-precipitated  $(Th,U)O_2$  mixed oxide powder will used to investigate only the effect on homogeneity and microstructure due to difference in powder characteristics. In the work presented in this section, the investigations will be focused on the pellets fabricated by CAP route and sintered in different atmospheres.

## **6.2 Pellets fabricated using pure oxide powders**

The objective was to fabricate pellets of  $(Th,U)O_2$  using CAP route without any addition of extraneous dopants to facilitate sintering and also eliminate inclusion of any unwanted chemical impurities. Therefore, investigations were performed on  $(Th,U)O_2$  pellets made using  $U_3O_8$  powder. The pellets were fabricated using the processes described in

Section 1.2 and the characteristics of the powders used in this study are given in Section 3.1.1. The CAP agglomerates showed maximum loading of 6.75%  $U_3O_8$ . Hence the green pellets of  $ThO_2-6.75\%U_3O_8$  were fabricated by both POP and CAP process. The green pellets were sintered in both oxidizing and reducing atmospheres as per the temperature profile shown in Figure 3.7 of Section 3.1.3 in the Chapter 3.

The pellets of  $ThO_2-6.75\%U_3O_8$  were sintered at different temperatures and heating rates in oxidizing conditions. In our trials, it was observed that quality of POP pellets and CAP pellets sintered in oxidizing conditions was quite poor with multiple cracks on the surface. The density variation observed was also large. The CAP pellet showed tendency of crumbling or disintegration on application of manual force. The possible reasons responsible for exhibition of poor pellet characteristics might be higher percentage of  $U_3O_8$  addition, higher O/M and O/M variation in the pellet and wide differential shrinkage characteristics between the powders. Hence further study on the pellets fabricated in the oxidizing condition was not addressed.

Further experiments using these green pellets were explored and investigated in reducing atmosphere of  $Ar-H_2$ . The results of the density measurements and thermo gravimetry analysis conducted on the sintered pellets are given in Table 6.1.

**Table 6.1: Characteristics of experimental ThO<sub>2</sub>-6%UO<sub>2</sub> pellets used for thermal property studies**

<b>Fabrication route</b>	<b>Sintering atmosphere</b>	<b>Density (% T.D)</b>	<b>O/M</b>	<b>Porosity (% T.D)</b>
POP	Ar-8%H <sub>2</sub>	91-95	2.005 ± 0.003	5-9
CAP	Ar-8%H <sub>2</sub>	90-94	2.008 ± 0.005	6-10

From the studies using U<sub>3</sub>O<sub>8</sub> with ThO<sub>2</sub> in oxidizing atmosphere, it was observed that sintering behavior was poor. Previous studies by Kutty et al [200] showed pellets using UO<sub>2</sub> and sintered in oxidizing conditions displayed lower densities 88-90 %T.D and O/M ratio higher than 2.00. Kutty et al [201] conducted studies on ThO<sub>2</sub>-2%U<sub>3</sub>O<sub>8</sub> in oxidizing atmosphere and reported high densities in the pellet but also indicated incomplete reduction of U<sub>3</sub>O<sub>8</sub> to UO<sub>2</sub>. They concluded in their study regarding addition of U<sub>3</sub>O<sub>8</sub> in small quantities assisted in sintering as a dopant. This agrees reasonably well with our observations wherein higher quantities of U<sub>3</sub>O<sub>8</sub> had adverse effect on the pellets during air sintering. Many authors [202-208] have studied the reduction of U<sub>3</sub>O<sub>8</sub> to UO<sub>2</sub> in H<sub>2</sub> atmosphere. The rate controlling step in reduction of U<sub>3</sub>O<sub>8</sub> in H<sub>2</sub> was absorption of H<sub>2</sub> molecule on the oxide surface [206]. The rate equation can be expressed as given in equation 21 below [207]:

$$\mathbf{dF/dt = 7.65 \times 10^8 \times (PA/T^{3/2})exp(-27700/RT)} \quad \mathbf{(21)}$$

where, F is the fraction remaining to be reduced in t seconds, P is the H<sub>2</sub> partial pressure and A is the specific area.

Kutty et al [200] in their studies using  $\text{ThO}_2\text{-}2\%\text{U}_3\text{O}_8$  found that  $\text{U}_3\text{O}_8$  did not fully reduced to  $\text{UO}_2$  even at 1300 K as it remains as  $\text{UO}_{2+x}$ . This concurred with the observations of DeHollander [206] and Perrin [208] and was in agreement with the fact that the rate of reduction of  $\text{U}_3\text{O}_8$  in  $\text{Ar-}8\%\text{H}_2$  atmosphere is a surface controlled phenomenon. It may be possible to reduce  $\text{U}_3\text{O}_8$  to  $\text{UO}_{2.00}$  in  $\text{Ar-}8\%\text{H}_2$  atmosphere even at  $700^\circ\text{C}$  if it were in powder form. In their pellets with 67 % T.D, they observed the reduction of  $\text{U}_3\text{O}_8$  to  $\text{UO}_2$  was not completed since the gas could not permeate through the dense mass of pellet. The reduction might have occurred only on a few surface layers but the inner layers still remained as  $\text{UO}_{2+x}$ . Thus the presence of higher concentration of oxygen interstitials resulted in large shrinkage. Similar observations could be correlated with our studies.

It could be seen that the pellets exhibited good characteristics with respect to their densities and O/M ratio. The pellets showed slightly hyper-stoichiometric values and the densities were quite comparable with the  $(\text{Th,Ce})\text{O}_2$  pellets sintered in similar conditions and as mentioned in Section 3.2. From this study it could be seen that sintering in reducing atmosphere at high temperatures has in fact helped in achieving the pellets densities as well as reducing the O/M to near stoichiometric value.

### **6.2.1 Micro homogeneity**

To evaluate micro-homogeneity in the sample, the distribution of uranium and thorium across the matrix of the pellet was analysed using alpha autoradiography technique. Daughter nuclides of thorium in its alpha decay hierarchy, such as  $\text{Ra}^{224}$  and  $\text{Rn}^{220}$ , emit alpha particles with higher energy as compared to that from uranium. The alpha tracks registered were contributed by the daughter products of thorium as those from uranium were

eliminated using a thin aluminium mylar film. The dark spots in the image correspond to alpha tracks generated by alpha particles. Preliminary investigations using alpha autoradiograph for the distribution of Th and U in the POP and CAP pellet are shown in Figures 6.1 (a) and 6.1 (b), respectively.

The alpha autoradiograph of POP pellet showed uniform alpha track density confirming that the uranium distribution across the pellet was uniform and homogeneous across the sample. The alpha autoradiograph of CAP pellet showed heterogeneous distribution of thorium and uranium. The darker regions in the autoradiograph indicated higher density of alpha tracks which correspond to the presence of thorium rich regions in the pellet. Hence uranium distribution all across the pellet was found to be varying in concentration at different regions in the CAP pellet.

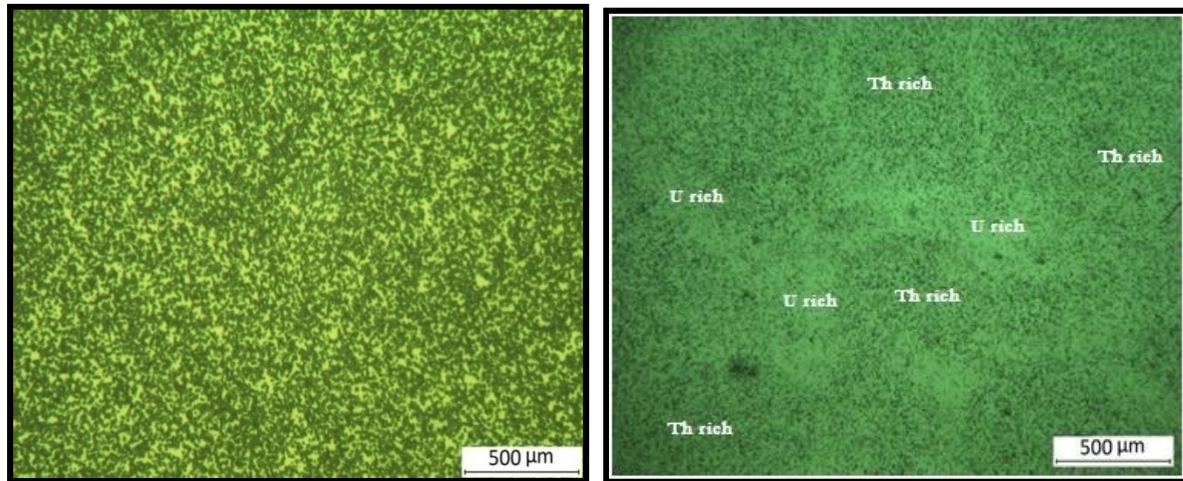


*Figure 6.1: Alpha autoradiograph of ThO<sub>2</sub>-6% UO<sub>2</sub> (a) POP pellet and (b) CAP pellet.*

### **6.2.2 Microstructure and homogeneity**

The microstructural investigations of ThO<sub>2</sub>-6% UO<sub>2</sub> CAP pellet using SEM revealed that the matrix consisted of duplex grain structure wherein fine grains and large grains both

were present as shown in Figure 6.2. It was observed that the pores were predominantly present in the larger grain boundary region. The size of these non-equiaxed type grains varied between 5–25  $\mu\text{m}$ . The average grain size of the sintered pellets measured by linear intercept method was found to be  $\sim 16 \mu\text{m}$ .

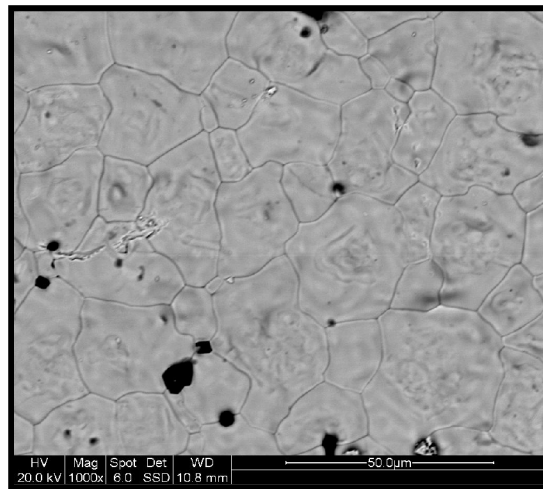


**Figure 6.2 :** SEM Microstructure of  $\text{ThO}_2$ -6wt.% $\text{UO}_2$  CAP pellet sintered in  $\text{Ar-8\%H}_2$  atmosphere.

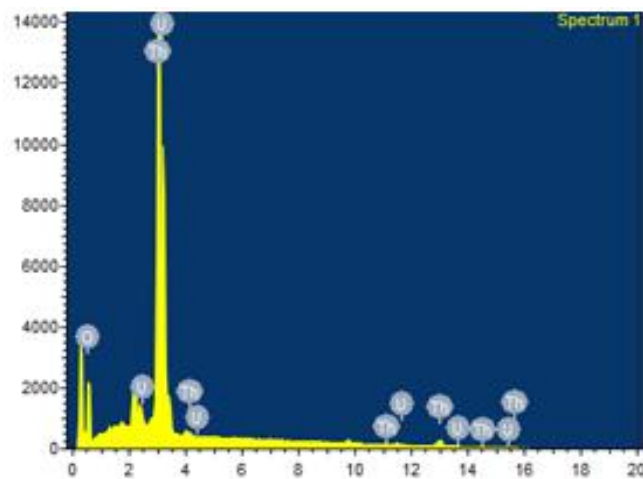


**Figure 6.3 :** EDS spectrum taken from the area shown in Figure 6.2 showing the presence of three elements, i.e., Th, U and O.

Energy Dispersive Spectroscopy (EDS) was done over the area shown in Figure 6.3 and the EDS spectrum, thus obtained, is shown in Figure 6.4. The elemental mapping of the area was done for the major elements present. The results of elemental mapping taken in this regard using EDS are shown in Figure 6.4.

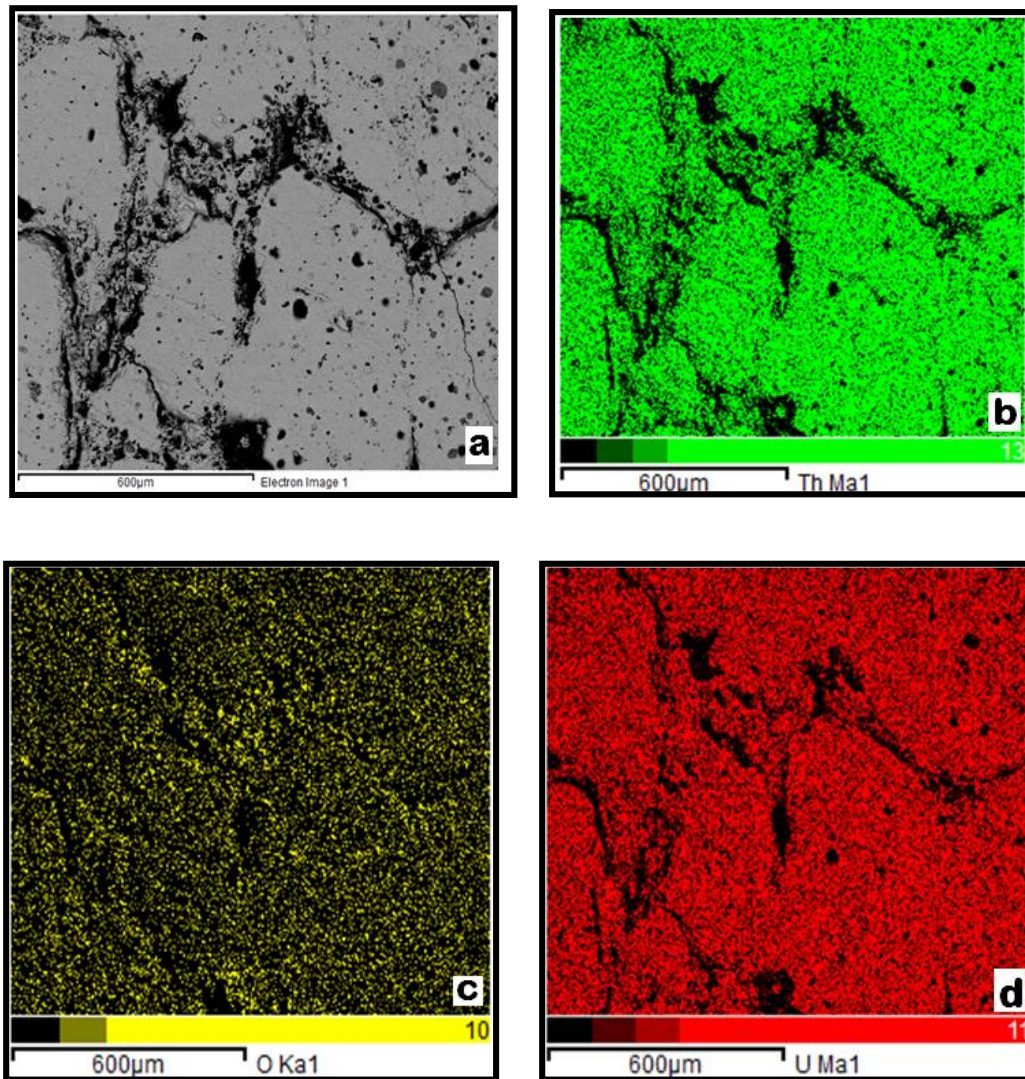


**Figure 6.4:** (a) Microstructure of  $\text{ThO}_2\text{-6\%UO}_2$  showing  $\text{U}_3\text{O}_8$  coating site (dark) and the initial  $\text{ThO}_2$  granules (b) elemental mapping of ‘Th’ coming from Th (Ma), (c) elemental mapping of O coming from O(Ka) and (d) elemental mapping of U coming from U(Ma). All the elemental mappings were done on the same area as shown in (a).

From the EDS spectrum, it can be seen that three elements namely uranium, thorium and oxygen were majorly present. The quantitative analysis for these elements obtained by EDS was done and their respective atomic/weight percentages are given in Table 6.2. Elemental mapping shows that presence of Th, U and O elements throughout the matrix of the pellet.

**Table 6.2 : Quantitative analysis of 'Th', 'U' and 'O' elements as obtained from EDS of ThO<sub>2</sub>-6%UO<sub>2</sub> CAP pellet.**

<b>Element</b>	<b>Weight (%)</b>	<b>Atomic (%)</b>
O (K)	13.85	70.02
Th (M)	81.78	28.50
U (M)	4.36	1.48
Totals	100.00	100.00

### 6.2.3 XRD

Room temperature XRD patterns of ThO<sub>2</sub> and ThO<sub>2</sub>- 6%UO<sub>2</sub> MOX powders are shown in Figure 6.5. It could be confirmed from the XRD analysis that no distinct peaks corresponding to U<sub>3</sub>O<sub>8</sub> and UO<sub>2</sub> were present which indicated complete solid solution formation of (Th,U)O<sub>2</sub> in the pellets of ThO<sub>2</sub>- 6 wt.% UO<sub>2</sub> MOX.

From the peak height positions obtained the corresponding lattice parameter ( $a_0$ ) were deduced. The measured lattice parameters of ThO<sub>2</sub> and ThO<sub>2</sub>-6%UO<sub>2</sub> were found to be 5.5967 and 5.5885 Å, respectively which matched very well with values of 5.599 and 5.585 reported in literature for respective compositions [209]. The decrease in lattice parameter due to incorporation of uranium atoms in the lattice was due to lower ionic radius of U<sup>4+</sup> (0.997 Å) compared to ionic radius of Th<sup>4+</sup> (1.05 Å).

The XRD pattern for pure  $\text{ThO}_2$  and  $\text{ThO}_2$ -6%  $\text{UO}_2$  (POP & CAP) is given Figure 6.5. The most intense peak at  $32^\circ$  has been zoomed and shown in Figure 6.6. Figure 6.6 clearly indicated the shift in peak position of  $\text{ThO}_2$ -6%  $\text{UO}_2$  due to uranium incorporation in thoria lattice from that of pure thoria. However, the  $(\text{Th},6\% \text{U})\text{O}_2$  CAP sample showed contribution of higher angle peaks in the XRD pattern which indicated presence of solid solution with varying higher uranium concentration in the pellet.

The O/M ratio of the CAP pellet and POP pellet was determined by TG method as described previously and are given in Table 3.6 in Section 3.3.3.

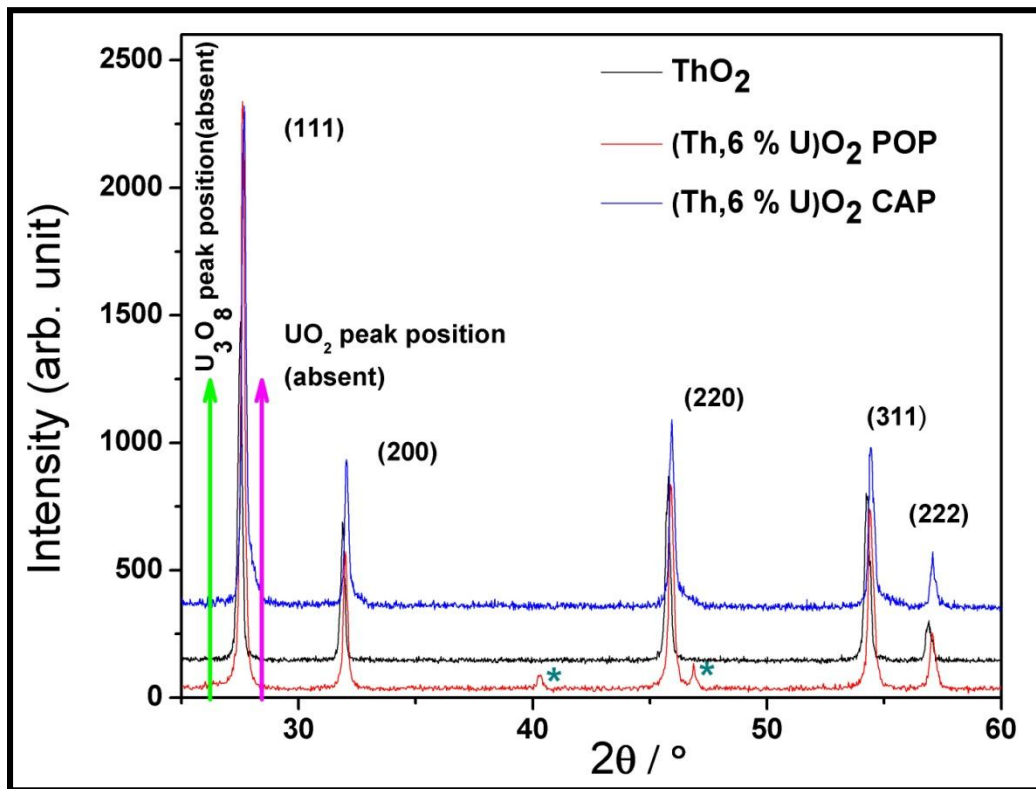


**Figure 6.5 :** XRD patterns of  $\text{ThO}_2$ -  $x$  wt.%  $\text{UO}_2$  ( $x = 0$  &  $6$ ) at room temperature. Peaks at  $40.47^\circ$  and  $47.12^\circ$  are due to Pt-Rh sample carrier.

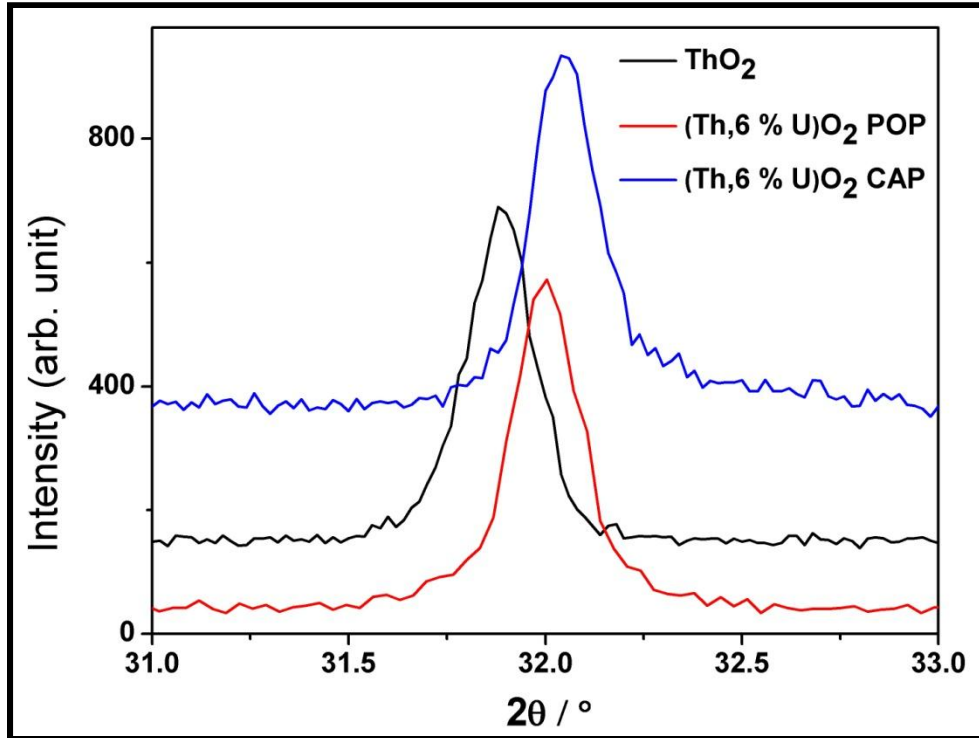


*Figure 6.6 : Expanded view of XRD plot between 31° and 33°.*

#### 6.2.4 Chemical analysis

ThO<sub>2</sub> and ThO<sub>2</sub>- 6 wt% UO<sub>2</sub> powders obtained by pulverization of sintered pellets were analyzed for trace impurities using high resolution sequential ICP-AES. It was observed that most of the elements were found to be in the range 0.3–260 ppm with a precision of maximum ± 7.3% RSD (relative standard deviation) which confirm a near total purity of the sample with respect to the above impurities. Dissolution studies for estimating ‘Th’ and ‘U’ were carried out and values reported were within ± 0.05% of weight gained on the spheroids. The chemical analysis confirmed complete removal of binder-cum-lubricants added and absence of any extraneous contamination due to process operations. The uncertainty of influence of impurities on thermal properties was also eliminated.

The sample pellets of  $(\text{Th},6\%\text{U})\text{O}_2$  were prepared by CAP process and POP process, the details of the which have been described in Chapter 3. The physical and microscopic characteristic features of microstructure (SEM) and homogeneity (alpha autoradiography and XRD) observed in the pellets have been discussed herein. As the POP pellets have both  $\text{ThO}_2$  and  $\text{U}_3\text{O}_8$  powders uniformly distributed in the green pellet whereas in CAP green pellets the  $\text{U}_3\text{O}_8$  powder particles are surrounding the  $\text{ThO}_2$  agglomerates (non uniformly distributed) there exists a gross homogeneity difference between the two. The effect of this homogeneity on the pellet characteristics was investigated as the surrogate materials has tendency of being hyper-stoichiometric and entirely different from the other surrogate material.

The pellets of  $\text{ThO}_2-6.75\%\text{U}_3\text{O}_8$  which were fabricated and sintered at 1823 K in air atmosphere for 4 h showed presence of physical defects such as cracks and poor integrity.

The possible explanation for exhibition of such behavior is that under oxidizing condition and at temperatures around 500°C  $\text{U}_3\text{O}_8$ , one of the stable oxide form of U, has tendency of forming  $\text{UO}_3$ .  $\text{UO}_3$  at further higher temperatures ( $> 1100^\circ\text{C}$ ) shows tendency of decomposition back to  $\text{U}_3\text{O}_8$  [201]. With increase in O/M the crystal of  $\text{U}_3\text{O}_8$  will dilate and cause volume expansion. Solid state solubility of  $\text{U}_3\text{O}_8$  in  $\text{ThO}_2$  is negligible [210–212]. Kutty et al [201] conducted studies using 2%  $\text{U}_3\text{O}_8$  addition to  $\text{ThO}_2$  in air and reported large number of oscillations in shrinkage rate curve. It was very evident in their study that during sintering allotrope modifications were occurring simultaneous to sintering. The sintering rate curve was a typical example of these reactions occurring over a range of temperatures. At intermediate temperatures of sintering  $1100^\circ-1500^\circ\text{C}$ , there is a considerable amount of deviation from stoichiometry generating more point defects which

might have assisted sintering. Another major observation of interest was that even at high temperatures  $U_3O_8$  has not fully reduced to stoichiometric  $UO_{2.00}$  which means O/M of the pellet subsequent to sintering was hyper-stoichiometric.

Considering the observations reported, in present study higher concentration of  $U_3O_8$  in the pellet must have been subjected to sufficient volume variation and inhibited sintering mechanisms in progress. Due to this incompatibility, the sintering as well as interdiffusion of atoms might be affected resulting in defects in the pellet. Therefore, quality of pellets was more affected in the case of CAP pellets and can be inferred that using  $U_3O_8$  with  $ThO_2$  for the fabrication of  $(Th,U)O_2$  pellets in oxidizing atmosphere affects the quality of pellet seriously. During sintering, the foremost important phenomenon which is in play is the reduction of  $U_3O_8$  to  $UO_2$  in both the pellets.

In XRD analysis presence of any unreduced  $U_3O_8$  or  $UO_2$  could not be detected. Hence it could be presumed that  $U_3O_8$  present in both type of pellets have been reduced during sintering. The reduction of  $U_3O_8$  to  $UO_2$  in  $H_2$  atmosphere has been widely studied [202–208]. In reduction of  $U_3O_8$ ,  $H_2$  molecules are to be absorbed on the oxide surface and which is the rate controlling step in the whole process of reduction [206]. Perrin et al [208] have conducted detailed study on reduction of  $U_3O_8$  into  $UO_2$  using  $H_2$  the overall reduction reaction occurred by three successive transformation stages. In first stage, the oxygen stoichiometry of  $U_3O_8$  was transformed into  $U_3O_{8-x}$  ( $x=0.2$ ) which was controlled by surface reaction step. In second stage, further reduction of  $U_3O_{8-x}$  into  $U_4O_9$ , the rate-limiting step for the inward growth of  $U_4O_9$  was the reactive desorption of water at the surface of the particles. Finally, the reduction of  $U_4O_9$  to  $UO_2$  was observed in which the rate-limiting step

was the growth of  $\text{UO}_2$  from  $\text{U}_4\text{O}_9$ . It has been reported that  $\text{U}_3\text{O}_8$  powder can be completely reduced to  $\text{UO}_2$  in hydrogen even at temperatures as low as 753 K. Therefore, it is expected that that  $\text{U}_3\text{O}_8$  present in  $\text{ThO}_2\text{-U}_3\text{O}_8$  green compacts used in this study will reduce to  $\text{UO}_2$  before the start of sintering.

It might be possible to reduce  $\text{U}_3\text{O}_8$  to  $\text{UO}_2$  in  $\text{Ar-8\%H}_2$  atmosphere even at 973 K if it is in powder form. Since in this study, green pellets have density around 67 %T.D, the reduction of  $\text{U}_3\text{O}_8$  to  $\text{UO}_2$  could not be completed. In order to achieve this, the gas would have to permeate through the dense mass of pellet. In POP pellets as  $\text{U}_3\text{O}_8$  particles are individually distributed, the specific surface area available for the reduction will be higher (lower than loosely packed powder) and will be reduced uniformly at a rate dependant on gas permeation into the pellet. But in the case of CAP pellets,  $\text{U}_3\text{O}_8$  particles being densely packed due to compaction the surface area for reduction was considerably lowered. The rate of reduction will therefore reduce considerably. Hence in the case of POP and CAP pellets the reduction process will be sustained for longer period alongwith sintering and the deviation from stoichiometry shall be responsible for enhancing the sintering kinetics.

Because of U diffusion in the matrix, solid solution formation with the surrounding  $\text{ThO}_2$  took place simultaneously to form  $(\text{Th,U})\text{O}_{2+x}$ . Since diffusion of uranium ( $D_U$ ) is proportional to square of the extent of hyper-stoichiometry ( $x^2$ ) [213], it is evident from here that addition of equivalent amount of  $\text{U}_3\text{O}_8$  in  $\text{ThO}_2$  to fabricate  $\text{ThO}_2\text{-UO}_2$  pellets by CAP process resulted in substantial reduction of sintering temperature and affects the kinetics of sintering by incorporation of higher defect concentration such as oxygen interstitials and cation vacancies. Enhanced diffusion of uranium and thorium, solid solution formation with

ThO<sub>2</sub> and subsequent reduction of the (Th,U)O<sub>2+x</sub> are simultaneous processes occurring with overall sintering (porosity removal) of the material. As and when UO<sub>2+x</sub> or (Th,U)O<sub>2+x</sub> get reduced to their stoichiometric state, the mobility of ions slows down and form solid solution with the available Th/U ratio in the adjacent area.

The area covered by diffusion of ions during the sintering is dependent on the concentration of defects generated, temperature and sintering atmosphere. In CAP pellet as the U<sub>3</sub>O<sub>8</sub> coating thickness varies from agglomerate to agglomerate the extent of ion mobility shall also vary accordingly. This led to the chemical inhomogeneity (of uranium distribution) in the matrix of the pellets. Whereas in POP pellets as the U<sub>3</sub>O<sub>8</sub> powder particles are in good contact with ThO<sub>2</sub> powder particles, this phenomenon of reduction and diffusion occurs uniformly across the pellet matrix. This results in uniform distribution of uranium across the pellet. Because of reducing atmosphere, high sintering temperatures and time subsequently the pellets irrespective mode of fabrication got reduced to their stoichiometric state by the end of sintering.

With this understanding, the results obtained in XRD studies, EPMA and alpha autoradiography can be well explained and correlated. The POP pellets will exhibit better homogeneity compared to CAP pellets because of difference in distribution of U<sub>3</sub>O<sub>8</sub> in the pellet. The solid solution formation in POP pellets will be better as compared to CAP pellets. The compositional variation in the POP pellets will be lower whereas in CAP pellet, though solid solution formation has taken place across the pellet there will be regions richer to regions poorer in uranium concentration. This was confirmed by elemental mapping using EDS (Energy Dispersive spectroscopy) where the presence of 'Th' and 'U' was noticed at all

places (Figure 6.4). So the chemical identity of the starting material was lost and U have diffused up to the centre of initial ThO<sub>2</sub> granules and Th have diffused to the areas of initial U<sub>3</sub>O<sub>8</sub> coating sites. In XRD analysis, contributions of peaks at angles higher than the maximum intense peak angle reflect presence of higher uranium containing solid solution. Similar observations could be made in alpha autoradiography of CAP pellet which showed regions of higher track densities and lower track densities.

Alpha autoradiograph of POP pellet showed uniform track density indicating uniform distribution of thorium and uranium across the pellet. Grain growth being a diffusion controlled phenomenon, it is governed by various parameters and conditions such as concentration of defects, type of defects, temperature. In POP pellet as the U<sub>3</sub>O<sub>8</sub> was uniformly distributed, the defects concentration across the pellet was also uniform resulting in uniform grain growth. The microstructure study showed POP pellets having uniformly sized grains distributed across the matrix. However in CAP pellets, grain growth will be predominant in regions with higher defect concentration. The regions of U<sub>3</sub>O<sub>8</sub> coating which have higher defect concentration will form larger grains compared to regions of lower defect concentration (thoria agglomerates) with smaller grains.

### **6.2.5 Thermal property evaluation**

The sample were taken from the sintered pellets of (Th,6%U)O<sub>2</sub> made by POP and CAP route randomly. The characteristics of experimental ThO<sub>2</sub>-6%UO<sub>2</sub> sample pellets used for thermal property investigations are given in Table 6.3.

*Table 6.3 : Characteristics of experimental  $\text{ThO}_2\text{-6\%UO}_2$  sample pellets used for thermal property studies.*

Fabrication route	Sintering atmosphere	Density (g/cc)	Density (%T.D)	O/M
POP	Ar-8% $\text{H}_2$	9.464	94.10	2.002
CAP	Ar-8% $\text{H}_2$	9.354	93.00	2.013

#### 6.2.4.1 Thermal expansion evaluation (Dilatometry)

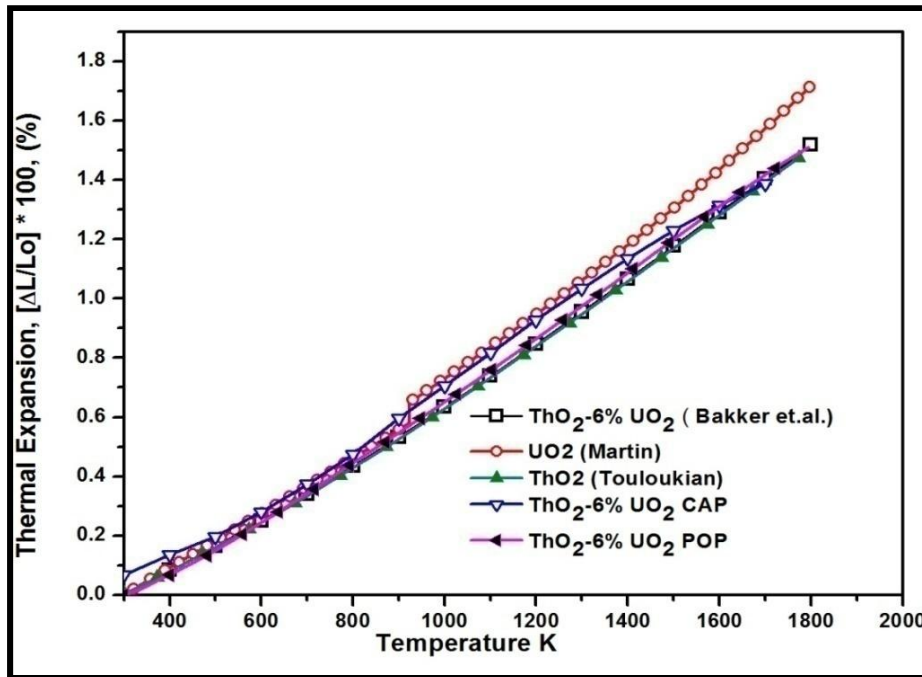


*Figure 6.7 : Percentage thermal expansion data as a function of temperature for  $\text{ThO}_2$  and  $\text{ThO}_2\text{-6\%UO}_2$  (CAP and POP pellets) as measured using dilatometer.*

The linear thermal expansion of ThO<sub>2</sub> and ThO<sub>2</sub>–6% UO<sub>2</sub> MOX (CAP and POP pellets) as a function of temperature (300–1773 K) were measured by dilatometer and are given in Figure 6.7. The reported data for pure ThO<sub>2</sub> [75], pure UO<sub>2</sub> [76] and interpolation data calculated as recommended by Bakker et al [74] for composition ThO<sub>2</sub>–6% UO<sub>2</sub> are also plotted for comparison in the same figure.

#### 6.2.4.2 MD Simulations

The experimentally measured thermal expansion coefficients of ThO<sub>2</sub> and (Th,U)O<sub>2</sub> MOX were compared with MD calculated and data in the literature are given in Table 6.4.

*Table 6.4 : Experimentally measured thermal expansion coefficients of ThO<sub>2</sub> and (Th,U)O<sub>2</sub> MOX compared with MD Calculated and data in the literature.*

<i>Thermal expansion coefficients (<math>10^{-6}K^{-1}</math>)</i>	<i>Remarks</i>
<b>ThO<sub>2</sub></b>	
10.28 (300–1800 K)	MD calculated [114]
9.99 (300–1773 K)	Dilatometry, experimental ThO <sub>2</sub> [114]
9.67 (293–1623 K)	HTXRD [210]
9.58 (293–1473 K)	HTXRD [214]
<b>(Th,U)O<sub>2</sub></b>	
10.47 (300–1800 K)	MD calculated, Th <sub>0.9375</sub> U <sub>0.0625</sub> O <sub>2</sub>
10.098 (300–1773 K)	Dilatometry, POP, ThO <sub>2</sub> –6wt%UO <sub>2</sub>
10.14 (300–1773 K)	Dilatometry, CAP, ThO <sub>2</sub> –6wt%UO <sub>2</sub>
10.37 (293–1623 K)	Th <sub>0.94</sub> U <sub>0.06</sub> O <sub>2</sub> , HTXRD [209]

### 6.2.4.3 Thermal Diffusivity

The thermal diffusivity measurements of pure  $\text{ThO}_2$  and  $\text{ThO}_2$ -6% $\text{UO}_2$  (POP and CAP) pellets at high temperatures between 873 K and 1873 K using laser flash method are shown in Figure 5.8. The thermal diffusivity measurements were carried out on samples derived from pellets used for thermal expansions studies. The details of the pellets are given in Table 6.1

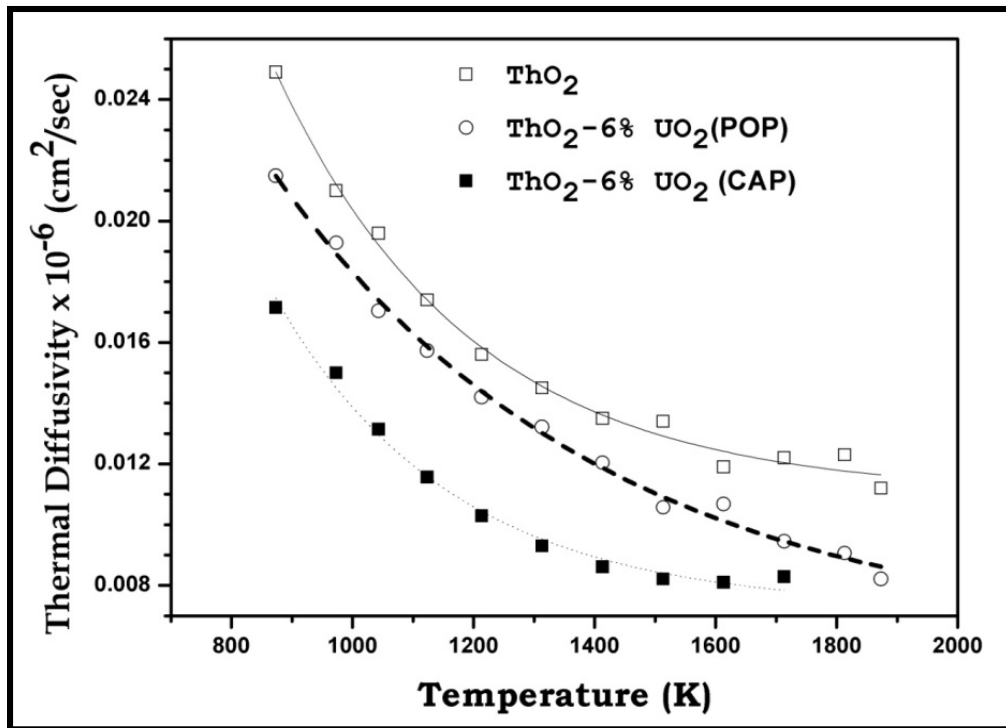


*Figure 6.8 : Thermal diffusivity plots of  $\text{ThO}_2$  and  $\text{ThO}_2$ -6% $\text{UO}_2$  (POP and CAP pellet) between temperature range of 873 K and 1873 K.*

### 6.2.4.4 Thermal conductivity

The experimentally deduced thermal conductivity values of pure  $\text{ThO}_2$  and  $\text{ThO}_2$  - 6% $\text{UO}_2$  (POP and CAP pellets) in the 873–1873 K temperature range and the MD calculated

thermal conductivity (corrected to 95% T.D) for similar compositions (400–2000 K temperature range) using the methodology described in Section 4.8 are plotted as a function of temperature in Figure 6.9. Thermal conductivity of the pellets by experimental derivation of thermal expansion and thermal diffusivity was calculated using the relation given in equation 5 of Section 3.2.10 in Chapter 3. The  $C_p$  values for the calculations were obtained by using Neumann–Kopp method of employing weighted average with heat capacity values of pure  $\text{ThO}_2$  and pure  $\text{UO}_2$  for the composition based on the study described in Section 4.7. Similar procedure was followed by Yang et al [215] for estimating the thermal conductivity of  $(\text{Th,U})\text{O}_2$  pellets in their studies

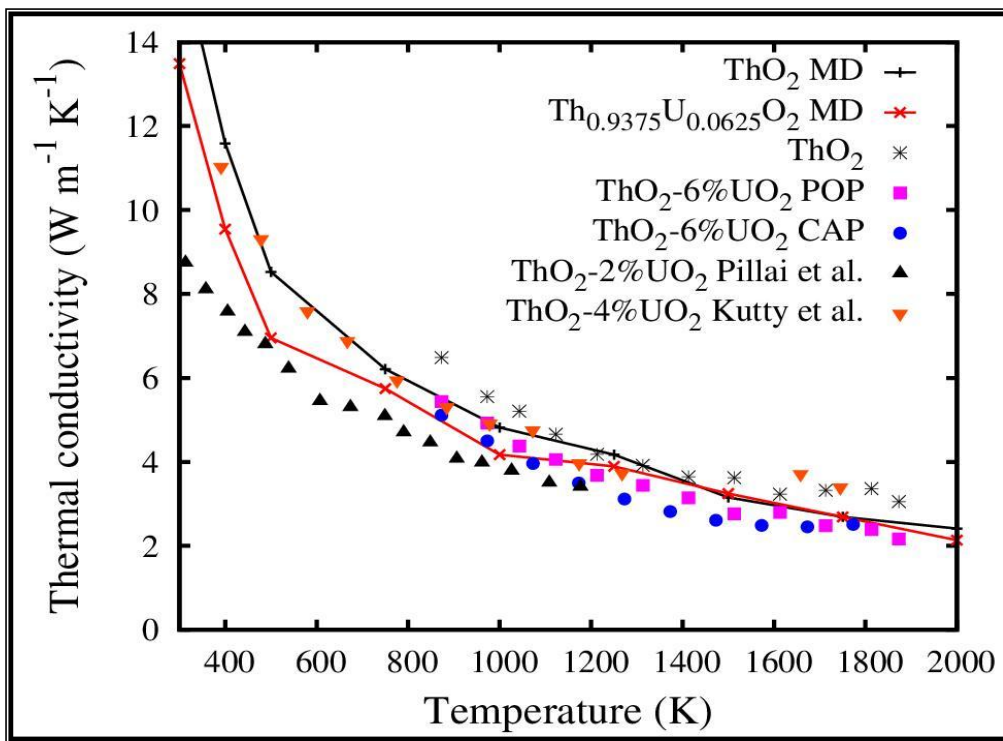


**Figure 6.9 :** Thermal conductivity as calculated by MD simulations as a function of temperature for  $\text{ThO}_2$  and  $\text{Th}_{0.9375}\text{U}_{0.0625}\text{O}_2$  compared with our experimental values of  $\text{ThO}_2$  and  $\text{ThO}_2$ -6wt%  $\text{UO}_2$  (POP and CAP) pellet (both corrected to 95 %T.D). Reported values of Pillai et al [90] and Kutty et al [25] are also plotted for comparison.

The ThO<sub>2</sub> and (Th,6%U)O<sub>2</sub> pellets were investigated for the thermal properties such as thermal expansion and thermal diffusivity. The specific heat, C<sub>p</sub>, of (Th,6%U)O<sub>2</sub> were obtained by using Neumann–Kopp method of employing weighted average with heat capacity values of pure ThO<sub>2</sub> and pure UO<sub>2</sub> for the composition.

The coefficient of thermal expansion (CTE) measured from dilatometer for ThO<sub>2</sub>–6wt.%UO<sub>2</sub> (both POP and CAP pellets) and ThO<sub>2</sub> were found to be lower than MD calculated and reported HTXRD values [209, 214]. This could be attributed to the density of the ThO<sub>2</sub>–6wt.%UO<sub>2</sub> MOX pellets which was lower (by 6–7%) compared to theoretical density because of presence of porosity. similar observation were made in our studies on (Th,Ce)O<sub>2</sub>. This deviation in CTE values was assigned to the influence of the porosity content, O/M ratio and the extent of homogeneity which varied in the samples because of difference in fabrication methods and conditions.

The experimental thermal expansion data were least squares fitted to a third degree polynomial equation for each sample. The fitting errors for all these compositions are within ± 1%. The recommended percentage thermal expansion data in the temperature range from 300 to 1773 K for CAP and POP pellets are given below (T in K):

**ThO<sub>2</sub>:**

$$(\Delta L/L_0) = -0.19730 + 5.6599 \times 10^{-4} \times T + 3.54902 \times 10^{-7} \times T^2 - 7.4276 \times 10^{-11} \times T^3 \quad (22)$$

**ThO<sub>2</sub>–6%UO<sub>2</sub> (POP):**

$$(\Delta L/L_0) = 0.1716 - 1.56136 \times 10^{-4} \times T + 1.2326 \times 10^{-7} \times T^2 - 3.9263 \times 10^{-11} \times T^3 \quad (23)$$

**ThO<sub>2</sub>-6%UO<sub>2</sub> (CAP):**

$$(\Delta L/L_0) = -0.20084 + 5.21632 \times 10^{-4} \times T + 4.3686 \times 10^{-7} \times T^2 - 1.0834 \times 10^{-11} \times T^3 \quad (24)$$

An important observation of our thermal expansion study was that the  $\alpha$  measured from dilatometer for ThO<sub>2</sub>-6wt.%UO<sub>2</sub> for both POP and CAP pellets were very similar indicating that CTE is almost independent of inhomogeneity and porosity effect of the pellets. The MD calculated  $a(T)$  for Th<sub>1-x</sub>U<sub>x</sub>O<sub>2</sub> ( $x = 0$  and  $0.0625$ ) matched well with the reported values (HTXRD) for ThO<sub>2</sub> and ThO<sub>2</sub>-6wt% UO<sub>2</sub> samples. The decrease in calculated lattice parameter as a function of U<sup>4+</sup> concentration could be attributed to smaller ionic radii of U<sup>4+</sup> (0.997 Å) compared to Th<sup>4+</sup> (1.05 Å) in eight-fold coordination. Yang et al [215] also reported similar observation of decrease in lattice parameter with UO<sub>2</sub> fraction in their studies on (Th, 35%U)O<sub>2</sub> and (Th,65%U)O<sub>2</sub>.

On comparison, it is clearly evident that the measured linear thermal expansion (%) over the temperature range in the present study was in excellent agreement with respect to the recommended values of Bakker et al [74] for ThO<sub>2</sub>-6%UO<sub>2</sub> MOX. Comparing with the thermal expansion studies conducted on (Th,Ce)O<sub>2</sub> mentioned in Table 4.3 of Section 4.9, it could be seen that CAP pellets showed higher coefficient of thermal expansion as compared to POP pellets in both the studies. It could also be observed from both the studies that MD calculated CTE were comparatively higher compared to HTXRD and Dilatometry conducted experiments. Though the composition of (Th,Ce)O<sub>2</sub> was slightly lower compared to that of (Th,U)O<sub>2</sub>, it could be observed that coefficient of thermal expansion was higher. The coefficient of thermal expansion of CeO<sub>2</sub> ( $11.76 * 10^{-6} \text{ K}^{-1}$ ) being comparatively higher than UO<sub>2</sub> ( $10 * 10^{-6} \text{ K}^{-1}$ ), addition of high CTE material might have influenced in contributing to

the increase due to decrease in lattice parameter. However it was evident that with the addition of  $\text{UO}_2$  similar to  $\text{CeO}_2$  and  $\text{PuO}_2$ , results in change in thermal expansion from pure  $\text{ThO}_2$ .

The thermal diffusivity of the  $\text{ThO}_2$ -6% $\text{UO}_2$  (CAP) pellet is significantly lower (15–20 %) compared to  $\text{ThO}_2$ -6% $\text{UO}_2$  (POP) pellet. This could be attributed to the fact that CAP pellets were having higher porosity than POP pellets and  $\text{UO}_2$  distribution in  $\text{ThO}_2$  matrix is also inhomogeneous for CAP pellets. The O/M values of POP and CAP pellets being very similar, it could be assumed that O/M did not have any role in affecting the thermal diffusivity properties in the present study.

The thermal conductivity of the  $\text{ThO}_2$  was found to decrease with incorporation of  $\text{UO}_2$  at lower temperature (500 K) than at higher temperature (1500 K). At higher temperatures (above 1200 K), the thermal conductivity of  $\text{Th}_{0.9375}\text{U}_{0.0625}\text{O}_2$  was lower compared to  $\text{ThO}_2$  (0.5– 1  $\text{Wm}^{-1}\text{K}^{-1}$  range). It is important to note that experimentally measured  $\kappa$  values for POP pellet was higher than the CAP pellet though the difference was insignificant and was within 5%. This emphasizes that cumulative effects of porosity majorly and O/M were together responsible for affecting the thermal conductivity properties of the CAP pellets.

The experimental values for  $\text{ThO}_2$ -6wt.% $\text{UO}_2$  (CAP and POP pellets) have been compared with experimentally determined thermal conductivity values of (Th, 2wt.%U) $\text{O}_2$  by Pillai et al [90] and (Th,4wt.%U) $\text{O}_2$  by Kutty et al [25] in Figure 6.9. Contrary to our studies and Kutty et al [25] which show good correlation of following the decreasing trend with increasing  $\text{UO}_2$  content, Pillai et al [90] reported much lower thermal conductivity

value. This was due to a static configuration technique used by Pillai et al [90] in contrast to dynamical configuration technique (in present study) for estimating the thermal conductivity and probably, the densities of the pellets might be much lower. It is well established that thermal conductivity of ThO<sub>2</sub> is higher than thermal conductivity of UO<sub>2</sub> [76, 77, 215]. The studies on (Th,U)O<sub>2</sub> by Yang et al [215] corroborate with findings of our studies that the thermal conductivity values obtained for (Th,U)O<sub>2</sub> were lower than that of ThO<sub>2</sub> and UO<sub>2</sub> and incorporation of UO<sub>2</sub> was responsible for this behavior. The lowering in the values of thermal conductivity of (Th,U)O<sub>2</sub> was large at lower temperatures and decreased with increasing temperatures.

One pair of *A* and *B* parameters of equation 14 can be obtained for each composition by linear fitting of  $1/\kappa$  (thermal resistivity) versus temperature data. Table 6.5 enlists *A* and *B* values obtained from the MD calculated and experimentally measured  $\kappa$  versus temperature data along with those values determined by Kutty et al [25] and suggested by Bakker et al [74].

**Table 6.5 : Constants *A* and *B* of the equation 14,  $1/\kappa = A+BT$ , for  $\text{ThO}_2$ ,  $(\text{Th,U})\text{O}_2$  MOX calculated from MD simulations and experimental measurements.**

<i>Sample</i>	<i>A(m.K/W)</i>	<i>B(m/W)x10<sup>-4</sup></i>
ThO <sub>2</sub> , MD calculated	0.0032	1.879
Th <sub>0.9375</sub> U <sub>0.0625</sub> O <sub>2</sub> , MD calculated	0.0174	1.784
ThO <sub>2</sub> , Experimental	0.0307	1.611
ThO <sub>2</sub> –6wt% UO <sub>2</sub> (POP), Experimental	0.0514	2.649
ThO <sub>2</sub> –6wt% UO <sub>2</sub> (CAP), Experimental	0.0547	2.548
ThO <sub>2</sub> , Kutty et al [25]	0.0334	1.374
ThO <sub>2</sub> –4wt.% UO <sub>2</sub> , Kutty et al [25]	0.0497	1.475
ThO <sub>2</sub> , Bakker et al [74]	0.0004	2.248
ThO <sub>2</sub> –6wt%UO <sub>2</sub> , Bakker et al [74]	0.0509	1.848

MD calculated *A* value shows an order of magnitude higher for Th<sub>0.9375</sub>U<sub>0.0625</sub>O<sub>2</sub> as compared to ThO<sub>2</sub> and *B* value remains almost constant. This general feature is matching well with reported data by Kutty et al [25] and suggested values by Bakker et al [74]. It also important to note that determined *A* values for CAP pellet is higher than POP pellet and this can be attributed to inhomogeneous distribution of UO<sub>2</sub> in ThO<sub>2</sub> matrix. Yang et al [215] have also in their studies reported strong dependence of parameter *A* on the composition. Hence inhomogeneous distribution contributes to more lattice defect centers resulting in higher phonon–lattice scattering cross–section.

### 6.3 Characterization of pellets fabricated using co-precipitated powders

The present study was further extended to study the effects of powder already possessing homogeneous composition with small quantity of  $U_3O_8$ . The main aim was to evaluate the pellets for their microstructure and homogeneity. Studies on co-precipitated powder using conventional route has been previously reported in literature [7]. Therefore, in this work investigations have been conducted on the CAP pellets only. In order to achieve better homogeneity,  $(Th,U)O_2$  powder obtained from a chemical co-precipitation route was used. In the studies using  $U_3O_8$  mentioned in the previous section, the microstructure exhibited by CAP pellets consisted of duplex grains colonies distributed across the matrix. The uranium concentration in the larger grained areas was found to be higher than that in fine grain areas. In this study, the CAP pellets were fabricated under similar conditions using co-precipitated powders of  $ThO_2$  and  $UO_2$  to investigate the effects on microstructure and homogeneity. The characteristics of co-precipitated powder of  $ThO_2$ -50% $UO_2$  chosen for the study are given in Section 3.1.1 of Chapter 3. The characteristics of the feed powders  $ThO_2$  and  $ThO_2$ - $UO_2$  used in this study are given in Table 3.1.

#### 6.3.1 Density

The density of the pellets of  $ThO_2$ -4% $UO_2$  made by coating  $ThO_2$ -50% $UO_2$  powder was found to be in the range of 93-95 %T.D. The  $ThO_2$ -4% $UO_2$  pellets sintered in Ar-8% $H_2$  showed a marginally higher density than those sintered in air. The densities of the pellets are given in Table 6.6.

*Table 6.6 : Composition, density and O/M ratio of ThO<sub>2</sub>-4%UO<sub>2</sub> CAP pellets fabricated using co-precipitated powder.*

Sample Composition	Coating powder	Sintering temperature and time	Sintering atmosphere	Density (%T.D)	O/M ratio
ThO <sub>2</sub> -4%UO <sub>2</sub>	ThO <sub>2</sub> -50% UO <sub>2</sub>	1400°C / 6h	Air	93.5	2.01
ThO <sub>2</sub> -4%UO <sub>2</sub>	ThO <sub>2</sub> -50% UO <sub>2</sub>	1650°C / 6h	Ar-H <sub>2</sub>	94.3	2.00

### 6.3.2 Microstructure

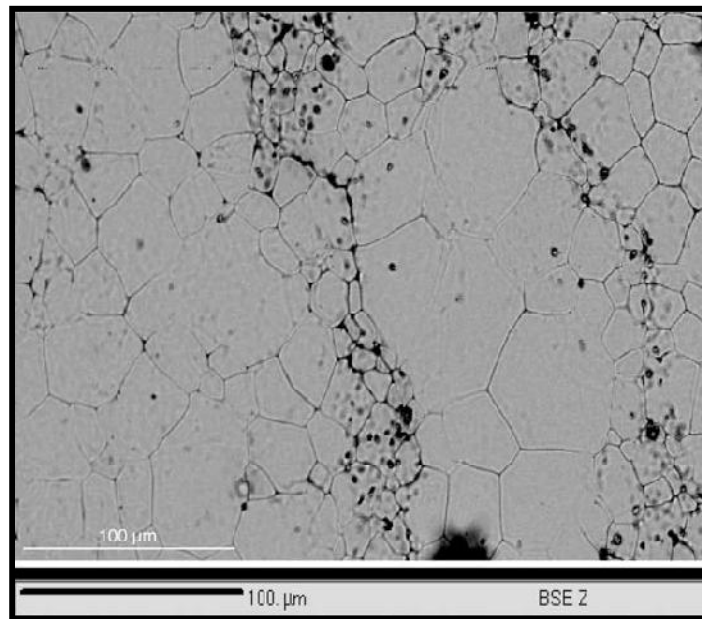


*Figure 6.10 : SEM photograph of ThO<sub>2</sub>-4%UO<sub>2</sub> pellet made by CAP co-precipitated powder and sintered in air at 1400°C for 6 h showing non-uniform grain structure.*

The studies show that the grain structure of ThO<sub>2</sub>-4%UO<sub>2</sub> pellet was found to be dependent on the sintering atmosphere. The grains of the ThO<sub>2</sub>-4%UO<sub>2</sub> pellet sintered in air showed a lot of variations in size. The microstructure of ThO<sub>2</sub>-4%UO<sub>2</sub> sintered in air is shown in Figure 6.10. The grains were found to be duplex in nature. The grain size

distribution gives appearance similar to ‘rock in sand’ structure. It was found that  $\text{ThO}_2$  grains in the large granules ( $\sim 40$  mesh) are small, while the  $(\text{Th,U})\text{O}_2$  grains in the fine powders are large. There were packets of fine grains uniformly distributed in the matrix. The size of each of the packet is in the range of  $75\text{--}100\ \mu\text{m}$ . The average size of these fine grains was about  $4\ \mu\text{m}$ . The pore distribution was found to be non-uniform, most of the pores being located on large grained areas. The packets of fine grains were found to be dense with a very small amount of porosity. The SEM photographs of  $\text{ThO}_2\text{--}4\%\text{UO}_2$  pellet sintered in  $\text{Ar}\text{--}\text{H}_2$  is shown in Figure 6.11.

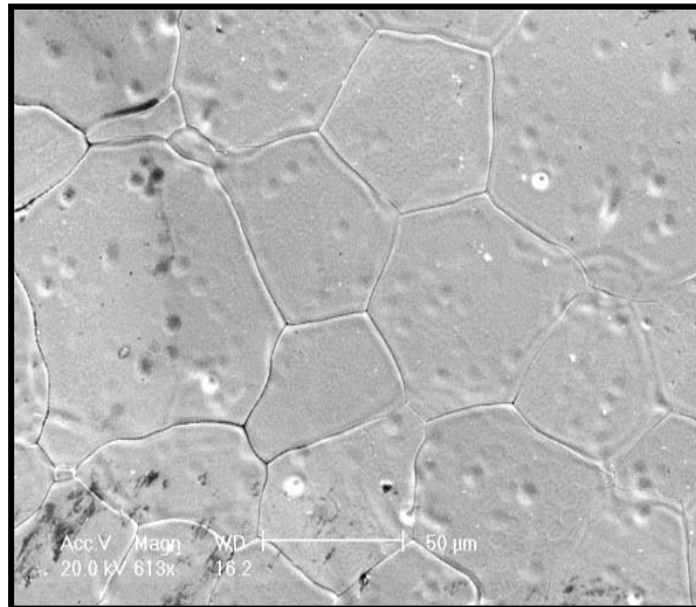


**Figure 6.11:** SEM photograph of  $\text{ThO}_2\text{--}4\%\text{UO}_2$  pellet made by CAP co-precipitated powder and sintered in  $\text{Ar}\text{--}8\%\text{H}_2$  ( $1650^\circ\text{C}$ , 6 h).

The grain size distribution of the  $\text{ThO}_2\text{--}4\%\text{UO}_2$  pellet sintered in reducing atmosphere at  $1650^\circ\text{C}$  for 6 h was more uniform compared to pellet sintered in air. The average grain size for this sample was  $45\ \mu\text{m}$ . Another interesting feature of this sample is that a lot of fine pores of about  $5\ \mu\text{m}$  diameter were trapped in the grains.

### 6.3.3 Uranium distribution

To measure the distribution of Th, U and O in the  $\text{ThO}_2$  rich matrix, a detailed study was carried out by scanning the electron beam across the duplex structure with EPMA.

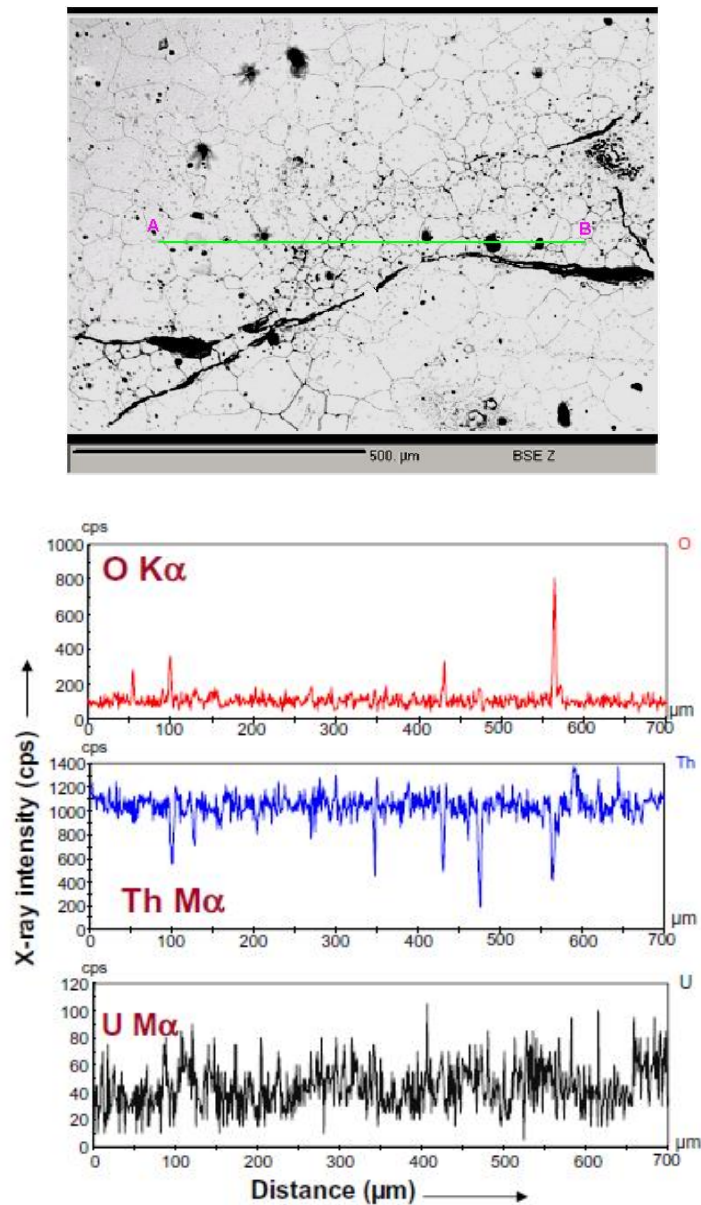


*Figure 6.12 : X-ray line scan for Th Ma, U Ma and O Ka across the grain structure of  $\text{ThO}_2$ -4% $\text{UO}_2$  pellet sintered in air (1400°C, 6 h).*

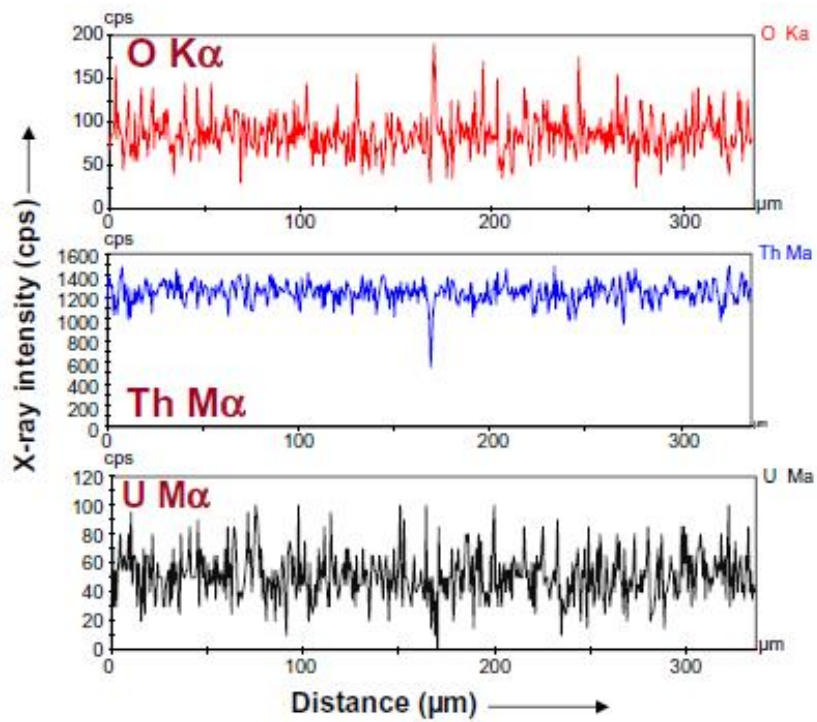
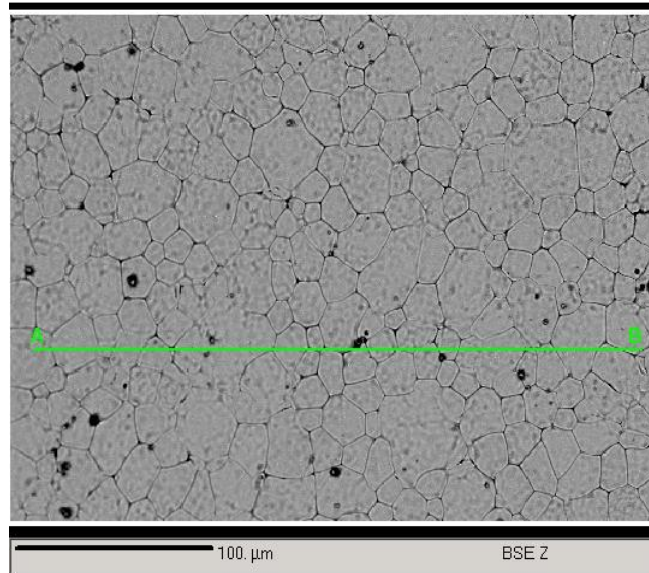


*Figure 6.13 : X-ray line scan for Th M $\alpha$ , U M $\alpha$  and O K $\alpha$  across the grain structure of ThO<sub>2</sub>-4%UO<sub>2</sub> pellet sintered in Ar-8%H<sub>2</sub> (1650°C, 6 h).*

An X-ray line scan result for Th  $M\alpha$ , U  $M\alpha$  and O  $K\alpha$  of the  $\text{ThO}_2$ -4% $\text{UO}_2$  pellet sintered in air is shown Figure 6.12. The line scan intensities show a marginal increase in U concentration in the large grains of  $\text{ThO}_2$ -4% $\text{UO}_2$  pellet. The scan was also carried out on the above composition sample sintered in Ar-8% $\text{H}_2$  and is given in Figure 6.13. The line scan shows that the uranium concentration does not change in the pellet.

For the pellet sintered in air, the line scanning of two separate colonies of fine grains revealed that uranium has diffused to the  $\text{ThO}_2$  granules and vice versa. Semi-quantitative analysis on the large grains (uranium rich) and also on the small grains (thorium rich) has been carried out. The uranium concentration in the large grains was slightly higher than that in the smaller grains. The average uranium concentrations were 3.65 and 3.40 wt% in the large and small grains, respectively. The concentration of uranium in large grains is substantially lower than that of the starting material.

This result confirms that an interdiffusion has occurred between  $\text{ThO}_2$  and  $(\text{Th,U})\text{O}_2$  across the interface. The distribution of uranium in  $\text{ThO}_2$ -4% $\text{UO}_2$  pellets sintered in Ar-8% $\text{H}_2$  atmosphere was found to be uniform throughout the pellet. The reason for better homogeneity of the pellet sintered in reducing atmosphere may be the higher temperature (1650°C) used for sintering. The oxygen potential of  $\text{Th}_{1-y}\text{U}_y\text{O}_{2+x}$  solid solution also increases with increase in temperature for the same uranium concentration (y). These factors helped in achieving better homogeneity for  $\text{ThO}_2$ -4% $\text{UO}_2$  pellet when sintered in reducing atmosphere.

### 6.3.4 XRD

The XRD data of ThO<sub>2</sub>-4%UO<sub>2</sub> pellets sintered either in Ar-H<sub>2</sub> or air showed the presence of only of fluorite phase. The O/M ratio of ThO<sub>2</sub>-4%UO<sub>2</sub> pellets sintered in Ar-8%H<sub>2</sub> was found to be 2.00 and that for the pellets sintered in air was found to be slightly higher (2.01). Table 6.7 gives the details of the lattice parameters and phases of the samples of the above compositions.

*Table 6.7 : Phase, Lattice parameter and O/M ratio of ThO<sub>2</sub>-4%UO<sub>2</sub> sintered pellets.*

<b>Coating powder</b>	<b>Sintering details</b>	<b>Phases present</b>	<b>Lattice parameter (nm)</b>	<b>Mol. Fraction of UO<sub>2+x</sub> in fluorite phase</b>	<b>O/M ratio</b>
ThO <sub>2</sub> -50%UO <sub>2</sub>	1400°C, 6h, Air	Fluorite	0.55912	0.0360	2.01
ThO <sub>2</sub> -50%UO <sub>2</sub>	1400°C, 6h, Ar-8%H <sub>2</sub>	Fluorite	0.55923	0.0365	2.00

The high density ThO<sub>2</sub>-UO<sub>2</sub> pellets could be fabricated by the CAP process using ThO<sub>2</sub> agglomerates and co-precipitated ThO<sub>2</sub>-UO<sub>2</sub> fine powders without the addition of any extraneous dopants or sintering aids. The size of colonies of fine grains were in the range 75–100 μm which was smaller compared to the size of the fine grained colony of 100–150 μm in CAP pellets prepared with pure oxide powders . These fine grained colonies were not very dense as some fine porosity could be observed in the pellets. These colonies represent the initial ThO<sub>2</sub> agglomerates, which were used for making green pellets. All the granules were found to get fused with each other and showed no boundaries indicating that diffusion has

occurred between  $\text{ThO}_2$  and  $(\text{Th,U})\text{O}_2$ . This was confirmed by the XRD patterns as shown in Figure 6.14.

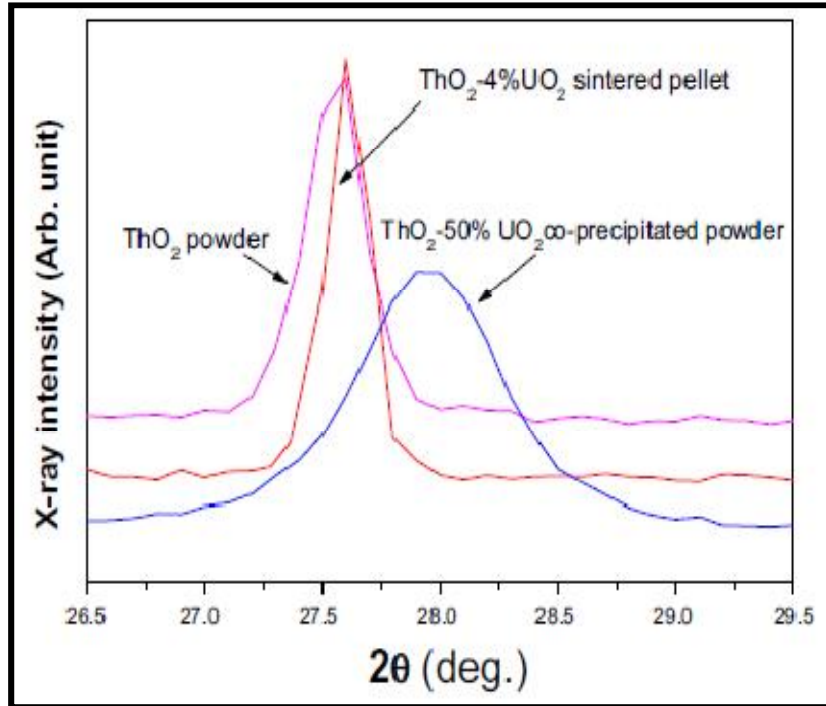


**Figure 6.14 :** XRD patterns of  $\text{ThO}_2$  and  $\text{ThO}_2$ -50% $\text{UO}_2$  powders used along with  $\text{ThO}_2$ -4% $\text{UO}_2$  sintered pellet (1400 °C in air for 6 h).

From the peak positions, it is clear that the solid solution has formed between  $\text{ThO}_2$  and  $\text{ThO}_2$ -50% $\text{UO}_2$ .  $\text{ThO}_2$  is the only stable oxide in the Th-O system in the condensed phase and it has very little non-stoichiometry compared to  $\text{UO}_2$ . Hence, the defect concentration in  $\text{ThO}_2$  is low. Since the grain growth is a diffusion related phenomenon, it depends upon the defect concentrations such as oxygen interstitials or metal vacancies. Therefore, the grain growth has not enhanced inside the colonies. The sintering temperatures also have a significant role in the process of grain growth. Generally, diffusion processes are more prominent at temperatures  $>0.5T_m$ . As the temperature of the sintering used in this

study was lower than  $0.5T_m$ , smaller grain sizes could be attributed to the sintering temperature. These two factors resulted in small grains in the initial  $\text{ThO}_2$  colonies.

The large grains observed in the coating can be explained as follows. The  $(\text{Th,U})\text{O}_2$  powders used for coating have a higher O/M ratio and larger surface area and have two phases. Such properties of surface area and O/M ratio cause to give higher density pellets after sintering. The larger surface area corresponds to higher surface energy. The driving force for sintering is the reduction in surface energy. The higher O/M ratio indicates the presence of higher concentration of oxygen interstitials. The presence of small amount of  $\text{U}_3\text{O}_8$  in the starting powder is also assumed to have made a significant contribution to enhance sintering. The amount of  $\text{U}_3\text{O}_8$  in  $\text{ThO}_2$ -50% $\text{UO}_2$  powder is given in Table 3.5. It has been demonstrated that the addition of small quantities of  $\text{U}_3\text{O}_8$  to  $\text{ThO}_2$  enhances sintering, resulting in formation of high quality  $\text{ThO}_2$ - $\text{UO}_2$  pellets without the use of conventional dopants such as  $\text{CaO}$  and  $\text{Nb}_2\text{O}_5$ , which also causes to reduce the impurity level in the pellets [200, 201]. On increasing the temperature, the deviation from stoichiometry becomes considerably large in the  $\text{ThO}_2$ - $\text{UO}_2$  pellets, generating a larger number of oxygen interstitial defects. Since the diffusion coefficient of U,  $D_U$ , is proportional to the square of the oxygen excess ( $x^2$ ) in the lattice, sintering as well as grain growth is enhanced thus resulting in larger grains.

Sintering in reducing atmosphere resulted in the formation of a uniform microstructure with very large grains with excellent homogeneity. In the materials of the fluorite structure, the metal atoms diffuse at a much smaller rate than the non-metal atoms. The latter will therefore be rate-controlling for any diffusion controlled high temperature

kinetic process. Though the predominant defects in the fluorite structure are anion defects, the less mobile cation defects, which occur at much smaller concentrations, are frequently rate determining for important high temperature mass transport processes, such as grain growth, sintering, plastic deformation and creep.

Although sintering in oxidizing atmosphere is enhanced by the presence of defects due to the non-stoichiometry, the higher temperature used in reducing atmosphere helps in creating more intrinsic defects and helps in sintering. The higher values of diffusion coefficient (two orders) at 1650°C and holding at that temperature for 6 h resulted in the destruction of the duplex structure and in the improvement of the microhomogeneity.

In other words, coating of the ThO<sub>2</sub> granules with (Th,U)O<sub>2</sub> powder gives comparatively more uniform microstructure than that with U<sub>3</sub>O<sub>8</sub> powder.

#### **6.4 Summary**

Following conclusions are drawn from studies both experimental and theoretical conducted on (Th,U)O<sub>2</sub> system fabricated by conventional powder pellet route and coated agglomerate pelletization route for various properties:

- i. The microstructure of CAP pellets of (Th,UO)<sub>2</sub> showed small grains in the centre of granules and large grains along the periphery.
- ii. The EPMA studies on CAP pellets of (Th,UO)<sub>2</sub> confirmed uranium concentration was slightly higher in large grained areas.
- iii. The experimental measurements of CTE of (Th,U)O<sub>2</sub> as a function of temperature and values are in good correlation with MD calculated values.

- iv. Thermal diffusivity and thermal conductivity studies revealed that results of  $(\text{Th,U})\text{O}_2$  pellets fabricated by coated agglomerate pelletization technique were quite comparable with that of pellets of similar composition fabricated by conventional powder metallurgical route over a range of temperatures from 873 K to 1773 K and the deviation was marginal.
- v. The experimental studies show that, CTE values are not affected by micro-inhomogeneity majorly. On the other hand, cumulative effect of the O/M and porosity affect the thermal conductivity especially in the lower temperature range.
- vi. Thermal conductivity of  $\text{ThO}_2$  and  $\text{ThO}_2$ -6 wt.%  $\text{UO}_2$  calculated by experimental measurements show good agreement with MD calculated as well as reported values.
- vii. Thermal conductivity of  $\text{ThO}_2$  decreased with the addition of  $\text{UO}_2$  which was prominent at temperatures below 1300 K.
- viii. Thermal diffusivity and thermal conductivity studies revealed that results of  $(\text{Th,U})\text{O}_2$  pellets fabricated by coated agglomerate pelletization technique were quite comparable with that of pellets of similar composition fabricated by conventional powder metallurgical route over a range of temperatures from 873 K to 1773 K and the deviation was marginal. The decrease in thermal conductivity of CAP pellets of  $(\text{Th,UO})_2$  pellet could be attributed to their higher O/M ratio and lower density.
- ix. Uniform grained microstructure and better homogeneity in CAP pellets could be achieved by using co-precipitated powders of  $(\text{Th,U})\text{O}_2$  instead of  $\text{U}_3\text{O}_8$  powder under reducing atmosphere sintering.

## CHAPTER 7. CONCLUSIONS

### 7.1 Main Conclusions

The main highlights of the studies on (Th,Ce)O<sub>2</sub>, (Th,U)O<sub>2</sub> and (Th,Pu)O<sub>2</sub> systems are collectively summarized below:

- i) The homogeneity of the powders in the green pellets had considerable effect on the sintering behavior of the pellets as well as on the pellet characteristics.
- ii) Sintering temperature was major factor influencing the densification phenomenon and was instrumental for high pellet densities especially in reducing atmosphere.
- iii) In CAP green pellets of hypo-stoichiometric materials such as Ce or Pu, sintering in reducing atmosphere lowers the valence state and thereby accelerates the diffusion kinetics. Higher cationic interdiffusion resulted in better homogeneity in pellets compared to that sintered in air.
- iv) Large variation was observed between the POP and CAP pellets with respect to homogeneity and density in the case of air sintering compared to sintering in reducing atmosphere. POP pellets showed higher density compared to CAP pellet when sintered in air.
- v) In all systems studied, POP and CAP pellets sintered in reducing atmosphere exhibited almost similar densities ~93%T.D due to high sintering temperatures.
- vi) POP pellets sintered in air and reducing atmosphere exhibited similar microstructure with average grain size of ~ 6 μm and pore size of 3 μm uniformly distributed in the matrix respectively.

- vii) The pellets fabricated by CAP process sintered in both oxidative and reducing atmospheres showed similar microstructure which was duplex in nature consisting of colonies of fine grains ( $\sim 4 \mu\text{m}$ ) and large grains ( $\sim 10\mu\text{m}$ ) in the case of oxidative sintering. The pores of size ( $\sim 3 \mu\text{m}$ ) were preferentially located in the vicinity of large grains. In the case of CAP pellets sintered in reducing atmosphere, sizes of the grains were larger (fine grains of  $\sim 5 \mu\text{m}$  and larger grains of  $\sim 26 \mu\text{m}$ ). The size of pores preferentially located at large grain regions was also higher ( $\sim 8\mu\text{m}$ ).
- viii) In CAP pellets a direct correlation of grain size with the concentration of dopants (Ce/U) could be established through EPMA studies.
- ix) Hyper-stoichiometric thorium mixed oxides exhibited poor sintering characteristics in oxidative atmosphere which could be attributed to poor solubility of  $\text{U}_3\text{O}_8$  and higher oxides formed, in  $\text{ThO}_2$  matrix.
- x) Use of co-precipitated powders of  $(\text{Th,U})\text{O}_2$  instead of  $\text{U}_3\text{O}_8$  powder aided in achieving uniform grained microstructure of average grain size  $\sim 45 \mu\text{m}$  and better homogeneity in CAP pellets by sintering in reducing atmosphere.
- xi) POP pellets sintered in reducing atmosphere had lower O/M ratio compared to CAP pellets.
- xii) The X-ray Diffraction studies on CAP and POP pellets confirmed presence of single phase solid solution in the pellets. POP as well as CAP samples showed a shift in XRD peak shift in peak maxima to higher angles compared to  $\text{ThO}_2$  peak indicating contraction of lattice due to substitution of Th by Pu /U/Ce atoms. XRD peaks of CAP sample indicated higher concentration of dopant in solid solution for

- same nominal composition as that of POP sample. Additionally XRD could also reveal presence of heterogeneity in the CAP sample.
- xiii) Thermogravimetry studies confirmed lower O/M ratio in POP samples compared to CAP samples. DTG studies showed single step oxidation of POP and CAP samples indicating presence of only one phase in concurrence with XRD studies.
  - xiv)  $C_p$  measured values of  $\text{ThO}_2$ -5% $\text{CeO}_2$  POP and CAP pellets (sintered in air and Ar- $\text{H}_2$  atmosphere) were within  $\pm 5\%$  deviation of Neumann-Kopp's values over the temperature range (300-763 K) confirming applicability and validity of Neumann-Kopp's values for estimating the thermal conductivity of (Th,Pu) $\text{O}_2$  MOX system using specific heat values of pure oxide systems.
  - xv) MD simulation studies validated by dilatometric experiments confirmed that the thermal expansion coefficient of (Th,Pu) $\text{O}_2$  increases with an increasing  $\text{PuO}_2$  content which was higher compared to that of  $\text{ThO}_2$ . The difference in fabrication methods and conditions affect the porosity content, O/M ratio and the extent of homogeneity in the samples which were cumulatively responsible for the deviation in CTE values among the pellet samples.
  - xvi) The MD calculated thermal expansion coefficients ( $\alpha$ ) values were higher than the experimentally measured  $\alpha$  values as MD calculations were performed on a model system with homogeneous distribution of  $\text{CeO}_2$  in  $\text{ThO}_2$  matrix with no incorporation of porosity and impurity effects.
  - xvii) Incorporation of  $\text{PuO}_2$  /  $\text{CeO}_2$ /  $\text{UO}_2$  which have higher thermal expansion coefficient and are also responsible for the decrease in the lattice parameter of the system causes increased interaction between the phonons and atoms.

- xviii) The coefficients of thermal expansion for  $\text{ThO}_2$ –6% $\text{PuO}_2$  pellets in the temperature range 300–1773K was found to be  $11.99 \times 10^{-6}/^\circ\text{C}$  whereas coefficient of thermal expansion for  $\text{ThO}_2$ –6% $\text{UO}_2$  was  $10.098 \times 10^{-6}/^\circ\text{C}$ . It was attributed to incorporation of U in Th lattice had lesser effect compared to Pu incorporation because of difference in coefficient of thermal expansion and higher lattice parameter.
- xix) The differential diametrical expansion between the POP and CAP pellets of 10mm diameter at 1000 K was calculated for  $(\text{Th},5\%\text{Ce})\text{O}_2$  and  $(\text{Th},1\%\text{Pu})\text{O}_2$  was found to be  $\sim 2.2 \mu\text{m}$  and  $\sim 1.2 \mu\text{m}$  respectively. For higher compositions up to  $(\text{Th},6\%\text{Pu})\text{O}_2$  the diametrical difference between the pellets is expected to be less than 30  $\mu\text{m}$ . Studies concluded that the thermal expansion effect on fuel was negligible and at lower temperatures the difference would be correspondingly smaller. The studies affirmed that the inhomogeneity exhibited by the CAP pellets has inconsequential or negligible effect on thermal expansion of pellet even at very high temperatures.
- xx) The pore characteristics (bigger pore sizes, higher porosity fraction, pore concentration along the grain boundaries and inter-connectivity of pores) and inhomogeneity in the CAP pellets were collectively responsible for decrease in thermal diffusivity and conductivity compared to POP pellets. The CAP pellets exhibited lower thermal conductivity compared to POP pellets because of higher scattering of phonon due to cumulative effect of porosity, inhomogeneity and lower O/M ratio compared to the POP pellets sintered in same atmosphere. The effect of inhomogeneity on thermal expansion and thermal conductivity was not very pronounced as compared to that of porosity and O/M (stoichiometry) of the MOX pellets. The difference in thermal conductivity values of  $(\text{Th},\text{Ce})\text{O}_2$  pellets processed

by different fabricated routes became insignificant at higher temperatures due to different pellet characteristics.

- xxi) Coulomb–Buckingham type potential model developed and used in the thermal property study could predict precisely the lattice parameters as a function of temperature for MOX solid solutions were in good agreement with experimental measurements on (Th,Ce)O<sub>2</sub>. Thermal conductivity of MD simulations using Coulomb–Buckingham–Morse–many–body (BMM) potential could evaluate mechanical and thermal properties of ThO<sub>2</sub> and (Th,Ce)O<sub>2</sub> MOX. Coulomb–Buckingham–Morse–many–body potential as well as Coulomb–Buckingham type potential model are useful for predicting thermal expansion and thermal conductivity values of ThO<sub>2</sub> and (Th,Ce)O<sub>2</sub> MOX. (Th,Ce)O<sub>2</sub> strongly depends on CeO<sub>2</sub> concentration at low temperatures and decreases with an increase in temperature. The decrease in thermal conductivity at 500 K is larger than that at 1500 K and at higher temperatures (above 900 K), the thermal conductivity of (Th,Ce)O<sub>2</sub> is almost independent of CeO<sub>2</sub> concentration. Moreover, thermal diffusivity values of CAP pellet are 5% lower than POP pellets in the 873–1513 K temperature range even though porosity content and O/M ratio of the POP and CAP pellets are almost similar. The difference can be attributed to the inhomogeneous distribution of PuO<sub>2</sub> in the ThO<sub>2</sub> matrix. The reduction in thermal diffusivity values of ThO<sub>2</sub>–1%PuO<sub>2</sub> (POP pellets) compared to pure ThO<sub>2</sub> is 20% at temperature 873 K and 7% at 1413 K. Similarly, the reduction in thermal diffusivity values of ThO<sub>2</sub>–6%PuO<sub>2</sub> (POP pellets) compared to pure ThO<sub>2</sub> is 46% at temperature 873 K and 37% at 1413 K.

- xxii) Marginal difference of  $< 4\%$  was observed between the thermal conductivity of CAP pellet ( $5.03 \text{ Wm}^{-1}\text{K}^{-1}$ ) and POP pellet ( $5.24 \text{ Wm}^{-1}\text{K}^{-1}$ ) at 873 K in the case of  $(\text{Th,Pu})\text{O}_2$  which further reduced with increased temperature. Studies predicted for a particular linear heat rating, the change in centreline temperature by replacement of POP pellet with CAP pellet would be about  $40^\circ\text{C}$ .
- xxiii) Both experimental and MD studies conclude that heterogeneous distribution of plutonium observed in the CAP pellets did not significantly impact the thermal conductivity of the fuel. The experimental measurements of CTE of  $(\text{Th,U})\text{O}_2$  as a function of temperature and values are in good correlation with MD calculated values. Thermal diffusivity and thermal conductivity studies revealed that results of  $(\text{Th,U})\text{O}_2$  pellets fabricated by coated agglomerate pelletization technique were quite comparable with that of pellets of similar composition fabricated by conventional powder metallurgical route over a range of temperatures from 873 K to 1773 K and the deviation was marginal. The micro-inhomogeneity and porosity had cumulative effect on the thermal conductivity specifically in the lower temperature range. Thermal conductivity of  $\text{ThO}_2$  and  $\text{ThO}_2$ -6 wt.%  $\text{UO}_2$  calculated by experimental measurements show good agreement with MD calculated as well as reported values. Thermal conductivity of  $\text{ThO}_2$  decreased with the addition of  $\text{UO}_2$  and was prominent at temperatures below 1300K. Thermal diffusivity and thermal conductivity studies revealed that results of  $(\text{Th,U})\text{O}_2$  pellets fabricated by coated agglomerate pelletization technique were quite comparable with that of pellets of similar composition fabricated by conventional powder metallurgical route over a range of temperatures from 873K to 1773 K and the deviation was marginal. The decrease in

- thermal conductivity of CAP pellets of (Th,U)O<sub>2</sub> pellet could be mainly attributed to their higher O/M ratio and lower density.
- xxiv) The segmented counts of CAP fuel pin gamma scan were within a statistical fluctuation of three standard deviations ( $\pm 3\sigma$ ) which is equivalent to  $\pm 6\sigma$  of the POP fuel pin gamma scan. PGS Studies on (Th,Pu)O<sub>2</sub> fuel pins confirmed that CAP pellets also conformed to statistical quality control limits.
- xxv) Ionic conductivity of POP pellets was higher compared to CAP pellets when sintered in air whereas in the case of sintered POP and CAP samples sintered in reducing atmosphere showed similar ionic conductivities. Studies concluded that inhomogeneity in the pellets affected their ionic conductivity.
- xxvi) Pellets (hypo-/ hyper-stoichiometric oxide) sintered in reducing atmosphere at high temperatures possessed optimal combination of desired properties such density, homogeneity, grain size and porosity required in nuclear fuels.

## **7.2 Novel Techniques Developed**

Furthermore, during the course of this research work, a few novel techniques were developed, investigated and employed.

- i. Alpha autoradiography coupled with UV-Vis spectroscopy and image analysis were effective techniques for quantification of homogeneity and composition estimation of (Th,Pu)O<sub>2</sub> pellets. These techniques had potential as an alternative to standard methods like SEM or EPMA for Pu bearing material. Besides these applications, these techniques could be employed possibly for:
  - determination of Pu content of unknown samples,

- homogeneity and compositional characterization of samples with higher Pu content,
  - most importantly, conduct characterization on pellets irrespective of associated doses, and
  - address some key issues of fuel fabrication.
- ii. Demonstration of microwave dissolution technique will largely benefit the fuel reprocessing because of its efficiency. Experiments using microwave and standard technique were carried out for dissolution of (Th,Pu)O<sub>2</sub> for chemical analysis of impurities and heavy metal content.

### **7.3 POP versus CAP**

The microstructure and homogeneity of the CAP pellets was found to be distinctively different from that of pellets fabricated by the conventional POP route. The CAP pellets had the duplex grain structure and the pores preferential concentrated at the grain boundaries of large grains of higher fissile concentration. This is expected to be beneficial for fuel performance in the reactor. Due to higher fissions in large grained regions of CAP pellets, there would be decreased fission gas release due to increased migration lengths. The released fission gas would be accommodated in the pores surrounding the large grains. Reduced fission gas release is known to help in maintaining the gap conductance and the pellet centerline temperature. The fine grains present should help in reducing the pellet clad mechanical interaction by reducing creep resistance and improving plasticity of the fuel at high temperatures. This should help in reducing the fuel related stress on the clad.

Furthermore, the experimental and theoretical studies provided conclusive evidence that the crucial thermal properties of the pellets are not much affected by the pellet inhomogeneity. Hence the in-reactor thermal behavior and associated other phenomena should not be adversely affected by replacement of POP fuel pellets with CAP fuel pellets.

Coated agglomerate pelletization (CAP) process because of its inherent advantages of being a safe, amenable to automation and remotization and with capability of high production of pellets with desired characteristic and properties for better in-reactor performance promises to be technologically viable and promising fabrication route for nuclear fuels especially containing high specific activity fissile materials. However, Irradiation studies using CAP fuel pellets required to be conducted to validate and critically evaluate the extent of effect of their microstructure, homogeneity and porosities on design life of fuel.

#### **7.4 Recommendations for Future Work**

The present work could be extended further which shall be useful for better understanding of fuel properties and its behavior. Some of the suggestions for future work are listed below:

- Studies using different binder material compatible with oleic acid for better agglomeration and improving further the properties may be explored.
- Further studies on CAP process may be conducted by using dopants for tailoring the microstructure or fissile material solution for attaining better homogeneity of fissile material distribution, if desired.
- Development of techniques for characterization of pellets in glove box environment, especially for Plutonium bearing pellets is highly necessitated.

- Microwave sintering studies of thoria based pellets and applicability on large quantities requires to be highly desirable to exploit the huge benefits of reduction in sintering time at lower temperatures. A further study of applicability in different sintering atmospheres also requires to be pursued.
- Post irradiation examination of irradiated CAP fuels for understanding and predicting the mechanism operational in the pellet and its behavior, it shall also help in developing computerised codes for better prediction of its behavior.
- Dissolution studies of CAP pellets of  $(\text{Th,Pu})\text{O}_2$  using microwave requires to be undertaken as it shall hugely impact the reprocessing activities by drastically cutting down the processing time and costs.
- Similar simulation using CAP for other fuel systems such as carbide, nitride etc. will be beneficial.

## References

---

1. Uranium 2014: Resources, Production and Demand, OECD Nuclear Energy Agency and the International Atomic Energy Agency.
2. IAEA–TECDOC–1450, Thorium fuel cycle– Potential benefits and challenges, International Atomic Energy Agency, Vienna, May 2005.
3. M. Lung, O. Gremm, Nucl. Engg. and Design, 180 (1998) 130–146.
4. C. Ganguly, Indian Journal of Technology, 28 (1990) 296– 319.
5. J. Belle, R.N. Berman. DOE/NE–0060, DE85 006670 (1984) 74.
6. Z. Xianfeng, M.J. Driscoll, M.S. Kazimi. Trans. Am. Nucl. Soc.80 (1999) 43.
7. T.R.G. Kutty, K.B. Khan , P.V. Achuthan , P.S. Dhami , A. Dakshinamoorthy , P.S. Somayajulu , J.P. Panakkal , Arun Kumar , H.S. Kamath. J. Nucl. Mat., 389 3 (2009) 351–358.
8. C. Ganguly, Bulletin of Materials Science,16 6 (1993) 509–522.
9. P.M. Khot, Y.G. Nehete, A.K. Fulzele, C. Baghra, A.K. Mishra, M. Afzal, J.P. Panakkal, H.S. Kamath. J. Nucl. Mater. 420 (2012) 1–8.
10. R.K. Sinha, A. Kakodkar, Nucl. Engg. and Design, 236 (2006) 683–700.
11. T. Soreng, A.P. Karande, A.K. Fulzele D.B. Sathe, A. Prakash, Mohd Afzal, J.P. Panakkal. NDE 2011, (2011), 319–321.
12. P.S. Somayajulu, Mohd. Afzal, Arun Kumar, H.S. Kamath, INSAC 2000, 1 (2000) 174.
13. H.S. Kamath, 14th Annual Conference of Indian Nuclear Society, (2003) 17–19.

14. R.J.M. Konings, O. Beneš, A. Kovács, D. Manara, D. Sedmidubský, L. Gorokhov, V.S. Iorish, V. Yungman, E. Shenyavskaya, and E. Osina, *J. Phys. Chem. Ref. Data*. Vol.43, No.1, (2014 ) 013101–013192.
15. J.R. Mathews, *J. Chem. Soc. Faradays Trans.* 83 (2) (1987) 1273.
16. J. Belle and B. Lustman, in: *Properties of UO<sub>2</sub>, Fuel Elements Conference, Paris, TID–7546, 1958, 442.*
17. D.R. Olander, *Fundamental Aspects of Nuclear Reactor Fuel Elements, TID–26711–P1, US Department of Energy, (1976), 145.*
18. D.L. Johnson, T.M. Clarke, *Acta Metall.* 12 (1964) 1173.
19. R.L. Coble, *J. Am. Ceram. Soc.* 41 (1958) 55.
20. D.L. Johnson and I.B. Cutler, *J. Am. Ceram. Soc.* 46 (1963) 541.
21. W.D. Kingery and M. Berg, *J. Appl. Phys.* 26 (1955) 1205.
22. L. Berrin and D.L. Johnson, in: G.C. Kuczynski, N.A. Hooton, C.F. Gibbs (Eds.), *Sintering and Related Phenomena, Gordon and Breach, New York, (1967), 369.*
23. D.L. Johnson, *J. Appl. Phys.* 40 (1969) 192.
24. T.R.G. Kutty, K.B. Khan, P.S. Somayajulu, A.K. Sengupta, J.P. Panakkal, A. Kumar, H.S. Kamath, *J. Nucl. Mater.* 373 (2008) 299–308.
25. T.R.G. Kutty, R.V. Kulkarni, P. Sengupta, K.B. Khan, K. Bhanumurthy, A.K. Sengupta, J.P. Panakkal, A. Kumar, H.S. Kamath, *J. Nucl. Mater.* 373 (2008) 309–318.
26. T.R.G. Kutty, P.S. Somayajulu, K.B. Khan, A. Kumar, H.S. Kamath, *J. Nucl. Mater.* 384 (2009) 303–310.

27. T.R.G. Kutty, M.R. Nair, P. Sengupta, U. Basak, A. Kumar, H.S. Kamath, *J. Nucl. Mater.* 374 (2008) 9–19.
28. A. Fernandez, K. Richter, J. Somers, *J. Alloys Compd.* 271 (1998) 616–619.
29. K. Richter, A. Fernandez, J. Somers, *J. Nucl. Mater.* 249 (1997) 121–127.
30. N. Boucharat, A. Fernandez, J. Somers, R.J.M. Konings, D. Haas, In: 6th IMF workshop, Strassbourg, *Prog. Nucl. Energy* 38 (2001) 291–294.
31. A. Fernandez, D. Haas, R.J.M. Konings, J. Somers, *J. Am. Ceram. Soc.* 85 (2002) 694–696.
32. M. Lung, A present review of the thorium nuclear fuel cycles. European Commission Report EUR–17771, Luxembourg (1997).
33. R.E. Brooksbank, J.R. Parrott, E.L. Youngblood, W.T. McDuffee, In: Conf–740523–1, VII International Congress of Societe Francaise de Radioprotection, (1974) Versailles, France.
34. R.E. Brooksbank, in: 2nd international conference of thorium fuel cycle, Gatlinburg, (1966).
35. J. Belle, R.M. Berman, Thorium dioxide: properties and nuclear applications. Naval Reactors Office, DOE. Government Printing Office, (1984) Washington, DC.
36. Hj. Matzke, in: T. Sorensen (Ed.), *Non–stoichiometric Oxides*, Academic, New York, (1981), 156.
37. Hj. Matzke, Atomic Energy Canada Ltd. Report AECL –2585, (1966).
38. A.B. Lidiard, *J. Nucl. Mater.* 19 (1966) 106.
39. P. Balakrishna, B.P. Varma, T.S. Krishnan, T.R.R. Mohan, P. Ramakrishnan, *J. Nucl. Mater.* 160 (1988) 88.

40. K.C. Radford, J.M. Pope, *J. Nucl. Mater.* 116 (1983) 305.
41. K. Ananthasivan, S. Anthonysamy, C. Sudha, A.L.E. Terrance, P.R. Vasudeva Rao, J. *Nucl. Mater.* 300 (2002) 217.
42. H.R. Hoekstra, S. Siegel, L.H. Fuchs, J.J. Katz, *J. Phys. Chem.* 59 (1955) 136.
43. M.D. Karkhanavala and A.M. George, *J. Nucl. Mater.* 19 (1966) 267.
44. H. Chevrel, P. Dehaut, B. Francois, J.F. Baumard, *J. Nucl. Mater.* 189 (1992) 175.
45. R. Paul, C. Keller, *J. Nucl. Mater.* 41 (1971) 133.
46. T.R.G. Kutty, P.V. Hegde, J. Banerjee, K.B. Khan, A.K. Sengupta, G.C. Jain, S. Majumder, H.S. Kamath, *J. Nucl. Mater.* 312 (2003) 224–235.
47. A.D. King, *J. Nucl. Mater.* 38 (1971) 347.
48. H.J. Matzke, *J. Nucl. Mater.* 21 (1967) 190.
49. D.R. Olander, *J. Nucl. Mater.* 144 (1987) 105.
50. H.J. Matzke, *J. Phys. Colloque C7* 37 (1976) 452.
51. R.J. Hawkins and C.B. Alcock, *J. Nucl. Mater.* 26 (1967) 112.
52. H. Furuya, *J. Nucl. Mater.* 26 (1968) 123.
53. M.T. Aybers, *J. Nucl. Mater.* 210 (1994) 73.
54. W.S. Young and I.B. Cutler, *J. Am. Ceram. Soc.* 53 (1970) 659–63.
55. J. Wang and R. Raj, *J. Am. Ceram. Soc.* 73 (1990) 1172–75.
56. K. Matsui, I. N. Ohmich, M. Ohgai, M. Enomoto, J. Hojo, *J. Am. Ceram. Soc.* 88 (12) (2005) 3346–52.
57. H. Palmour, M.L. Huckabee, T.M. Hare, in ed. M.M. Rustic, *Sintering – New Developments*, Elsevier, Amsterdam, (1979) 46.
58. M.L. Huckabee and H. Palmour, *Ceramic Bull.* 51 (1972) 574.

59. J.E. Dorn, in: R. Maddin (Ed.), Creep and Recovery, American Society for Metals, Cleveland, OH, (1957), p. 255.
60. R.P.C. Schram, J. Nucl. Mater. 344(2005)223–229.
61. A.C. Momin and K.S. Venkateswarlu, BARC report BARC–1171, Bhabha Atomic Research Centre, Trombay (1982).
62. M. Amaya, K. Une, M. Hirai, J. Nucl. Sc. Tech. 41 (2004) 108–15.
63. C. Ronchi and G.J. Hyland, J. Alloys Compd. 213/214 (1994) 159–68.
64. J.K. Fink and M.C. Petri, in: Thermophysical Properties of Uranium Dioxide, Argonne National Laboratory Report, ANL/RE–97/2 (February 1997).
65. J.C. Southard, J. Amer. Chem. Soc., 63 (1941) 3142–46.
66. D.F. Fischer, J.K. Fink, L. Leibowitz, J. Nucl. Mater. 118 (1983) 342–48.
67. D.F. Fischer, J.K. Fink, L. Leibowitz, J. Nucl. Mater. 102 (1981) 220–22.
68. R.A. Young, J. Nucl. Mater. 87 (1979) 283–96.
69. S. Dash, S.C. Parida, Z. Singh, B.K. Sen, V. Venugopal, J. Nucl. Mater. 393 (2009) 267–81.
70. R.V. Krishnan and K. Nagarajan, J. Therm. Anal. Calorim. 102 (2010) 1135–40.
71. R. Kandan, R. Babu, P. Manikandan, R.V. Krishnan, K. Nagarajan, J. Nucl. Mater. 384 (2009) 231–35.
72. S. Anthonysamy, J. Joseph, P.R. Vasudeva Rao, J. Alloys Compd. 299 (2000) 112–17.
73. G.E. Moore, K.K. Kelley, J. Amer. Chem. Soc. 69 (1947) 2105.
74. K. Bakker, E.H.P. Cordfunke, R.J.M. Konings, R.P.C. Schram, J. Nucl. Mater. 250 (1997) 1–12.

75. Y.S. Touloukian, R.K. Kirby, R.E. Taylor, T.Y.R. Lee, Thermal Expansion. Nonmetallic Solids (IFI/Plenum, New York, 1970).
76. D.G. Martin, J. Nucl. Mater. 152 (1988) 94.
77. J.K. Fink, J. Nucl. Mater. 279 (2000) 1–18.
78. A.C. Momin, E.B. Mirza, M.D. Mathews, J. Nucl. Mater. 185 (1991) 308.
79. P. Rodriguez, C.V. Sundaram, J. Nucl. Mater. 100 (1981) 227.
80. A.K. Tyagi and M.D. Mathews, J. Nucl. Mater. 278 (2000) 123–25.
81. S. Anthonysamy, G. Panneerselvam, S. Bera, S.V. Narasimhan, P.R. Vasudeva Rao, J. Nucl. Mater. 281 (2000) 15–21.
82. A.C. Momin, J. Nucl. Mater. 185 (1991) 308–310.
83. A.C. Momin, M.D. Karkhanavala, High Temp. Sci. 10(1978) 45.
84. C.P. Kempter, R.O. Elliott, J. Chem. Phys. 30 (1959) 1524–1526.
85. J.R. Springer, E.A. Eldrige, M.U. Goodyear, T.R. Wright, J.F. Langedrost, Battelle Memorial Institute Report BMI–X–10210, 1967.
86. M.H. Rand, in: Thorium: Physico–chemical properties of its compounds and alloys, Atomic Energy Review, Special issue no. 5, IAEA, Vienna, 1975, p.7.
87. R.M. Berman, T.S. Tully, J. Belle, I. Goldberg, (1972) The thermal conductivity of polycrystalline thoria and thoria–urania solid solution. LMWR Development Program WAPD–TM–908.
88. P.S. Murti and C.K. Mathews, J. Phys. D 24 (1991) 2202–2209.
89. P.G. Lucuta, H.J. Matzke, I.J. Hastings, J. Nucl. Mater. 232 (1996) 166–180.
90. C.G.S. Pillai and P. Raj, J. Nucl. Mater. 277 (2000) 116–119.

91. J. Belle, R.M. Berman, W.F. Bourgeois, I. Cohen, R.C. Daniel, (1967) Thermal conductivity of bulk oxide fuels. WAPD–TM–586, Bettis Atomic Power Laboratory, West Mifflin.
92. W.D. Kingery, J. Francl, R.L. Cobble, T. Vasilos, J. Am. Ceram. Soc. 37(1954)107–110.
93. C. Ronchi, M. Sheindlin, M. Musella, G.J. Hyland, J. Appl. Phys 85(1999)776–789.
94. D.C. Jacobs, (1969) Report WAPD–TM–758, Bettis Atomic Power Laboratory, West Mifflin.
95. J. Matolich and V.W. Storhok (1970) Thermal diffusivity measurements of irradiated oxide fuels. Battelle Memorial Institute Report BMI–RX–10274, Columbus.
96. R. K. Bhagat, K. Krishnan, T.R.G. Kutty , Arun Kumar, H.S. Kamath , S. Banerjee, J. Nucl. Mat. 422 (2012) 152–157.
97. A.K. Tyagi, B.R. Ambekar, M.D. Mathews, J. Alloys Compd. 337 (2002) 277– 281.
98. M.D. Mathews, B.R. Ambekar, A.K. Tyagi, J. Nucl. Mater. 288 (2001) 83–85.
99. D. Barrier, A.A. Bukaemskiy, G. Modolo, J. Nucl. Mat., 352 (2006) 357–364.
100. H.S. Kim, C.Y. Joung, B.H. Lee, J.Y. Oh, Y.H. Koo, P. Heimgartner, J. Nucl. Mater. 378 (2008) 98–104.
101. C.F. Chen, J. Kelly, O. Asphjell, P.A. Papin, R.T. Forsyth, D.R. Guidry, D.J. Safarik, A.L Lobet, J. Am. Ceram. Soc., 97(10) (2014) 3062–3070.
102. O. Yildiz, J. Nucl. Mater. 366 (2007) 266–271.
103. A.A. Bukaemskiy, D.Barrier, G.Modolo, J. Alloys Compd. 485 (2009) 783–788.
104. M.D. Mathews, B.R. Ambekar, A.K. Tyagi, J. Nucl. Mat., 280 (2000) 246–249.
105. V. Grover, A.K. Tyagi, Ceram. Int. 31 (2005) 769.

106. V. Grover, P. Sengupta, K. Bhanumurthy, A.K. Tyagi, *J. Nucl. Mater.*, 350 (2006) 169–172.
107. M. Murabayashi, Thermal conductivity of ceramic solid solutions. *J Nucl. Sci. Technol.* 7 (1970) 559–563.
108. T. Nelson, D.R. Rittman, J.T. White, J.T. Dunwoody, M. Kato, K.J. McClellan, *J. Am. Cer. Soc.*, 97(11) (2014) 3652–3659.
109. C. Sevik, T. Cag˘in, *Rev. B: Condens. Matter Mater. Phys.* 80 (2009) 014108–014114.
110. V. Kanchana, G. Vaitheeswaran, A. Svane, A. Delin, *J. Phys.: Condens. Matter* 18 (2006) 9615–9624.
111. H.Y. Xiao, W.J. Weber, *J. Phys. Chem. B* 115 (2011) 6524–6533.
112. S.C. Middleburgh, G.R. Lumpkin, R.W. Grimes, *Solid State Ionics* 253 (2013) 119–122.
113. T.Y. Shvareva, V. Alexandrov, M. Asta, A. Navrotsky, *J. Nucl. Mat.* 419 (2011) 72–75.
114. P.S. Ghosh, P.S. Somayajulu, A. Arya, G.K. Dey, B.K. Dutta, *J. Alloys Compd.* 638 (2015) 172–181.
115. S.J. Paprocki, D.L. Keller, W.M. Pardue, USAEC Report APEX–696, Nuclear Materials and Propulsion Operation, General Electric, October, 1961.
116. M.D. Freshley and H.M. Mattys, Hanford Power Products Division, Richland, Washington, HW–76300, 1962.
117. M.D. Freshley and H.M. Mattys, Hanford Power Products Division, Richland, Washington, HW–76302, 1963.

118. A.T. Jeffs, *Trans. Am. Nucl. Soc.* 11 (1968) 497.
119. D.E. Ramissen, M.W. Benecke, W.R. Jentzen, R.B. McCord, *Trans. Am. Nucl. Soc.* 32 (1979) 246.
120. R.N.R. Mulford and F.H. Ellinger, *J. Phys. Chem.* 62 (1958) 1466–1467.
121. *Gmelin Handbook der Anorganischen Chemie, Thorium, Suppl, vols C1 and C2* 8th edn. (1978) Springer, Berlin.
122. S. Peterson and C.E. Curtis, *Thorium ceramics data manual volume I—oxide*. Report ORNL–4503 (1970) Oak Ridge Nation Laboratory, Oak Ridge.
123. IAEA–TECDOC 1496, *Thermophysical properties database of materials for light water reactors and heavy water reactors* (2006), International Atomic Energy Agency, Vienna.
124. U. Basak, A.K. Sengupta, C. Ganguly, *J. Mater. Sci. Lett.* 8(1989) 449–450.
125. A.T. Jeffs, R.R. Boucher, L.R. Norlock, Report AECL–2675, (1967) Atomic Energy Canada Limited, Chalk River.
126. A.T. Jeffs, AECL–3294, (1969) Atomic Energy Canada Limited, Chalk River.
127. C. Cozzo, D. Staicu, J. Somers, A. Fernandez, R.J.M. Konings, *J. Nucl. Mater.* 416 (2011) 135–141.
128. C. Swanson Gerald, *Oxygen Potential of Uranium–Plutonium Oxide as determined by Controlled–Atmosphere Thermogravimetry*. Dissertation, LA–6083–T, (1975).
129. R.K. Kirby and T.A. Hahn, National Bureau of Standards, *Standard Reference Material 737*.
130. K.V. Vrinda Devi, T. Soreng, J.P. Panakkal, H.S. Kamath, *Nucl. Tech.*, 164 (2), 305–308.

131. O.J. Wick, Plutonium Handbook, Vol.1, American Nuclear Society, Illinois, 1980.
132. S. Omar and J.C. Nino, *Acta Mat.* 61 (2013) 5406–5413.
133. R. D. Shannon, *Acta Crystallogr. A* 32, 751–767 (1976).
134. M.N. Rahaman, *Ceramic processing and sintering*, ISBN 9780824709884, CRC Press, 2003. New York.
135. W. Miao, Y. Wu, H. Zhou, W. Han, F. Ru, *Mat. Lett.* 30 (1970) 411–414.
136. M.N.Rahaman and Y.C.Zhou, *J. Eur. Cer. Soc.*, 15(1995) 939–950.
137. F. F. Lange, *J. Am. Ceram. Soc.*, 72 [1] (1989) 3–15.
138. F. F. Lange, *J. Am. Ceram. Soc.*, 67 [2] (1984) 83–89.
139. F. F. Lange and M. Metcalf, *J. Am. Ceram. Soc.*, 66 [6] (1983) 398–406.
140. R. G. Frey and J. W. Halloran, *J. Am. Ceram. Soc.*, 67 [3] (1984) 199–203.
141. W.H. Rhodes, *J. Am. Ceram. Soc.*, 64 [1] (1981)19–22.
142. R. M. Batista and E. N. S. Muccillo, in: *ECS Transactions*, 61 (1) (2014) 361–367.
143. J. T. S. Irwine, D. C. Sinclair, A.R. West, *Adv. Mater.* 2, 3 (1990) 132–138.
144. T. Van Dijk and A. J. Burggraaf, *phys. stat. sol. (a)* 63, (1981) 229 –240.
145. K. C. Radford and R. J. Bratton, *J. Mater. Sci.* 14 (1979) 66–69.
146. I. Barin, “Thermochemical data of pure substances”, Third edition, VCH publication, 1995.
147. H.Y. Xiao, Y. Zhang, W.J. Weber, *Acta Mat.*, 61 (2013) 467–476.
148. R. Kandan, R. Babu , P. Manikandan, K.R. Venkata, K. Nagarjan, *J. Nucl. Mater.* 384(2009) 231–235.
149. R. Agarwal, R. Prasad, V. Venugopal, *J. Nucl. Mat.*, 322 (2003) 98–110.

150. M.W.D. Cooper, M.J.D. Rushton, R.W. Grimes, *J. Phys. Condens. Matter*, 26 (2014) 105401.
151. M.W.D. Cooper, S.T. Murphy, P.C.M. Fossati, M.J.D. Rushton, R.W. Grimes, in: *Proc. R. Soc. A* 470 (2014) 14.
152. M.D. Mathews, B.R. Ambekar, A.K. Tyagi, *J. Nucl. Mater.* 288 (2001) 83.
153. L. Gerward, J. Staun Olsen, L. Petit, G. Vaitheeswaran, V. Kanchana, A. Svane, *J. Alloys Compd.* 400 (2005) 56.
154. T. Arima, S. Yamasaki, Y. Inagaki, K. Idemitsu, *J. Alloys Compd.* 400 (2005) 43.
155. R.K. Behera, C.S. Deo, *J. Phys.: Condens. Matter* 24 (2012) 215405.
156. P.S. Ghosh, P.S. Somayajulu, R. Krishnan, N. Pathak, A. Arya, G.K. Dey, *J. Alloys Compd.* 650 (2015) 165–177.
157. S. Plimpton, *J. Comput. Phys.* 117 (1995) 1–19.
158. P.P. Ewald, *Ann. Phys.* 64 (1921) 253.
159. R. Hill, *Proc. Phys. Soc. London* 65 (1952) 349.
160. A. Reuss, *Z. Angew. Math. Phys.* 9 (1929) 49.
161. W. Voigt, *Ann. Phys. (Leipzig)* 38 (1889) 573.
162. M.D. Mathews, B.R. Ambekar, A.K. Tyagi, *J. Nucl. Mater.* 288 (2001) 83–85.
163. M.D. Mathews, B.R. Ambekar, A.K. Tyagi, *J. Nucl. Mater.* 280 (2000) 246–249.
164. A.K. Tyagi, M.D. Mathews, B.R. Ambekar, R. Ramachandran, *Thermochem. Acta* 421 (2004) 69.
165. L.G.V. Uitert, H.M. O’Byryan, M.E. Lines, H.J. Guggenheim, G. Zydig, *MAT. Res. Bull.*, 12 (1977) 251.
166. T. Ihle and D.M. Kroll, *Phys. Rev. E* 63, 020201(R) (2001).

167. Jean–Pierre Rivet, *Complex Systems* 1 (1987) 839–851.
168. M.W.D. Cooper, S.T. Murphy, M.J.D. Rushton, R.W. Grimes, *J. Nucl. Mater.* 461 (2015) 206–215.
169. P. Klemens, in: *Thermal Conductivity and Lattice Vibrational Modes*, vol. 7, Academic Press, New York, 1959.
170. K. Une, S. Kashibe, K. Ito, *J. Nucl. Sci. Technol.*, 30, (1993) 221–231.
171. H. Zimmermann, *J. Nucl. Mater.* 75 (1978) 154–161.
172. J. A. Turnbull, *J. Nucl. Mater.* 50 (1974) 62–68.
173. I.J. Hastings, *J. Am. Ceram. Soc.*, 66, C–150 (1983) 284–288.
174. Y. Harada and S. Doi, *J. Nucl. Sci. Tech.* 35, 6 (1998), 411–418.
175. M. D. Freshley, D. W. Brite, J.L. Daniel, P.E. Hart, *J. Nucl. Mater.* 62, (1976) 138–166.
176. H. Assmann, H. Stehle, *Nucl. Eng. Des.* 48, (1978) 49–67.
177. G.M.H. Maier, H. Assmann, W. Doerr, *J. Nucl. Mater.* 153, (1988) 213 –220.
178. P. S. Somayajulu, A. Sengupta, A. K. Karande, R. Malav, D. K. Das, Mohd. Afzal, *J. Radioanal. Nucl. Chem.*, DOI 10.1007/s10967–015–4411–z, 1–9.
179. T.S. Rao, B.B. Shriwastwa, J.N. Dubey, B.P. Patil, K.N. Chandrasekharan, V.D. Pandey, S. Majumdar, *Radiation Measurements* 36 (2003) 747 – 750.
180. I.H. Shaikh, J.N. Dubey, Jyoti Gupta, B.B. Shriwastwa, K.V. Vrinda Devi, P.S. Somayajulu, K.B. Khan, Arun Kumar, in: *Proc. of National Conference on Power from Thorium: Present Status and Future Directions*, Mumbai, ( 2014), 103.
181. M. El Ghazaly, H.E. Hassan, *Results in Physics*, 4 (2014) 40–43.

182. J.S. Herring, P.E. MacDonald, K.D. Weaver, C. Kullberg, *Nucl. Engg. and Design*, 203 (2001) 65–85.
183. Y. Yun, P.M. Oppeneer, H. Kim, K. Park, *Acta Mater.* 57 (2009) 1655–1659.
184. Hj. Matzke, in: T. Sorensen (Ed.), *Non–stoichiometric Oxides*, Academic Press, New York, 1981, 156.
185. Hj. Matzke, *J. Chem. Soc. Faradays, Trans. 2*, 86 (1990) 1243.
186. A.B. Lidiard, *J. Nucl. Mater.* 19 (1966) 106.
187. W.C. Pritchard, R.L. Nance, Los Alamos Report, Los Alamos, LA–3493, 1965.
188. T.D. Chikalla, C.E. McNeilly, R.E. Skavdahl, *J. Nucl. Mater.* 12 (1964) 131.
189. T.R.G. Kutty, P.V. Hegde, K.B. Khan, S. Majumdar, D.S.C. Purushotham, *J. Nucl. Mater.* 281 (2000) 10.
190. T.R.G. Kutty, P.V. Hegde, R. Keswani, K.B. Khan, S. Majumdar, D.S.C. Purushotham, *J. Nucl. Mater.* 264 (1999) 10.
191. T.R.G. Kutty, K.B. Khan, P.V. Hegde, A.K. Sengupta, S. Majumdar, D.S.C. Purushotham, *J. Nucl. Mater.* 297 (2001) 120.
192. K.V. Vrinda Devi and J.P. Panakkal, *Nucl. Engg. and Design*, 255 (2013) 132– 137.
193. M.D. Mathews, B.R. Ambekar, A.K. Tyagi, *J. Nucl. Mater.* 288 (2001) 83–85.
194. M.D. Mathews, B.R. Ambekar, A.K. Tyagi, *J. Nucl. Mater.* 280 (2000) 246–249.
195. D. Das and S. R. Bharadwaj (eds.), in: *Thoria–based Nuclear Fuels, Green Energy and Technology*, DOI: 10.1007/978–1–4471–5589–8\_2, Springer–Verlag London 2013.
196. I.S. Kurina, L.S. Gudkov, V.N. Rumyantsev, *Atomic Energy* 92 (2002) 461, 54.

197. D.R. Olander, in: *Fundamental Aspects of Nuclear Reactor Fuel Elements*, TID-26711-P1, US Department of Energy, 1976.
198. S.E. Lemehov, V. Sobolev, P. Van Uffelen, *J. Nucl. Mater.* 320 (2003) 66.
199. R.A. Young, *J. Nucl. Mater.* 87 (1979) 283.
200. T.R.G. Kutty, P.V. Hegde, K.B. Khan, U. Basak, S.N. Pillai, A.K. Sengupta, G.C. Jain, S. Majumdar, H.S. Kamath, D.S.C. Purushotham, *J. Nucl. Mat.*, 305 (2002) 159–168.
201. T.R.G. Kutty, P.V. Hegde, K.B. Khan, T. Jarvis, A.K. Sengupta, S. Majumdar, H.S. Kamath, *J. Nucl. Mat.*, 335 (2004) 462–470.
202. C.W. Kuhlman, in Report MCW-215, 1949.
203. S. Aronson and J.C. Clayton, *J. Inorg. Nucl. Chem.* 7 (1958)384.
204. K.W. Song, K.S. Kim, Y.H. Jung, *J. Nucl. Mater.* 27(2000) 356.
205. J. Belle, B. Lustman, in: *Properties of UO<sub>2</sub>*, Fuel Elements Conference, Paris, TID-7546, 1958, 442.
206. W.R. DeHollander, Hanford Report, HW-46685, 1956.
207. S. Aronson, in: J. Belle (Ed.), *UO<sub>2</sub>: Properties and Nuclear Applications*, USAEC, 1961, p. 415.
208. S. Perrin, M. Pijolat, F. Valdivieso, M. Soustelle, in: *High Temperature Corrosion and Materials Chemistry*, 203rd Meeting of The Electrochemical Society, Paris, 2003.
209. A.K. Tyagi, M.D. Mathews, B.R. Ambekar, R. Ramachandran, *Thermochemica Acta* 421 (2004) 69.
210. F. Hund, G. Niessen, *Z. Elektrochem.* 56 (1952) 972.
211. Y. Harada, *J. Nucl. Mater.* 245 (1997) 217–223.

212. R. Paul, C. Keller, *J. Nucl. Mater.* 41 (1971) 133.
213. K.W. Lay, R.E. Carter, *J. Nucl. Mater.* 30 (1969) 74.
214. A.K. Tyagi and M.D. Mathews, *J. Nucl. Mater.* 278 (2000) 123.
215. J.H. Yang, K.W. Kang, K.W. Song, C.B. Lee, Y.H. Jung, *Nucl. Tech.*, 47 (2004) 113–119.